Compact Binaries

Part I

Frank Verbunt

this version: March 13, 2015

these lecture notes will be extended and adapted as the course proceeds. please check the date above to see whether your download is the most recent one.

Astronomical and physical constants

Physical constants are constant, but the values we assign to them improve with the quality of measuring apparatus. That is why the date must be given at which the value one uses is taken. The *National Institute of Standards and Technology* in Maryland, U.S.A., keeps track of new measurements of physical constants, and every few years updates the list of recommended values. The information is collected on a website: `http://physics.nist.gov/cuu/Constants` This site also gives the paper in which the (updates of) the constants are described. From the December 2007 preprint of this paper we copy Table *XLIX* below, which is based on the 2006 adjustment.

Quantity	Symbol	Numerical value	Unit	Relative std. uncert. u_r
speed of light in vacuum	c, c_0	299 792 458	m s^{-1}	(exact)
magnetic constant	μ_0	$4\pi \times 10^{-7}$	N A^{-2}	
		$= 12.566\,370\,614... \times 10^{-7}$	N A^{-2}	(exact)
electric constant $1/\mu_0 c^2$	ϵ_0	$8.854\,187\,817... \times 10^{-12}$	F m^{-1}	(exact)
Newtonian constant of gravitation	G	$6.674\,28(67) \times 10^{-11}$	m^3 kg^{-1} s^{-2}	1.0×10^{-4}
Planck constant	h	$6.626\,068\,96(33) \times 10^{-34}$	J s	5.0×10^{-8}
$h/2\pi$	$\hbar$	$1.054\,571\,628(53) \times 10^{-34}$	J s	5.0×10^{-8}
elementary charge	e	$1.602\,176\,487(40) \times 10^{-19}$	C	2.5×10^{-8}
magnetic flux quantum $h/2e$	Φ_0	$2.067\,833\,667(52) \times 10^{-15}$	Wb	2.5×10^{-8}
conductance quantum $2e^2/h$	G_0	$7.748\,091\,7004(53) \times 10^{-5}$	S	6.8×10^{-10}
electron mass	m_e	$9.109\,382\,15(45) \times 10^{-31}$	kg	5.0×10^{-8}
proton mass	m_p	$1.672\,621\,637(83) \times 10^{-27}$	kg	5.0×10^{-8}
proton-electron mass ratio	m_p/m_e	1836.152 672 47(80)		4.3×10^{-10}
fine-structure constant $e^2/4\pi\epsilon_0\hbar c$	α	$7.297\,352\,5376(50) \times 10^{-3}$		6.8×10^{-10}
inverse fine-structure constant	α^{-1}	137.035 999 679(94)		6.8×10^{-10}
Rydberg constant $\alpha^2 m_e c/2h$	R_∞	10 973 731.568 527(73)	m^{-1}	6.6×10^{-12}
Avogadro constant	N_A, L	$6.022\,141\,79(30) \times 10^{23}$	mol^{-1}	5.0×10^{-8}
Faraday constant $N_A e$	F	96 485.3399(24)	C mol^{-1}	2.5×10^{-8}
molar gas constant	R	8.314 472(15)	J mol^{-1} K^{-1}	1.7×10^{-6}
Boltzmann constant R/N_A	k	$1.380\,6504(24) \times 10^{-23}$	J K^{-1}	1.7×10^{-6}
Stefan-Boltzmann constant $(\pi^2/60)k^4/\hbar^3 c^2$	σ	$5.670\,400(40) \times 10^{-8}$	W m^{-2} K^{-4}	7.0×10^{-6}
Non-SI units accepted for use with the SI				
electron volt: (e/C) J	eV	$1.602\,176\,487(40) \times 10^{-19}$	J	2.5×10^{-8}
(unified) atomic mass unit 1 u $= m_u = \frac{1}{12} m(^{12}C)$ $= 10^{-3}$ kg mol^{-1}/N_A	u	$1.660\,538\,782(83) \times 10^{-27}$	kg	5.0×10^{-8}

Table C.1 Physical Constants, from `http://physics.nist.gov/cuu/Constants`

Note that the first three constants are *defined* and therefore have no measurement errors!

In addition to the constants given in Table C.1, we list in Table C.2 some derived physical constants (from the same source, Table L), and also some astronomical constants, taken from Section K6 of the *Astronomical Almanac for the year 2006*. The astronomical constants are *defined* by the Interational Astronomical Union at values close to the actual value, and therefore have no errors, unlike the measured values.

In the exercises throughout this lecture, use 3 digits; except in the computer exercises, where the full accuracy is used.

quantity	symbol	numerical value (w. error)
	Additional physical constants	
neutron mass	m_n	$1.674927211(84) \times 10^{-27}$ kg
	$=$	1.00866491597(43) amu
$a \equiv 4\sigma/c$	a	$7.56591(25) \times 10^{-1?}$ J cm^{-3}K^{-4}
electron radius	$r_e = e^2/4\pi\epsilon_o m_e c^2$	$2.817940325(28)\times10^{-15}$ m
e Compton wavelength	$\hbar/m_e c = r_e/\alpha$	$3.861592678(26)\times10^{-13}$ m
Bohr radius	$a_\infty = 4\pi\epsilon_o\hbar^2/m_e c^2 = r_e/\alpha^2$	$0.5291772108(18)\times10^{-10}$ m
wavelength at 1 keV	hc/keV	12.3984191(11) Å keV^{-1}
Rydberg energy	$m_e c^2\alpha^2/2$	13.6056923(12) eV
Thomson cross section	$\sigma_T = 8\pi {r_e}^2/3$	0.665245873(13) barn
a	$a \equiv 4\sigma/c$	$7.56577(5)\times10^{-16}$ J m^{-3} K^{-4}
Wien constant	$b = \lambda_{\max}T$	$2.8977685(51)\times10^{-3}$ m K
	Astronomical constants	
solar mass	$GM_\odot$	$1.32712442076\times10^{20}$ m^3 s^{-2}
solar mass	$M_\odot$	1.9884×10^{30} kg
solar radius	$R_\odot$	6.96×10^8 m
astronomical unit	*A.U.*	$1.49597871 \times 10^{11}$ m
Julian year	yr	365.25×86400 s
	unofficial:	
solar luminosity	$L_\odot$	$\simeq 3.85 \times 10^{26}$ J s^{-1}
parsec	pc	$\simeq 3.086 \times 10^{16}$ m
Solar temperature	T_{eff}	$\simeq$5780 K
Hubble constant	H_o	70 km s^{-1} Mpc^{-1}

Table C.2 Additional physical constants
from `http://physics.nist.gov/cuu/Constants` Table L
and astronomical constants, from Astronomical Almanac for 2006, K6

Some remarks on angles

A circle is divided in 360 degrees ($^\circ$), each degree in 60 minutes ($'$), and minute in 60 arcseconds ($''$). 2π radians thus correspond to $360 \times 60 \times 60$ arcseconds, i.e. $1''$ corresponds to $\simeq 4.848 \times 10^{-6}$radians. The circle of right ascension is divided into 24 hours (^{h}), each hour in 60 minutes (^{m}), each minutes in 60 seconds (^{s}). The arcsecond ($''$) has a fixed size on the celestial dome, whereas the second (^{s}) has an extent which depends on the declination. At the equator 1^h corresponds to 15°, at declination δ, 1^h corresponds to $15^\circ \cos\delta$.

Chapter 1

Historical Introduction

This chapter gives a brief historical overview of the study of binaries in general and compact binaries in particular, and in doing so explains some of the terminology that is still used.

1.1 History until 1900[1]

It has been noted long ago that stars as seen on the sky sometimes occur in pairs. Thus, the star list in the Almagest of Ptolemaios, which dates from ±150 AD, describes the 8th star in the constellation Sagittarius as 'the nebulous and double (διπλοῦς) star at the eye'. After the invention of the telescope (around 1610) it was very quickly found that some stars that appear single to the naked eye, are resolved into a pair of stars by the telescope. The first known instance is in a letter by Benedetto Castelli to Galileo Galilei on January 7, 1617, where it is noted that Mizar is double.[2] Galileo observed Mizar himself and determined the distance between the two stars as 15″. The discovery made its way into print in the 'New Almagest' by Giovanni Battista Riccioli in 1650, and as a result Riccioli is often credited with this discovery. In a similar way, Huygens made a drawing showing that θ Orionis is a triple star (Figure 1.1), but the presence of multiple stars in the Orion nebula had already been noted by Johann Baptist Cysat SJ[3] 1618.

The list of well-known stars known to be double when viewed in the telescope includes the following:

year	star	published by	comment
1650	Mizar (ζ UMa)	Riccioli	found earlier by Castelli
1656	θ Ori	Huygens	triple, found earlier by Cysat
1685	α Cru	Fontenay SJ	
1689	α Cen	Richaud SJ	
1718	γ Vir	Bradley	
1719	Castor (α Gem)	Pound	
1753	61 Cygni	Bradley	

[1] This Section borrows extensively from Aitken 1935

[2] see the article on Mizar by the Czech amateur astronomer Leos Ondra on `leo.astronomy.cz`

[3] SJ, Societatis Jesu, i.e. from the Society of Jesus: a Jesuit. Jesuits attached great importance to education and science, and during the counter-reformation trained good astronomers. Examples are the first European astronomers in China: Ricci (1552-1610) and Verbiest (1623-1688); and the rediscoverers of ancient Babylonian astronomy: Epping (1835-1894) and Kugler (1862-1929)

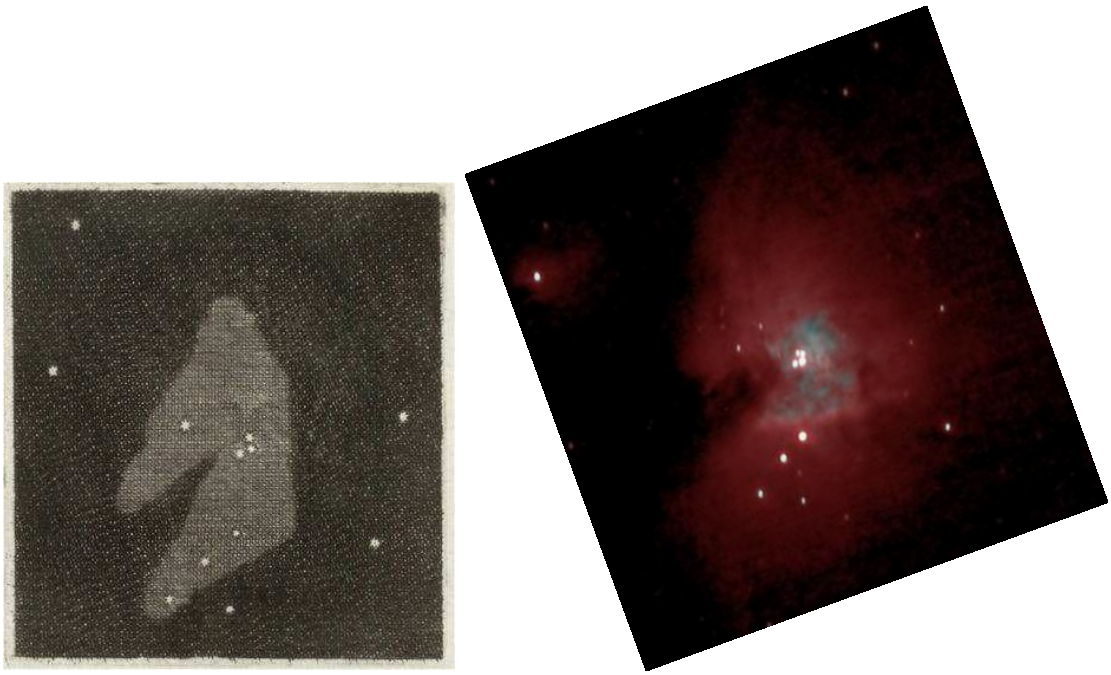

Figure 1.1: *Drawing of the Orion nebula made by Huygens (left) compared with a modern photograph (from* `www.integram.com/astro/Trapezium.html`*, right).*

All these doubles were not considered to be anything else than two stars whose apparent positions on the sky happened to be close. Then in 1767 the British astronomer John Michell noted and proved that this closeness is not due to chance, in other words that most pairs are real physical pairs. An important consequence is that stars may have very different intrinsic brightnesses. Michell argues as follows (for brevity, I modernize his notation). Take one star. The probability p that a single other star placed on an arbitrary position in the sky is within x° ($=0.01745x$ rad) from the first star is given by the ratio of the surface of a circle with radius of x degrees to the surface of the whole sphere: $\pi \times (0.01745x)^2/(4\pi) \simeq 7.615 \times 10^{-5}x^2$, for $p \ll 1$. The probability that it is not in the circle is $1-p$. If there are n stars with a brightness as high as the faintest in the pair considered, the probability that none of them is within x degrees is $(1-p)^n \simeq 1-np$, provided $np \ll 1$. Since for the first star we also have n choices, the probability of no close pair anywhere in the sky is $(1-p)^{n\times n} \simeq 1-n^2p$. As an example, Michell considers β Capricorni, two stars at $3'20''$ from one another, i.e. $x = 0.0555$, with $n = 230$. The probability of one such a pair in the sky due to chance is 1 against 80.4. With a similar reasoning, Michell showed that the Pleiades form a real star cluster.

visual binary

statistical

As an aside, we consider the Bright Star Catalogue. For each star in this catalogue, we compute the distance to the nearest (in angular distance) other star, and then show the cumulative distribution of nearest distances in Figure 1.2. (Stars in the catalogue with the exact position of another star, or without a position, have been removed from this sample.) We then use a random generator to distribute the same number of stars randomly over the sky, and for these plot the cumulative nearest-distance distribution in the same Figure. It is seen that the real sky has an excess of pairs with distances less than about 0.1°.

Starting in 1779 William Herschel compiled a list of close binaries. In doing so he was following an idea of Galileo: if all stars are equally bright, then a very faint

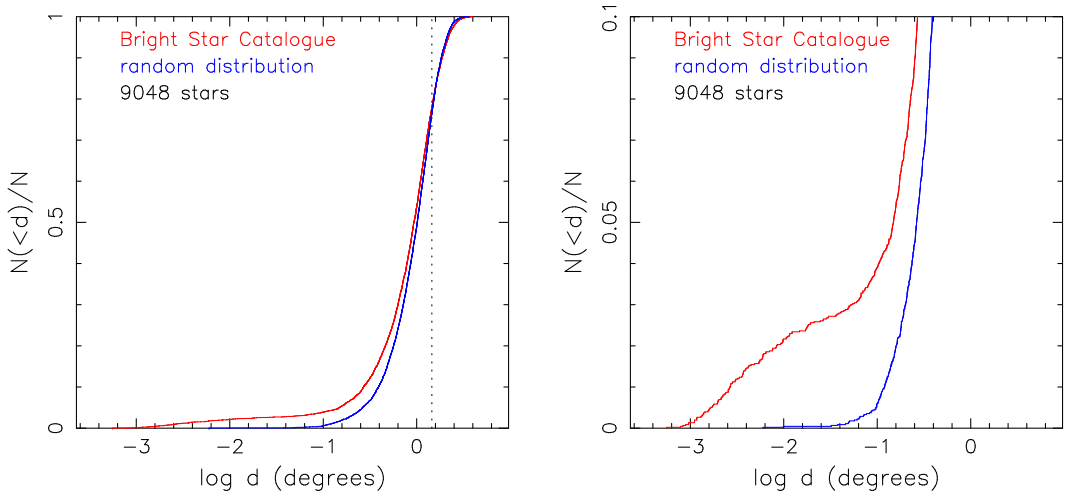

Figure 1.2: *Cumulative distribution of the angular distance to the nearest star for the stars in the Bright Star Catalogue (only stars with an independent catalogued position are included), and for the same number of stars distributed randomly over the sky.*

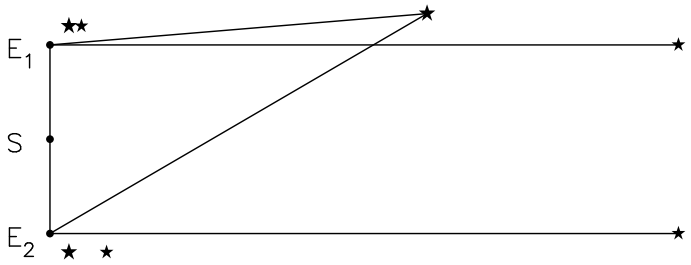

Figure 1.3: *Illustration of Galileo's idea of measuring the parallax from a close pair of stars. If all stars are equally bright intrinsically, the fainter star is much further than the bright star, and its change in direction as the Earth (E) moves around the Sun (S) negligible with respect to that of the bright star. The figure shows the change in relative position as the Earth moves from E_1 to E_2 half a year later.*

star next to a bright one must be much further away. From the annual variation in angular distance between the two stars, one can then accurately determine the parallax of the nearer, brighter star (Figure 1.3). Herschel found many such pairs, which he published in catalogues. He notes that close pairs can be used to test the quality of a telescope and of the weather (Herschel 1803).

Herschel first assumed that the double stars are not physical, but soon realised that most must be physical pairs, and then defined single and double stars (Herschel 1802):

> *When stars are situated at such immense distances from each other as our sun, Arcturus, Capella, Sirius, Canobus* (sic)*, Markab, Bellatrix, Menkar, Shedir, Algorah, Propus, and numerous others probably are, we may then look upon them as sufficiently out of reach of mutual attractions, to deserve the name of insulated stars.*
>
> *If a certain star should be situated at any, perhaps immense, distance behind another, and but very little deviating from the line in which we see*

the first, we should then have the appearance of a double star. But these stars, being totally unconnected, would not form a binary system. If, on the contrary, two stars should really be situated very near each other, and at the same time so far insulated as not to be materially affected by the attraction of neighbouring stars, they will then compose a separate system, and remain united by the bond of their own mutual gravitation towards each other. This should be called a real double star; and any two stars that are thus mutually connected, form the binary system which we are now to consider.

Chapter 2.1

It is easy to prove, from the doctrine of gravitation, that two stars may be so connected together as to perform circles, or similar ellipses, round their common centre of gravity. In this case, they will always move in directions opposite and parallel to each other; and their system, if not destroyed by some foreign cause, will remain permanent.

Apparently unaware of Michell's earlier work, Herschel computed the probability of getting a pair of stars with magnitudes 5 and 7, respectively, within 5″ of one another, given the numbers of stars with magnitudes 5 and 7. He concluded that such close pairs are real binaries.

Herschel observed α Geminorum, also known as Castor, between November 1779 and March 1803. The less luminous of the two stars was to the North, and preceding (i.e. with smaller right ascension) during this time, and to the accuracy of Herschel's measurements always at the same distance of the brighter star. By taking multiple observations on the same day, he obtained an estimate of the error with which he determined the positional angle: under ideal circumstances somewhat less than a degree. He used an observation by Bradley in 1759, confirmed by Maskelyne in 1760, that the two stars of Castor were in line with the direction between Castor and Pollux, to extend his time range. Herschel gives his data only in tabular form; plots of his values are given in Figure 1.4. For a circular orbit, Herschel concludes from the change between 1759 and 1803 that the binary period is about 342 years and two months (a modern estimate is 467 yrs; see Table 3.1). Herschel argues that it is virtually impossible that three independent rectilinear motions of the sun and the two stars of Castor produce the observed apparent circular orbit. He strenghtens the argument by considering five other binaries, viz. γ Leonis, ϵ Bootis ('This beautiful double star, on account of the different colours of the stars of which it is composed'), ζ Herculis, δ Serpentis and γ Virginis.

visual binary individual

The list of close pairs of stars increased with time, and some astronomers specialised in finding them. In Dorpat (modern Tartu in Estonia) Frederich Struve systematically scanned the sky between the North pole and $-15°$, examining 120 000 stars in 129 nights between November 1824 and February 1827. With bigger telescopes, close pairs were increasingly found. Therefore the lists of binaries became longer and longer, especially after John Herschel's suggestion was followed to include individual measurements of angular distance and position angle with the date of observation. Flammarion's selection of only those pairs where orbital motion had been observed was very helpful.

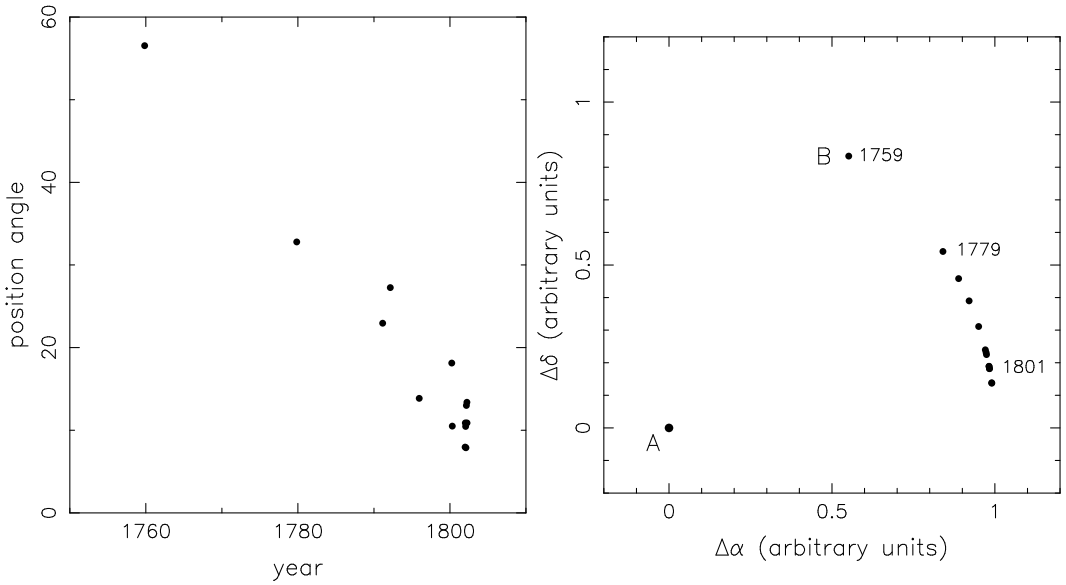

Figure 1.4: *William Herschel observed the position angle of the two stars in Castor between 1779 and 1803; and added a measurement by Bradley from 1759, and discovered the motion of the two stars in the binary orbit.*

year	astronomer	$N_{\rm bin}$	comment
1779	Mayer	80	faint companions to bright stars
1784	W. Herschel	703	
1823	J. Herschel & J. South	380	southern sky
1827	Struve	3110	
1874	J. Herschel	10 300	published postumously
1878	Flammarion	819	only pairs with observed binary motion

The micrometer, invented by W. Herschel, was continously improved so that measurements of angular distances and position angles became increasingly accurate. Further improvements came with photography, which, as Hertzsprung remarked, provides a 'permanent document'. The first binary to be photographed, in 1857 by Bond, was... Mizar.

Methods to derive the orbital parameters from a minimum of 4 observations were developed by Savary (1830), Encke (1832), and J. Herschel (1833), and many others. In these methods, an important consideration is to minimize the number of computations; as a result they are now only of historic interest.

Meanwhile another binary phenomenon had gradually been understood. In 1670 Geminiano Montanari had discovered that the star β Persei varies in brightness. β Persei is also called Algol, 'the Demon', the Arabic translation of Ptolemy's Medusa, whose severed head Perseus is holding[4]. John Goodricke discovered in 1782 that the variation is periodic, with about two-and-a-half days (modern value: 2.867 d), and suggested as one possibility that the darkening was due to the passage of a giant planet in front of the star. *eclipsing binary*

This suggestion was spectacularly confirmed when a third method of studying

[4]Contrary to what has been asserted, therefore, the name Algol does not suggest that the Arabic astronomers already knew about the variability.

binaries was implemented: the measurement of radial velocity variations. In 1889 Pickering showed that the spectral lines of... Mizar doubled periodically, reflecting Doppler variations due to the orbital motion. In the same year Vogel showed that the spectral lines of Algol were shifted to the red before the eclipse, and to the blue after the eclipse, and thereby confirmed the eclipse interpretation of Goodricke. A binary in which the orbital variation is observed in the spectral lines of both stars, like Mizar, is called a *double-lined spectroscopic binary*, if the spectral lines of only one star are visible in the spectrum, we speak of a *single-lined spectroscopic binary*.

spectroscopic binary

single- or doublelined

It is now known that the spectroscopic period of Mizar is 20.5 d, much too short for the two stars that Castelli and Galileo observed through their telescopes and that Bond photographed. In a visual binary, the brighter star is usually (but confusingly not always) referred to as star A, the fainter one as star B. The 20.5 d period shows that Mizar A is itself a binary. Mizar B is also a binary, with a 175.6 d period.

The first catalogue of spectroscopic binaries was published in 1905 by Campbell, with 124 entries. The catalogue that Moore published in 1924 already had 1054 entries. Methods for deriving the binary parameters were devised by Rambaut in 1891, and by Lehman-Filhés in 1894. Soon the number of orbits determined from spectroscopy surpassed the number of visually determined orbits. The reason is straightforward: spectroscopic orbits must be short to be measurable, a visual orbit long. Therefore a spectroscopic orbit can be found in a shorter time span. Equally important is that a spectroscopic binary can be detected no matter what its distance is, whereas the detection of visual orbits requires nearby binaries.

1.2 Lightcurves and nomenclature

As the number of eclipsing binaries grew, different types were discriminated. The simplest type, often called the Algol type, shows two eclipses per orbit, of which the deeper one is called the primary eclipse. To interpret this, consider a binary of a hot and a cold star. When the cold star moves in front of the hot star, the eclipse is deep, and when the hot star moves in front of the cool star, the eclipse is shallow.

primary eclipse

When the two stars in a binary are far apart and non-rotating, they are spherical, and thus the lightcurve is flat between the eclipses. When the stars are closer they are deformed under the influence of one another, elongated along the line connecting the centers of the two stars. Thus the surface area that we observe on earth is largest when the line of sight to the Earth is perpendicular to the line connecting the two stars, and this is reflected in a lightcurve that changes throughout the orbit. Such variations are called *ellipsoidal variations*. When both stars touch, their deformation causes large variations throughout the orbit. To describe the form of the stars under the influence of one another's gravity, we must compute the equilibrium surfaces in the potential of two stars: the *Roche geometry*.

ellipsoidal variations

Chapter 3.4

The study of lightcurves showed up more and more details, or complications, depending on your point of view....

Thus, if one small star disappears for a time behind a bigger star, the minimum of its eclipse is flat (i.e. of constant flux). Clearly, the length of ingress and egress, and of the bottom of the eclipse, contain information on the relative sizes of the two binary stars. Rapidly rotating stars are flattened, leading to different eclipse forms. Stars can have variable spots on them, leading to variable lightcurves. Gas can flow from one star to the other, leading to asymmetric lightcurves, and in fact also to

Chapter 4.3.1

rotation

spots

gas streams

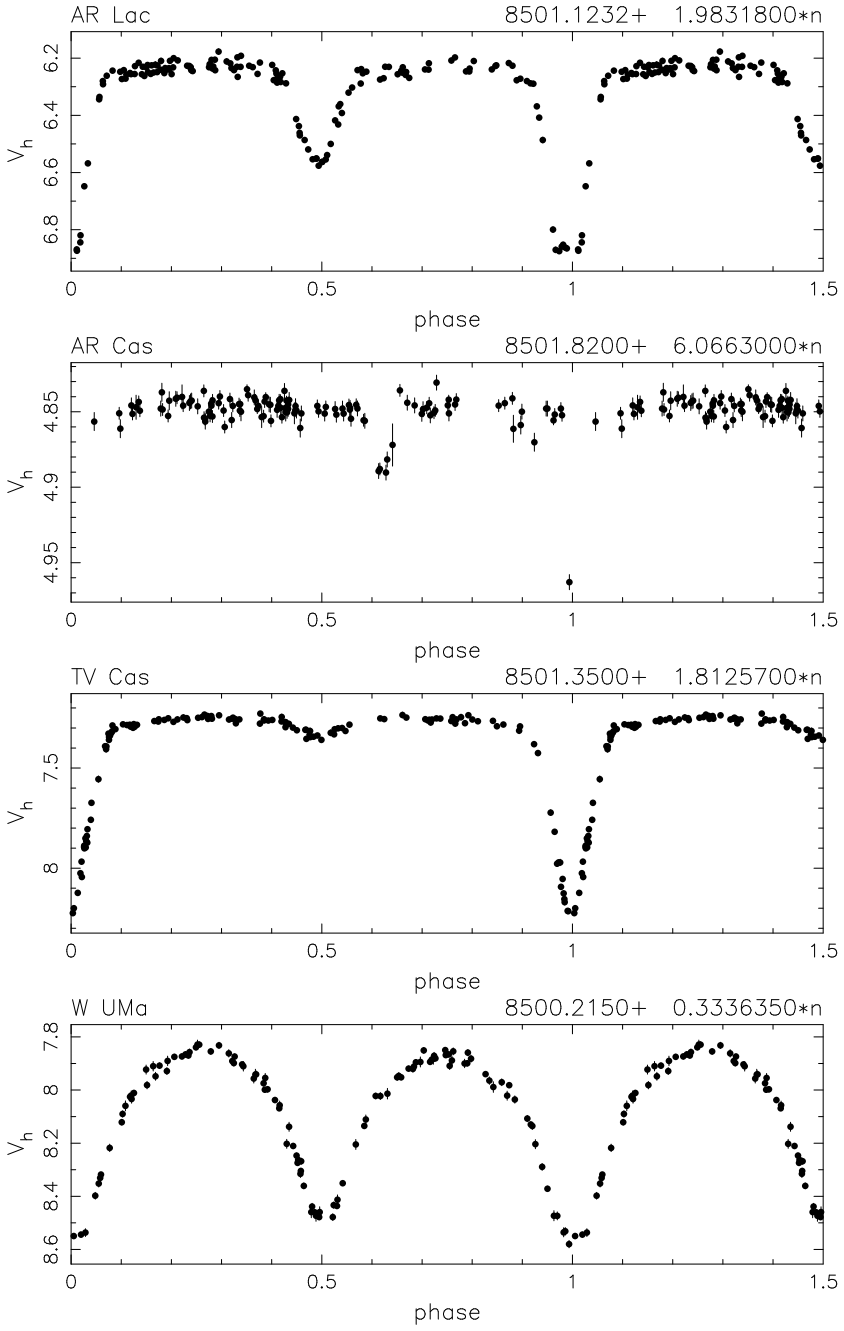

Figure 1.5: *Various examples of lightcurves, taken from the Hipparcos Catalogue. One-and-a-half orbital period is shown for each star. The top curve shows two eclipses per orbit, separated by half the orbital period; the curve of AR Cas shows two eclipses asymmetrically located over the orbital period. TV Cas shows ellipsoidal variations, and the contact binary W UMa even more so.*

asymmetric radial velocity curves, even in circular orbits. A hot star may heat the facing surface of its companion, thus reducing or even inverting the light changes when the companion is eclipsed. In the course of the 20th century observations and interpretation of radial velocity curves and lightcurves were continuously improved. The variation in interpretation also led to a proliferation of names for various binary types, usually after a prototype.

heating

So one can encounter statements like 'AR Lac is an RS CVn variable', or 'AR

Cas is an Algol type variable'. To understand this we make a short digression into nomenclature. To designate variable stars, Argelander introduced the following, alas rather convoluted, system. The first variable discovered in a constellation Con is called R Con, the second one S, the third one T and so on to Z. Argelander thought that variability was so rare, that this would be enough. It isn't! and one continues with RR, RS, ... RZ, SS, ST, ... SZ to ZZ. After that follows AA, AB, ... AZ, BB, BC, ... BZ, etc. until QZ. The letter J is not used (probably for fear of confusion with I). After this, one starts enumerating: V335 Con, V336 Con, etc., where V stands for variable. So we now know that AR Lac is the 71th variable discovered in the constellation Lacerta.[5]

nomenclature
variable stars

Thus, eclipsing binaries often have a designation as a variable star. It should be noted, however, that many variable stars are not binaries; most are pulsating variables, like RR Lyrae, some are magnetically active stars, like the flare star UV Ceti, and some are young stars with the forming disk still present, like T Tau.

The number of prototypes after which a class of objects is named is rather large; in general the World Wide Web is the best place to start finding out what type of star the prototype is. We will encounter designations of particular classes of binaries throughout these lecture notes, but two may be mentioned here. A short-period binary in which one star has evolved into a subgiant or giant, whereas the other is still on the main sequence, is called an RS CVn type variable. Such binaries are often eclipsing, and further stand out through magnetic activity that causes stellar spots and X-ray emission. When the giant expands, it may at some point start transferring mass to its companion: it has then become an Algol system.

RS CVn type
Algol type

The maximum size that a star can have before gas flows over from its surface to the other star is called the *Roche lobe* (Roche 1859[6]). When a star fills its Roche lobe, one expects in most cases that tidal forces have circularized the orbit.

Roche-lobe overflow

The relatively recent physical classification of a binary does not always agree with the old lightcurve nomenclature. The statement 'AR Cas is an Algol type variable' is a good example. From Figure 1.5 we see that the orbit of AR Cas is eccentric: thus, the giant presumably does not fill its Roche lobe in this system, as also indicated by the absence of ellipsoidal variations, and AR Cas is better classified as an RS CVn system.

An often used classification of binaries refers to the sizes of the stars with respect to their Roche lobes. If both stars are smaller than their Roche lobe, the binary is *detached*. If one star fills its Roche lobe, the binary is *semi-detached*; if both stars fill or over-fill their Roche lobes, i.e. the stars touch, the binary is a *contact binary*, also called a W UMa system, after its prototype.

detached, semi-detached, contact

It is very difficult to determine from the lightcurve alone whether a star is just close to filling its Roche lobe, or actually fills it. For this reason, a classification of lightcurves based on this distinction, i.e. EA for detached, EB for semidetached, and EW for contact, is becoming obsolete. Nonetheless, clearly separated stars are easily recognisable from the absence of ellipsoidal variations and from the eccentricity of the orbit (as derived from the unequal time intervals between the primary and secondary eclipse), e.g. AR Cas in Figure 1.5; and contact binaries from the strong variation of the lightcurve throughout the orbit, e.g. W UMa in Figure 1.5.

EA,EB,EW

[5]For an amusing description on the origins of this convoluted system, see Townley 1915

[6]Roche computed the maximum size of the atmosphere of a comet before the Sun disrupts it!

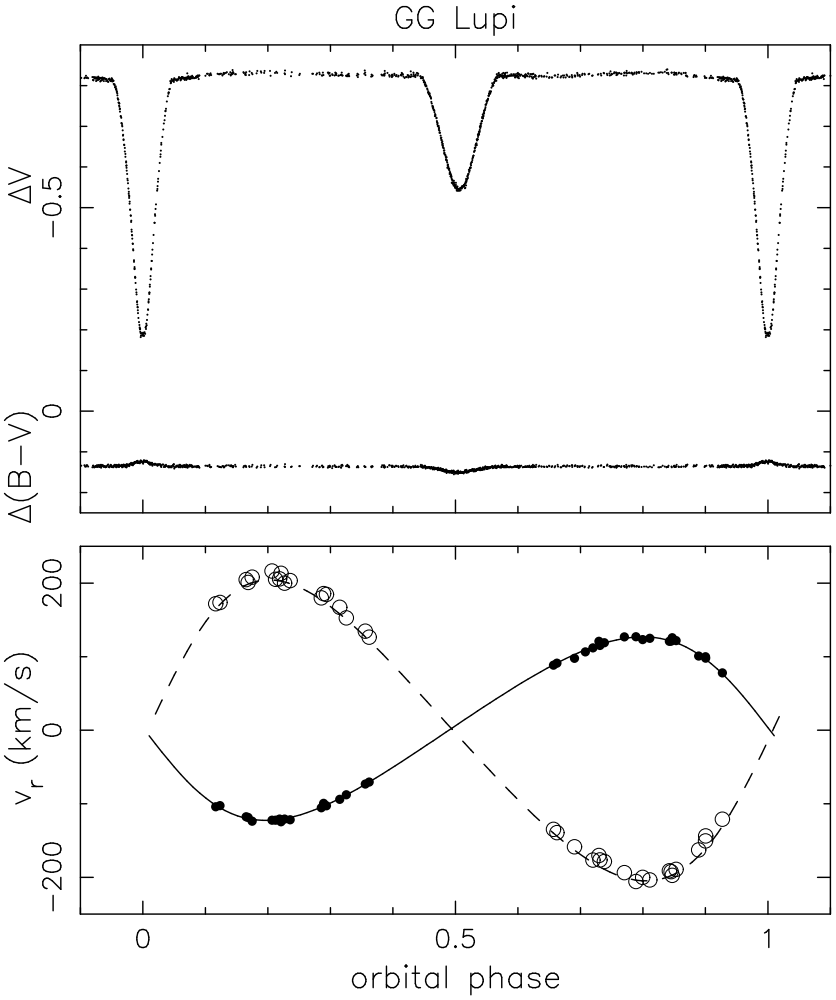

Figure 1.6: *Lightcurves and radial–velocity curves of the binary GG Lup (B7 V + B9 V). The orbital period is 1.85 d. In the lightcurves the changes of V and $B-V$ with respect to a constant comparison star are plotted. In the radial-velocity plot the theoretical curves have been added to the observed data points for the more massive star (•, solid line), and for the lighter star (∘, dashed line). After Clausen et al. (1993) and Andersen et al. (1993).*

1.3 The development of modern binary research

In the 20th century more and more data were gathered from binaries, in studies of the orbits of *visual binaries*, the velocities of *spectroscopic binaries*, and the flux variations of *eclipsing binaries*. An important development in the 1970s followed the design of the velocity correlator by Griffin. The standard way to measure a stellar velocity is to obtain a high-quality, high-resolution spectrum, and then fit the spectral lines. This requires large amounts of observing time on large telescopes. The velocity correlator works as follows (Griffin 1967):

velocity correlator

> *Suppose a widened spectrogram is obtained, through the optics of a spectrometer, of, say, a bright K star; and that it is returned after processing to the focal surface where it was exposed, the telescope being turned to the same star. If the spectrogram is replaced accurately in register with the stellar spectrum, all the bright parts of the spectrum will be systemat-*

ically obstructed by heavily exposed emulsion, and rather little light will pass through the spectrogram. If it is not in register, the obstruction of the spectrum will not be systematic and the total transmission will be greater.

The spectrum can be used for the measurement of velocities of other stars, simply by measuring the transmitted light as a function of the position, regulated with a screw. With this instrument, radial velocities with an accuracy as good as 1 km/s can be obtained in relatively short observing times. Slightly modified versions of the velocity correlator were made for a number of telescopes, and became the work horses for long-term studies of spectroscopic binaries. For the first time, systematic studies of the binary frequency in stars near the Sun, and of stars in selected stellar clusters, became possible. In particular Mayor and his collaborators of the Observatoire de Genève contributed to these studies with the CORAVEL.

The work horse of choice for many years for the fitting of lightcurves and radial velocities was the computer code developed by Wilson & Devinney. It computed which surface elements of the two stars in a binary were visible at each orbital phase, and added the fluxes from these elements. Often, the spectrum of each element was taken to be a black body spectrum, and colour corrections to stellar spectra were made only for the summed flux and colours. For spherical stars the analysis is relatively straightforward, but for a deformed star one must take into account that the measured radial velocity may not reflect the velocity of the centre of mass. An example of data of high quality, allowing the determination of masses, radii and luminosities to within a few percent, is given in Figure 1.6.

Chapter 3.4.1 *Wilson & Devinney code*

Chapter 3.3

The theory of binaries came into being with the understanding of the evolution of stars, the first ideas of which were developed in the 1920s by Eddington. Main sequence stars evolve into giants, and giants leave white dwarfs upon shedding their envelope. Massive giants can shed their envelope in a supernovae explosion and leave a neutron star or a black hole. The study of binaries is an important aspect of the study of stellar evolution, as it provides accurate masses and radii, for comparison with stellar evolution. It also may pose questions that stellar evolution has to answer. A nice example is the Algol paradox.

Chapter 4

From stellar evolution, we know that the more massive star in a binary evolves first. It was therefore a nasty surprise when it was discovered that the giant in Algol systems is usually less massive than its unevolved companion! This 'Algol paradox' was solved by Kuiper (1941), when he realized that mass is being transferred from the giant to its main-sequence companion: apparently enough mass has already been transferred that the initially more massive star has become the less massive star by now. The evolution of such binaries under the influence of mass transfer has been described in the 1960s in a number of classical papers by Paczyński and by Kippenhahn & Weigert. Our understanding of stellar evolution, and by extension, of the evolution of binaries continues to increase as our understanding of for example opacities, the equation of state, and nuclear reactions continues to be improved.

Algol paradox

From the observational point of view the end of the 20th century saw a number of very large changes, which have completely transformed astronomy in general, and the studies of binaries in particular.

Space research made it possible to study stars at previously inaccessible wavelengths: ultraviolet and X-rays, and more recently infrared. The shorter wavelengths

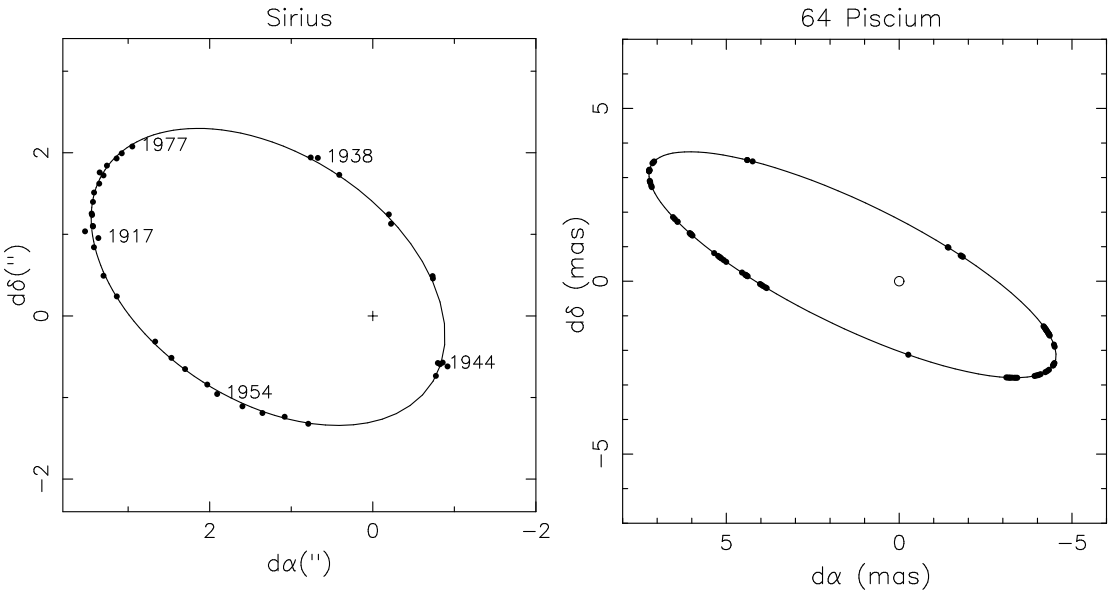

Figure 1.7: *Left: orbital motion of Sirius A with respect to a fixed point on the sky (+, after correction for proper motion). The orbital period is 50.09 yr. Right: the 13.8 d orbit of 64 Piscium with respect to its companion (•) is resolved with the Palomar Testbed Optical Interferometer. After Gatewood & Gatewood (1978) and Boden et al. (1999).*

started the wholly new topic of the study of binaries with neutron stars and black holes, and greatly extended the research of binaries with white dwarfs. **Chapter 12**

Larger telescopes became possible with the technology of supporting thin mirrors with a honeycomb structure, thus allowing mirrors of 8 m diameter.

Optical interferometers became possible when technology allowed distances between mirrors to be regulated with an accuracy better than one-tenth of the wavelength of observation: i.e. first in the infrared. The technique has been pioneered by Michelson in the beginning of the 20th century, and allowed Pease (1927) to make the first interferometric resolution of a binary, viz.. . . Mizar A. In the last decades of the 20th century, routine interferometric measurements became possible, allowing milliarcsecond resolution (e.g. Figure 1.7).

Infrared detectors opened up the field of pre-main-sequence stars (Figure 1.8).

CCD cameras allow much more rapid observations, which can be calibrated much more easily than photographic plates. This allows standard photometry with an accuracy of 1% or better, and rapid spectroscopy. It also makes the data immediately available in digital format

Computers allow the handling of much larger data sets, and the correct handling of them. In earlier studies, fitting of radial velocity data and of visual orbits had to be done in an approximate fashion, often not allowing realistic error estimates. With computers, a much more correct way of data analysis and fitting is possible. The development of *software* is an important aspect of this. For many instruments, an automatic data reduction is provided to the users: the *pipeline* reduction. If one considers the pipeline not good enough, there are software pacakages which allow inter-active data reduction. However, as instruments become more and more complicated, the pipeline written by the experts is more often the best option.

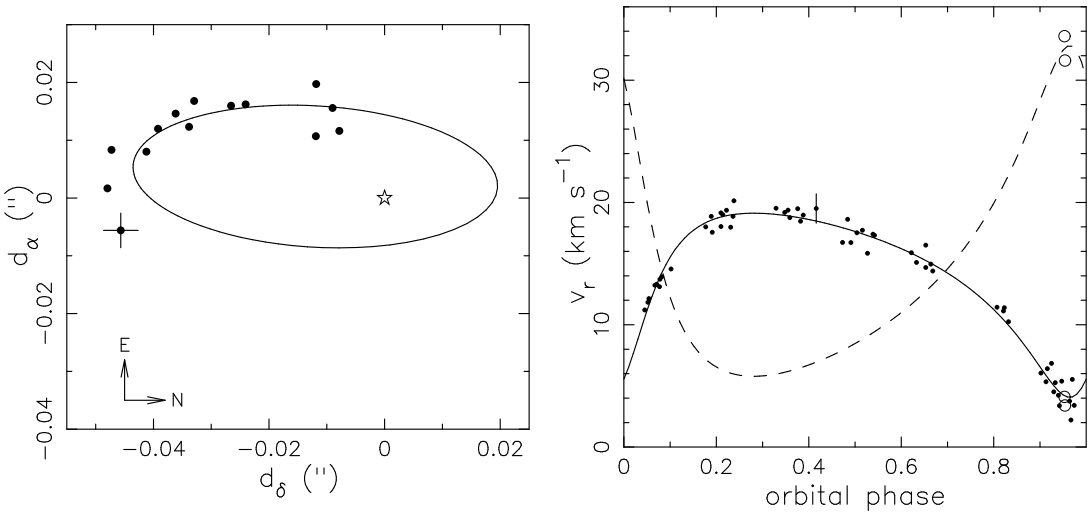

Figure 1.8: *Visual orbit and radial velocity curve of the T Tau star 045251+3016 in the Taurus Auriga star forming region. After Steffen et al. (2001)*

Computers also allow much more detailed computation of the evolution of single stars, and by extension of binaries. They also allow more accurate computation of stellar atmosphere models, for comparison with light curves.

The combination of these developments leads to other advances:

Data bases can be constructed much more easily now that the data are often digital from the start. They require much storage space, and thus large computers. The World Wide Web allows access to many of these data bases, including standardized analysis software.

Velocity Correlation for CCD spectra can be done on the computer: the spectrum of the object can be compared to a whole library of (observed or theoretical) stellar spectra, allowing not only the determination of the velocity, but also of stellar spectrum parameters as temperature, gravity, and metallicity. Radial velocities can now be measured with an accuracy better than 10 m/s, depending on the stellar type.

Lightcurve fitting. With the faster computers today it is possible to fit a stellar spectrum directly to each surface element; this is important because it allows correct application of limb-darkening. With the more accurate CCD data, more orbital phases can be studied. With genetic algorithms, all parameters can be fitted simultaneously.

Visibility fitting. An interferometer measures the interference pattern between different sources of light, e.g. the two stars in a binary, combined from several apertures, i.e. the separate mirrors of the interferometer. The strength of the interference is expressed as the *visibility* and depends on the angular distance between the two stars, and on the distances between the mirrors of the interferometer. Rather than first derive the angular distance and position angle of the stars, and then fit these, one can now directly fit the observed visibilities.

Automated or semi-automated observations have led to an important role of small telescopes. Typically, a small telescope surveys the sky, and discovered an object with interesting variability or colour. A followup with a 1 m telescope then may give a better lightcurve, and if the system is still deemed interesting a radial velocity

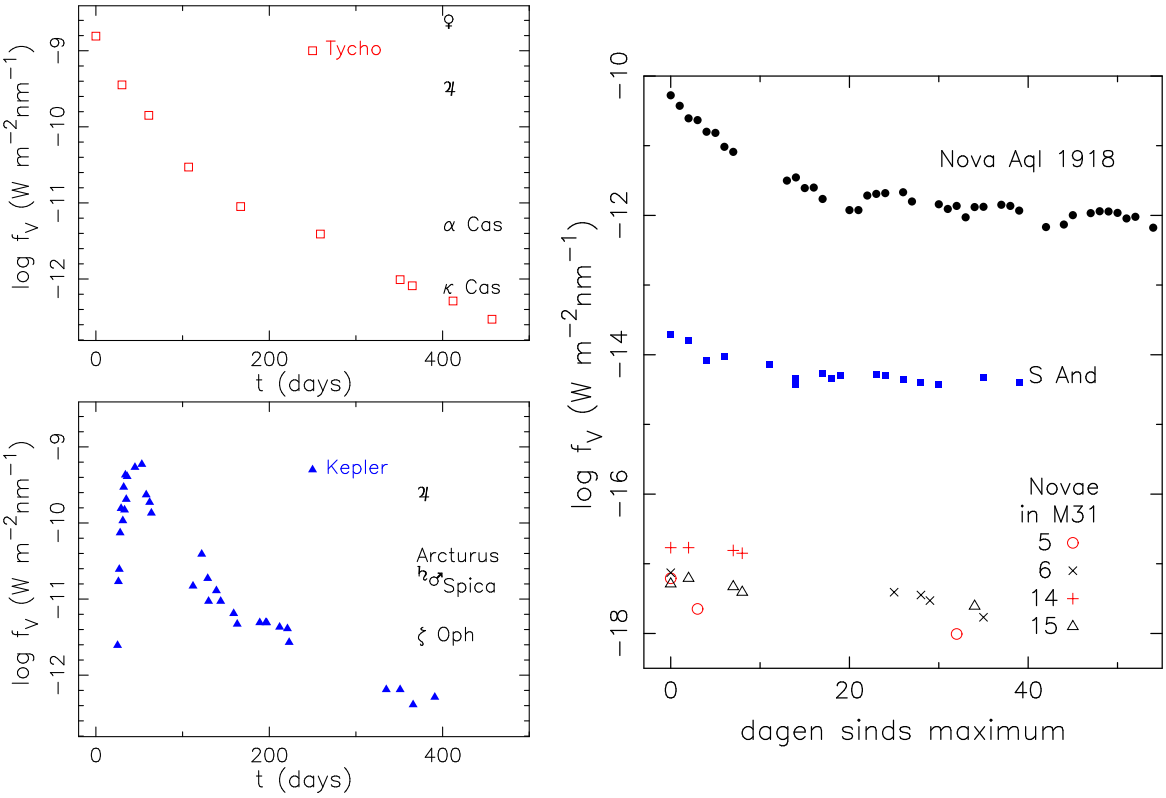

Figure 1.9: *Left: the brightness of the Novae Stellae of Tycho and Kepler were expressed by comparison with planets or nearby stars: this enables us to reconstruct the brightness variations of these stars. Right: the lightcurves of the 'nova' in the Andromeda Nebula, S And, compared to that of nova Aquilae 1918, and of several fainter variables, viz. ordinary novae, in M 31.*

curve is obtained with an 8 m telescope. This type of observations has led to the determination of accurate masses and radii of very-low-mass stars and of brown dwarfs.

Chapter 4.3

1.4 Compact binaries

The discovery of compact binaries is closely related to the study of stars with irregular variability and of X-ray sources.

The placid and seemingly constant sky is occasionally perturbed by the appearance of what appears to be a new star. In Europe such a star was Nova Stella, or briefly: Nova. The plural is Novae (Stellae). Some of these new stars were so bright that they were visible even during day time. Examples studied in Europe are those of 1572 (Tycho's Nova) and 1604 (Kepler's Nova). When ancient Chinese, Japanese and Korean chronicles were excerpted and translated (in 1846, more in 1871), several older examples were found, inclding those in the years 185, 1006 (the brightest of all, also seen in the Middle East and Europe), 1054 and 1181. Several hundred other novae, less bright and only visible at night, are also mentioned in the chronicles. An early-modern European new star was the one discovered by Blaeu in Cygnus: Nova Cygni, also known as P Cygni.

Gradually it became clear that one should discriminate supernovae and novae.

In 1885 a nova had been discovered in the Andromeda nebula, M 31. This nova was about 10^{-4} times as bright as the nova in Aquila of 1918, called S Aquilae. It was concluded that M 31 is about 100 times further away that Nova Aquilae, and thus a nebula in our own galaxy. Starting in 1910, however, photographs taken with the new telescope at Lick Observatory showed fainter variables in M 31, at 10^{-3} of the brightness level of S Aquilae. If these fainter variables were ordinary novae, two conclusions followed: The Andromeda Nebula is much further away, and thus much bigger, than previously thought: it is a true 'Island in the Universe', just like our own Milky Way. Also, S Aquilae must have been extremely bright: not a nova, not a supernova.

In the 1920s the structure of white dwarfs was described by Chandrasekhar, on the basis of the assumption that the pressure in these stars is that of a degenerate electron gas. When the neutron was discovered, it was soon realized that a star in which the pressure is that of a degenerate neutron gas, that the radius of such a neutron star would be some thousand times smaller than that of a white dwarf, i.e. on the order of 10 km. Baade and Zwicke then understood that the collapse of a star (or its core) to such a small size releases an enormous amount of energy, $\Delta E \sim GM^2/R$, enough to provide the energy of the supernovae.

The nature of novae became clear when it was discovered in the 1940s that they arose in binaries, in which a white dwarf accretes mass from a companion. This matter piles up on the surface of the white dwarf, and concists mainly of hydrogen and helium. When the layer is sufficiently deep, the pressure and temperature at its bottom are high enough for hydrogen-fusion to start. The energy released is enough to lift the surface layer and let it expand to the size of a giant, causing a rise in luminosity by a factor $\sim$10 000. As the outer layer disperses, the surface shrinks to its original level and accretion resumes, until the next outburst. Most novae have been seen in outburst just once, but a number of novae has shown several outbursts: these are called recurrent novae.

Dwarf novae show small outbursts, in which the luminosity rises by a factor $\sim$100. For most dwarf novae many outbursts have been observed. A typical outburst can last a few days to two weeks, and the intervals between the outbursts range from weeks to months. In the 1960s it was discovered that dwarf novae are binaries in which a white dwarf accretes matter from a low-mass ($< M_\odot$) companion. The dwarf novae arise when the mass transport through the disk changes. In the related class of nova-like variables the accretion disk does not show such large variations, but only small, but continuous flickering. The orbital periods of these systems range from 80 mins to 8-9 hours. In some cases the donor of the white dwarf is also a white dwarf: the orbital periods of these ultracompact binaries range from the current record holder of 5 min to some 40-60 mins.

These compact binaries with white dwarfs were discovered to have counterparts with a neutron star after the study of the sky in X-rays, which started from 1967. Several hundred very bright X-ray sources were discovered, concentrated towards the galactic plane, and on this plane toward the center of the galaxy. Most of these were found to be binaries in which a low-mass star transfers mass to a neutron star. These systems are called low-mass X-ray binaries. A dozen is now known to house a black hole: all of these are transient, i.e. they are faint most of the time and only become (very) bright at intervals, often of many years. Some transients contain a neutron star.

When mass transfer is a low-mass X-ray binary with a neutron star stops, the neutron star may turn on as a (recycled) radio pulsar. (Pulsar is short for: pulsating source of radio emission.) Most such pulsars have low-mass white-dwarfs as companions, the cores of giants that tranferred their outer layers to the neutron star. In some cases, the neutron star is accompanied by another neutron star.

Compact binaries are studied for a variety of reasons. The two most important are

- the structure of neutron stars is related to their equation of state, and the maximum possible mass gives information about this equation at nuclear and supranuclear densities
- compact stars can make compact binaries which emit gravitational waves. Such binaries can be used to study and test general relativity

Another reason is that many cataclysmic variables have accretion disks, which can be studied in detail because the time scales of their variability is short, and because nearby cataclysmic variables are relatively bright. It is hoped that understanding accretion disks in these systems will help understanding accretion disks around the supermassive black holes in Active Galactic Nuclei.

1.5 These lecture notes

The first part of this Lecture Course is set up as follows. First we derive the relative orbit of two stars under the influence of their mutual gravitation (Chapter 2), and then we derive the visual orbit, the radial velocity curve, and the eclipse lightcurve for a binary observed from Earth (Chapter 3). We briefly indicate how observations can be fitted to these theoretical curves. In these chapters we assume perfectly spherical masses. In Chapter 4 we show how parameters of binaries are derived from the observations, and discuss a number of interesting cases. Consequence for the orbit and orbital evolution of non-sphericity are discussed in Chapter 5.

Chapter 6 discusses the structure of degenerate stars, i.e. white dwarfs and neutron stars.

1.6 Exercises

The following sites may be useful:
general information on astronomical objects `simbad.u-strasbg.fr` this site also has links to catalogues.
popular site on stars `stars.astro.illinois.edu/sow/sowlist.html`
reference search `cdsads.u-strasbg.fr/abstract_service.html` `adsabs.harvard.edu/abstract_serv`

Exercise 1. Use the Web to find the Bayer names for the stars Markab, Algorah and Propus mentioned in the quotation on page 3 from Herschel.

Exercise 2. Use SIMBAD and the Hipparcos Catalogue to find the distance to Mizar. Noting that Galileo measured the distance between Mizar A and B as $15''$, give a rough estimate of the orbital period.

Exercise 3. Get the pdf-file of the paper in which Herschel gives his measurements of the orbit of Castor AB; and of the paper in which Griffin explains the velocity correlation method.

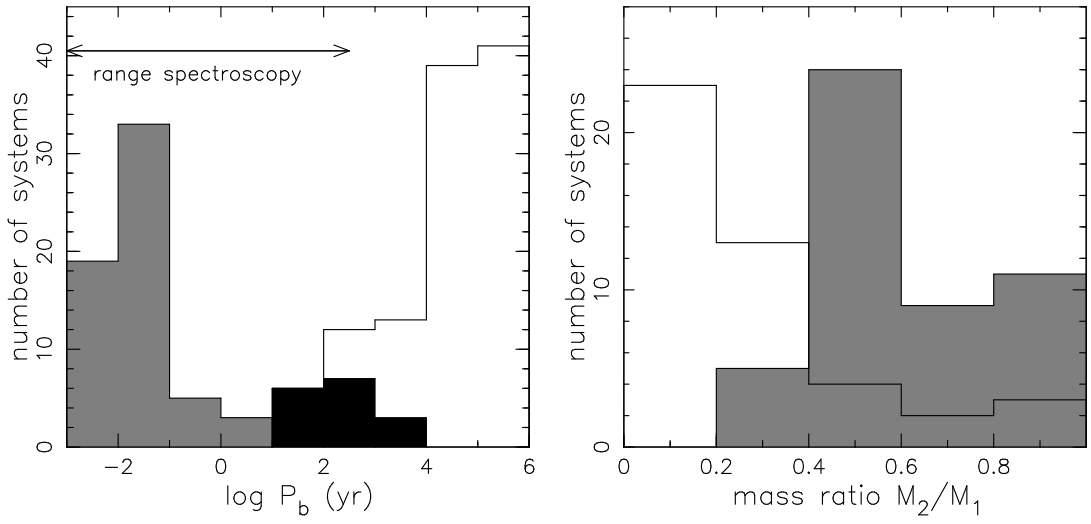

Figure 1.10: *Distribution of orbital periods (left) and mass ratios (right) of O stars as observed (i.e. not corrected for selection effects). Spectroscopic binaries are indicated with gray, visual binaries with white, and speckle binaries with black histograms. After Mason et al. (1998)*

Exercise 4. Confirm from the lightcurves of GG Lup (Figure 1.6) that the primary eclipse is the eclipse of the hotter star.

Exercise 5. Consider a binary of two O stars, each with a mass of $20\,M_\odot$. The nearest O stars are at about 250 pc. With an angular resolution of $0.1''$ and a radial velocity accuracy of 5 km/s, determine the minimum period for studying this binary as a visual binary, and the maximum period for studying its radial-velocity curve. Assume that a reliable study requires an amplitude 5 times bigger than the measurement accuracy. Compare the results with Figure 1.10. How do the limits change when the accuracy is improved by a factor 100 (as has happened since 1980)?

1.7 References with the Historical Introduction

this list is as yet incomplete.

1. R.G. Aitken. *The binary stars.* Reprint in 1964 by Dover Publications, New York, 1935.

2. A. Boden, B. Lane, M. Creech-Eakman et al. The visual orbit of 64 Piscium *ApJ*, 527:360–368, 1999.

3. J. Andersen, J. Clausen, A. Gimemez. Absolute dimensions of eclipsing binaries, XX. GG Lupi: young metal-deficient B stars. *AA*, 277:439–451, 1993.

4. J. Clausen, J. Garcia, A. Gimemez, B. Helt, L, Vaz. Four colour photometry of eclipsing binaries, XXXV. Lightcurves of GG Lupi: young metal-deficient B stars. *AAS*, 101:563–572, 1993.

5. G. Gatewood and C. Gatewood A study of Sirius *ApJ*, 225:191–197, 1978.

6. J. Goodricke. On the periods of the changes of light in the star Algol. *Philosophical Transactions*, 74:287–292, 1784.

7. R.F. Griffin. A photoelectric radial-velocity spectrometer. *ApJ*, 148:465–476, 1967.

8. W. Herschel. Catalogue of 500 new nebulae, nebulous stars, planetary nebulae, and clusters of stars; with remarks on the construction of the heavens. *Philosophical Transactions*, 92:477–528, 1802.

9. W. Herschel. Account of the changes that have happened, during the last twenty-five years, in the relative situation of double-stars; with an investigation of the causes to which they are owing. *Philosophical Transactions*, 93:339–382, 1803.

10. R. Kippenhahn. Mass exchange in a massive close binary system. *A&A*, 3:83–87, 1969.

11. R. Kippenhahn and A. Weigert. Entwicklung in engen Doppelsternsystemen. I. Massen- auschtausch vor und nach Beendigung des zentralen Wasserstoff-Brennens. *Zeitschr. f. Astroph.*, 65:251–273, 1967.

12. G.P. Kuiper. On the interpretation of β Lyrae and other close binaries. *ApJ*, 93:133–177, 1941.

13. B. Mason, D. Gies, W. Hartkopf, W. Bagnuolo, Th. ten Brummelaar, and H.McAlister ICCD speckle observations of binary stars. XIX. An astrometric spectroscopic survey of O stars. *AJ*, 115:821–847, 1998.

14. J. Michell. An inquiry into the probable parallax, and magnitude of the fixed stars, from the quantity of light which they afford us, and the particular circumstances of their situation. *Philosophical Transactions*, 57:234–264, 1767.

15. B. Paczyński. Evolution of close binaries. I. *Acta Astron.*, 16:231, 1966.

16. B. Paczyński. Evolution of close binaries. IV. *Acta Astron.*, 17:193–206 & 355–380, 1967.

17. F.G . Pease. Interferometer Notes. IV. The orbit of Mizar. *PASP*, 39:313–314, 1927.

18. G.B. Riccioli. *Almagestum novum, astronomiam veterem novamque complectens: observationibus aliorum, et propriis novisque theorematibus, problematibus, ac tabulis promotam.* Victorius Benatius, Bononia (=Bologna), Vol.1 Part 1, p.422, 1651.

19. É. Roche. Recherches sur les atmosphères des comètes. *Annales de l'Observatoire imperial de Paris*, 5:353–393, 1859.

20. A. Steffen, R. Mathieu, M. Lattanzi, et al.˙ A dynamical mass constraint for pre-main-sequence evolutionary tracks: the binary NTT 045251+3016 *AJ*, 122:997–1006, 2001.

21. S.D. Townley, Designation of variable stars. *PASP*, 27:209–213, 1915.

Chapter 2

The gravitational two-body problem

In this chapter we derive the equations that describe the motion of two point masses under the effect of their mutual gravity, in the classical Newtonian description.

2.1 Separating motion of center of mass and relative orbit

Suppose we have two masses, M_1 at position $\vec{r_1}$ and M_2 at position $\vec{r_2}$. The equations of motion for the two bodies are

$$M_1 \ddot{\vec{r_1}} = -\frac{GM_1M_2}{|\vec{r_1} - \vec{r_2}|^2}\,\vec{e_{12}} \tag{2.1}$$

$$M_2 \ddot{\vec{r_2}} = +\frac{GM_1M_2}{|\vec{r_1} - \vec{r_2}|^2}\,\vec{e_{12}} \tag{2.2}$$

where a dot $\cdot$ denotes a time derivative, and where $\vec{e_{12}}$ is a vector of unit length in the direction from M_2 to M_1.

We now define two new coordinates, one denoting the center of mass:

$$\vec{R} \equiv \frac{M_1\vec{r_1} + M_2\vec{r_2}}{M_1 + M_2} \tag{2.3}$$

and one the vector connecting the two masses:

$$\vec{r} \equiv \vec{r_1} - \vec{r_2} \tag{2.4}$$

Adding equations 2.1 and 2.2 gives

$$M_1\ddot{\vec{r_1}} + M_2\ddot{\vec{r_2}} = 0 \qquad \Rightarrow \qquad \ddot{\vec{R}} = 0 \tag{2.5}$$

which implies that the center of mass has a constant velocity:

$$\dot{\vec{R}} = \text{constant vector} \tag{2.6}$$

Dividing Eqs. 2.1 and 2.2 by M_1 and M_2, respectively, and subtracting the results, one obtains

$$\ddot{\vec{r_1}} - \ddot{\vec{r_2}} = -\left(\frac{1}{M_1} + \frac{1}{M_2}\right)\frac{GM_1M_2}{|\vec{r_1} - \vec{r_2}|^2}\,\vec{e_{12}} \qquad \Rightarrow \qquad \mu\ddot{\vec{r}} = -\frac{GM_1M_2}{r^3}\,\vec{r} \tag{2.7}$$

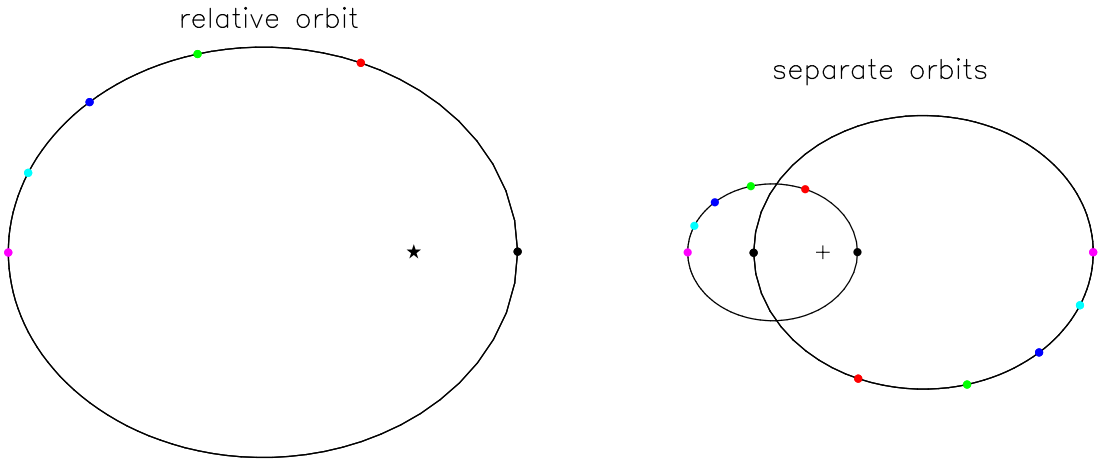

Figure 2.1: *Relation between the relative orbit (left) and absolute orbits (right) of a binary, in this case Sirius, as expressed by Eq. 2.9.*

where we have introduced the *reduced mass*:

$$\mu = \frac{M_1 M_2}{M_1 + M_2} \tag{2.8}$$

We have now split the equations of motion 2.1 and 2.2 into an equation 2.6 for the motion of the center of mass, and an equation 2.8 for the motion of the vector connecting the masses. To see how the vectors for the masses $\vec{r_1}$ and $\vec{r_2}$ can be obtained once we have solved Eq. 2.7, we solve Eqs. 2.3 and 2.4 for them:

$$\vec{r_1} = \vec{R} + \frac{M_2}{M_1 + M_2}\vec{r} \quad ; \qquad \vec{r_2} = \vec{R} - \frac{M_1}{M_1 + M_2}\vec{r} \tag{2.9}$$

From this equation we learn that the orbits of M_1 and M_2 with respect to the center of mass have the same form, and that the sizes of the orbits are inversely proportional to the masses.

Consider the angular momentum of a particle with mass μ:

$$\vec{L} \equiv \mu\vec{r} \times \dot{\vec{r}} = \text{constant vector} \tag{2.10}$$

where $\times$ denotes the outer product. That the angular momentum is constant, follows from its time derivative, noting that the force is along the line connecting the masses, $\vec{r} \parallel \ddot{\vec{r}}$ (Eq. 2.7):

$$\dot{\vec{L}} = \mu\left(\dot{\vec{r}} \times \dot{\vec{r}} + \vec{r} \times \ddot{\vec{r}}\right) = 0 \tag{2.11}$$

Thus the angular momentum vector $\vec{L}$ is conserved, and has a fixed direction, perpendicular to both $\vec{r}$ and $\dot{\vec{r}}$. This implies that the orbital plane of both masses is fixed, perpendicular to the angular momentum vector. We can therefore describe the motion of the masses with two coordinates, in this plane. For these coordinates we choose cylindrical coordinates r and ϕ, which lead to

$$\dot{\vec{r}} = \dot{r}\hat{r} + r\dot{\phi}\hat{\phi} \qquad \text{and} \qquad \dot{\vec{r}}^2 = \dot{r}^2 + r^2\dot{\phi}^2 \tag{2.12}$$

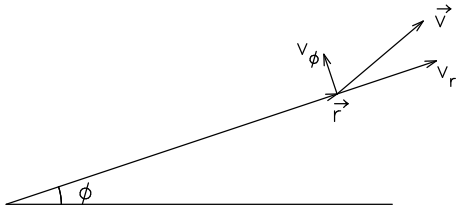

Figure 2.2: *Illustration of Eq. 2.12;* $\vec{v} \equiv \dot{\vec{r}}$.

with $\hat{r}$ the unit vector in the direction of $\vec{r}$ and $\hat{\phi}$ the unit vector perpendicular to $\vec{r}$ (and in the orbital plane). For the angular momentum we obtain in these coordinates:

$$\vec{L} = r\hat{r} \times \mu \left(\dot{r}\hat{r} + r\dot{\phi}\dot{\hat{\phi}} \right) = \mu r^2 \dot{\phi} \left(\hat{r} \times \dot{\hat{\phi}} \right) \tag{2.13}$$

and for its scalar length:

$$L = \mu r^2 \dot{\phi} \tag{2.14}$$

The total energy of the two masses is given by the sum of the kinetic and potential energies:

$$E = \frac{1}{2} M_1 \dot{\vec{r}_1}^{\,2} + \frac{1}{2} M_2 \dot{\vec{r}_2}^{\,2} - \frac{G M_1 M_2}{r} \tag{2.15}$$

By substituting the time derivatives of $\vec{r_1}$ and $\vec{r_2}$ after Eq. 2.9 we can rewrite this as

$$E = \frac{1}{2} \left(M_1 + M_2 \right) \dot{\vec{R}}^{\,2} + \frac{1}{2} \mu \dot{\vec{r}}^{\,2} - \frac{G M_1 M_2}{r} \tag{2.16}$$

Thus the total energy can be written as the kinetic energy derived from the motion of the center of mass, and the kinetic and potential energy in the relative orbit.

2.2 The relative orbit

To solve the relative orbit, we first write down the energy and angular momentum of the relative orbit per unit of reduced mass:

$$\epsilon \equiv \frac{E_{\rm bin}}{\mu} \equiv \frac{1}{2}(\dot{r}^2 + r^2\dot{\phi}^2) - \frac{G(M_1 + M_2)}{r} \tag{2.17}$$

$$l \equiv \frac{L}{\mu} = r^2 \dot{\phi} \tag{2.18}$$

Both ϵ and l are constants of motion. We now use Eq. 2.18 to eliminate $\dot{\phi}$ from Eq. 2.17, and find

$$\epsilon = \frac{1}{2}\dot{r}^2 - \frac{G(M_1 + M_2)}{r} + \frac{1}{2}\frac{l^2}{r^2} \tag{2.19}$$

We first investigate this equation qualitatively by defining an effective potential

$$\epsilon = \frac{1}{2}\dot{r}^2 + V_{\rm eff} \quad \text{where} \quad V_{\rm eff} \equiv -\frac{G(M_1 + M_2)}{r} + \frac{1}{2}\frac{l^2}{r^2} \tag{2.20}$$

The effective potential depends on the angular momentum l. Depending on the total energy ϵ we can have various types of orbits (see Figure 2.3).
1) $\epsilon > 0$: the particle moves from $r = \infty$ to a minimal distance, and back out again.

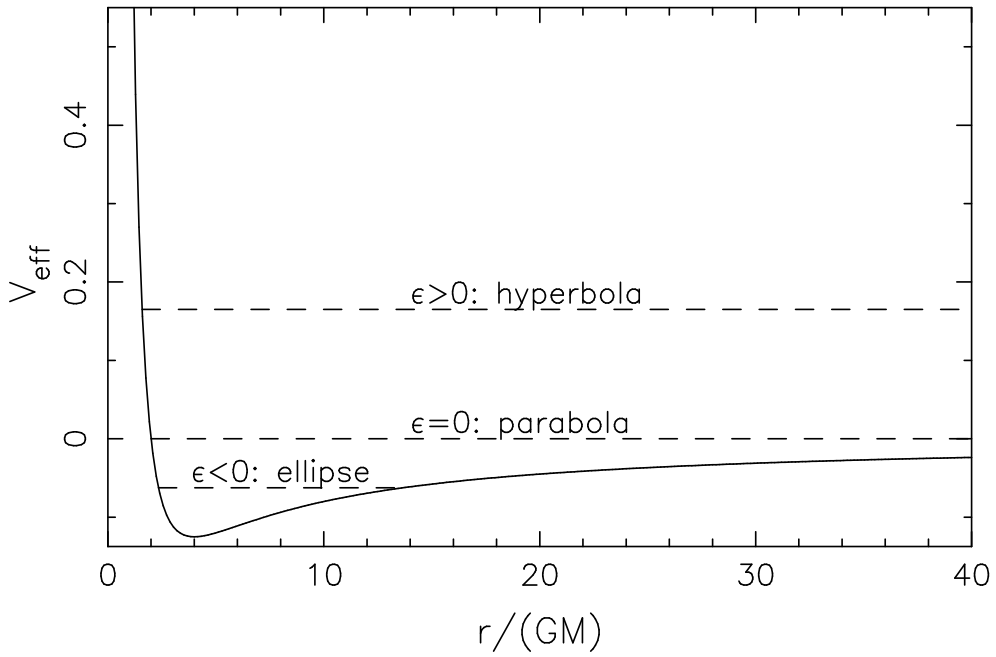

Figure 2.3: *Possible orbits; the values are for $l = 2GM$ where $M \equiv M_1 + M_2$*

It has a finite radial velocity $\dot{r}$ at $r = \infty$.
2) $\epsilon = 0$: idem, with radial velocity equal to zero at $r = \infty$.
3) $\epsilon < 0$: the orbit is bound, between r_{min} and r_{max}

At the minimum of $V_{\rm eff}(r)$, which may be found from $\partial V_{\rm eff}/\partial r = 0$, the orbit is circular. Thus, for each given angular momentum l, the circular orbit is the orbit with the smallest total energy. No matter how small the angular momentum l is, a circular orbit is always possible. Another property of the classical solution is: the larger the energy, the closer to the origin the particle can come, but it can never ever reach the origin, as long as $l > 0$.

To solve the orbit analytically, we write r as a function of ϕ:

$$\frac{dr}{d\phi} = \frac{\dot{r}}{\dot{\phi}} = \frac{r^2}{l}\left(2\epsilon + \frac{2G(M_1+M_2)}{r} - \frac{l^2}{r^2}\right)^{1/2} \tag{2.21}$$

Next, we substitute $u = 1/r$ to find

$$(\frac{du}{d\phi})^2 = \frac{1}{l^2}(2\epsilon + 2G(M_1+M_2)u - l^2u^2) \tag{2.22}$$

the solution of which is given by

$$u = \frac{1}{r} = \frac{1}{p}(1 + e\cos[\phi - \phi_o]) \equiv \frac{1}{p}(1 + e\cos\nu) \tag{2.23}$$

with

$$\frac{1}{p} = \frac{G(M_1+M_2)}{l^2} \quad \text{and} \quad 2\epsilon = \frac{[G(M_1+M_2)]^2}{l^2}(e^2-1) \tag{2.24}$$

(verify! by entering the solution in Eq. 2.22). Here ϕ_o is an integration constant; we will see below that it corresponds to periastron. Because ϕ_o is constant, we have $\dot{\nu} = \dot{\phi}$.

Eq. 2.23 is the equation for a conic section: in the Newtonian description of gravity, the relative orbit of a two masses in their mutual gravitational fields is always a conic section.

2.2.1 Some properties of elliptic motion

We will now show that, in the case of a bound orbit, when $\epsilon < 0$, the orbit corresponds to an ellipse, with eccentricity $e < 1$. The shortest distance, periastron, is reached for $\nu = 0$ at $r = p/(1+e)$, and the longest distance, apastron, for $\nu = \pi$ at $r = p/(1-e)$. The sum of the periastron and apastron distances is the major axis of the ellipse, $2a$, and from this we find $p = a(1-e^2)$. p is called the semi-latus rectum, a the semi-major axis of the ellipse. Entering this result in Eqs. 2.24 and 2.23 we obtain

$$l^2 = G(M_1 + M_2)a(1-e^2) \qquad \text{and} \qquad \epsilon = -\frac{G(M_1+M_2)}{2a} \tag{2.25}$$

and

$$r = \frac{a(1-e^2)}{1+e\cos\nu} \tag{2.26}$$

We write the relative velocity as $v^2 \equiv \dot{r}^2 + r^2\dot{\phi}^2$. We combine Eqs. 2.17 and 2.25, noting that the total orbital energy ϵ is constant, to find

$$v^2 = G\left(M_1 + M_2\right)\left(\frac{2}{r} - \frac{1}{a}\right) \tag{2.27}$$

For peri- and apastron we get

$$r_p = a(1-e) \qquad \text{and} \qquad r_a = a(1+e) \tag{2.28}$$

Hence with Eq. 2.27 the velocities v_p and v_a at peri- and apastron are

$$v_p = \sqrt{\frac{G(M_1+M_2)}{a}\,\frac{1+e}{1-e}}; \qquad v_a = \sqrt{\frac{G(M_1+M_2)}{a}\,\frac{1-e}{1+e}} \tag{2.29}$$

(These velocities can also be derived directly by comparing the energy Eq. 2.17 and angular momentum Eq. 2.18 at peri- and apastron.)

Now draw a coordinate system with the origin (C in Fig. 2.4) in the middle of the major axis of the ellipse, with the X-axis along the major axis, and the Y-axis along the minor axis. In this coordinate system we have from Eq. 2.26 and 2.28:

$$X = ea + \frac{a(1-e^2)\cos\nu}{1+e\cos\nu} = \frac{a(e+\cos\nu)}{1+e\cos\nu} \qquad \text{and} \qquad Y = \frac{a(1-e^2)\sin\nu}{1+e\cos\nu} \tag{2.30}$$

For $X = 0$ we have $\cos\nu = -e$, and entering this in the equation for Y, we find the minor axis b:

$$b = a\left(1-e^2\right)^{1/2} \tag{2.31}$$

With these results it is now easily shown that

$$\left(\frac{X}{a}\right)^2 + \left(\frac{Y}{b}\right)^2 = 1 \tag{2.32}$$

i.e. the relative orbit is an ellipse.

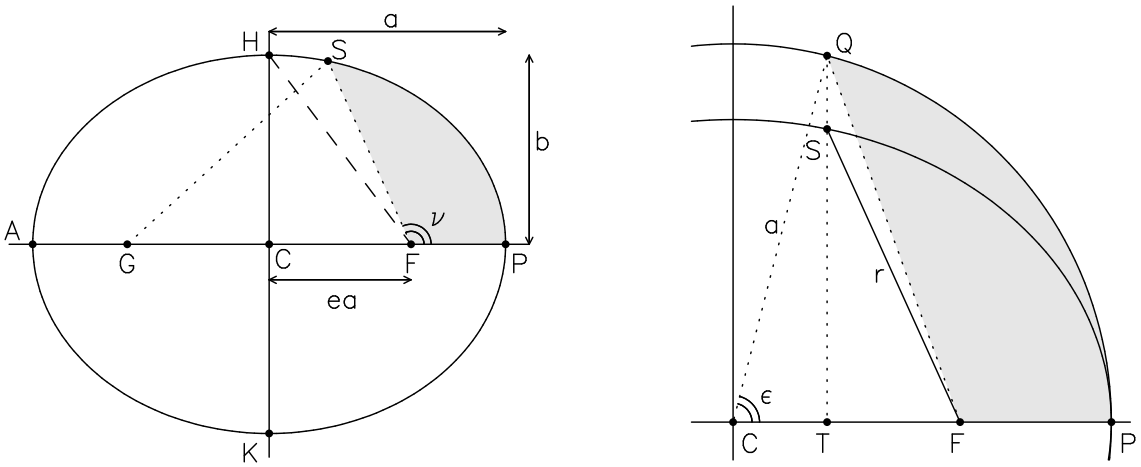

Figure 2.4: *Left: Drawings of ellipse with center C, focus F, periastron P, and apastron A. Right: Detail to illustrate derivation of equation of Kepler (Eq. 2.36).*

2.2.2 The equation of Kepler

Having established the form of the orbit $r(\nu)$, we wish to know the position as a function of time $r(t)$.

We start by deriving the second law of Kepler, that the radius vector $\vec{r}$ covers equal area in equal times. Consider an infinitesimal time interval Δt. The area ΔO covered in this interval is $\Delta O = (1/2)|\vec{r} \times \dot{\vec{r}} \Delta t|$. Thus

$$\frac{dO}{dt} = \frac{1}{2}|\vec{r} \times \dot{\vec{r}}| = \frac{1}{2}|\vec{r} \times (\dot{r}\hat{r} + r\dot{\phi}\hat{\phi})| = \frac{l}{2} \equiv \frac{L}{2\mu} = \text{constant} \tag{2.33}$$

This is the second law of Kepler, also called the law of equal areas. By integrating we find that the area covered increases linearly with time:

$$O(t) = O(0) + \frac{L}{2\mu}t \tag{2.34}$$

We define in Figure 2.4 semi-major axis AC=CP= a, and semi-minor axis HC=CK= b. The foci of the ellipse are F at $X = ea$ and G at $X = -ea$. The periastron P has a distance to the focus F given by PF$\equiv r_p = (1-e)a$; the apastron A has a distance to focus F given by AF$\equiv r_a = (1+e)a$. If we have a point S on the ellipse, then the sum of the distances of this point to the foci is $GS + SF = 2a$.

The motion of the point S along the ellipse in a Kepler orbit is such that the area covered by FS, the area FPS shaded grey in Fig. 2.4 left, increases linearly with time, according to Eq. 2.34. We add to the ellipse a circle around the center C with radius a (Figure 2.4 right), and note from Eq. 2.32 that this circle can be found from the ellipse X, Y by multiplying for each X the corresponding Y value with a/b. Draw a line perpendicular to the semi-major axis through S, and call the point where this line cuts the semi-major axis T and where it cuts the circle Q. Then QC= a and QT/ST= a/b. The area FPQ in the circle (indicated grey in Fig. 2.4 right) is a/b times the area FPS in the ellipse (indicated grey in Fig. 2.4 left), and thus also increases linearly with time. We write this as:

$$\frac{M}{2\pi} \equiv \frac{\text{Area(FPS)}}{\text{Area(ellipse)}} = \frac{\text{Area(FPQ)}}{\text{Area(circle)}} = \frac{\text{Area(CPQ)} - \text{Area(CFQ)}}{\pi a^2} \tag{2.35}$$

where M increases linearly with time. Now write angle QCF as ε. The area of the circle sector is Area(CPQ)= $0.5\varepsilon a^2$. With QC= a we have QT= $a\sin\varepsilon$, and the area of triangle CFQ= $0.5\text{CF}\times\text{QT}= 0.5ae \times a\sin\varepsilon = 0.5a^2 e\sin\varepsilon$. The last equality of Eq. 2.35 can then be written:

$$\frac{M}{2\pi} = \frac{0.5\varepsilon a^2 - 0.5a^2 e\sin\varepsilon}{\pi a^2} \Rightarrow M = \varepsilon - e\sin\varepsilon \tag{2.36}$$

This is Kepler's equation. M is called the mean anomaly, and ε the eccentric anomaly. To express $r \equiv$FS in terms of ε we note that ST= (b/a)QT= $b\sin\varepsilon$, thus $\text{ST}^2 = b^2\sin^2\varepsilon = a^2(1-e^2)\sin^2\varepsilon$ where we use Eq. 2.31, and therefore

$$r^2 \equiv \text{FS}^2 = \text{ST}^2 + \text{TF}^2 = \text{ST}^2 + (\text{CF} - \text{CT})^2 = a^2\left(1 - e\cos\varepsilon\right)^2 \tag{2.37}$$

hence

$$r = a(1 - e\cos\varepsilon) \tag{2.38}$$

To express ν as a function of ε we combine Eqs. 2.26 and 2.38 into

$$1 - e\cos\varepsilon = \frac{1-e^2}{1+e\cos\nu} \qquad \Rightarrow \qquad \tan\frac{\nu}{2} = \sqrt{\frac{1+e}{1-e}}\tan\frac{\varepsilon}{2} \tag{2.39}$$

(Since the derivation of the right hand side equation is somewhat convoluted we give the steps explicitly: From the left equation, we have

$$\cos\nu = \frac{cos\varepsilon - e}{1 - e\cos\varepsilon} \qquad \text{hence} \qquad \sin\nu = \frac{\sqrt{1-e^2}sin\varepsilon}{1 - e\cos\varepsilon} \tag{2.40}$$

Thus, with Eq. 2.50,

$$\tan\frac{\nu}{2} = \sqrt{\frac{1-\cos\nu}{1+\cos\nu}} = \sqrt{\frac{(1+e)(1-\cos\varepsilon)}{(1-e)(1+\cos\varepsilon)}} \tag{2.41}$$

from which Eq. 2.39 follows.)

2.3 Exercises

Exercise 6. The general definition of the angular momentum is

$$\vec{L} = \int_V \rho(\vec{r}\times\vec{v})dV \tag{2.42}$$

In the case of two point masses, this can be written

$$\vec{L} = M_1\vec{r_1}\times\dot{\vec{r_1}} + M_2\vec{r_2}\times\dot{\vec{r_2}} \tag{2.43}$$

Show that this can be written also as

$$\vec{L} = (M_1 + M_2)\vec{R}\times\dot{\vec{R}} + \mu\vec{r}\times\dot{\vec{r}} \tag{2.44}$$

so that the angular momentum can be split, analogously to the energy, in the angular momentum of the center of mass and the angular momentum in the binary.

Exercise 7. Start from the second law of Kepler, Eq. 2.34, to derive his third law:

$$\left(\frac{2\pi}{P}\right)^2 = \frac{G(M_1 + M_2)}{a^3} \tag{2.45}$$

Exercise 8a. Geometrical interpretation of the *semi-latus rectum*. In Figure 2.4 draw a line from the focal point F to the ellipse, perpendicular to the major axis. This line is called the semi-latus rectum. Show that its length is $a(1 - e^2)$.
b. Prove the statement that for any point S on the ellipse, the sum of the distances to the two focal points equals the major axi: GS+SF=$2a$. (Hint: write GS in terms of a, e and ε)

Exercise 9: an alternative derivation for the velocities v_p and v_a at peri- and apastron. The orbital angular momentum and the orbital energy are given by Eq. 2.25. Use the equality of energy and angular momentum at periastron with energy and angular momentum at apastron, to write two equations for v_p and v_a, and then solve for these two velocities.

Mathematical intermezzo: adding angles, half-angles

We reiterate some useful goniometric relations.

$$\begin{aligned} e^{ix} &= \cos x + i \sin x \\ e^{iy} &= \cos y + i \sin y \\ e^{i(x+y)} &= e^{ix} e^{iy} \\ \text{hence} & \qquad (2.46) \\ \cos(x+y) &= \cos x \cos y - \sin x \sin y \qquad (2.47) \\ \sin(x+y) &= \cos x \sin y + \sin x \cos y \qquad (2.48) \end{aligned}$$

In the case where $x = y$ we have

$$\cos(2x) = \cos^2 x - \sin^2 x = 1 - 2\sin^2 x = 2\cos^2 x - 1 \tag{2.49}$$

from which we have

$$2\sin^2 x = 1 - \cos(2x),\ 2\cos^2 x = 1 + \cos(2x) \Rightarrow \tan^2 x = \frac{1 - \cos(2x)}{1 + \cos(2x)} \tag{2.50}$$

Mathematical intermezzo: projection and rotation

In general, a vector $\vec{r}$ in a plane can be written as consisting of components along the X and Y axes: $X = r\cos\phi$ and $Y = r\sin\phi$. If we wish to switch from one coordinate system X, Y to another one X_1, Y_1, we construct a rotation matrix, as follows. Suppose the new coordinate system is at angle $-\theta$ from the previous one. We are looking for a matrix for which

$$\begin{pmatrix} X_1 \\ Y_1 \end{pmatrix} = \begin{pmatrix} R_{11} & R_{12} \\ R_{21} & R_{22} \end{pmatrix} \begin{pmatrix} X \\ Y \end{pmatrix} \tag{2.51}$$

The unit vector along the X axis is projected on the new coordinate axes as $X_1 = \cos\theta$ and $Y_1 = \sin\theta$. Therefore we take $R_{11} = \cos\theta$ and $R_{21} = \sin\theta$. The unit vector along the Y axis is projected on the new coordinate axes as $X_1 = -\sin\theta$ and $Y_1 = \cos\theta$. Therefore we take $R_{12} = -\sin\theta$ and $R_{22} = \cos\theta$. Herewith we have constructed the rotation matrix $\mathcal{R}(-\theta)$.

Consider the vector r which we want to express in a new coordinate system, rotated $-\theta$ with respect to the original system. Eq. 2.51 becomes:

$$\begin{pmatrix} r\cos\phi_1 \\ r\sin\phi_1 \end{pmatrix} = \begin{pmatrix} \cos\theta & -\sin\theta \\ \sin\theta & \cos\theta \end{pmatrix} \begin{pmatrix} r\cos\phi \\ r\sin\phi \end{pmatrix} \tag{2.52}$$

executing the multiplications, we have

$$r\cos\phi_1 = r(\cos\theta\cos\phi - \sin\theta\sin\phi) = r\cos(\theta + \phi)$$

and

$$r\sin\phi_1 = r(\sin\theta\cos\phi + \cos\theta\sin\phi) = r\sin(\theta + \phi)$$

Note that the rotation does not change the length of the vector r. Hence, perhaps not surprisingly, we see that *a rotation of $-\theta$ of the coordinate system corresponds to the addition of θ to the position angle of the original vector.*

In 3-d space, we may choose the Z-axis perpendicular to the plane we just described, and the rotation along $-\theta$ now is written as a rotation around the Z axis:

$$\mathcal{R}_z(\theta) = \begin{pmatrix} \cos\theta & -\sin\theta & 0 \\ \sin\theta & \cos\theta & 0 \\ 0 & 0 & 1 \end{pmatrix} \tag{2.53}$$

Thus, we see the close connection between projecting a vector and a rotation of the coordinate system.

Analogously, a rotation over $-\theta$ around the X-axis can be shown to be given in 3-d coordinates by:

$$\mathcal{R}_x(-\theta) = \begin{pmatrix} 1 & 0 & 0 \\ 0 & \cos\theta & -\sin\theta \\ 0 & \sin\theta & \cos\theta \end{pmatrix} \tag{2.54}$$

Chapter 3

Observing binaries

In this chapter we first derive the equation for the visual orbit of a binary, and briefly describe how it can be fitted. We then derive the radial velocities of the binary members, and describe how they are fitted. The visual orbit and radial velocities provide information about the masses of the stars. Eclipsing binaries allow us to obtain observational information on the radii of the stars. If the stars are spherical, the analysis of the eclipse is relatively straightforward. However, the mutual gravity of the stars leads to non-sphericity. In the last Section of this chapter we discuss the Roche geometry which describes the surfaces of stars in a binary, and briefly explain how this affects the analysis of eclipse observation. The non-sphericity of the stars also implies that their gravity deviates from the $1/r^2$-law. The discussion of this deviation and its effect on the binary orbit are deferred to a later Chapter.

3.1 Projecting the binary orbit

Some angles involved in converting the binary orbit into the observed visual orbit are illustrated in Figure 3.1. To obtain the position of the star in the plane perpendicular to the line of sight, we perform two subsequent rotations. The angle ω is the angle between the long axis of the ellipse, and the line o which is the intersection of the orbital plane with the plane perpendicular to the line of sight. We project r onto o (the new X-axis) and l (the new Y axis). As derived in the intermezzo, this corresponds to adding ω to the position angle ν. We then rotate around o, the new X axis, over the inclination angle $-i$.

The coordinate system in the plane of the sky has o as its X-axis and m as its Y-axis. It is customary to take the X-axis towards the North, and thus we require a third rotation, over the angle Ω between o and the North-South line, to obtain the final coordinates. In Equation:

$$\begin{pmatrix} x' \\ y' \\ z' \end{pmatrix} = \mathcal{R}_z(-\Omega)\mathcal{R}_x(-i)\mathcal{R}_z(-\omega) \begin{pmatrix} r\cos\nu \\ r\sin\nu \\ 0 \end{pmatrix} =$$

$$\mathcal{R}_z(-\Omega)\mathcal{R}_x(-i) \begin{pmatrix} \cos\omega & -\sin\omega & 0 \\ \sin\omega & \cos\omega & 0 \\ 0 & 0 & 1 \end{pmatrix} \begin{pmatrix} r\cos\nu \\ r\sin\nu \\ 0 \end{pmatrix} =$$

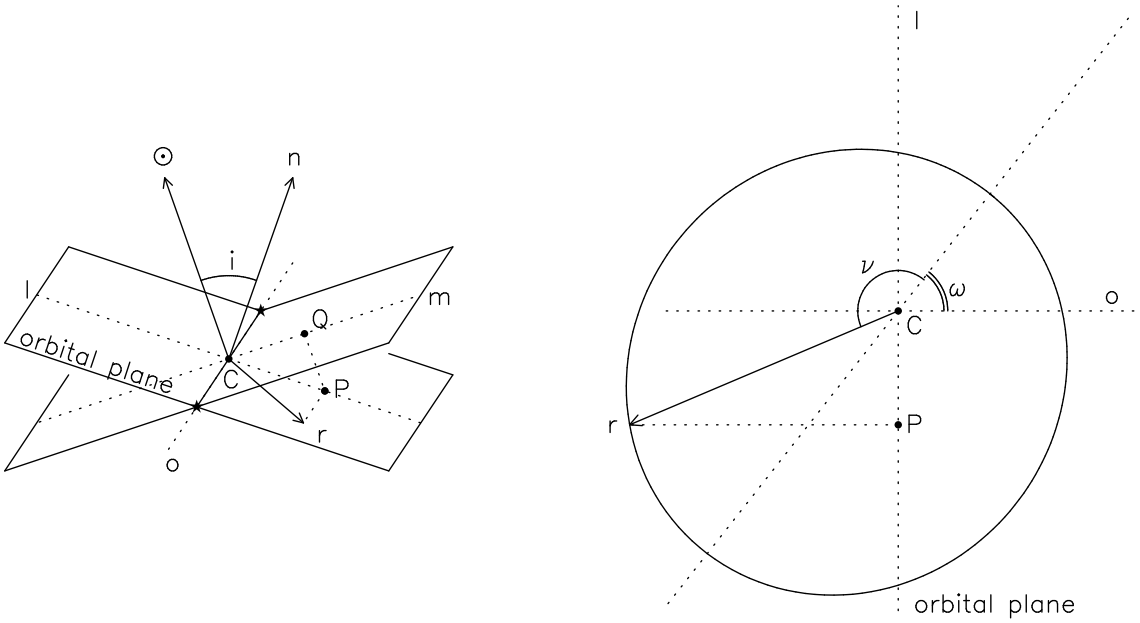

Figure 3.1: *Illustration of the planes involved in observing binary motion. C is the center around which the star moves. n is the normal to the binary plane, passing through C; the celestial plane is drawn through C, perpendicular to the line of sight ($\odot$). The angle between n and $\odot$ is the inclination i, which thus is also the angle between the two planes. l is the line through C, perpendicular to the intersection o of the two planes, in the orbital plane. m is the line through C perpendicular to the intersection, in the celestial plane. Thus, l, $\odot$, n and m are all in one plane, the plane through C perpendicular to the intersection. The vector r connects C with the location of the star, the projection in the orbital plane of r on l is CP, the projection of CP on m is CQ, and $PQ \equiv z$ is the distance of the star to the celestial plane. The angle between r and the semi-major axis is ν (zero at periastron), the angle between the intersection and the semimajor axis is ω.*

$$\mathcal{R}_z(-\Omega)\mathcal{R}_x(-i)\begin{pmatrix} r\cos(\omega+\nu) \\ r\sin(\omega+\nu) \\ 0 \end{pmatrix} =$$

$$\mathcal{R}_z(-\Omega)\begin{pmatrix} 1 & 0 & 0 \\ 0 & \cos i & -\sin i \\ 0 & \sin i & \cos i \end{pmatrix}\begin{pmatrix} r\cos(\omega+\nu) \\ r\sin(\omega+\nu) \\ 0 \end{pmatrix} = \mathcal{R}_z(-\Omega)\begin{pmatrix} r\cos(\omega+\nu) \\ r\sin(\omega+\nu)\cos i \\ r\sin(\omega+\nu)\sin i \end{pmatrix}$$

Computationally, it is easier to write the third rotation on the left hand side of this equation, i.e. to multiply the last equality left and right with $\mathcal{R}_z(\Omega)$. This leads to:

$$\begin{pmatrix} \cos\Omega & \sin\Omega & 0 \\ -\sin\Omega & \cos\Omega & 0 \\ 0 & 0 & 1 \end{pmatrix}\begin{pmatrix} \rho\cos\theta \\ \rho\sin\theta \\ z \end{pmatrix} = \begin{pmatrix} \rho\cos(\theta-\Omega) \\ \rho\sin(\theta-\Omega) \\ z \end{pmatrix} = \begin{pmatrix} r\cos(\omega+\nu) \\ r\sin(\omega+\nu)\cos i \\ r\sin(\omega+\nu)\sin i \end{pmatrix}$$

So finally, we can wrap up the computation, by writing the last equations as

$$x \;=\; r\cos(\omega+\nu) \tag{3.1}$$

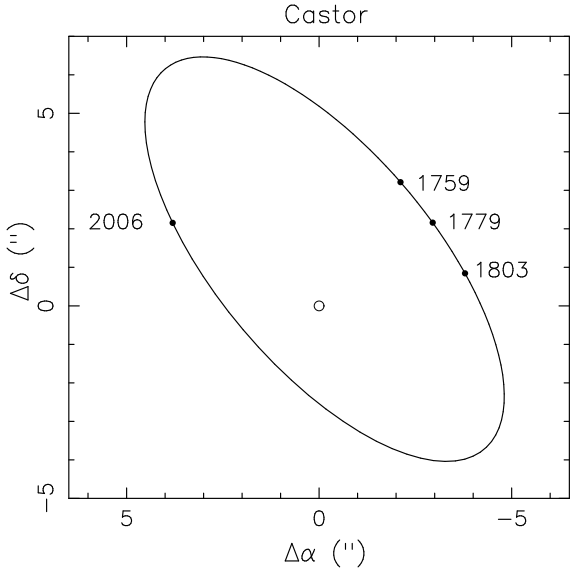

Figure 3.2: *Modern computation of the orbit of Castor B relative to Castor A. The positions in various years are indicated. Compare with Herschel's observations in Figure 1.4.*

parameter	symbol	Castor AB
orbital period	P	467.0 yr
time of periastron passage	T	1958.0
semi-major axis	a	$6.805''$
eccentricity	e	0.343
inclination	i	114.5°
angle periastron/node-line	ω	249.5°
angle North/node-line	Ω	41.3°

Table 3.1: *Parameters required to describe a visual orbit, their symbols, and as an example the values for Castor (from Heintz 1988).*

$$y = r\sin(\omega+\nu)\cos i \tag{3.2}$$
$$z = r\sin(\omega+\nu)\sin i \tag{3.3}$$
$$\rho = \sqrt{x^2+y^2} \tag{3.4}$$
$$\theta = \Omega + \operatorname{atan}\frac{y}{x} \tag{3.5}$$

3.1.1 Computing and fitting the visual orbit

To illustrate the computation of the relative positions of two stars in a binary at time t, we compute the relative position of Castor B with respect to Castor A at the time of Herschel's first observation. We use the orbital parameter as determined by Heintz (1988), listed in Table 3.1.

Step 1. Herschel's first observation is from 11 May 1779. Since the period is in years, we write this as $t = 1779.36$. We compute the mean anomaly from:

$$M = \frac{2\pi}{P}(t-T) \tag{3.6}$$

and find $M = -2.403$ radians.

Step 2. We solve the eccentric anomaly ε from Kepler's equation Eq. 2.36, to find: $\varepsilon = -2.585$ radians
Step 3. We compute the radius vector in the orbital plane r and the real anomaly ν from Eqs. 2.38 and 2.39. Results: $r = 8.787''$ and $\nu = -2.747$.
Step 4. We compute the coordinates with respect to the line of nodes, in the plane of the sky, and from this the radius vector and position angle with respect to the North, from Eqs. 3.1-3.5. Results: $x = -0.324$, $y = -3.641$, $\rho = 3.656$, $\theta - \Omega = -95.08°$, hence $\theta = -53.78°$, equivalent to $\theta = 306.22°$. The tricky thing here is to obtain $\theta - \Omega$ in the right quadrant. If one computes atan(y/x), the answer is the same for x and y both negative as for x and y both positive, but the quadrant in which the result lies is not the same!
Step 5. We can now plot the relative position of the two stars. Putting Castor A at the origin, and noting that the angle θ by definition increases from the North, anti-clockwise. The relative position can be expressed in the directions of right ascension and declination, as:

$$\Delta\alpha = \rho \sin\theta \qquad \text{and} \qquad \Delta\delta = \rho \cos\theta \tag{3.7}$$

Note that in the figure, as on the sky, the right ascension increases towards the left.

The inverse problem from plotting a known orbit is to solve the orbital parameter from a set of observations $\Delta\alpha_i$, $\Delta\delta_i$ obtained at N times t_i. For a set of assumed values for the orbital parameters listed in Table 3.1 we can compute for each observing time t_i the model values $\Delta\alpha_m(t_i)$ and $\Delta\delta_m(t_i)$. If the measurement errors in right ascension and declination at time t_i are $\sigma_{\alpha,i}$ and $\sigma_{\delta,i}$ respectively, and if these errors are Gaussian, the quantity to be minimized is:

$$\chi^2 = \sum_{i=1}^{N} \left[\frac{(\Delta\alpha_i - \Delta\alpha_m(t_i))^2}{{\sigma_{\alpha,i}}^2} + \frac{(\Delta\delta_i - \Delta\delta_m(t_i))^2}{{\sigma_{\delta,i}}^2} \right] \tag{3.8}$$

In general, this minimization cannot be done directly, but must be done with successive improvements on an initial trial solution. The solution to the problem consists of 1) the best parameter values 2) the errors on the parameter values 3) the probability that the model describes the observed orbit (as given by the probability that the model would give rise to a χ^2 with the observed value or larger).

The minimization provides us with the values for the parameters listed in Table 3.1. Of these parameters, T, i, ω and Ω are not essential for the binary itself, but only indicate relations with the direction to and time measurement on Earth. Relevant parameters for the binary are the orbital period P, the eccentricity e and the semi-major axis a. From the visual orbit alone, a is only known in angular units.

If the orbits of both stars can be measured separately with respect to the sky (after correction for parallax and proper motion), then from Eq. 2.9 we see that the ratio of the semi-major axes gives the ratio of the masses: $a_1/a_2 = M_2/M_1$.

If the distance to the binary is known, for example because its parallax is measured, or because it is in a star cluster, we can compute the semi-major axis in cm, and thus from Kepler's third law Eq. 2.45 derive the total mass.

If both distance and mass ratio are known we can derive the masses M_1 and M_2 separately.

3.2 Radial velocities

From Eq. 3.3 we have the distance z of the star to the plane perpendicular to the line of sight. The derivative of z corresponds to (a component of) the radial velocity:

$$\dot{z} = \dot{r}\sin(\omega+\nu)\sin i + r\dot{\nu}\cos(\omega+\nu)\sin i$$

To rewrite this, we first use the angular momentum, as expressed in Eq. 2.18, and then rewrite it, using Eqs. 2.25 and 2.26:

$$r\dot{\nu} = r\dot{\phi} = \frac{l}{r} = \sqrt{\frac{G(M_1+M_2)}{a(1-e^2)}}(1+e\cos\nu) \tag{3.9}$$

Next, we take the time derivative of Eq. 2.26 and rewrite it with Eq. 3.9:

$$\dot{r} = \frac{a(1-e^2)}{(1+e\cos\nu)^2}e\sin\nu\,\dot{\nu} = \frac{a(1-e^2)}{(1+e\cos\nu)^2}e\sin\nu\,\frac{l}{r^2} = \sqrt{\frac{G(M_1+M_2)}{a(1-e^2)}}e\sin\nu \tag{3.10}$$

Entering these results Eq 3.9 and 3.10 into the equation for $\dot{z}$, we find

$$\begin{aligned}\dot{z} &= \sqrt{\frac{G(M_1+M_2)}{a(1-e^2)}}\sin i\,[\cos(\omega+\nu)+e\cos\nu\cos(\omega+\nu)+e\sin\nu\sin(\omega+\nu)] \\ &= \sqrt{\frac{G(M_1+M_2)}{a(1-e^2)}}\sin i\,[\cos(\omega+\nu)+e\cos\omega] \equiv K\,[\cos(\omega+\nu)+e\cos\omega]\end{aligned} \tag{3.11}$$

where the last equality defines K.

In practive, an observed velocity does not belong to the reduced mass, but to one of the two stars. Let us for the moment consider that the star whose radial velocity is measured is labeled 1. We define

$$K_1 \equiv \frac{a_1}{a}K = \sqrt{\frac{G(M_1+M_2)}{a^3(1-e^2)}}a_1\sin i \Rightarrow a_1\sin i = \left(\frac{P}{2\pi}\right)(1-e^2)^{1/2}K_1 \tag{3.12}$$

where we have further used that $a_1/a = M_2/(M_1+M_2)$ (see Eq. 2.9). With K_1 we derive a useful quantity, called the *mass function* for star 1. Multiply the third law of Kepler Eq. 2.45 left and right with $(a_1\sin i)^3/G$, and use Eq. 3.12 to find the mass function $f(M_1)$:

$$f(M_1) \equiv \frac{M_2^3\sin^3 i}{(M_1+M_2)^2} = \frac{P}{2\pi G}K_1^3\left(1-e^2\right)^{3/2} \tag{3.13}$$

From Eq. 3.11 we see that the parameters K, e and ω define the radial velocity curve. K defines the amplitude of the velocity curve, and e (through the non-linearity of ν with time) and ω (as a phase angle) define the form of the curve. In an observed binary, the motion of the center of mass must be added to the average velocity. To visualize how the average radial velocity can differ from zero, consider an eccentric binary with the major axis in the plane of the sky. There are two possibilities: the maximum velocity away from us is at periastron (or at apastron), then the maximum velocity towards us is at apastron (or at periastron), and thus the average of these two is away from us (towards us).

If both velocity amplitudes K_1 and K_2 are measured, we have the mass ratio, as can be seen from dividing the two mass functions Eq. 3.13 and its analogon for star 2: $M_1/M_2 = K_2/K_1$. We also have lower limits to each of the two masses M_1 and M_2, from the mass functions. But further than this one cannot go.

If the inclination is known and both amplitudes then we can solve both masses separately, as well as the semi-major axis.

3.3 Computing eclipses

For the moment we assume that both binary stars are spherical. A spherically symmetric star gives the same flux no matter from which direction it is observed, provided it is not eclipsed. For this reason, it is relatively easy to compute its eclipse by a spherical companion.

Before we do this, we reiterate some basic equations that describe the flux leaving a stellar surface. We start by considering a unit surface of the star; this is sufficiently small to be considered flat. The energy flux $dF_\lambda(\theta)$ at wavelength λ leaving the surface under an angle θ with the normal to the surface is given by

$$dF_\lambda(\theta) = I_\lambda(\theta)\cos\theta d\omega = I_\lambda(\theta)\cos\theta\sin\theta d\theta d\phi \tag{3.14}$$

We obtain the flux leaving the unit surface by integrating over the spatial angle $d\omega$; due to symmetry, the integration over ϕ gives 2π, and we obtain:

$$F_\lambda = 2\pi\int_0^{\pi/2} I_\lambda(\theta)\cos\theta\sin\theta d\theta \equiv 2\pi\int_0^1 I_\lambda(\mu)\mu d\mu \tag{3.15}$$

where we have defined $\mu \equiv \cos\theta$. Integrated over the stellar surface, we obtain the (monochromatic) luminosity of the star

$$L_\lambda = 4\pi R^2 F_\lambda \tag{3.16}$$

Now consider the star from a large distance, and compute the flux f_λ through a unit surface at that distance. The light reaching us from the center of the star leaves its surface along the normal, but the light reaching us from positions away from the center leaves the star at an angle to the surface. A circle at projected distance $r = R\sin\theta$ from the star center has a projected surface $2\pi r dr = 2\pi R^2\sin\theta\cos\theta d\theta$, and at large distance d subtends a spatial angle $d\omega = 2\pi(R/d)^2\sin\theta\cos\theta d\theta$. The radiation from this circle leaves the stellar surface under an angle θ. From the definition of the intensity I according to Eq. 3.14, we can write the flux f_λ as

$$f_\lambda = \frac{2\pi}{d^2}\int_0^R rI_\lambda(r)dr = 2\pi\left(\frac{R}{d}\right)^2\int_o^{\pi/2} I_\lambda(\theta)\cos\theta\sin\theta d\theta = F_\lambda\left(\frac{R}{d}\right)^2 \tag{3.17}$$

From this we see that energy is conserved as the flux travels from the stellar surface to distance d:

$$L_\lambda = 4\pi R^2 F_\lambda = 4\pi d^2 f_\lambda \tag{3.18}$$

This assumes, of course, that there is no interstellar absorption; for the moment we will continue to make this assumption.

A stellar atmosphere model provides the flux F_λ leaving a unit surface of the star. The model depends on 1) the effective temperature 2) the gravity at the

parameter	symbol
radius of star 1	R_1
effective temperature of star 1	T_1
radius of star 2	R_2
effective temperature of star 2	T_2

Table 3.2: *Parameters added to those of Table 3.1 for the study of an eclipsing binary. In principle the metallicity of both stars should be added; however, this are usually determined not from the eclipses, but from the out-of-eclipse spectra.*

stellar surface $g \equiv GM/R^2$, usually expressed as $\log g$ 3) the abundances of the elements. If the whole star is observed, this is sufficient for a description of the stellar spectrum. When part of the surface is blocked, as in an eclipse, we need the intensity $I_\lambda(\theta)$ as a function of angle with the normal. These intensities are also provided by a stellar atmosphere model. The drop of intensity with angle θ is called limb-darkening, and is caused by the fact that the radiation leaving the star at a large angle originates in a region closer to the stellar surface, and therefore cooler than the deeper layer which produces the radiation leaving the stellar surface along the normal. It is best to use these intensities, tabulated as a function of θ; but when these are not available (as in many old studies), one can take recourse to an approximate formula. Often an equation was used of the form

$$I_\lambda(\mu) = I_\lambda(1)\,(a_0 + a_1\mu) \tag{3.19}$$

or higher order approximations. The constants a_0 and a_1 in general may depend on wavelength. For quick estimates one may use the Eddington approximation, which has $a_0 = 2/5$ and $a_1 = 3/5$. The normalization $I_\lambda(1)$ must be chosen to give the correct flux F_λ with Eq. 3.15.

With this background we are ready to compute the eclipse lightcurve. In addition to the orbital parameters listed in Table 3.1 we now have the parameters listed in Table 3.2

To compute a lightcurve, one first divides the orbit into a number of time intervals. For each time, one proceeds as follows.

Step 1. Compute the projected distance ρ between the two stars, just as in the case of the visual binary, with the parameters of Table 3.1.

Step 2. Check, with the parameters from Table 3.2, whether $R_1 + R_2 > \rho$. If not, both stars are seen in full, and the total flux is the sum of the fluxes of the two stars. If $R_1 + R_2 < \rho$ the eclipse is in progress, and we must continue.

As an example, Figure 3.3 show the apparent orbit on the sky of a recently discovered eclipsing brown dwarf, and also the projected distance between the stars as a function of time.

Step 3. Give the eclipsed star index 1, and the eclipser index 2. Compute for each $r = R_1 \sin\theta$ which fraction of the ring at r is covered. Some rings (e.g. those with $r < \rho - R_2$) are wholly visible, others are wholly covered, as illustrated in Figure 3.4. (For details, see Section 3.3.2.)

Step 4. Finally, integrate $I_\lambda(\mu)$ over the visible part of the star. (Alternatively, integrate $I_\lambda(\mu)$ over the eclipsed part, and subtract the result from the out-of-eclipse flux.) The intensity $I_\lambda(\mu)$ is found by looking up the appropriate stellar atmosphere model, characterized by T_1 and $\log g_1 = \log(GM_1/{R_1}^2)$. The integral can be done by dividing the stellar surface in a finite number of (projected) surface rings.

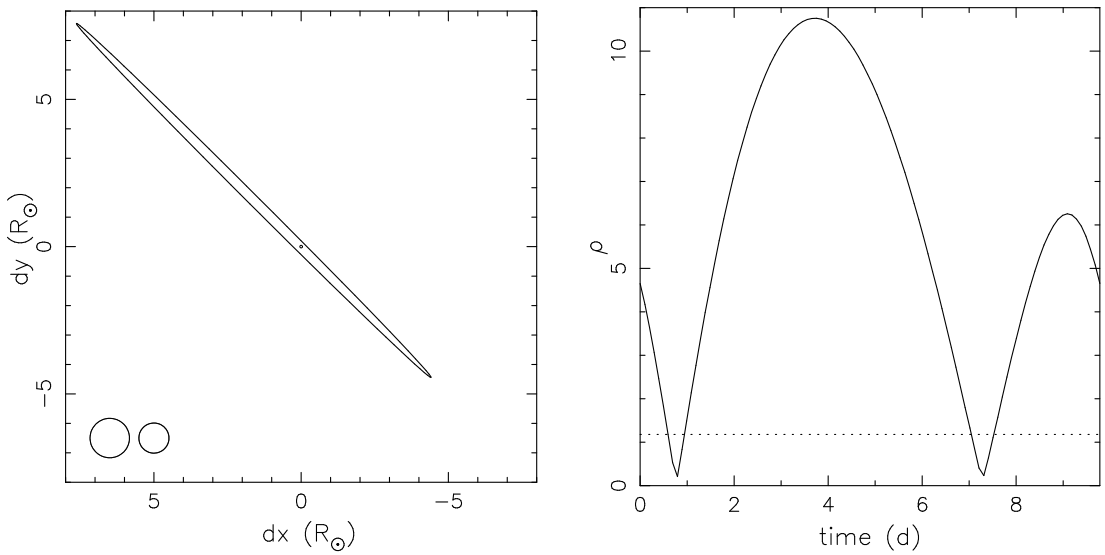

Figure 3.3: *Left: apparent orbit on the sky of the binary brown dwarf 2M J05352184−0546085 as determined from the radial velocities and eclipses; note that the angle with North is arbitrarily chosen. In the left-low corner the sizes of the two stars are indicated. Right: projected distance ρ between the centers of the stars as a function of time. The sum of the radii of both stars is indicated as a horizontal dotted line. The eclipses occur where $\rho < R_1 + R_2$. (See Stassun et al. 2007)*

The effect of limb-darkening is to make the eclipse narrower: at the beginning of the eclipse (called ingress) and at the end (egress), the change in flux is less for a limb-darkened atmosphere, and when the center of the star is eclipsed the variation is stronger in a limb-darkened atmosphere.

In fitting lightcurves, one most often uses data from many orbits, which are averaged into an average lightcurve. This implies that the orbital period is found from a separate analysis, and known before the eclipse lightcurves are fitted. Thus, the separation where the eclipse begins (or ends) directly gives the sum of the two radii, in units of the semi-major axis. Note that the radii of the stars scale with the distance, so that $R_{1,2}$ are only known in angular size, i.e. as $R_{1,2}/d$. The fluxes of both stars, as observed on earth, scale with $(R_{1,2}/d)^2$. This implies that the solution of the lightcurve can only deliver the stellar radii in angular units. The only place where the stellar masses enter is in the choice of $\log g$ for the stellar atmosphere model; this choice also is best made on the basis of the analysis of the out-of-eclipse spectrum, and is usually not very sensitive to the stellar mass.

3.3.1 Uniform disk

We first consider the case of constant intensity $I_\lambda(\theta) = I_\lambda = \text{constant}$. From Eq. 3.15 we find the flux at the surface

$$F_\lambda = \pi I_\lambda \tag{3.20}$$

and from Eq. 3.17 the flux observed at distance d

$$f_\lambda = 2\pi \left(\frac{R}{d}\right)^2 I_\lambda(\theta) \int_o^{\pi/2} \cos\theta \sin\theta d\theta = \pi I_\lambda \left(\frac{R}{d}\right)^2 \tag{3.21}$$

The latter equation could also have been derived by combining Eqs. 3.20 and 3.18.

The uniform disk assumption is often made in conjunction with the assumption that the emitted spectrum is given by the Planck function:

$$B_\lambda d\lambda = \frac{2\pi hc^2}{\lambda^5}\frac{1}{e^{hc/\lambda kT}-1}d\lambda \equiv \frac{C_1}{e^{C_2/T}-1} \tag{3.22}$$

where

$$C_1 = 1.10\,10^6\left(\frac{806\,\mathrm{nm}}{\lambda}\right)^5 \mathrm{watt\,m^{-2}nm^{-1}}; \qquad C_2 = \frac{806\,\mathrm{nm}}{\lambda}17850.8\,\mathrm{K} \tag{3.23}$$

Note that 806 nm is the effective wavelength of the I filter.

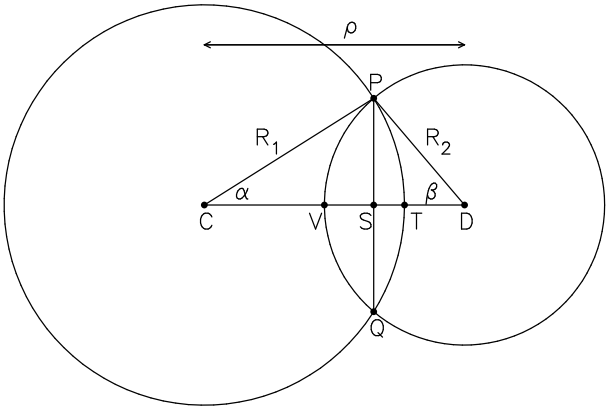

Illustration of the computation of the eclipsed area when a star with radius R_1 covers part of the star with radius R_2, for distance ρ between the centers.

Now consider two stars, with radii R_1, R_2 and uniform intensities $I_{\lambda 1}$, $I_{\lambda 2}$. Away from the eclipse, when the projected distance ρ between the stars exceeds the sum of the radii, the flux observed at distance d is

$$f_\lambda = \pi I_{\lambda 1}\left(\frac{R_1}{d}\right)^2 + \pi I_{\lambda 2}\left(\frac{R_2}{d}\right)^2 \tag{3.24}$$

We first consider the case where star 1 eclipses part of star 2, i.e. the circles outlining both stars intersect in two points (P and Q in Figure 3.3.1). The flux observed from star 2 is diminished by the eclipsed lenticular surface PVQT; the flux of star 1 is not affected. The intersection points P,Q are connected by a line which is a chord in both circles, subtended by angles 2α (from center of star 1) and 2β (from center of star 2) given by the cosine-rule as:

$$A \equiv \cos\alpha = \frac{\rho^2 + R_1^2 - R_2^2}{2\rho R_1} \qquad B \equiv \cos\beta = \frac{\rho^2 + R_2^2 - R_1^2}{2\rho R_2} \tag{3.25}$$

To compute the eclipsed area we first consider the right hand side of the lenticular surface, i.e. area PSQT, and in particular the upper half PST. The area of PST may be computed by subtracting triangle CSP from the circle sector CTP. The area of the triangle is $0.5{R_1}^2\cos\alpha\sin\alpha$, the area of the sector $\alpha/(2\pi)$ times the area $\pi{R_1}^2$ of the projected area of star 1. Therefore the right hand part of the lenticular area is given by

$$\mathrm{PSQT} = 2\mathrm{PST} = (\alpha - \sin\alpha\cos\alpha){R_1}^2 \tag{3.26}$$

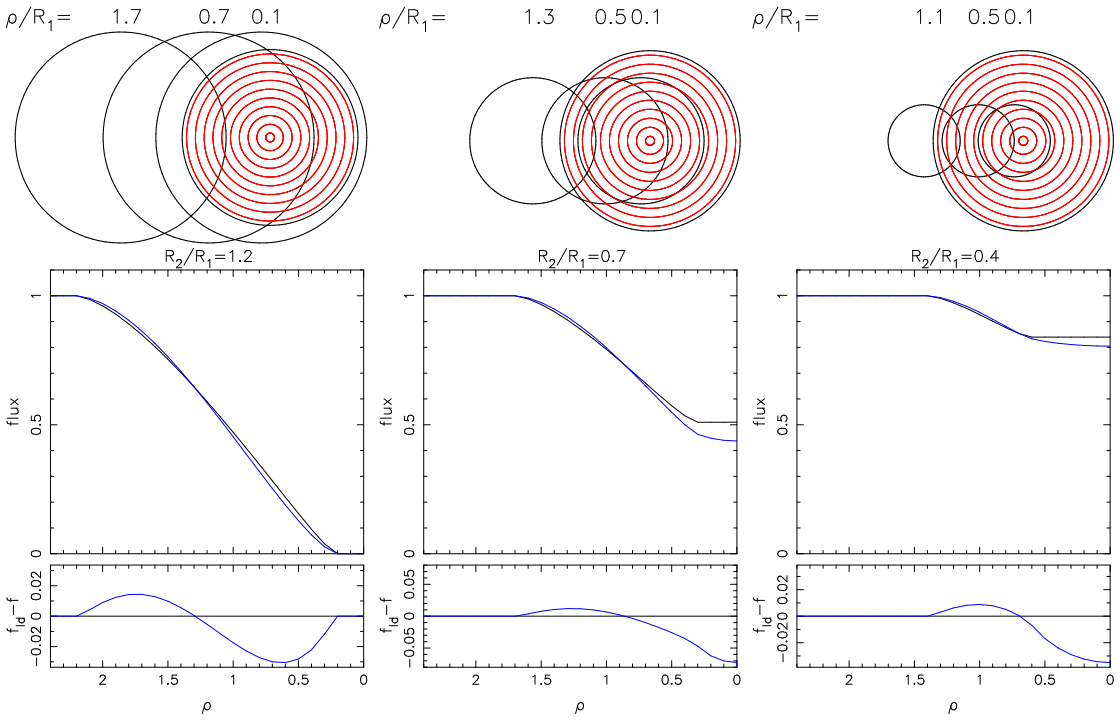

Figure 3.4: *Various eclipse geometries and fluxes. For three ratios of stellar radii R_2/R_1, where R_1 is the eclipsed star, and the flux of star 2 is ignored. The top graphs illustrate the geometry, and the lower graphs the non-eclipsed flux. The fluxes are computed for a homogenous circle (f, for I =constant), and for a sphere with Eddington limb darkening ($f_{\rm ld}$). The latter are shown in blue, and the difference with the homogeneous circle, $f_{\rm ld} - f$, is also shown. Note that the fluxes are plotted as a function of distance between the stars, NOT as a function of time.*

Analogously we find for the left hand part

$$\mathrm{PSQV} = 2\mathrm{PSV} = (\beta - \sin\beta\cos\beta){R_2}^2 \tag{3.27}$$

Finally we express the eclipsed full lenticular area as a fraction of the projected surface of star 2, $\pi {R_2}^2$,

$$w \equiv \frac{\mathrm{PVQT}}{\pi {R_2}^2} = \frac{\arccos(A) - A\sqrt{1-A^2}}{\pi}\left(\frac{R_1}{R_2}\right)^2 + \frac{\arccos(B) - B\sqrt{1-B^2}}{\pi} \tag{3.28}$$

and obtain the flux during partial eclipse of star 2 as

$$f_\lambda = \pi I_{\lambda 1}\left(\frac{R_1}{d}\right)^2 + (1-w)\pi I_{\lambda 2}\left(\frac{R_2}{d}\right)^2 \tag{3.29}$$

When there is no intersection between the outlines of the stars, even though $\rho < R_1 + R_2$, there are two possibilities: star 2 is wholly covered ($w = 1$) if $R_1 > R_2$, or maximally covered with $w = (R_1/R_2)^2$ if $R_1 < R_2$.

3.3.2 Eclipse of limb-darkened star

Eq. 3.17 suggests that the integral is most easily computed after conversion to coordinate μ. However, for an eclipse we do need the radius in the computation of the

eclipsed fraction, and also prefer a more uniform coverage in r rather than in μ. We therefore define $x \equiv r/R$ to rewite Eq. 3.17 as

$$f_\lambda = \frac{1}{d^2}\int_0^R 2\pi r I_\lambda(r)dr = \frac{2\pi R^2}{d^2}\int_0^1 x I_\lambda(x)dx$$

With the definition $\Xi \equiv xI(x)$, the integral can be written as a sum over rings with constant r:

$$f_\lambda = \frac{2\pi R^2}{d^2}\Delta x \sum_i x_i I_\lambda(x_i) \equiv \frac{2\pi R^2}{d^2}\Delta x \sum_i \Xi_i \tag{3.30}$$

An eclipse is in progress for each phase at which $\rho < R_1 + R_2$. For each such ρ, we compute the arccos of the eclipsed angle ϕ for each ring r as by first computing

$$z \equiv cos(\phi) = \frac{r^2 + \rho^2 - {R_1}^2}{2\rho r}$$

If $-1 < z < 1$, we can indeed compute $\phi = \arccos(z)$, and the eclipsed fraction of the ring; the fractions covered are given by ϕ/π. If $|z| > 1$ the ring does not intersect the outline of the eclipsing star 2, with radius R_2, which means that it is either fully eclipsed, or not eclipsed at all (see Fig. 3.4). The eclipsed flux is then computed from

$$f_{\lambda,e} = \frac{2R^2}{d^2}\Delta x \sum_i \phi_i \Xi_i$$

and the observed flux from

$$f_{\lambda,o} = f_\lambda - f_{\lambda,e}$$

The (monochromatic) luminosities of both stars scale with the square of the distance of the binary, and often the uncertainty is the luminosities is dominated by the distance uncertainty. In that case, the *ratio* of the luminosities may be more accurate than either luminosity separately.

3.4 Roche geometry and the Von Zeipel theorem

A star no longer is spherical when it is rotating and/or when it feels the gravity of another star. This deviation of spherical symmetry has an effect at various points in the study of binaries. We briefly investigate the deformation of and limit to the stellar surface due to the presence of a companion star, and the effect of the deformation on the eclipse and on the radial velocity curve, which requires an adapted method of fitting observations of a binary when deformations are important (Chapter 3.4.1). Some other processes that affect the lightcurve are briefly mentioned also (Chapter 3.4.2).

The potential in a binary is determined by the gravitational attraction of the two stars, and by the motion of the two stars around one another. For simplicity, we assume that the potential of each star separately, can still be written as that of a point source; and we discuss a binary with a circular orbit. In the binary frame, one has

$$\Phi = -\frac{GM_1}{r_1} - \frac{GM_2}{r_2} - \frac{\omega^2 r_3^2}{2} \tag{3.31}$$

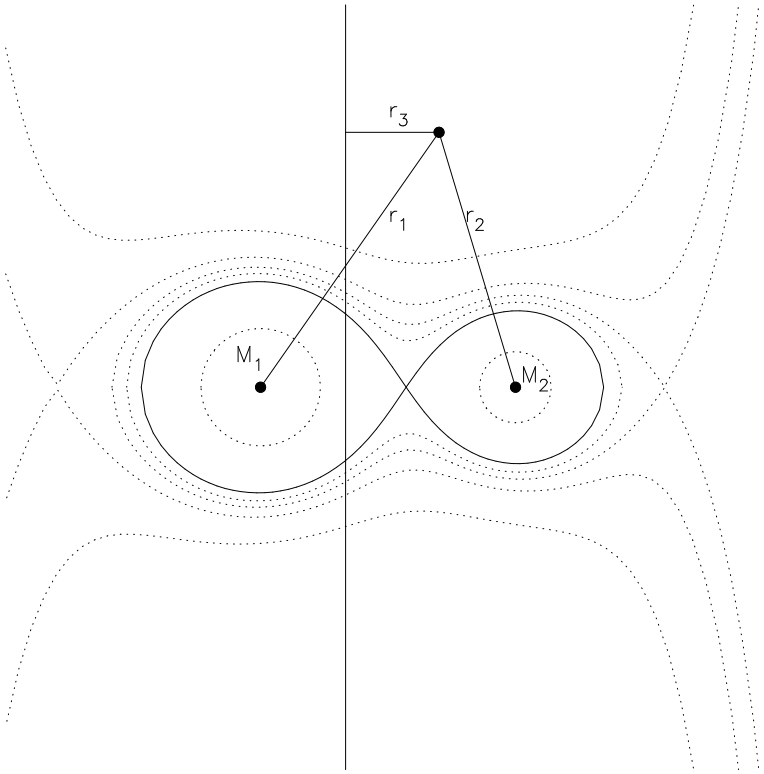

Figure 3.5: *Roche lobe geometry for a mass ratio $M_1/M_2 = 2$. Equipotential surfaces are shown for different values of $-\Phi = C$. For the largest value of C the surface consist of two separate lobes, one around each star. The Roche lobe is the surface around both stars that passes through the inner Lagrangian point. Also shown are the surfaces containing the two outer Lagrangian points. The vertical line is the rotation axis.*

where r_1 and r_2 are the distances to the center of the stars with mass M_1 and M_2, respectively; ω is is the orbital angular velocity, given by

$$\omega \equiv \frac{2\pi}{P_b} = \sqrt{\frac{G(M_1 + M_2)}{a^3}} \tag{3.32}$$

and r_3 is the distance to the axis of rotation of the binary (see Figure 3.5). Writing Eq. 3.31 in dimensionless units (mass in units of the total mass, and distances in units of the semi-major axis a), one sees that the form of the surfaces of constant Φ depends only on the mass ratio M_1/M_2.

We can discriminate four types of surfaces of $-\Phi = C$, with C a positive constant. For large C, the potential surface consists of two closed surfaces, one around each star. For a critical value of C, the two closed surfaces touch, in the inner Lagrangian point. The surface at this value of C is called the Roche lobe (see Roche 1859). For smaller values of C we have a closed surface around both stars, and for very small values the surfaces become open.

The volume of the Roche lobe can be calculated numerically. A useful approximate formula for the average radius of the Roche lobe around the most massive star (with mass M_1) is:

$$\frac{R_L(M_1)}{a} \simeq 0.38 + 0.2\log\frac{M_1}{M_2} \tag{3.33}$$

which is accurate to 2 % for mass ratios $0.2 < M_1/M_2 < 20$. For the average radius of the Roche lobe around the less massive star, with mass M_2, one may use the approximate formula:

$$\frac{R_L(M_2)}{a} \simeq 0.46 \left(\frac{M_2}{M_1 + M_2} \right)^{1/3} \tag{3.34}$$

which is accurate to 2 % for mass ratios $M_2/M_1 < 0.8$. An approximate equation valid for all mass ratios is

$$R_{L1} = \frac{0.49a}{0.6 + q^{-2/3} \ln(1 + q^{1/3})} \quad \text{where} \quad q \equiv \frac{M_1}{M_2} \tag{3.35}$$

A particle within the Roche lobe is attached to one star; a particle on the Roche lobe can move to the other star. Thus, if a star reaches the size of the Roche lobe, mass transfer may ensue. This can occur because the star expands in the course of its evolution, or because the binary shrinks. An evolving star in a binary can fill its Roche lobe for the first time as it expands on the main sequence (Case A), as it expands after hydrogen exhaustion (Case B), or as it expands after helium exhaustion (Case C). Which of the three cases applies, depends on the size of the Roche lobe, which in turn depends on the distance between the two stars and (to a lesser extent) on the mass ratio (see Eqs. 3.33-3.35).

If star a star has a deformed, but stationary structure, hydrostatic equilibrium still holds: the gradient of the pressure P is balanced by the gravitational force, which can be written as the derivative of the gravitational potential Φ:

$$\nabla P = -\rho \nabla \Phi \tag{3.36}$$

Thus, the gradient of the pressure is everywhere parallel with the gradient of the potential: this implies that surfaces of constant potential are also surfaces of constant pressure $P = P(\Phi)$. In Eq. 3.36, we then find that ρ is a function of the potential only, since it depends only on $P(\Phi)$ and Φ. Thus, equipotential surfaces also have a constant density $\rho = \rho(\Phi)$, and via the equation of state also a constant temperature $T = T(\Phi)$.

The equation of radiative transport is:

$$\nabla T = -\frac{3\kappa\rho}{4\sigma} \frac{1}{4T^3} \quad F_{\rm rad} \tag{3.37}$$

where κ is the opacity, σ the Stefan-Boltzmann constant, and $F_{\rm rad}$ the radiative flux. In a deformed star, the distances between equipotential surfaces are different in different directions. Since equipotential surfaces have a constant temperature, the temperature derivative must also be different in different directions: smaller (larger) when the equipotential surfaces are further apart (closer). With Eq. 3.37 we find that the flux across an equipotential surface, and thus the flux at the stellar surface, varies. This is called the Von Zeipel theorem (see Von Zeipel 1924). This theorem was first used in the context of rapidly rotating single stars, to show that the effective temperatures at the equator are lower than at the poles. Similarly in a binary, a star that fills its Roche lobe has a lower effective temperature near the inner Lagrangian point. This effect is called *gravity darkening*.

3.4.1 Fitting binary observations in Roche geometry

When a star in a binary is deformed from a sphere, its eclipses will look different, for two reasons:

- the geometry of the eclipse is different
- the temperature, and therefore the flux and the spectrum, varies over the stellar surface, due to the Von Zeipel theorem

The center of light of the deformed star no longer necessarily coincides with the center of mass. This implies that the radial velocity measurements are also affected. Also, the strength of a spectral line depends on the temperature and the gravity, and therefore varies over the surface of a deformed star. This also tends to displace the measured velocity from the velocity of the center of mass of the star.

To really compute these effects, one would require a three-dimensional model of the stellar interior. In the absence of such models, various simplifications are made, of which the most important is the assumption that the effective temperature T_e of a stellar surface element scales with the gradient of the potential there according to

$$\frac{T_e}{T_{e,pole}} = \left(\frac{F}{F_{pole}}\right)^{0.25} = \left(\frac{\nabla\Phi}{\nabla\Phi_{pole}}\right)^{g} \tag{3.38}$$

where $F \equiv \sigma {T_e}^4$ is the energy flux leaving the surface. The exponent g depends on the type of star, and for a star with a radiative envelope has the value $g = 0.25$, that follows from simple application of the Von Zeipel theorem Eq. 3.37. For stars with a convective envelope, the value of g is lower, $g = 0.08$.

By integrating F over the stellar surface, and equating the result with the stellar luminosity, one finds the normalization constant F_{pole}.

It is then straightforward, but computationally expensive, to compute a lightcurve. First compute the form of the surface of each star, which is an equipotential surface, characterized by Eq. 3.31 with a constant Φ. For the sake of computation, this surface is divided in small elements. Next assign each surface element of the star a spectrum with the appropriate effective temperature and gravity, and then compute for each viewing angle which surface elements are visible, and add their contributions to the flux, or for the spectrum to the flux distributions taking into account the Doppler shift due to the velocity of the surface element with respect to the observer. Thus computing the flux and radial velocity at each orbital phase one may compare to the observations, and where necessary adapt the binary parameters to improve the fit.

The main effect of the deformation of a star into a pear shape is the *ellipsoidal variation*. At conjunction of the two stars, we see smaller areas than when the stars are in the plane of the sky. Thus the flux observed from the binary varies throughout the orbit, with two minima each orbit at conjunction, and two maxima in between. Figure 1.5 shows several examples, and also illustrates that the amplitude of the ellipsoidal variation is larger when a star is closer to filling its Roche lobe, i.e. when it is more deformed. Obviously, the amplitude of the variation also depends on the inclination, being largest at $i = 90°$.

The first widely used code to fit a binary lightcurve is that of Wilson & Devinney (1971). This early version still had many simplifications. In particular it described

the radiation emitted by each surface element as a black body, only applying colour corrections (from black body to stellar atmosphere spectrum) to the integrated flux. In the course of time, as computers became faster, the code has been improved. An example of a modern version is given by Orosz & Haushildt (2000), The latter code takes into account the effects of *limb darkening* (see discussion near Eq. 3.19). These codes find the best solution by minimizing a optimization function, in particular the χ^2 function.

It is impossible to find the best parameters of the binary reliably by using a standard routine for this minimization as the Levenbergh-Marquardt routine (described in e.g. *Numerical Recipes*, Chapter 15.5, Press et al. 1992), because the number of parameters is too large. Orosz has therefore experimented with another method, the *genetic algorithm* which cleverly uses random numbers to search the parameter space for the best solution, and this works very well. An very clear description of the genetic algorithm and its applications is given by Charbonneau (1995; in particular the first 9 pages). An interesting extension is the use of *black sheep*, i.e. bad descendents from good parents, in the genetic algorithm scheme. This is discussed by Bobinger (2000).

3.4.2 Further complications of light curve fitting

Apart from the Roche geometry, various other effects are visible in the lightcurve, and depending on one's interest can be considered as unnecessary complications or interesting sources of extra information... We mention four of these.

The first is rapid rotation of a star, which leads to a flattened form, and thus to an altered eclipse lightcurve. It also affects the radial velocity curve: for example, when the part of the star that rotates away from us (towards us) is eclipsed, the observed radial velocity is dominated by the rotation towards us (away from us) by the part of the star that is not eclipsed, and thus shifts the radial velocity to smaller (bigger) values. This may be a noticable effect.

The second effect is the heating of a star by its companion: the radiation of one star impinges on the surface of its companion, and if sufficiently strong, heats it. When a small but hot, luminous star is accompanied by a cool star, the lightcurve may be completely dominated by the heated side facing the hot star. In this case there is only one maximum in the lightcurve per orbit, when the heated face is oriented towards Earth.

A third effect is the presence of spots. This is detectable through a variable lightcurve: as spots change their intensity and/or position, the lightcurve also changes. The spots are cooler, and therefore emit a different spectrum; the effect is largest when the spot faces the Earth, and absent when it is occulted. If a few large spots are present, their properties can be derived from careful analysis of the lightcurve and the radial velocities. However, if many weaker spots are present, they merely add noise to the lightcurve, a unique solution no longer being possible. A common procedure is such a case is to average the lightcure over many orbits, hoping that the effects of the spots average out... If the Sun is any guidance, spots may also be accompanied by flares, sudden increases in the luminosity. Again, if one strong flare occurs, we can study it; if a large number of small flares occur at each time, they add irreducable noise.

A final important effect is the presence of gas streams from one star to the other,

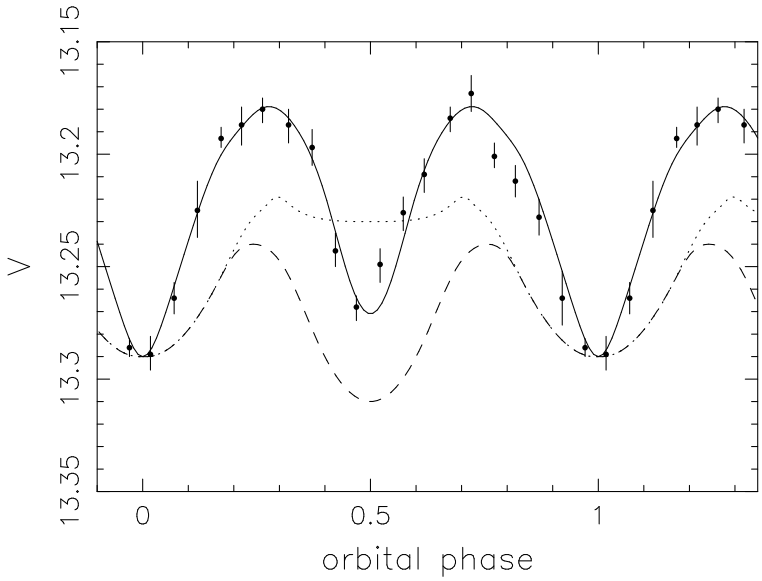

Figure 3.6: *SMC X-1 is a bright X-ray source in the Small Magellanic Cloud, in which an O star fills its Roche lobe and transfers mass via an accretion disk to a neutron star. The observed orbital light curve of SMC X-1 (•) is shown together with the predicted variations due to ellipsoidal variation only (−−), due to ellipsoidal variation plus X-ray heating (· · ·), and due to these two effects plus an accretion disc (—). Not that the disk eclipses part of the heated side of the companion near phase 0.5. After Tjemkes et al. (1986).*

in particular when one star fills its Roche lobe. Such a gas stream from a star that fills its Roche lobe may directly hit the other star, in particular in a close binary, or it may form a disk around the other star. Theoretically the light produced by such a stream and/or disk is not well understood. Lightcurve fitting programmes have very simplified prescriptions for gas streams and disks. In general it must be stated that the presence of a strong disk complicates the lightcurve analysis, and makes the solution less secure.

Recently, some observational data have reached a level of accuracy where relativistic effects become important! In the non-relativistic case, ellipsoidal variations are symmetric. When the orbital velocities are high, however, Doppler boosting becomes noticable: when the star moves towards us, it flux is enhanced; when it moves away from us, its flux is reduced. Thus the flux of one ellipsoidal maximum is higher than that of the other maximum.

3.5 Exercises

Exercise 10. Pick a year from 1600+n20, with n between 0 and 25, and compute the position of Castor B relative to Castor A, following the steps outlined above. Step 2 must be done iteratively. A stable method is to find two values of ε where the function $F(\varepsilon) \equiv M - \varepsilon - e \sin \varepsilon$ changes sign, and then half the interval in which this happens successively until the remaining interval is small enough for the required accuracy.

Exercise 11. Find the parallax of Castor, from the Hipparcos catalogue. Use this to compute the total mass of Castor A+B, and the radial velocity difference

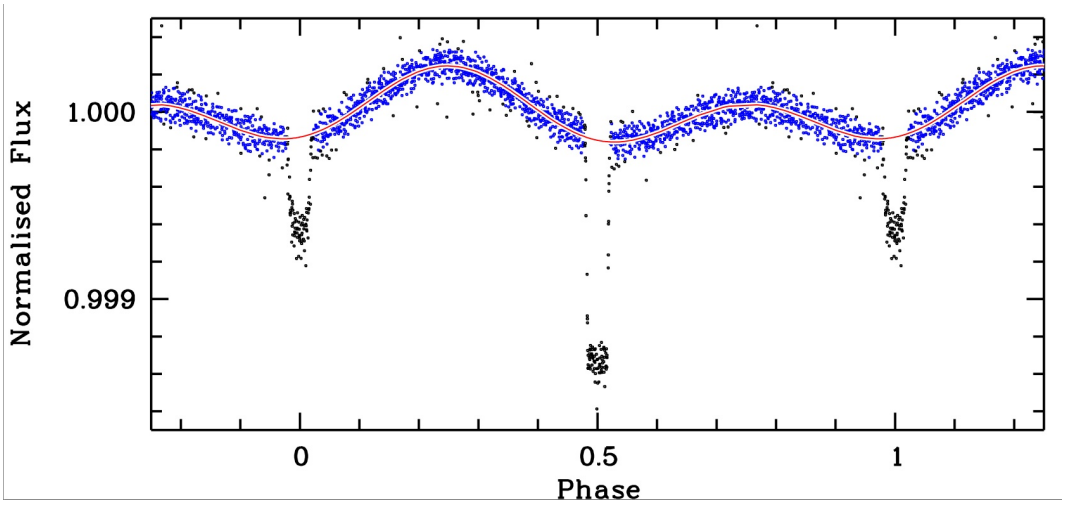

Figure 3.7: *The orbital lightcurve of KOI 74, as obtained with the Kepler satellite may be approximated (away from the eclipses) as the sum of a sine wave with half the orbital period (the ellipsoidal variation) and a sine wave with the orbital period (Doppler-boosting). From Van Kerkwijk et al. (2010).*

between the two stars at the time of Herschel's first observation. At that time $\nu = -157.4°$.

Exercise 12. Consider the mass funtion Eq. 3.13. a. Show that the measurement of the velocity amplitude of star 1, K_1, provides a lower limit to the mass of the companion M_2.
b. What is the most likely value for the inclination?
c. In binaries with a pulsar, the analysis of the pulse arrival times gives the projected orbital velocity of the pulsar, K_1. To estimate the mass of the pulsar companion, one often assumes a pulsar mass $M_1 = 1.4 M_\odot$, and a value for the inclination of 60°. Explain this chosen value for i.
d. PSR 1953+29 has a mass function $f(M) = 0.00272 M_\odot$. Compute the mass of the companion under the assumptions listed in c).

Exercise 13. a. Rewrite Eq. 3.31 in dimensionless units, by writing all distances in units of semi-major axis a and all masses in units of M_2, and show that the form of the Roche surfaces depends only on the mass ratio M_1/M_2.
b. At the inner Lagrangian point, the net force is zero. Write the equation for this. Write r_2 and r_3 for the inner Lagrangian point in terms of a and r_1. Finally, make the equation dimensionless, in the form $\mathcal{F}(r_1/a) = 0$. $\mathcal{F}(x)$ indicates 'function of x.
c. Note: we can use the Newton-Raphson method on the dimensionless equation of b) to solve for the inner Lagrangian point. Knowing its place we can calculate its potential Φ, the potential of the Roche surface. We can derive similar equations as in b) for the second and third Lagrangian points.

Exercise 14. The radius of a 5 $M_\odot$ star increases on the main sequence from 2.67 $R_\odot$ to 6.52 $R_\odot$. During hydrogen shell burning the radius increases to 115 $R_\odot$. The companion is a 4 $M_\odot$ star. Compute the maximum orbital period at which case A mass transfer ocurs in this system, and the maximum orbital period for case B.

Computer Exercise 1. Write a computer code to compute the projected orbit of a visual binary, and check it correctness with your intermediate and final results in Exercise 10.

Computer Exercise 2. A binary of two brown dwarfs has he following parameters: orbital period 9.77962,d, semi-major axis $8.8\,R_\odot$, eccentricity 0.333, inclination 89.2°, angle of priastron $\omega = 217°$. The brown dwarfs have radii and effective temperatures $0.68\,R_\odot$ and 2725 K for dwarf 1, $0.49\,R_\odot$ and 2899 K for dwarf 2. (Thus the smaller dwarf is hotter!) In the following you may assume that the stars are spherical. The binary has a distance of 460 pc.

a. compute the flux f_I near Earth of the binary out-of-eclipse.

b. use your computer code to compute ρ as a function of orbital phase, and determine the phases during which the binary is eclipsed.

c. compute the eclipse lightcurve

Chapter 4

Fundamental parameters of stars derived from binaries

Fundamental parameters as mass, radius, luminosity and effective temperature are most accurately derived from binaries. In this chapter we discuss some examples to illustrate the derivation of such parameters, and some uncertainties inherent in these derivations, on the basis of an article on visual binaries (by Hummel et al. 1995) and an article on double-lined eclipsing binaries (by Andersen 1991). We also discuss three additional binaries to illustrate various additional methods, and the application of binary studies in distance determinations of clusters.

4.1 Visual binaries

With this section, read Hummel et al. (1995). In working the examples, we use the best parameter values; in actual scientific practice one should also propagate the errors on these parameters to errors in the derived fundamental parameters.

4.1.1 Deriving the masses: π And

Dividing the mass function for the primary (Eq. 3.13) by its equivalent for the secondary, and entering the values of K_i for π And from Table 4.1 we obtain the mass

Table 4.1: *Parameters of three binaries discussed in the article by Hummel et al . (1995) and used in the worked examples in this section. The velocity amplitudes K_i and period P are from spectroscopic observations, the eccentricity e and inclination i are from the visual orbit.*

binary:	π And	β Aur	θ Aql
K_1 (km/s)	47.5	107.75	51.0
K_2 (km/s)	117.4	111.25	63.7
P (d)	143.6065	3.96	17.1243
e	0.552	0.	0.607
i ($^\circ$)	103.	76.	143.5
a ($''$)	0.00669	0.0033	0.0032
f_V (10^{-12}watt m^{-2}nm^{-1})	0.663	6.81	2.00
f_{V1}/f_{V2}	1.45	1.20	4.09

ratio $M_1/M_2 = K_2/K_1 = 2.47$. We rewrite the mass function of the primary as

$$f(M_1) = \frac{P}{2\pi G} {K_1}^3 \left(1-e^2\right)^{3/2} = M_2 \sin^3 i \frac{1}{\left(\frac{M_1}{M_2}+1\right)^2} \tag{4.1}$$

and enter the mass ratio and the values from the visual orbit in it, to find $M_2 \simeq 12 M_\odot$ and thus $M_1 \simeq 29 M_\odot$. As discussed by Hummel et al. these masses are much too high to be compatible with the observed spectral type. The reason for this wrong result is probably that the value for the velocity of the secondary is spurious.

This serves as a warning that published velocities and velocity amplitudes are not always as accurate as advertised. It is always advisable to read the observational article carefully and form an informed opinion on the reliability of the results.

4.1.2 Deriving the distance: β Aur

Eq. 3.12 gives the semi-major axis of the primary; adding to this the equivalent equation for the secondary we obtain

$$a \sin i = (a_1 + a_2) \sin i = \frac{P}{2\pi} \left(1-e^2\right)^{1/2} (K_1 + K_2) \tag{4.2}$$

Entering the values for K_i from the spectroscopic orbit and the period, eccentricity and inclination from the visual orbit of β Aur (Table 4.1) we immediately obtain the physical semimajor axis $a = 0.082$ AU, which we may compare with the semimajor axis in arcseconds from the fit of the visual orbit (Table 4.1). The combination of these two values for the semimajor axis gives the distance of the binary. Noting that $1''$ at 1 pc corresponds to 1 AU, hence that $0.0033''$ at x pc corresponds to $0.0033x$ AU, we find $x = 0.082/0.0033 = 24.8$ pc.

4.1.3 Radius and temperature: θ Aql

The visual flux f_V of θ Aql relates to the added fluxes f_{Vi} of both stars[1]. The visual flux ratio has been derived from the eclipse depths (see Table 4.1). The total flux of the binary may be written

$$f_V = f_{V1} + f_{V2} = f_{V1} \left(1 + \frac{f_{V2}}{f_{V1}}\right) \tag{4.3}$$

Entering f_V and f_{V1}/f_{V2} from Table 4.1 we obtain $f_{V1} = 1.61 \times 10^{-12}$watt m^{-2}nm^{-1}.

Analogous to the example for β Aur, we can derive the distance to θ Aur as 76.9 pc, and we use this to compue the visual luminosity of the primary, $L_{V1} = 4\pi d^2 f_{V1} = 1.14 \times 10^{26}$ watt nm^{-1} $= 203 L_{V\odot}$. We assume here, mainly because of the small distance, that interstellar absorption may be ignored. Deriving in the same way the blue flux f_{B1} we obtain the primary colour $f_{V1}/f_{B1} = 0.511$.

To progress from here, we must obtain the bolometric correction, i.e. the ratio of bolometric to visual luminosity (L/L_V), and the effective temperature from tabulated stellar atmosphere model spectra. Stellar atmosphere model spectra depend on the

[1]We could also have written f_{550}, i.e. the flux at 550 nm; but we prefer f_V to indicate that the flux is a weighted average over the V-filter; we will also write U (for 365 nm), B (440 nm) and I (806 nm).

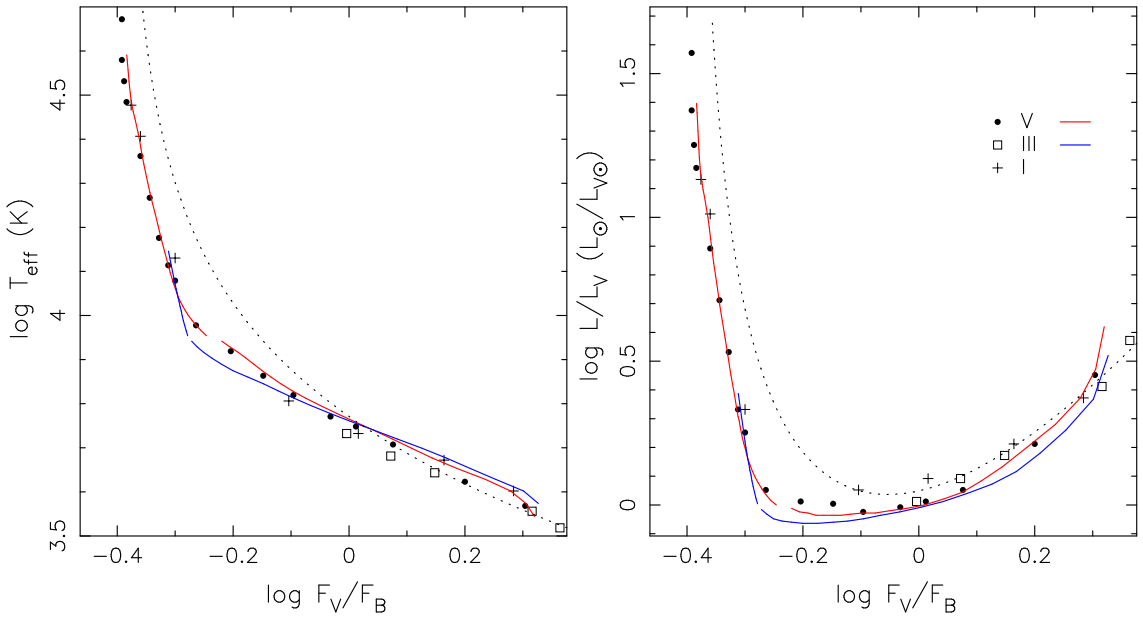

Figure 4.1: *Modern relation between colour and temperature (left) and bolometric correction (right), from Bessell et al. (1998, solid lines). For comparison some old values are also shown with symbols as indicated, from Mihalas & Binney (1981), who took their numbers from Allen (1973) and Strand (1963), who in turn compiled from others. . . . The dotted lines indicate the Planck function.*

effective temperature $T_{\rm eff}$, on the gravitational acceleration g (usually given as $\log g$), and on the metallicity (or more accurately, the abundances of all relevant elements). Hummel et al. note that the two stars of θ Aql have the same colours, and use $\log L/L_V(L_\odot/L_{V\odot}) = 0.156$ and $T_{\rm eff} = 10800\,{\rm K}$ for both.

Thus one obtains for the primary $L_1/L_\odot = 10^{0.156} L_{V1}/L_{V\odot}$, hence $L_1 = 291 L_\odot$. With

$$\log \frac{L}{L_\odot} = 2 \log \frac{R}{R_\odot} + 4 \log \frac{T_{\rm eff}}{T_\odot} \qquad \text{where} \qquad T_\odot \simeq 5780\,{\rm K} \tag{4.4}$$

we obtain $R_1 = 4.9 R_\odot$.

In general one will find that the masses are more accurate than the luminosities or temperatures. The reason for this is one needs models to convert from colours to bolometric luminosities or effective temperatures, and that this conversion can have large uncertainty: it changes with author and with time. This is illustrated in Figure 4.1 where modern values are compared with those from an excellent textbook from 1981, which in turn based its tables on much older books, which in turn. . . . It is seen that at some colours, the differences are appreciable. In applying conversions with use of tables, one must also make sure to use the same calibrations for the fluxes that were used by the astronomers who compiled the tables.

4.2 Double-lined spectroscopic, eclipsing binaries

With this section, read Andersen, 1991. The extra information provided to a double-lined spectroscopic orbit by eclipses is the inclination, and through this the absolute dimensions of the stars and the binary orbit. As Andersen remarks, the main problem in assessing uncertainties of the derived parameters are systematic

errors: in practice this implies that the actual errors are rather bigger than the formal errors given by the fitting procedure.

Velocities can be measured from individual lines of known laboratory wavelength, by fitting the line profile. Problems that arise with this procedure are the possibility of blends; and the possibility that different lines arise at different depths in the atmosphere, and thus give different velocities! Balmer lines are especially troublesome; experience shows that errors as large as 30% may arise from the use of Balmer lines as the main velocity indicators. It is clearly better to use relatively narrow lines. A consequence is that velocities can be measured much less accurately for O stars than for G stars.

It is more common nowadays to determine the velocity from a cross-correlation of the observed spectrum with a template spectrum, as discussed in Chapter 1. For the template in the cross-correlation, one can use a model spectrum. Troublesome parts from the spectrum (e.g. with Balmer lines) are excluded from the cross-correlation. The advantage of this method is that the depth of the cross correlation improves not only with the correct velocity, but also with the correctness of the spectrum. This means that the cross-correlation also provides information on the parameters that set the spectrum: effective temperature, gravitational acceleration, metallicity, and rotation of the star. If no model spectrum is available, one can determine the average of all the spectra that one has taken from the object and use this as a template. In this case iteration is necessary: having determined a preliminary set of velocities, one constructs a new template by shifting all spectra to the same rest-wavelength, and then does a new cross-correlation. This procedure already converges after a few iterations.

To provide information on the temperature of the stars, the photometry must be obtained for at least two bands. A source of uncertainty is the reddening of the system. Most systems listed by Andersen are very nearby, and the reddening is small, so that the uncertainty is also small. With CCDs, photometry is often very accurate – depending on the flux of the star; the dominant uncertainty in the monochromatic luminosities is usually the distance. This means that the ratio of the monochromatic luminosities is generally much more accurate than the luminosities themselves. In Figure 4.2 the radius and luminosity are shown as a function of mass for main-sequence stars. The values come from double-lined spectroscopic eclipsing binaries. The Sun is also shown.

The radii show appreciable spread at each mass; probably mainly due to evolution. The zero-age main-sequence radius may be approximated as

$$\frac{R}{R_\odot} = \left(\frac{M}{M_\odot}\right)^n \tag{4.5}$$

where $n = 0.6$ for $M > M_\odot$ and $n = 1$ for $M < M_\odot$. The theoretical mass-radius relation for stars of sub-solar mass is still problematic. Baraffe & collaborators have shown that for low-mass stars on must incorporate full atmosphere models into the stellar structure equations to obtain a correct model.

The luminosities of main-sequence stars are well-defined as a function of mass; and may be approximated with

$$\frac{L}{L_\odot} = \left(\frac{M}{M_\odot}\right)^{3.8} \tag{4.6}$$

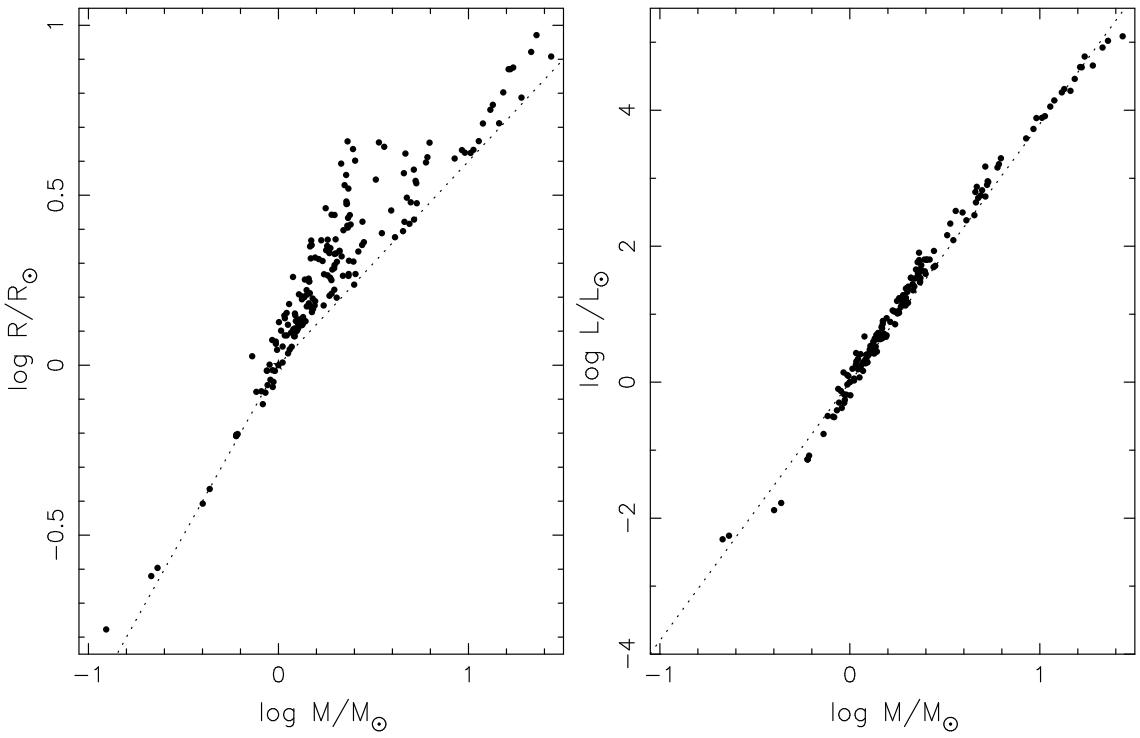

Figure 4.2: *Radius and luminosity for main sequence stars as a function of mass. Only values known with an accuracy of $\leq 2\%$ are used in this Figure. Data from Torres, Andersen & Giménez (2010); Masses and radii for HAT-TR-205-013 are added (Beatty et al. 2007), the luminosities for these very cool stars are not well-known. Dashed lines give the ZAMS mass-radius relation according to Eq, 4.5 and mass-luminosity relation according to Eq. 4.6.*

Table 4.2: *Parameters of main-sequence stars as function of spectral type. Masses, radii, luminosities and spectral type from Andersen (1991); from these,* $\log g$ *and* $T_{\rm eff}$ *are computed, and the colors for these parameters are found in Bessell et al. (1998). Some quantities are normalized on solar units;* $L_{V\odot} = 5.6 \times 10^{23} watt\, nm^{-1}$.

SpT	M	R	$\log L$	$T_{\rm eff}$	$\log L_V$	$\log L/L_V$	log	log	log
	$(M_\odot)$	$(R_\odot)$	$(L_\odot)$	(K)	$(L_{V\odot})$	$(L_\odot/L_{V\odot})$	f_B/f_U	f_V/f_B	f_I/f_V
Main sequence									
O8V	22.0	7.90	5.10	38900	3.71	1.39	-0.68	-0.38	-0.66
B2V	9.0	4.30	3.63	22400	2.77	0.86	-0.57	-0.35	-0.63
B5V	5.0	2.90	2.66	15600	2.16	0.49	-0.46	-0.33	-0.60
A0V	2.5	1.80	1.51	10200	1.42	0.09	-0.25	-0.27	-0.56
A5V	1.9	1.50	1.06	8590	1.08	-0.02	-0.19	-0.22	-0.50
F0V	1.5	1.30	0.67	7420	0.71	-0.04	-0.22	-0.15	-0.41
F5V	1.3	1.20	0.43	6800	0.46	-0.03	-0.23	-0.10	-0.35
G0V	1.2	1.10	0.30	6470	0.33	-0.03	-0.22	-0.07	-0.32
G5V	1.0	1.00	0.00	5780	0.00	0.00	-0.15	0.01	-0.25
K0V	0.9	0.85	-0.33	5180	-0.39	0.06	-0.01	0.08	-0.18
M1V	0.6	0.55	-1.22	3860	-1.64	0.42	0.28	0.29	0.12
M4V	0.4	0.40	-1.87	3110	-2.80	0.92	0.29	0.35	0.56

From the mass, radius and luminosity one may compute the gravitational acceleration g and effective temperature $T_{\rm eff}$ of the atmosphere; and from atmosphere models (which are calibrated with accurately measured stars) one may then obtain the absolute monochromatic luminosities and colours. The results are given in Table 4.2.

For very cool objects, the bolometric corrections are unknown; for very-low-mass stars and brown dwarfs, observers derive absolute monochromatic luminosities, rather than effective temperatures or bolometric luminosities. For such stars, instead of the mass-luminosity relation, one has the mass-monochromatic-luminosity $M-L_\lambda$ relation.

4.3 Some interesting binaries

In this section we discuss binary studies that illustrate variants on the analysis methods discussed above, and that are interesting for a variety of reasons. The binary HAT-TR-205-013 illustrates the use of rotational velocity in the determination of the parameters of the lowest-mass main-sequence star. The binary 2MASSJ05352184-0546085 gives the parameters of two brown dwarfs. The binary HD 23642 gives the distance to the Pleiades. We give brief descriptions here, and refer to the original papers for more detail. The variant techniques are flagged in the margin.

4.3.1 The lowest main-sequence mass: HAT-TR-205-013 B

One of the methods to detect planets around other stars is to look for transits of the planet. If a planet has a radius R_p and passes in front of the star with radius R, a fraction $(R_p/R)^2$ of the stellar surface is covered, and flux that we detect is reduced accordingly. Analysis of the transit lightcurve provides information on the limb darkening of the star.

Interestingly, a Jupiter-like planet has a size comparable to that of low-mass main-sequence stars, and some candidate planets found from transits turn out to be stars of spectral type late M. They are easily distinguished from planets because they cause much larger variations in the radial velocity of the primary.

In the case of HAT-TR-205-013, Beatty et al. (2007) determine the parameters of the late dwarf, as follows. (HAT stands for Hungary-made Automated Telescope; to discover transits a network of six 11 cm telescopes is used, see Bakos et al. 2004; 205 is the number of the survey field.) The parameters determined first are a, a_1, R_2, R_1, and i. The transit lightcurve provides three relations between these parameters. Roughly speaking, the length of the eclipse in units of the orbital period depends mostly on R_1/a, the eclipse depth on R_2/R_1, and the lengths of ingress and egress on $s = a\cos i$, the closest projected distance of the star centers [2]. (See Exercise 16 and Figure 4.3.) A fourth relation is given by the radial velocity curve of star 1, which shows that $e = 0$, and gives $a_1 \sin i$ (see discussion leading to Eq. 3.13). If star 2 contributes significantly to the spectrum, its radial velocity provides the fifth relation between the parameters. Here, however, star 2 is not seen in the spectrum, and the required fifth relation is found from the observed (i.e. projected) rotation velocity $v_{\rm rot,o}$ of star 1. *It is assumed that the rotation of star 1 is locked to the orbit,*

rotation velocity

[2] Beatty et al. write this in dimensionless form, with $b \equiv s/R_1$

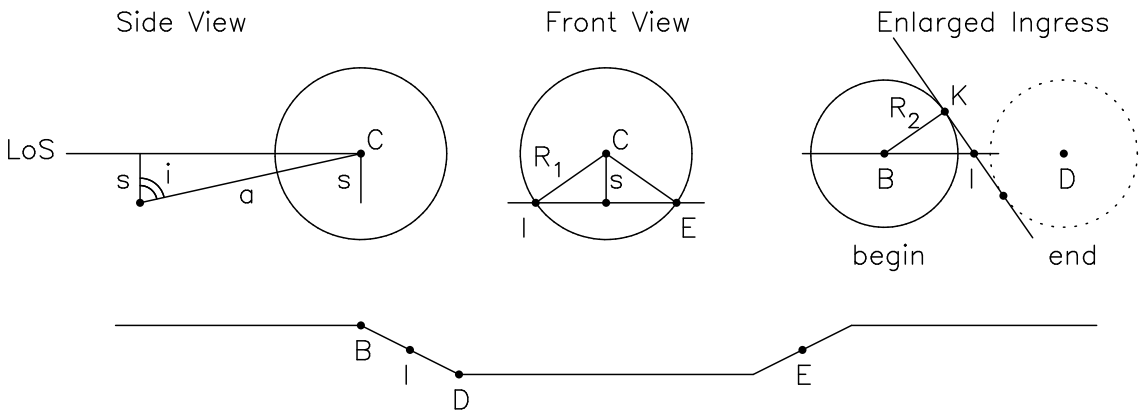

Figure 4.3: *Slightly simplified geometry to show the effect of the impact parameter s on form of the transit lightcurve. The left graph shows the definition of s: it is the shortest projected distance of the center of star 2 to the center of star 1. LoS is the line of sight towards the Earth, and a the distance between the stars. The middle graph shows the path of star 2 in front of star 1; it is simplified (assuming $R_1 \ll a$) because in reality the path between ingress I and egress E should be slightly curved (part of an ellipse if the orbit is circular), with the pericenter in the middle. The ingress is shown in more detail in the right graph, where the line through IK is the edge of the star; the short stretch of the circular edge is approximated with a straight line (assuming $R_2 \ll R_1$). The resulting lightcurve is shown schematically in the lower graph. As the center of star 1 moves along BD, ingress starts (ends) at B (D), where its projected circle first (last) touches the edge of star 1. Mid-ingress is at I. Since BID is along IE (see middle graph), and BK is parallel to IC, we have $s/R_1 = KI/BI = \sqrt{1-(R_2/BI)^2}$. This shows that the length of ingress, proportional to BI, depends on s. For $s = 0$ $BI = R_2$. (For s close to 1 the approximation that the edge of the star is a straight line breaks down.)*

Table 4.3: *Measured quantities and parameters of the binary HAT-TR-205-013, from Beatty et al. (2007).*

a/R_1	5.9(1)	M_1 ($M_\odot$)	1.04(13)
R_2/R_1	0.1309(6)	M_2 ($M_\odot$)	0.124(10)
$s/R_1 = a\cos i/R_1$	0.37(5)	R_1 ($R_\odot$)	1.28(4)
$v_{\rm rot}\sin i$ (km/s)	29(1)	R_2 ($R_\odot$)	0.167(6)
K_1 (km/s)	18.3(5)	a ($R_\odot$)	7.5(3)
P (d)	2.23074(1)		
e	0		

hence $v_{\rm rot} = \Omega R_1 = (2\pi/P)R_1$, hence

$$v_{\rm rot,o} = v_{\rm rot}\sin i = \frac{2\pi}{P}R_1\sin i \qquad \Rightarrow \qquad \frac{P}{2\pi}v_{\rm rot,o} = R_1\sin i \tag{4.7}$$

Once the parameters a, a_1, R_2, R_1, and i are determined, the total mass and the individual masses can be found with Kepler's third law, Eq. 2.45, and from the ratio a_1/a.

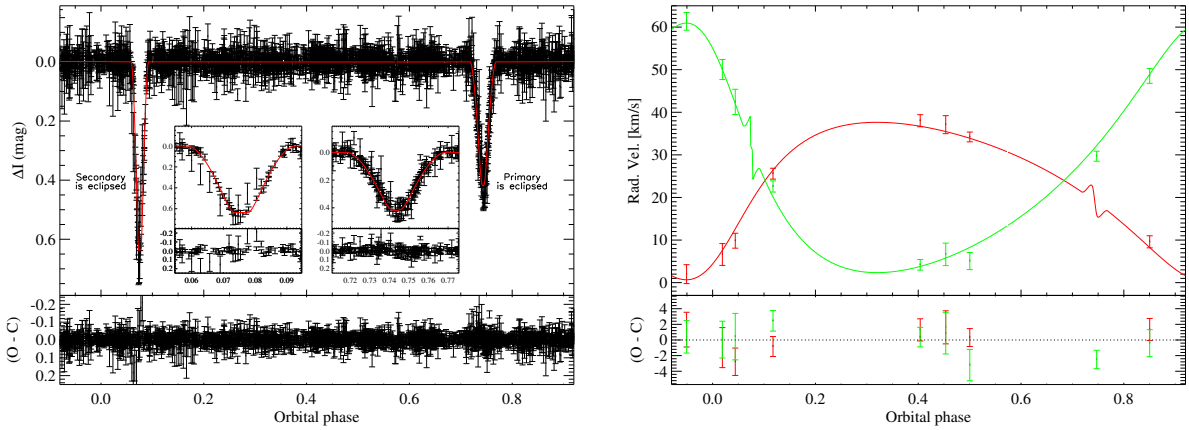

Figure 4.4: *Eclipse lightcurve and radial velocity curve of the brown dwarf binary 2MASSJ05352184−0546085. Note the effect of ingress and egress on the theoretical radial velocity curve of the eclipsed star. From Stassun et al. (2007)*

Table 4.4: *Parameters of the brown-dwarf binary 2MASSJ05352184−0546085 and of the Pleiades binary HD 23642 (Stassun et al. 2007, Groenewegen et al. 2007)*

	2MASS	HD		2MASS	HD
K_1 (km/s)	18.5(7)	99.2(3)	M_1 ($M_\odot$)	0.057(5)	2.22(3)
K_2 (km/s)	29.3(8)	140.8(3)	M_2 ($M_\odot$)	0.036(3)	1.57(2)
P (d)	9.77962(4)	2.4611335(7)	R_1 ($R_\odot$)	0.68(2)	1.84(4)
e	0.333(6)	<0.002	R_2 ($R_\odot$)	0.49(2)	1.59(4)
i (°)	89.2(2)	77.6(2)	L_1 ($L_\odot$)	0.022(2)	
a ($R_\odot$)	8.8(2)	11.95(2)	L_2 ($L_\odot$)	0.015(2)	
T_2/T_1	1.064(4)	0.768(4)	T_1 (K)	2725	9950

4.3.2 The brown-dwarf binary 2MASSJ05352184−0546085

Cool stars and brown dwarfs are best discovered in the infrared. The 2 μ All Sky Survey is an efficient source for new discoveries of such objects. Stassun et al. (2007) analyse an eclipsing binary in the Orion Nebula Cluster. Radial velocities are measured through a technique of Broadening Functions, which is a variant of the cross-correlation technique; it works better when the velocity difference between the stars is comparable to the resolution of the observed spectra (Rucinski 1999). The broad-band I light curve is analysed assuming that the surfaces of the stars radiate as black bodies. Radial velocities and lightcurve are analysed with the Wilson-Devinney code, and give the parameters listed in Table 4.4.

broadening functions

A first remarkable result is that the brown dwarfs are rather large for their mass: this can be understood by their young age. The Orion Nebula Cluster is thought to be ~ 1 Myr old, and in this time brown dwarfs have not relaxed to their equilibrium radius.

A second remarkable result is that the less massive star is hotter: this follows immediately from the observation that the eclipse of the less massive star is deeper. Since the temperatures of both stars are almost equal, it is unlikely that this result is the consequence of the difference between real brown-dwarf atmosphere spectra and Planck spectra. Stassun et al. suggest that the lower temperature of the primary can be explained if it is ~ 0.5 Myr older than the secondary.

Membership of the Orion Nebula is in agreement with the systemic radial velocity (γ) of the binary: 24.1(4) km/s, compared to the velocity 25.0±1.5 km/s of the cluster. It is also in agreement with the distance derived from the luminosity and spectrum. The spectral type M6.5 for the primary implies (through measurements of the M6.5 star LHS 292) a temperature of 2725 K, and a bolometric correction $L/L_K = 3800$ (the K-band is around 2μm). The temperature of the secondary is found from T_2/T_1. The luminosities of the stars derived from their radii and effective temperatures are given in the Table. The bolometric flux can be derived from the K-band out-of-eclipse flux $f_K = 1.59 \times 10^{-18}$watt m^{-2}nm^{-1} and the bolometric correction. Comparison of these numbers gives the distance of the binary as 456±34 pc, compatible with the distance to the Orion nebula of 480±80 pc.

4.3.3 The distance to the Pleiades from binary HD 23642

The distance to the Pleiades determined by the HIPPARCOS mission was a big surprise: it was significantly closer (116(3) pc) than results found from main-sequence fitting (about 130 pc). If correct, the HIPPARCOS distance implies that the main sequence of the Pleiades is 37% fainter than the main sequence of stars near the Sun!

The binary HD 23642 has been studied to resolve this discrepancy: it is a member of the Pleiades, and by determining its distance one also determines the cluster distance.

Groenewegen et al. (2007) first use cross-correlation techniques of model spectra with the observed spectra to derive the temperatures and effective gravities of both stars, and to derive their radial velocities as a function of phase. The fit to radial velocities and lightcurves then provides the other binary parameters listed in Table 4.4.

The distance is determined by comparing model fluxes in different filters with observed fluxes. In general, for a star with radius R at distance d, the flux observed on Earth f_λ is related to the flux leaving 1 m^2 of the stellar surface through:

$$4\pi R^2 F_\lambda = 4\pi d^2 f_\lambda \tag{4.8}$$

We know the observed flux f_λ and from the fitting also the radius R, thus if we can determine F_λ we have the distance. This determination can be done for either star separately, or for the out-of-eclipse flux of the binary as a whole.

Groenewegen et al. use two methods to determine F_λ. In Method A one uses a stellar atmosphere *model*, determined by the stellar temperature, $\log g$ and metallicity, to compute the flux F_λ at wavelength λ for 1 m^2 at the stellar surface. In Method B one uses an *empirical relation* between the effective temperature and F_λ, or alternatively between the colour and F_λ. Groenewegen et al. use the colours f_V/f_B and f_K/f_V. In both cases, a correction for interstellar absorption towards the Pleiades must be made. The distance obtained for HD 23642 is 138.0±1.3 pc.

colour-flux relation

The consensus nowadays is that the HIPPARCOS distance is not correct.

4.4 Exercises

Exercise 15. Use the Hipparcos catalogue to find the parallaxes of β Aur and θ Aql, and compare with the distances derived from the visual orbit and observed fluxes.

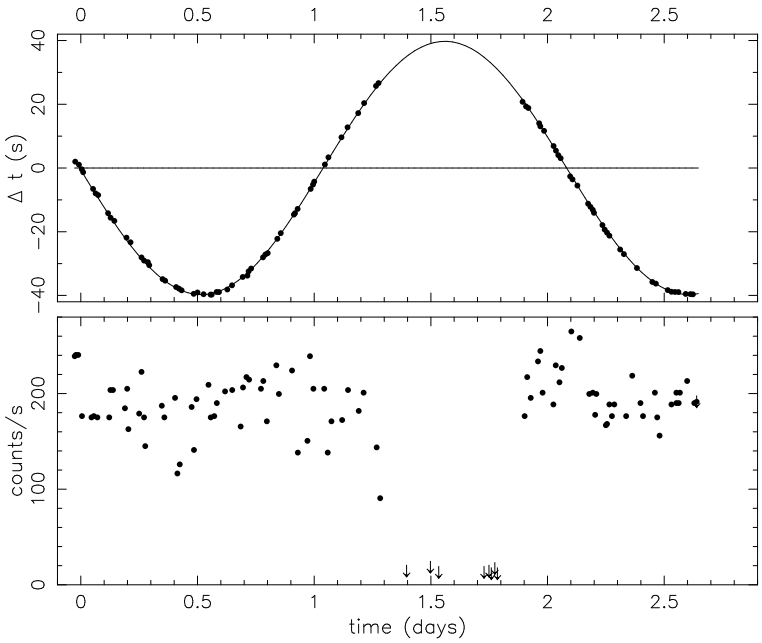

Figure 4.5: *Below: the X-ray intensity observed from Cen X-3 (dots, upper limits indicated with arrows); above: the time difference Δt between the observed pulse arrival time and the arrival time predicted for a constant pulse period.*

Which distances are most accurate?

Exercise 16. Use the measured quantities listed in the left-hand column of the Table 4.3, to derive the binary parameters given in the right-hand side.

Exercise 17. We use the mass function $f(M)$ for a circular orbit to study the parameters of the high-mass X-ray binary Cen X-3: a binary in which an X-ray pulsar is in orbit around a high-mass star. Consider a binary of stars with masses M_1 and M_2, and orbital period P_b. The orbit is circular, the orbital inclination (i.e. the angle between the line of sight from the Earth and a line perpendicular to the orbital plane) is i. The radial velocity of star 1 has been determined, and it varies as a sine wave, with amplitude K_1. The mass function for a circular orbit is

$$f(M) \equiv \frac{{M_2}^3 \sin^3 i}{(M_1 + M_2)^2} = \frac{4\pi^2}{G} \frac{(a_1 \sin i)^3}{P_b^2} = \frac{K_1^3}{2\pi G} P_b \tag{4.9}$$

where a_1 is the semi-major axis of the orbit of star 1 with respect to the center of mass.

a. In Figure 4.5 we see some data of Cen X-3. A sine wave describes the time arrival times well, i.e. the orbit is circular. The orbital period is 2.087 days, the amplitude of the time-delay curve is 39.7466 s. Compute the mass function of Cen X-3. Show that the mass function provides a lower limit to the mass of the companion of the X-ray pulsar.

b. We see that the neutron star is eclipsed by its O star companion. t is the eclipse length. Assume that the O star is a sphere (i.e. ignore its deformation by tidal forces) and show that the ratio of the radius of the O star R to the radius of the orbit a is given by

$$\frac{R}{a} = \sqrt{1 - \cos^2\left(\frac{\pi t}{P_b}\right) \sin^2 i} \tag{4.10}$$

c. We can use Eq. 4.10 to determine R/a from t/P_b, as a function of i. Assuming that the donor fills its Roche-lobe, we can use Eq. 3.33 to determine the mass ratio M_1/M_2, and then from Eq. 4.9 both masses separately. Determine t/P_b from Fig. 4.5, and calculate M_1 and M_2 for inclinations of 70° and 90°. Note that the masses of the neutron star are rather small. This is due in part by our neglect of the deformation of the O star by tidal forces.

Chapter 5

Tidal forces

Tidal forces lead to a coupling in the binary of the spin of the stars with the orbital revolution. If energy is dissipated, angular momentum can be exchanged between the orbit and the spin of the stars.

We discuss some aspects of this with use of three articles

- Hut (1980) shows on the basis of a general analysis that the minimum energy situation of a binary is reached if the angular momenta of the orbit and of the two stars are aligned, and if both stars corotate with the orbit, i.e. their rotation period equals the binary period
- Hut (1981) gives simple analysis of the effect of the deformation of a star on the evolution of the binary orbit, and provides a good physical insight into the tidal forces. We examine only the first 5 pages of this article, which give the outline.
- Verbunt (2007) discusses the evolution of the rotation of the Earth and of the revolution of the Moon as driven by the spin-orbit coupling.

5.1 Exercises

Exercise 18a. Compute the total angular momentum of a binary consisting of two stars with masses $M_{1,2}$ and radii $R_{1,2}$, and how that it can be separated into the angular momentum of the orbit and the angular momenta of the two stars around their own axex of rotation. Start from Eq. 2.42, assume that the stars are perfectly spherical, and save on computing by clever use of anti-symmetry. The orbital angular velocity is Ω, the angular velocities of the stars around their own axes are $\omega_{1,2}$.
b. Consider synchronous rotation, $\Omega = \omega_1 = \omega_2$ and derive the condition for which the rotation of the two stars around their own axes can be neglected.

Exercise 19. (After Counselman, C. 1973, ApJ 180, 307.) Two stars with masses M and m, with $M \gg m$, orbit one another in a circular orbit with angular velocity n. The star with mass M also rotates around its own axis with angular velocity ω and its moment of inertia is kMR^2. We consider the orbital energy and angular momentum, i.e. ignore the kinetic enery and angular momentum of the center of mass.
a. Compute the total angular momentum L' and the total energy E' of this binary

system, expressed in m, M, n and ω. Define:

$$\sigma^2 \equiv \frac{GM}{R^3}; \qquad \kappa \equiv \left(\frac{m}{kM}\right)^{1/4}\left(1+\frac{m}{M}\right)^{1/6}$$

$$\Omega \equiv \frac{\omega}{\sigma}\kappa^{-3}; \qquad N \equiv \left(\frac{n}{\sigma}\right)^{1/3}\kappa^{-1}$$

and show

$$L \equiv \frac{L'}{kMR^2\kappa^3\sigma} = \Omega + N^{-1}; \qquad E \equiv \frac{E'}{kMR^2\kappa^6\sigma^2} = \frac{1}{2}\left(\Omega^2 - N^2\right)$$

b. sketch lines of constant E in the N-Ω plane for E = 0,0.5,-0.5; and for constant L for L = 0,1,2,-1,-2. Argue from this sketch that the location where a line of constant angular momentum is tangent to a line of constant energy corresponds to an extremum of energy for fixed angular momentum. This implies that the tangent point is an equilibrium situation. Show that in such a point $\Omega = N^3$, i.e. $\omega = n$ (synchronous rotation). Sketch this line in the figure as well.
c. compute in the equilibrium point from b):

$$\left(\frac{\partial E}{\partial N}\right)_{L=\text{const}} \qquad \text{and} \qquad \left(\frac{\partial^2 E}{\partial N^2}\right)_{L=\text{const}}$$

When is the equilibrium of synchronous rotation stable?

Bibliography

[1] C.W. Allen. *Astrophysical quantities*. Athlone Press, London, 1973.

[2] J. Andersen. Accurate masses and radii of normal stars. *A&A Review*, 3:91–126, 1991.

[3] T. Beatty, J. Fernandez, D. Latham, and et al. The mass and radius of the unseen M-dwarf companion in the single-lined eclipsing binary HAT-TR-205-013. *ApJ*, 663:573–582, 2007.

[4] M.S. Bessell, F. Castelli, and B. Plez. Model atmospheres broad-band colors, bolometric corrections and temperature calibrations for O-M stars. *A&A*, 333:231–250 (Erratum: 337, 321), 1998.

[5] A. Bobinger. Genetic eclipse mapping and the advantage of Black Sheep. *A&A*, 357:1170–1180, 2000.

[6] P. Charbonneau. Genetic algorithms in astronomy and astrophysics. *ApJS*, 101:309–334, 1995.

[7] C. Counselman. Outcomes of tidal evolution. *ApJ*, 180:307–316, 1973.

[8] M. Groenewegen, L. Decin, M. Salarsi, and P. De Cat. The Pleiades eclipsing binary HD 23642 revisited. *A&A*, 463:579–587, 2007.

[9] W.D. Heintz. The Castor system. *PASP*, 100:834–838, 1988.

[10] C.A. Hummel, J.T. Armstrong, D.F. Busher, D. Mozurkewich, A. Quirrenbach, and M. Vivekanand. Orbits of small angular scale binaries resolved with the MARK III interferometer. *AJ*, 110:376–390, 1995.

[11] P. Hut. Stability of tidal equilibrium. *A&A*, 92:167, 1980.

[12] P. Hut. Tidal evolution of close binary systems. *A&A*, 99:126–140, 1981.

[13] D. Mihalas and J. Binney. *Galactic astronomy. Structure and kinematics*. Freeman, San Francisco, 1981.

[14] J. Orosz and P. Hauschildt. The use of the `nextgen` model atmospheres for cool giants in a light curve synthesis code. *A&A*, 364:265–281, 2000.

[15] W.H. Press, S.A. Teukolsky, W.T. Vetterling, and B.P. Flannery. *Numerical Recipes: The Art of Scientific Computing*[2]. Cambridge U. P., Cambridge, 1992.

[16] É. Roche. Recherches sur les atmosphères des comètes. *Annales de l'Observatoire imperial de Paris*, 5:353–393, 1859.

[17] S. Rucinski. Determination of broadening functions using the singular value decomposition (SVD) technique. In J.B. Heanrshaw and C.D. Scarfe, editors, *Precise stellar radial velocities*, ASP Conference Series 185, pages 82–90. ASP, San Francisco, 1999.

[18] K.G. Stassun, R.D. Mathieu, and J.A. Valenti. A surprising reversal of temperatures in brown-dwarf eclipsing binary 2MASS J05352184−0546085. *ApJ*, 664:1154–1166 (erratum: 674, 615), 2007.

[19] K.A. (ed.) Strand. *Basic Astronomical Data*. University of Chicago Press, Chicago, 1963.

[20] S.A. Tjemkes, J. van Paradijs, and E.J. Zuiderwijk. Optical lightcurves of massive X-ray binaries. *A&A*, 154:77–91, 1986.

[21] G. Torres, J. Andersen, and A. Giménez. Accurate masses and raidii of normal stars: modern results and applications. *Ann.Rev.A.A.*, 18:67–126, 2010.

[22] M.H. van Kerkijk, S.A. Rappaport, R.P. Breton, S. Justham, Ph. Podsiadlowski, and Z.W.. Han. Observations of Doppler boosting in Kepler light curves. *ApJ*, 715:51–58, 2010.

[23] F. Verbunt. *The Earth and the Moon: from Halley to lunar ranging and shells*. `www.astro.ru.nl/~fverbunt/binaries/earth.pdf`, Utrecht, 2007.

[24] H. Von Zeipel. The radiative equilibrium of a rotating system of gaseous masses. *MNRAS*, 84:665–684, 1924.

[25] R.E. Wilson and E.J. Devinney. Realization of accurate close-binary light curves: application to MR Cygni. *ApJ*, 166:605–619, 1971.

Chapter 6

Structure of compact stars

The structure of a star is determined by an interplay between the various physical forces: nuclear forces, electro-magnetic forces, and gravity. Because of the very different strengths of these forces, we can separate the local and global properties of matter: there is a clear *separation* in the range of the forces. Gravity is extremely weak, and only becomes noticeable once we deal with a very large amount of matter, i.e. at distances that are long compared to the characteristic range of nuclear or electromagnetic forces. If we consider a small volume, we can therefore derive the thermodynamic properties of matter – i.e. the relations between pressure, temperature, density, and composition of the gas – while ignoring gravity. The structure of the star as a whole then follows from the interplay between these local properties of matter and the global mass distribution in the star.

In stellar matter, shear forces and viscosity are usually not important. The pressure is therefore isotropic, and can be described as a scalar quantity. In general, pressure depends on the composition of the gas (the kinds of particles present), on the density, and on the temperature. As we will see, the pressure P in neutron stars depends on the density ρ alone, $P = P(\rho)$. The matter in white dwarfs and neutron stars is degenerate, i.e. quantum mechanical effects are important.

Let us start by looking at the equations for a degenerate gas.

6.1 The equation of state for a degenerate gas[1]

At very high densities or very low temperatures, the classical description of matter breaks down, and a quantum mechanical description is required. A gas for which quantum mechanical effects are important is called a *degenerate* gas. The most important difference from the classical description is that in quantum mechanics the number of available slots in momentum-space is limited, as follows: *for a unit-volume in $\vec{r}$-space the volume in $\vec{p}$-space is divided into boxes with volume h^3*, where h is the Planck constant. For Fermions we have Pauli's exclusion principle which tells us that each box is allowed to contain g particles, where g is the degeneration factor (or statistical weight), given by twice the spin number plus one. For electrons, protons and neutrons $g = 2$.

We can illustrate this quantization of momentum-space as follows. Consider a dense gas, with average distance in the x-direction between the particles of Δx. According to Heisenberg's uncertainty principle, the accurracy with which position

[1]This Section is based on Lecture Notes 'Neutron Stars' by John Heise, 1972

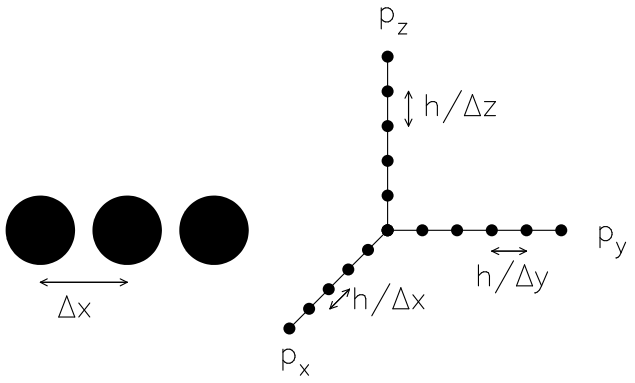

Figure 6.1: *For particles with distances Δx, Δy and Δz in space (left), the momentum space is divided in boxes with size $h^3/(\Delta x \Delta y \Delta z)$ (right).*

and momentum of a single particle can be determined simultaneously is limited by $\Delta x \Delta p_x \gtrsim h$. Pauli's exclusion principle now says that within this accuracy no two particles may be in the same state, i.e. that the minimal allowed difference in momentum for identical particles is given by $\Delta p_x \gtrsim h/\Delta x$. An analogous reasoning can be made for the y and z directions. We then get a picture as Figure 6.1.

The volume occupied by one grid point in momentum-space is $h^3/(\Delta x \Delta y \Delta z)$. In a volume V_p in momentum space, we can therefore locate $gV_p \Delta x \Delta y \Delta z/h^3$ particles. One particle occupies a volume $\Delta x \Delta y \Delta z$ in $\vec{r}$-space, so that *per unit volume of $\vec{r}$-space* a number of gV_p/h^3 particles can be located in a volume V_p of momentum space.

Another illustration may be derived from the Schrödinger equation for the wave function ψ for a particle of mass m

$$i\hbar \frac{\partial \psi}{\partial t} = -\frac{\hbar^2}{2m} \nabla^2 \psi \tag{6.1}$$

where $\hbar \equiv h/(2\pi)$, which has the solution

$$\psi(\vec{r}, \vec{p}) = \text{const} \times \exp(\frac{i}{\hbar}(\vec{p} \cdot \vec{r} - Et)) \qquad \text{where} \qquad E = \frac{p^2}{2m} \tag{6.2}$$

Again consider particles with distances Δx in the x-direction. To avoid destructive interference of the wave functions of different particles with one another, their momenta must be multiples of $h/\Delta x$: $p_n = nh/\Delta x$. Analogous reasoning may be applied to the y and z directions, and the above picture is obtained again, with the same way of counting available slots in momentum space.

Thus, while the number of particles in a given volume V_p of momentum space may be infinitely large in the classical description, we must take into account an upper limit to the number of fermion particles in this volume in the quantum mechanical description. This limitation leads to the Fermi-Dirac distribution f, as a function of energy ϵ, valid for fermions:

$$f(\epsilon) = \frac{1}{e^{-\alpha + \beta\epsilon} + 1} \tag{6.3}$$

The meaning of the constants α and β will be discussed below. We give a brief derivation of the Fermi-Dirac distribution.

6.1.1 Derivation of the Fermi-Dirac distribution

Consider a volume V_p in momentum space, chosen so that all particles in this volume have the same energy ϵ_i. The number of available positions in this volume is $Z_i = gV_p/h^3$. The number of possible ways to choose n_i positions from Z_i is given by the binomial coefficients $\begin{pmatrix} Z_i \\ n_i \end{pmatrix}$. The number of ways to locate n_i particles in Z_i, n_j particles in Z_j, n_k particles in Z_k, etc., then follows as

$$W = \Pi_i \frac{Z_i!}{n_i!(Z_i - n_i)!} \tag{6.4}$$

By colliding with one another, the particles continuously redistribute themselves over the different locations in momentum space, i.e. the different n_i vary by an amount δn_i. The most probable distribution is therefore that distribution which can be realized in most ways, i.e. for which W has a maximum. Because the number of particles is so large, the actual distribution of the particles will lie *very* close to the most probable distribution. W reaches its maximum when its variation is zero, i.e. $\delta W = 0$. For convenience, we determine the equivalent condition $\delta \ln W = 0$. In doing so, we use Stirling's equation $\ln n! \simeq n \ln n - n$, which is very accurate for very high n.

$$\delta \ln W = \delta \left[\Sigma_i (\ln Z_i! - \ln n_i! - \ln(Z_i - n_i)!)\right] = \Sigma_i \delta n_i \left[-\ln n_i + \ln(Z_i - n_i)\right] \tag{6.5}$$

Before continuing, we must take into account that the collisions which redistribute the particles, i.e. which cause the n_i to vary, must conserve the total number of particles per unit volume, and must conserve the total energy per unit volume. These conditions can be written

$$\Sigma_i n_i = N \qquad \text{and} \qquad \Sigma_i (n_i \epsilon_i) = E \tag{6.6}$$

With Lagrange's multiplicator method, we rewrite these conditions as $\alpha \Sigma_i (\delta n_i) = 0$ and $-\beta \Sigma_i (\epsilon_i \delta n_i) = 0$ and add them to Eq.6.5 to find

$$\delta \ln W = \Sigma_i \delta n_i \left(-\ln n_i + \ln(Z_i - n_i) + \alpha - \beta \epsilon_i\right) \tag{6.7}$$

This is zero for all δn_i if Eq.6.3 is satisfied, where $f(\epsilon_i) \equiv n_i/Z_i$ is the *occupation fraction*, i.e. the fraction of the total number of available positions with energy ϵ_i that is occupied. The parameters α and β can be determined by entering the solution Eq.6.3 into conditions Eq.6.6. We will do this below for the classical limit, and note for now that α is mainly dependent on the particle number density, whereas $\beta \equiv 1/(kT)$ depends on the energy.

6.1.2 Relation between Fermi-Dirac, Bose-Einstein and Planck

We make a little detour here to show the relation between the various distribution equations in quantum mechanics. First, note that in deriving the Fermi-Dirac equation, we have used four statements:

1. phase space is quantized, i.e. at each energy ϵ_i there is a finite number Z_i of boxes in momentum space

2. the exclusion principle holds, i.e. each box can only contain g particles

3. the number of particles is conserved

4. the total energy is conserved

That is *all* the physics we need to derive the Fermi-Dirac equation! The remainder is mathematics.

The exclusion principle does not apply to bosons, which may share a box. The number of ways to distribute n_i bosons in Z_i boxes is therefore $(n_i+Z_i-1)!/[n_i!(Z_i-1)!]$. (Think of this as the number of ways to arrange in a row n_i indistinguishable particles and Z_i-1 indistinguishable boundaries between the Z_i boxes.) Starting from this, but otherwise following the derivation of the Fermi-Dirac equation, we find the Bose-Einstein distribution:

$$\frac{n_i}{Z_i-1} \simeq \frac{n_i}{Z_i} = \frac{1}{e^{-\alpha+\beta\epsilon}-1} \tag{6.8}$$

Thus, to derive the Bose-Einstein function, we only use numbers 1,3 and 4 of the list above. What about the Planck function? The difference between the Planck function and the Bose-Einstein function arises because the number of photons need not be conserved. (For example, if an electron in an atom absorbs a photon to jump from orbit 1 to orbit 3, it can emit two photons by returning to orbit 1 via orbit 2.) Thus, the derivation of the Planck function does not contain a Lagrange condition for the conservation of particles, i.e. the term with α drops out. The Planck function is simply the Bose-Einstein function with the α dropped:

$$\frac{n_i}{Z_i-1} \simeq \frac{n_i}{Z_i} = \frac{1}{e^{\beta\epsilon}-1} \tag{6.9}$$

In other words, to derive the Planck function, we only need numbers 1 and 4 of the list above, i.e. energy is conserved and phase space is quantized. This was how Bose derived the Planck function, and it illustrates how the Planck function immediately implies quantization. (The extension of Bose's equation to the Bose-Einstein equation was found by Einstein after he added conservation of number of particles; the Fermi-Dirac equation had to wait for the exclusion principle to be formulated.)

6.1.3 Limits of the Fermi-Dirac equation

Let us look at the Fermi-Dirac equation in some more detail. To understand the physical meaning of α and β, we start with the classical limit of the equation, which is the limit for which the exponent in the denominator is much bigger than one, so that we may write

$$f(\epsilon) = e^{\alpha-\beta\epsilon} \tag{6.10}$$

The energy ϵ of a particle depends only on its momentum p; for example in the non-relativistic case we have $\epsilon = p^2/(2m)$. We may therefore write the number of particles in a unit volume of $\vec{r}$-space with momentum p as

$$n(p)dp = \frac{g}{h^3}4\pi p^2 e^{\alpha-\beta p^2/(2m)}dp \tag{6.11}$$

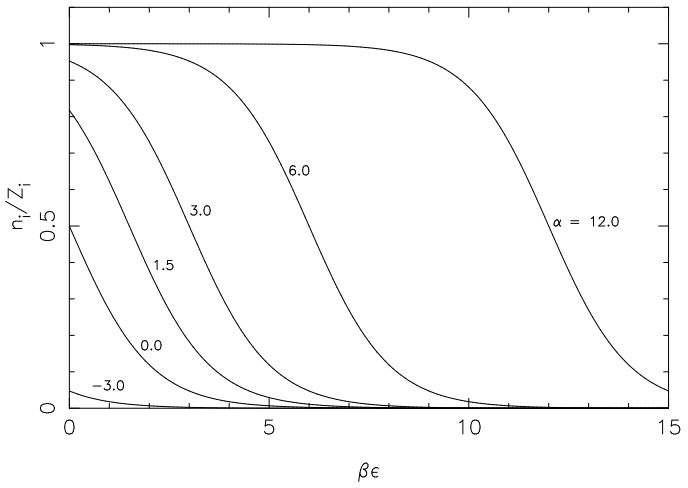

Figure 6.2: *The Fermi-Dirac function for various values of* α.

Comparing this with the Maxwell-Boltzmann equation, we see that $\beta = 1/(kT)$. For the total number of particles in a unit volume in $\vec{r}$-space we find

$$n = \int_0^\infty n(p)dp = \frac{g}{h^3}(2\pi mkT)^{3/2}e^\alpha \tag{6.12}$$

This tells us that $\alpha \propto \ln(n/T^{3/2})$. α is very small, i.e. $\alpha \ll -1$, for small density, or for high temperature. A different notation which is often used has $\mu \equiv \alpha/\beta$; μ is called the chemical potential of the gas. Thus, the classical limit applies for a gas in which the density is very small, or which has a very high temperature. Intuitively, we understand that low density allows a classical description, because at low density the particles are far from filling all available positions in momentum space, and are not constrained by the quantum mechanical limitation to the number of available positions.

For a number of higher values of α, the Fermi-Dirac function is plotted in Figure 6.2. It can be seen that for high values of α, the Fermi-Dirac equation can be well approximated with

$$f(\epsilon) = 1 \quad \text{for} \quad \beta\epsilon \lesssim \alpha \qquad \text{and} \qquad f(\epsilon) = 0 \quad \text{for} \quad \beta\epsilon > \alpha \tag{6.13}$$

A gas for which this approximation holds is called a *fully degenerate* gas. For such a gas, all possible states up to an energy ϵ_F are occupied, and no states at higher energy are occupied. Correspondingly, in momentum space all positions up to a limiting momentum p_F are filled. ϵ_F and p_F are called the Fermi energy and Fermi momentum. The number of positions in the sphere with radius p_F, and hence the number density for a fully degenerate gas in $\vec{r}$-space is

$$n = \frac{4\pi}{3}p_F^3\frac{g}{h^3} \tag{6.14}$$

and for the pressure we use $P = \int 2p_z v_z f(\vec{p})d\vec{p}$ to find

$$P = \int_0^\infty \int_0^{\pi/2} \int_0^{2\pi} 2p\cos\theta v\cos\theta\frac{g}{h^3}d\phi\sin\theta d\theta p^2 dp = \frac{4\pi g}{3h^3}\int_0^{p_F} p^3 v dp \tag{6.15}$$

6.1.4 Non-relativistic fully degenerate gas

For a non-relativistic gas we substitute $v = p/m$ in Eq.6.15 and use $g = 2$ to find

$$P = \frac{8\pi}{15mh^3}p_F^5 = \frac{1}{5m}\left(\frac{3h^3}{8\pi}\right)^{2/3} n^{5/3} \tag{6.16}$$

where we used Eq.6.14 to eliminate p_F.

In a white dwarf the gas is a mixture of ions (e.g. carbon and oxygen ions) and electrons. For each component of the gas we can roughly determine the particle density at which that component becomes degenerate from

$$\frac{1}{5m}\left(\frac{3h^3}{8\pi}\right)^{2/3} n^{5/3} \sim nkT \Rightarrow n \sim \frac{8\pi}{3h^3}\left(5mkT\right)^{3/2} \tag{6.17}$$

i.e. the transition between ideal and degenerate occurs near a number density that scales with $m^{3/2}$. For electrons, the transition occurs therefore at much lower number density, i.e. if we increase the gas density, the electrons become degenerate long before the ions become degenerate. At these densities the electron pressure P_e dominates completely over the pressure from the ions (Eq.6.16), but the mass density ρ is still dominated by the ions. For the total pressure in such a mixture we use Eq. 6.16 to write

$$P \simeq P_e = \frac{1}{5m_e}\left(\frac{3h^3}{8\pi}\right)^{2/3}\left(\frac{\rho}{\mu_e m_p}\right)^{5/3} \tag{6.18}$$

where μ_e is the mass per electron of the gas mixture, in units of the proton mass m_p.

In a neutron star, the number density of neutrons dominates, $n_n \gg n_p = n_e$, and the total pressure is

$$P \simeq P_n = \frac{1}{5m_n}\left(\frac{3h^3}{8\pi}\right)^{2/3}\left(\frac{\rho}{m_n}\right)^{5/3} \tag{6.19}$$

6.1.5 Fully relativistic fully degenerate gas

For a relativistic gas we may write $v = c$ so that

$$P = \frac{8\pi c}{12h^3}p_F^4 = \frac{c}{4}\left(\frac{3h^3}{8\pi}\right)^{1/3} n^{4/3} \tag{6.20}$$

Note that the mass of the degenerate particle doesn't enter the equation of pressure in the fully relativistic case.

In a white dwarf we have

$$P \simeq P_e = \frac{c}{4}\left(\frac{3h^3}{8\pi}\right)^{1/3}\left(\frac{\rho}{\mu_e m_p}\right)^{4/3} \tag{6.21}$$

and in a neutron star

$$P \simeq P_n = \frac{c}{4}\left(\frac{3h^3}{8\pi}\right)^{1/3}\left(\frac{\rho}{m_n}\right)^{4/3} \tag{6.22}$$

6.1.6 General fully degenerate gas

In general the relation between energy E and momentum p may be written

$$E = mc^2 \left(1 + \frac{p^2}{m^2c^2}\right)^{1/2} \tag{6.23}$$

and the relation between velocity and momentum is

$$v = \frac{p}{m} \left(1 + \frac{p^2}{m^2c^2}\right)^{-1/2} \tag{6.24}$$

We now cannot find an explicit solution any more, but we can construct a parametrized solution. To do this we solve the integral for the pressure

$$P = \frac{8\pi}{3mh^3} \int_0^{p_F} \frac{p^4 dp}{(1 + \frac{p^2}{m^2c^2})^{1/2}} \tag{6.25}$$

by substituting

$$\frac{p}{mc} \equiv \sinh \frac{t}{4} \tag{6.26}$$

so that

$$p_F = mc \sinh \frac{t}{4} \tag{6.27}$$

$$E_F = mc^2 \cosh \frac{t}{4} \tag{6.28}$$

$$P = \frac{\pi m^4 c^5}{12h^3} (\sinh t - 8 \sinh \frac{t}{2} + 3t) \tag{6.29}$$

$$n = \frac{8\pi m^3 c^3}{3h^3} \sinh^3 \frac{t}{4} \tag{6.30}$$

The relation between pressure P and density n (or ρ) is found by calculating P and n (or ρ) for a series of values of the parameter t.

6.1.7 A mixture of electrons, neutrons and protons

At densities $\rho \gtrsim 10^{11}\,\mathrm{g\,cm^{-3}}$, as in neutron stars, matter consists mainly of electrons e^-, neutrons n and protons p. To derive the properties of such a mixture, we consider the reactions

$$p + e^- \to n + \nu \qquad \text{and} \qquad n \to p + e^- + \bar{\nu} \tag{6.31}$$

where ν and $\bar{\nu}$ are the electron neutrino and anti-neutrino, respectively. In equilibrium, the minimum energy is reached, so that no energy can be gained by further reactions. This means

$$E_p + E_e = E_n + E_\nu \tag{6.32}$$

In a fully degenerate gas, the energies are dominated by the Fermi–energies, and thermal energy may be ignored. Because neutrinos escape from the neutron star, their number density and hence their Fermi energy is zero, so that

$$E_p + E_e = E_n \tag{6.33}$$

This is called *neutrino neutrality*.

The total charge is zero, hence the number density of electrons equals that of protons. With Eq.6.30 this may be written

$$m_e c \sinh \frac{t_e}{4} = m_p c \sinh \frac{t_p}{4} \tag{6.34}$$

whereas for the Fermi energies we may write with Eq.6.28

$$m_e c^2 \cosh \frac{t_e}{4} + m_p c^2 \cosh \frac{t_p}{4} = m_n c^2 \cosh \frac{t_n}{4} \tag{6.35}$$

To find the equation of state in parametrized form, we take a series of values of, for example, t_e. With Eq.6.34 we calculate t_p, and then with Eq.6.35 t_n. This then allows us to determine the partial pressures of the electrons, neutrons and protons, as well as the number densities of each type of particle. By adding the separate densities, we find the total density. For densities $\rho \gtrsim 10^{12}\,\mathrm{g\,cm^{-3}}$ we find that neutrons dominate the number densities (see Exercise 3.7). Hence the name neutron star!

6.1.8 The equation of state for fully catalysed matter

What we considered above are the equations of state for an ideal gas, in which no forces are present. In a real gas, the particles exert forces on one another, and this affects the equation of state. We consider the equation of state for fully catalysed matter, i.e. matter in which the nuclear abundances $Z_i, Z_j, ...Z_n$ have adapted so that the internal energy per baryon is minimal. For temperatures $T \lesssim 10^9$K the thermal energy of such matter is negligible with respect to the Fermi-energies, and we call such matter cold catalysed matter.

Suppose we compress a ball of matter to ever larger densities. At low densities, $\rho \lesssim 10^5\,\mathrm{g\,cm^{-3}}$, Fe^{56} is the most stable form. At increasing densities the pressure at first is determined by the repelling Coulomb forces of the electron shells surrounding the iron cores. Such forces determine the structure of planets. We define the compression modulus as

$$\gamma = \left(\frac{\partial \ln P}{\partial \ln \rho} \right)_{ad} \tag{6.36}$$

where *ad* stands for adiabatic, i.e.no energy is added or lost. For a polytrope $\gamma = 1 + 1/n$. At small densities γ is very large: it is difficult to compress matter.

As densities increase further, the distances between the Fe cores becomes comparable to the Bohr radii of ever smaller electron shells. The electrons of those shells therefore detach from the individual nuclei: this is called pressure ionization. At densities with distances between the Fe cores less than the innermost Bohr radius, the matter is fully ionized. This happens at about $\rho \simeq 10^5\,\mathrm{g\,cm^{-3}}$. The pressure is thus determined by the increasing number of electrons, where the electrons are fully degenerate: $\gamma = 5/3$. At densities up to $10^7\,\mathrm{g\,cm^{-3}}$ the electrons become relativistically degenerate, and γ drops to 4/3.

At a density in excess of $1.4 \times 10^7\,\mathrm{g\,cm^{-3}}$ the electrons become sufficiently energetic to be captured by the Fe^{56}_{26} cores, transforming these into Ni^{62}_{28} cores. As density increases further, similar electron capture leads to more and more neutron-rich cores. Because of the disappearance of electrons, the pressure increases less fast, and γ drops to 1.26. The neutron-rich cores are loosely bound, and at a density $\sim 2 \times 10^{11}\,\mathrm{g\,cm^{-3}}$ the neutrons start 'dripping' from the cores. Because of the

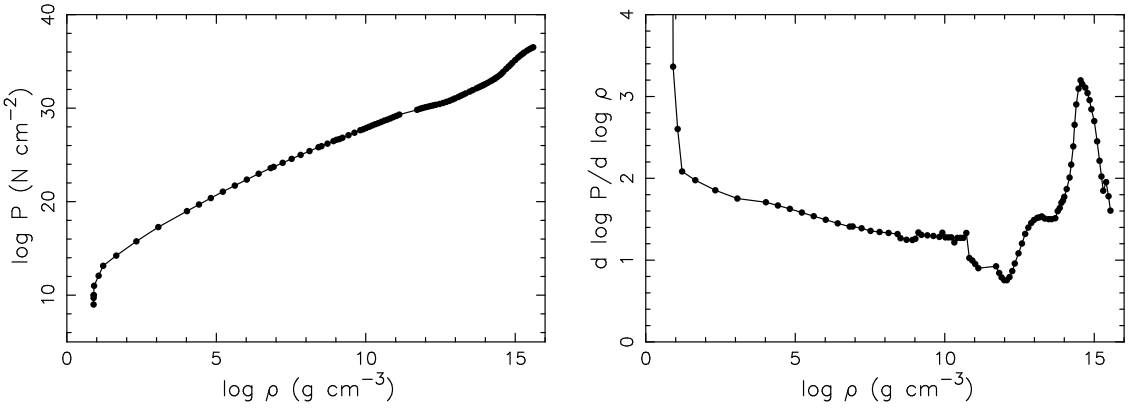

Figure 6.3: *The equation of state for fully catalysed matter, and the compression modulus derived from it.*

rapid disappearance of electrons the pressure remains almost constant between 3 and $4 \times 10^{11}\,\mathrm{g\,cm^{-3}}$, and γ approaches 0. Above $4 \times 10^{11}\,\mathrm{g\,cm^{-3}}$ all protons and neutrons have detached from the cores, and matter consists only of electrons, neutrons and protons. The degenerate neutron pressure increases γ to 5/3. At densities above $10^{13}\,\mathrm{g\,cm^{-3}}$ the neutrons become relativistic. Nuclear interactions become important at these densities. As these interactions are poorly understood, the equation of state at these high densities is poorly known.

In Figure 6.3 the equation of state and the accompanying γ is shown as a function of density. At low densities the Coulomb repulsion causes the radius to increase with mass. This applies to planets. When most atoms are ionized, and the electrons become degenerate, the radius decreases with mass. This applies to the white dwarfs. A maximum mass is reached at a central density of about $2.4 \times 10^8\,\mathrm{g\,cm^{-3}}$. Between this density and about $2.7 \times 10^{13}\,\mathrm{g\,cm^{-3}}$ solutions can be found for smaller masses, but these solutions are unstable, and any perturbation leads to collapse. Stable solutions are possible again at densities between $2.7 \times 10^{13}\,\mathrm{g\,cm^{-3}}$ and $6 \times 10^{15}\,\mathrm{g\,cm^{-3}}$: these are the neutron stars. For higher densities the solutions are unstable again. At these densities collapse to a black hole is unavoidable.

6.2 Equations for the structure of a degenerate star

Amongst the equations for stellar structure are the equation of hydrostatic equilibrium

$$\frac{dP}{dr} = -\frac{GM(r)}{r^2}\rho \tag{6.37}$$

where $M(r)$ is the mass within a sphere of radius r, and the equation of mass conservation

$$\frac{dM(r)}{dr} = 4\pi r^2 \rho \tag{6.38}$$

These two first order differential equations may be combined into a single second order differential equation:

$$\frac{1}{4\pi r^2}\frac{\mathrm{d}}{\mathrm{d}r}\left(\frac{r^2}{G\rho}\frac{\mathrm{d}P}{\mathrm{d}r}\right) = -\rho \tag{6.39}$$

In general the pressure is a function of both density and temperature, $P = P(\rho, T)$, so that we need equations describing the temperature structure of the star. For degenerate objects, however, the pressure is a function of density only, $P = P(\rho)$, and the structure of the star can be solved without information about the temperature.

6.2.1 The polytrope equation

To see this, we write the pressure as

$$P = K\rho^{1+\frac{1}{n}} \tag{6.40}$$

where K is a constant, and n is called the *polytrope index*. The density is written with a dimensionless variable θ as

$$\rho = \rho_c \theta^n \tag{6.41}$$

We may then combine the last three equations into

$$\left[\frac{(n+1)K}{4\pi G}\rho_c^{\frac{1}{n}-1}\right]\frac{1}{r^2}\frac{d}{dr}\left(r^2\frac{d\theta}{dr}\right) = -\theta^n \tag{6.42}$$

We now transform to a dimensionless radius by substituting

$$r \equiv a\xi \qquad a \equiv \left[\frac{(n+1)K}{4\pi G}\rho_c^{\frac{1}{n}-1}\right]^{1/2} \tag{6.43}$$

to obtain the *polytrope equation*

$$\frac{1}{\xi^2}\frac{d}{d\xi}\left(\xi^2\frac{d\theta}{d\xi}\right) = -\theta^n \tag{6.44}$$

This equation may be solved numerically, for various values of n, where we use the boundary conditions at the center of the star $\xi = 0$

$$\theta(0) = 1, \qquad \left(\frac{d\theta}{d\xi}\right)_{\xi=0} = 0. \tag{6.45}$$

The first condition uses the freedom to scale θ (see Eq.6.41) and the second condition follows from symmetry with respect to $r = 0$, so that $dP/dr = 0$ at $r = 0$. The solutions for $n = 1.5$ and for $n = 3$ are shown in Figure 6.4.

The function θ drops monotonically to zero, and the position where θ reaches zero corresponds to the radius of the stellar surface. For a polytrope with $n = 1.5$ the value for ξ at which θ is zero is $\xi_1 \simeq 3.65375$; for a polytrope of $n = 3$ at $\xi_1 \simeq 6.89685$. The mass $M(\xi)$ of a polytrope within radius ξ can be found by rewriting Eq.6.38 in terms of the polytrope function, and by integrating the result, which gives (see Exercise 4.5).

$$M(\xi) = -4\pi\left[\frac{(n+1)K}{4\pi G}\right]^{3/2}\rho_c^{(3-n)/(2n)}\xi^2\frac{d\theta}{d\xi} \tag{6.46}$$

The mass of the whole star is found by using this equation at $\xi = \xi_1$. The numerical solution provides the value for $-(\xi^2 d\theta/d\xi)_{\xi=\xi_1} = 2.714$ for the $n = 1.5$ polytrope,

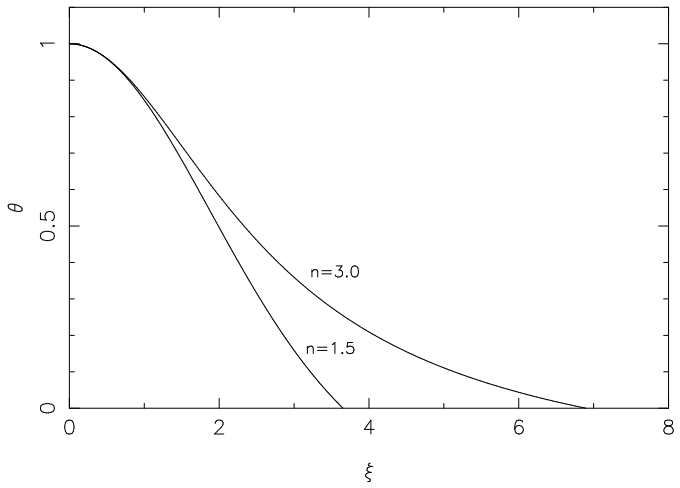

Figure 6.4: *The solutions for $n = 1.5$ and $n = 3.0$ of the polytrope equation Eq.6.44.*

and $= 1.89$ for the $n = 3$ polytrope. By elimination of ρ_c from Eq.6.46, using Eq.6.43, we obtain the mass–radius relation for a polytrope.

Consider for example a white dwarf with central density $\rho_c = 10^5\,\mathrm{g\,cm^{-3}}$. In such a white dwarf, the pressure is non-relativistically degenerate, so that we have a polytrope with $n = 1.5$. Eq.6.18 gives K. This immediately gives us the radius of the white dwarf with Eq.6.43 and $\xi_1 = 3.65675$. The mass follows from Eq.6.46. In general, the mass-radius relation for non-relativistically fully degenerate white dwarfs is $R \propto M^{-1/3}$. Analogously we may consider a non-relativistically fully degenerate neutron star.

In the case of fully relativistic fully degenerate matter Eqs.6.43-6.46 show that the mass is a constant! For white dwarfs

$$M_{Ch} = 1.457 \left(\frac{2}{\mu_e}\right)^2 M_\odot \tag{6.47}$$

How should we interpret this mass, which is called the Chandrasekhar limit? Consider first a low-mass white dwarf, which is non-relativistically fully degenerate. If we increase the mass, the core will become more dense, and at some point the core will become relativistically degenerate. If we continue to increase the mass, a larger and larger fraction of the star becomes relativistically degenerate, until at the mass given by Eq.6.47 the whole star is relativistically degenerate. If we then add more mass, Eqs.6.37,6.38 no longer have a solution, i.e. no equilibrium between gravity and pressure is possible: the star collapses.

In principle, we could apply a similar reasoning to the neutron star; as a first approach, this gives a reasonable impression of its structure. We note immediately from Eq. 6.47 that the Chandrasekhar limit for a neutron star is about 5.6 $M_\odot$. In detail, we must be more accurate, due to two complications.

6.2.2 Realistic structure computation of a neutron star

The first complication is that at the compactness of a neutron star, we can no longer use the classical equations 6.37 and 6.38, but we must use their general-relativistic equivalents. This is quite doable, as general relativity is well understood. In fact, all that has to be done is to replace Eqs. 6.37 and 6.38 with the general relativistic

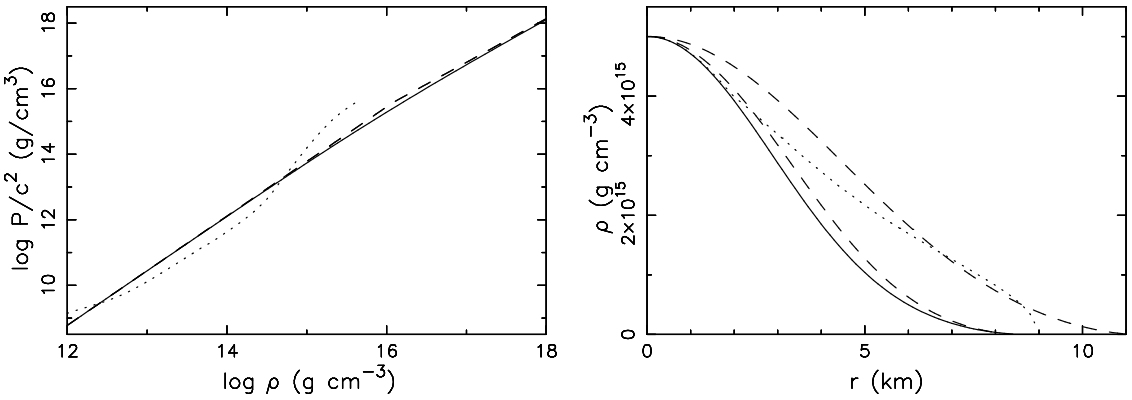

Figure 6.5: *Left: the approximate equation of state of a mixture of neutrons, protons and electrons as found by combining the non-relativistic and relativistic limits (Eqs. 6.16, 6.20; dashed line) lies close to the full solution (Eqs. 6.29, 6.30 and 6.34, 6.35; solid line). A more realistic equation of state, which includes the effect of nuclear forces, has a higher pressure for the central density of a neutron star. Right: different models for a neutron star with the same central density, obtained by numerically integrating the structure equations with different equations of state. The line styles indicate the equation of state used, as in left panel. The upper dashed line is a solution based on Newtonian gravity (Eqs.6.37, 6.38), the other three are based on general relativity (Eqs.6.48,6.49). The masses of these models are* 2.4 $M_\odot$ *and* 1.0 $M_\odot$ *for the dashed lines,* 0.8 $M_\odot$ *for the solid line, and* 2.1 $M_\odot$ *for the dotted line.*

equivalents. Hydrostatic equilibrium becomes

$$\frac{dP}{dr} = -\frac{G(M^*(r) + 4\pi r^3 \frac{P}{c^2})(\rho^* + \frac{P}{c^2})}{r^2(1 - \frac{2GM^*(r)}{rc^2})} \tag{6.48}$$

where the equivalence of energy (hence pressure) and mass is taken into account both in the mass $M(r)$ and in the density ρ, which now consist of rest mass terms M^* and ρ^* and pressure terms. The r^2 in the denominator is multiplied with a correction term which takes into account the curvature of space. These terms will be (partially) explained in the chapter on general relativity. The rest mass is conserved

$$\frac{dM^*(r)}{dr} = 4\pi r^2 \rho^* \tag{6.49}$$

Equations 6.48 and 6.49 are called the Tolman Oppenheimer Volkov equations.

As shown in Figure 6.5 the general relativistic equations lead to a star which is smaller in radius and mass – for the same central density and equation of state – than the Newtonian equations of gravity.

The second complication is that we cannot use a polytrope throughout the star, because the ratio of the numbers of electrons, protons and neutrons depends on the density (as explained in discussing Eqs.6.34,6.35), so that K in the polytropic pressure relation Eq.6.40 is no longer a constant. We can solve the full set of Eqs. 6.25-6.30; this gives an equation of state close to the approximate equation found by combining the two polytropic equations 6.37,6.38. The neutron stars based on these equations of state for a free gas of neutrons, protons and electrons have a mass

less than 1 $M_\odot$ when computed from the general relativistic structure equations. A more massive neutron star, like those observed near 1.4 $M_\odot$, requires an equation of state with higher pressure at the same central density. A more realistic equation of state, such as the one shown in Figure 6.3, takes account of nuclear forces. As shown in Figure 6.5, such an equation indeed can explain neutron stars with masses as observed.

6.3 Temperature structure of a degenerate star

In a gas with a temperature gradient, heat is transported until the temperature difference is erased. Fourier discovered empirically that the energy flux Q is proportional to the temperature gradient:

$$Q = -\kappa \nabla T \tag{6.50}$$

The minus sign in the right hand side indicates that the energy flows from the high temperature to the low temperature regions. The heat-conduction coefficient κ is proportional to the free path length of the particles, to their average velocity, and to their density.

To derive this, we first consider more generally a gas in which a quantity G varies. We choose the z-axis along the gradient. Consider a particle that moves a distance equal to the free path length l in a direction that makes an angle θ with the z-axis, and then collides with another particle. The difference in G between the particle and its surroundings then is equal to $dG = -l\cos\theta(\partial G/\partial z)$. The number of particles with velocity v in direction θ passing per unit of time through a unit surface perpendicular to the z-axis is $(n/4\pi)v\cos\theta\sin\theta d\theta d\phi$. To obtain the transport of G through the unit surface element we integrate over θ and ϕ:

$$Q = \int_0^{\pi}\int_0^{2\pi} l\cos\theta\frac{\partial G}{\partial z}\frac{n}{4\pi}v\cos\theta\sin\theta d\theta d\phi = \frac{lnv}{3}\frac{\partial G}{\partial z} \tag{6.51}$$

We also have to integrate over the velocity distribution. If the free path length l does not depend on v, this integration simply leads to replacing v in Eq.6.51 with the average velocity $\bar{v}$.

We apply this to the temperature derivative and the heat flow. For G we write the energy per particle $3kT/2$ and find

$$Q = -\frac{lnk\bar{v}}{2}\frac{\partial T}{\partial z} \tag{6.52}$$

and thus we have theoretically derived the empirical relation of Fourier.

In a degenerate gas, the conduction coefficient is very high. The first reason for this is that most particles have the Fermi momentum, and thus a high velocity, so that $\bar{v}$ is high. Secondly, all those collisions are forbidden which would bring particles into a momentum position which is already filled: thus the free path length is very high. This high conduction coefficient causes the interior of white dwarfs (degenerate electron gas) and of neutron stars (degenerate neutron gas) to be virtually isothermal. A temperature gradient only exists in a thin atmosphere near the surface, as we will discuss in a moment.

6.3.1 Atmospheres and cooling of white dwarfs

How thick is the atmosphere? Its pressure scale height H_p is given by

$$H_p = \frac{kT}{\mu m_p g} = \frac{kTR^2}{\mu m_p GM} \tag{6.53}$$

where g is the gravitational acceleration. For a neutron star with mass $1.4\,M_\odot$ and radius $R = 10$ km, with an atmosphere of pure iron, $\mu = 56$, and a surface temperature of 10^6K, we find that the atmospheric scale height is less than 0.01 cm!

A simple derivation for the cooling time, given by Mestel, goes as follows. The equation relating the luminosity of a star to the temperature derivative is

$$\frac{dT}{dr} = -\frac{3\kappa\rho L(r)}{4acT^3 4\pi r^2} \tag{6.54}$$

We combine this equation with Eq.6.37, and apply the result to the surface layer of the star, where luminosity and mass have reached the surface value, i.e.$L(r) = L$ and $M(r) = M$. We further use the Kramers opacity law approximation:

$$\kappa = \kappa_o \rho T^{-3.5} \qquad \text{where} \qquad \kappa_o = 4.34 \times 10^{24} Z(1+X)\,\mathrm{cm^2\,g^{-1}} \tag{6.55}$$

to find

$$\frac{dP}{dT} = \frac{4ac4\pi GMT^{6.5}}{3\kappa_o L\rho} \tag{6.56}$$

We eliminate the density from this equation by applying the equation of state. Near the surface of a star, even a white dwarf or a neutron star, this is the equation of state for non-degenerate matter. We find

$$PdP = \frac{4ac4\pi GM}{3\kappa_o L}\frac{k}{\mu m_p}T^{7.5}dT \tag{6.57}$$

We integrate this equation over the atmosphere of the star, using the boundary conditions $T(R) = P(R) = 0$. Using the equation of state once more, we find

$$\rho = \left(\frac{32ac\pi GM\mu m_p}{25.5\kappa_o Lk}\right)^{1/2} T^{3.25} \tag{6.58}$$

This equation describes the density in the atmosphere of any star (within the approximation of Kramer's law). We now apply it to the atmosphere of a degenerate white dwarf, and in particular to the layer where the electrons are just becoming degenerate, i.e.the point where the atmosphere connects to the isothermal interior. We denote quantities in this layer with index $*$. By equating the degenerate electron pressure to the non-degenerate electron pressure we have for the density ρ_*

$$\frac{\rho_* kT_*}{\mu_e m_p} = C\left(\frac{\rho_*}{\mu_e}\right)^{5/3} \Rightarrow \rho_* = \left(\frac{k}{m_p C}\right)^{3/2}\mu_e T_*^{3/2} = 2.4\times 10^{-8}\,\mathrm{g\,cm^{-3}}\mu_e T_*^{3/2} \tag{6.59}$$

where C is given in Eq. 6.18. Combined with Eq.6.58 this equation relates the internal temperature of the white dwarf to the luminosity:

$$L = \frac{32\pi acGM\mu}{25.5\kappa_o\mu_e^2}\left(\frac{m_p}{k}\right)^4 C^3 T_*^{3.5} = 5.7\times 10^5\,\mathrm{erg\,s^{-1}}\frac{\mu}{\mu_e^2}\frac{1}{(1+X)Z}\frac{M}{M_\odot}T_*^{3.5} \equiv C_1 T_*^{3.5} \tag{6.60}$$

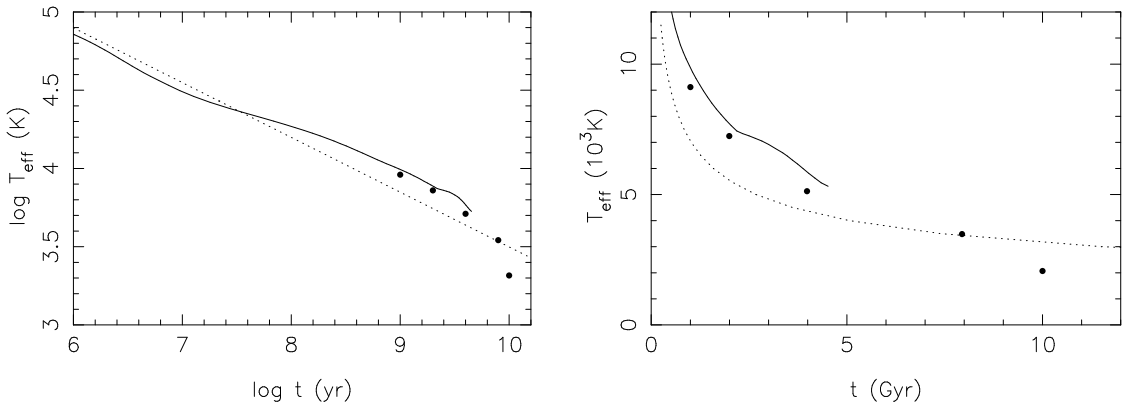

Figure 6.6: *The cooling for a CO white dwarf of* $0.6\ M_\odot$ *with a helium atmosphere according to Eq. 6.65 (dashed line), and according to more sophisticated models (solid line, for the coolest stars •). The simple theory is not too bad, but to obtain accurate ages for old white dwarfs, the sophisticated models are indispensable.*

How long does this luminosity take to drain the internal energy? The internal energy of a white dwarf is mainly in the non-degenerate ions. Thus the total thermal energy can be written in terms of the internal temperature

$$U = \frac{3}{2} k T_* \frac{M}{A m_p} \tag{6.61}$$

where A is the atomic mass of the nuclei, and this energy leaks away as radiation

$$L = \frac{dU}{dt} \tag{6.62}$$

We integrate this equation to find the internal energy, and thus via Eq.6.61 the internal temperature, as a function of time:

$$t - t_o = \frac{3kM}{5Am_pC_1}\left(T_*^{-5/2} - T_o^{-5/2}\right) \simeq \frac{3kM}{5Am_pC_1} T_*^{-5/2} \tag{6.63}$$

where T_o is the internal temperature at time t_o, and where the approximation is valid once significant cooling has taken place: $T_* \ll T_o$. We now use Eq. 6.60 to eliminate T_* from this equation, and enter the constants C_1, C and κ_o to find

$$\tau \simeq 7.2 \times 10^7\,\mathrm{yr} \frac{1}{A}\left[\frac{Z(1+X)\mu_e^2}{\mu}\right]^{2/7}\left(\frac{M/\,M_\odot}{L/\,L_\odot}\right)^{5/7} \tag{6.64}$$

which tells us that the cooling time increases as the luminosity of the white dwarf decreases. We may also write the last equation in terms of the effective temperature using $L = 4\pi R^2 \sigma {T_{\rm eff}}^4$ and the approximate mass-radius relation $R/\,R_\odot \simeq 0.011(M/\,M_\odot)^{-1/3}$ (valid for $M \lesssim 0.6\,M_\odot$, to find

$$\tau = 9.5 \times 10^9\,\mathrm{yr} \frac{1}{A}\left[\frac{Z(1+X)\mu_e^2}{\mu}\right]^{2/7}\left(\frac{M}{M_\odot}\right)^{25/21}\left(\frac{T_{\rm eff}}{10^4\,\mathrm{K}}\right)^{-20/7} \tag{6.65}$$

As a numerical example we consider a carbon oxygen white dwarf of $0.6\,M_\odot$, with an atmosphere consisting mainly of helium. A refers to the core, and for an

Figure 6.7: *Left: theoretical cooling track for young neutron stars (solid line), together with observed X-ray luminosities for ordinary and recycled radio pulsars (open and filled circles, respectively; the arrow is an upper limit). The X-rays for some young pulsars and all recycled X-ray pulsars are too high for pure thermal emission, and must therefore be magnetospheric. Right: X-ray luminosity of radio pulsars as a fraction of the spindown energy* $L_{sd} \equiv I\Omega\dot{\Omega}$. *The dotted line indicates* $L_x/L_{sd} = 0.001$. *The recycled radio pulsars lie on the same average relation as the ordinary pulsars.*

roughly equal mix of carbon and oxygen we take $A = 14$. For the values of X, Z, μ_e and μ we must take the atmospheric values; we take the hydrogen content zero, $X = 0$, and for the metallicity $Z = 0.1$, thus, $\mu \simeq 1.4$ and $\mu_e = 2$. The cooling times to $T_{eff} = 5 \times 10^4$ K, 10^4 K, and 5000 K are 4.8×10^6 yr, 4.8×10^8 yr, and 3.5×10^9 yr, respectively. Cool white dwarfs have ages which are a significant fraction of the age of the Galaxy!

The study of old white dwarfs has received new impulses now that many of them have been found, in the galactic disk, in globular clusters, and – perhaps most spectacularly – in the Hubble Deep Field (a very long integration on a field which with smaller telescopes appears to be empty), i.e. in the galactic halo. The theory for cooling has also been improved, mainly by using better opacities and full atmospheric models: interesting in particular is the result that at temperatures below 5000 K, molecular hydrogen has high opacity at red wavelengths, so that white dwarfs with pure hydrogen atmospheres become blue again when they cool below this. Such is the case for the coolest white dwarfs in the Hubble Deep Field. Other improvements take into account that a cool white dwarf can crystallize, which leads to an extra energy release of order kT per ion, and that a very low level of nuclear fusion can still take place in early stages of the cooling.

6.3.2 Cooling of neutron stars

A neutron star is born very hot, but cools rapidly through the emission of neutrinos in reactions in which protons change into neutrons under emission of a positron and a neutrino, and neutrons change into protons under emission of an electron and an anti-neutrino:

$$n \rightarrow p + e^- + \bar{\nu} \tag{6.66}$$

Once the temperature has dropped considerably, degeneracy sets in, and reaction Eq.6.66 is no longer possible! The neutrino produced in this reaction carries away some energy and momentum, so that the proton and electron have to share less energy and momentum than the neutron had. As a result one of these particles (because of the mass ratio usually the electron) would end up with a momentum below its Fermi surface: but there all positions are already filled! Thus the neutron can no longer decay directly – and the star remains a neutron star....

Cooling is still possible via indirect reactions, in which a neutron borrows energy from another neutron to be able to decay:

$$n + n \rightarrow n + p + e^- + \bar{\nu} \qquad \text{followed by} \qquad p + e^- + \rightarrow n + \nu \tag{6.67}$$

Detailed calculations show that this and similar cooling mechanisms are still more efficient for a neutron star than the energy leak through the atmosphere near the

Figure 6.15: RGS spectra of three nearby, thermally emitting neutron stars. The top panel shows RX J1605.3+3249, for which the spectrum shows clear evidence for an absorption feature. Overdrawn is the best-fit model, a slightly extincted black body with two Gaussian absorption features. The second and third panel show the spectra of RX J0720.4−3125 and J1308.6+2127, with the same model overdrawn for comparison. Both have similar temperatures, but RX J0720.4−3125 has no absorption, while RX J1308.6+2127 has much stronger absorption.

surface, until the internal temperature has dropped to $\sim 10^3$K. To compare the internal temperature with the observed surface temperature, we must calculate an atmosphere model.

With the gratings on Chandra and XMM the first real spectra of single neutron stars are now becoming available, and they are quite surprising. The spectrum of the nearby single neutron star RX J0720.4−3125 shows no absorption or emission lines, and looks much more like a black body spectrum than like the spectrum expected from a simple pure hydrogen or pure iron atmosphere at the high-gravity surface of a neutron star. Other spectra of single neutron stars with similar temperature show very broad absorption features (Figure 6.15). This is now being investigated, and it appears that a) the magnetic field play a role in the spectrum – which explains why stars at (almost) the same temperature have different spectra, and b) vacuum polarization is important – which explains that the absorption features are very broad.

6.4 Exercises

Exercise 20. Estimate the density at which the transition occurs between non-relativistic and relativistic degenerate matter, for fully degenerate electron pressure and for fully degenerate neutron pressure.

Exercise 21. Calculate the Fermi momentum and energy for electrons and protons in a degenerate gas, in which the particle density is $10^{36}\,\mathrm{cm}^{-3}$ for both electrons and protons. To forgo unnecessary computing, remember that $\cosh x = \sqrt{\sinh^2 x + 1}$. Show that the electrons are relativistically degenerate, and that the protons are still non-relativistic. Express the Fermi energies in terms of the rest mass mc^2, and estimate the temperature at which the thermal energy kT is equal to the Fermi energy. Argue that such temperatures allow transitions between neutrons and protons again. These transitions lead to energy loss in the form of neutrinos, causing a young neutron star to cool rapidly.

Exercise 22. Derive Eq.6.29. In order to do so, first show that

$$\sinh^4 x = \frac{\cosh 4x}{8} - \frac{\cosh 2x}{2} + \frac{3}{8} \tag{6.68}$$

Exercise 23. Show that Eq.6.9 is indeed identical to the Planck function

$$B_\nu d\nu = \frac{2\pi h\nu^3}{c^2}\frac{1}{e^{h\nu/kT}-1}d\nu \tag{6.69}$$

after insertion of Z_i.

Exercise 24. Calculate the constants K of Eq.6.40 for non-relativistic and relativistic degenerate matter for electron degeneracy and for neutron degeneracy. Consider non-relativistic polytrope models at the same mass to estimate the ratio between the radii of a neutron star and of a white dwarf.

Exercise 25. Argue that the integral in Eq.6.51 should indeed have π as an upper bound, and not $\pi/2$.

Computer Exercise 3. a) Write a computer code to compute the structure of a white dwarf. To do so, we rewrite the differential equations as difference equations. For the conservation of mass, Eq. 6.37, we write:

$$\Delta M(r) = 4\pi r^2 \rho(r)\Delta r \qquad A$$

and for hydrostatic equilibrium Eq. 6.38:

$$\Delta P(r) = -\frac{GM(r)}{r^2} \quad \rho(r)\Delta r \qquad B$$

To solve two first order differential equations, we need two boundary conditions. We choose for these:

1. in the center, $R = 0$, the mass is zero: $M(0) = 0$
2. a value for the central pressure P_c

We see from Eq. B and the boundary condition 1 that the pressure reaches a maximum in the center: $dP/dr_{R=0} = 0$. (We can also derive this from the spherical symmetry: starting from the center, the change in P is the same for a small distance Δr and for a step $-\Delta r$; with Eq. B it then follows that $(\Delta P)_{R=0} = -(\Delta P)_{R=0}$, i.e.

$(\Delta P)_{R=0} = 0$.) This implies that a small sphere of constant pressure, and thus, via Eq. B, constant density surrounds the center. Thus the first two steps for a numerical solution are:
a) calculate the central density from the central pressure, with Eq. 6.18 or Eq. 6.21
b) calculate the mass of a sphere with constant density $\rho(0)$ and radius Δr:

$$M(\Delta r) = \frac{4\pi}{3}\rho(0)\Delta r^3 \tag{6.70}$$

The third, fourth and fifth steps are:
c) calculate the change in pressure ΔP and in mass ΔM $r = \Delta r$ and $r = \Delta r + \Delta r = 2\Delta r$ by entering the values for M and ρ at $r = \Delta r$ in the right hand sides of Eq. A and B
d) use the results to compute the values at $r = 2\Delta r$:

$$M(2\Delta r) = M(\Delta r) + \Delta M \tag{6.71}$$

$$P(2\Delta r) = P(\Delta r) + \Delta P \tag{6.72}$$

e) calculate the new density from the new pressure, with Eqs. 6.18,6.21.

Because of the minus sign in Eq. B the newly found pressure, and with it the density, are smaller than the central pressure and density. We can repeat the last three steps in a loop. Writing the quantities at $r = n\Delta r$ with index n, we have:
f) $(\Delta P)_n$ and $(\Delta M)_n$ with Eqs. A,B from M_n and ρ_n
g) $M_{n+1} = M_n + \Delta M_n$ and $P_{n+1} = P_n + \Delta P_n$
h) ρ_{n+1} volgt uit P_{n+1}
We repeat steps f-h again and again, until the pressure drops below zero: then the density is zero as well, in other words, we have reached the edge of the star. In parctice we stop when the pressure is too low for Eq. 6.18 to be valid, i.e. when the pressure becmes ideal. The last found values for mass and radius are the mass M and radius R of the whole degenerate star.
b) repeat the calculation above for different central densities, and mae a plot of radius as a function of mass.

It is important to choose a good value for Δr in the above calculations: if we take Δr too large the result is very inaccurate; if we take Δr too small rounding off errors made by the computer will dominate. (To see this consider the limiting case of a very small step in Δr, for which the changes in P and M are smaller than the accuracy with which the computer stores these numbers.)

Computer Exercise 4. In this execrise we adapt the code from the previous one, to make it compute the structure of a neutron star. We do this in three steps.
a) Compute the polytrope constants in Eqs. 6.19,6.22 and use these to solve the structure of a neutron star with Eqs.(A) and (B) above. For computational ease it may help to use P/c^2 as a variable, rather than P itself. The maximum mass is near $5.6\,M_\odot$ according to these calculations, too high...
b) Replace Eq.(B) with its equivalent in General Relativity, with use of Eq. 6.48, and compute the structure of a neutron star. The maximum mass is near $0.7\,M_\odot$ according to these calculations, too low...
c) Use a realistic equation of state, provide in a table on the course website.

Computer Exercise 5. With Exercise 21 in mind, write a computer code to calculate the ratio of the numbers of neutrons to the numbers of electrons at electron number densities from $n_e = 10^{36}\,\mathrm{cm}^{-3}$ to $10^{39}\,\mathrm{cm}^{-3}$.

6.5 Literature

Thermodynamik und Statistik by A. Sommerfeld is a nice and good book, in which one may find the derivation of the equations of state, and a clear discussion of the heat transport. Application to neutron stars may be found in *Black Holes, White Dwarfs and Neutron Stars* by S. Shapiro and S. Teukolsky. Polytropes are discussed in (too much) detail in *Stellar Structure* by S. Chandrasekhar. A modern discussion of the cooling of white dwarfs is given by M. Wood 1992 ApJ 386, 539 and by B. Hansen 1999 ApJ 520, 680; the white dwarfs in the Hubble Deep Field were found by R. Ibata et al. 1999, ApJ 524, L95. Electromagnetism is lucidly explained in the book *classical electrodynamics* by J.D. Jackson.

Chapter 7

Electromagnetism of neutron stars[1]

The model in general use for the magnetic field of a radio pulsar is that of a magnetic dipole. In this chapter we derive the equations describing a magnetic dipole and the radiation it emits.

7.1 Energy equation for electromagnetism and potentials

The equations of Maxwell *in vacuo* are

$$\nabla \cdot \vec{E} = 4\pi\rho \tag{7.1}$$

$$\nabla \times \vec{E} = -\frac{1}{c}\frac{\partial \vec{H}}{\partial t} \tag{7.2}$$

$$\nabla \cdot \vec{H} = 0 \tag{7.3}$$

$$\nabla \times \vec{H} = \frac{4\pi}{c}\vec{J} + \frac{1}{c}\frac{\partial \vec{E}}{\partial t} \tag{7.4}$$

Here $\vec{E}$ and $\vec{H}$ are the electric and magnetic field respectively, ρ is the charge density, and $\vec{J}$ the current. To obtain an energy equation, we take the inner product of $\vec{H}$ with Eq. 7.2 and of $\vec{E}$ with Eq. 7.4 and subtract the results. Applying the vector identity $\nabla \cdot (\vec{a} \times \vec{b}) = \vec{b} \cdot (\nabla \times \vec{a}) - \vec{a} \cdot (\nabla \times \vec{b})$ we find:

$$\frac{\partial}{\partial t}\frac{E^2 + H^2}{8\pi} + \vec{J} \cdot \vec{E} + \frac{c}{4\pi}\nabla \cdot (\vec{E} \times \vec{H}) = 0 \tag{7.5}$$

Now integrate this equation over a volume V and apply the theorem of Gauss to find

$$\frac{\partial}{\partial t}\int_V \frac{E^2 + H^2}{8\pi} dV + \int_V \vec{J} \cdot \vec{E} dV + \frac{c}{4\pi}\int_O (\vec{E} \times \vec{H}) \cdot d\vec{O} = 0 \tag{7.6}$$

The first term is the change in energy density $(E^2 + H^2)/8\pi$, the second term the change in kinetic energy of the charges (to see this write $\vec{J}$ as the sum of the individual charges $\vec{J} = \sum e\vec{v}$, so that $\vec{J} \cdot \vec{E} = \sum e\vec{v} \cdot \vec{E}$), and the third term is

[1] This Chapter is copied from Lecture Notes 'Neutron Stars' by John Heise, 1972

the energy flux through the surface of the volume (as will become clear below, at Eq. 7.38). The vector $(c/4\pi)\vec{E}\times\vec{H}$ is called the Poynting flux.

For applications of Maxwell's equations it is often convenient to write $\vec{E}$ and $\vec{H}$ in terms of a scalar potential ϕ and a vector field $\vec{A}$. Remembering that the divergence of a rotation is zero, we note from Eq. 7.3 that $\vec{H}$ can be written

$$\vec{H} = \nabla \times \vec{A} \tag{7.7}$$

Entering this in Eq. 7.2 we find

$$\vec{E} = -\frac{1}{c}\frac{\partial \vec{A}}{\partial t} - \nabla \cdot \phi \tag{7.8}$$

where ϕ may be chosen freely, since the rotation of a gradient is zero ($\nabla \times (\nabla\phi) = 0$ for all ϕ). We use Equations 7.7 and 7.8 in equations 7.2 and 7.4, and use another vector identity $\nabla \times (\nabla \times \vec{a}) = \nabla(\nabla \cdot \vec{a}) - \nabla^2\vec{a}$, to find

$$\nabla^2\phi + \frac{1}{c}\frac{\partial}{\partial t}\nabla \cdot \vec{A} = -4\pi\rho \tag{7.9}$$

$$\nabla^2\vec{A} - \frac{1}{c^2}\frac{\partial^2\vec{A}}{\partial t^2} - \nabla(\nabla \cdot \vec{A} + \frac{1}{c}\frac{\partial\phi}{\partial t}) = -\frac{4\pi}{c}\vec{J} \tag{7.10}$$

Now we use the freedom that we have to choose ϕ and take it so that $(1/c)\partial\phi/\partial t = -\nabla \cdot \vec{A}$. This is called the Lorentz gauge. With it we find

$$\nabla^2\phi - \frac{1}{c^2}\frac{\partial^2\phi}{\partial t^2} = -4\pi\rho \tag{7.11}$$

$$\nabla^2\vec{A} - \frac{1}{c^2}\frac{\partial^2\vec{A}}{\partial t^2} = -\frac{4\pi}{c}\vec{J} \tag{7.12}$$

For a given charge distribution ρ and current distribution $\vec{J}$ we solve equations 7.11 and 7.12 first, and then obtain $\vec{E}$ and $\vec{H}$ from eqs. 7.8 and 7.9.

7.2 Electrostatics and magnetostatics

In a stationary situation the time derivatives in eqs. 7.11 and 7.12 can be dropped.

Let us first consider a static charge distribution of a number of point charges e_a at positions $\vec{R}_a$. With the δ-function we write the charge distribution as a sum of individual charges: $\rho = \sum e_a\delta(\vec{r} - \vec{R}_a)$. The solution of the static case of Eq. 7.11 is Coulomb's Law

$$\phi(\vec{r}) = \sum \frac{e_a}{|\vec{r} - \vec{R}_a|} \tag{7.13}$$

At large distances from the charges, $\vec{r} \gg \vec{R}_a$, we may expand ϕ in terms of $\vec{R}_a/\vec{r}$. With the general expansion of a function f

$$f(\vec{r} - \vec{R}_a) = f(\vec{r}) - \vec{R}_a \cdot \nabla f(\vec{r}) \tag{7.14}$$

we rewrite Eq. 7.13 as

$$\phi(\vec{r}) = \frac{\sum e_a}{r} - \sum e_a\vec{R}_a \cdot \nabla\frac{1}{r} \tag{7.15}$$

The sum $\sum e_a \vec{R}_a \equiv \vec{d}$ is called the dipole moment of the system of charges. When the total charge is zero, $\sum e_a = 0$, the dipole moment does not depend on the choice of the origin, so that

$$\phi(\vec{r}) = \vec{d} \cdot \nabla \frac{1}{r} = \frac{\vec{d} \cdot \nabla \vec{r}}{r^3} \tag{7.16}$$

With Eq. 7.8 the electric field follows:

$$\vec{E}(\vec{r}) = -\frac{1}{r^3}\nabla(\vec{d} \cdot \vec{r}) - (\vec{d} \cdot \vec{r})\nabla\frac{1}{r^3} = \frac{3(\vec{n} \cdot \vec{d}) - \vec{d}}{r^3} \tag{7.17}$$

where $\vec{n} \equiv \vec{r}/r$ is the unit vector in the direction of $\vec{r}$. Eq. 7.17 is the equation for a dipole electric field, valid at large distance.

In an analogous fashion we derive the magnetic dipole field. Write the current distribution as $\vec{J} = \sum e_a \vec{v}_a \delta(\vec{r} - \vec{R}_a)$, and the solution of Eq. 7.12 in the static case is

$$\vec{A} = \frac{1}{c} \sum \frac{e_a \vec{v}_a}{|\vec{r} - \vec{R}_a|} \tag{7.18}$$

At large distance we expand once more with Eq. 7.14 to obtain

$$\vec{A} = \frac{1}{cr} \sum e_a \vec{v}_a - \frac{1}{c} \sum e_a \vec{v}_a (\vec{R}_a \cdot \nabla \frac{1}{r}) \tag{7.19}$$

In stationary cases the total current is most often zero: $\sum e_a \vec{v}_a = 0$. We rewrite the second term in Eq. 7.19 by noting that in the stationary case

$$\frac{d}{dt}(\sum e_a \vec{R}_a (\vec{R}_a \cdot \vec{r})) = 0 = \sum e_a \vec{v}_a (\vec{R}_a \cdot \vec{v}_a) + \sum e_a \vec{R}_a (\vec{v}_a \cdot \vec{r}) \tag{7.20}$$

and by use of the vector identity $(\vec{R}_a \times \vec{v}_a) \times \vec{r} = (\vec{r} \cdot \vec{v}_a)\vec{R}_a - (\vec{R}_a \cdot \vec{v}_a)\vec{v}_a$ to obtain

$$\vec{A} = -\frac{1}{2c} \sum e_a \frac{(\vec{R}_a \times \vec{v}_a) \times \vec{r}}{r^3} = \frac{1}{c} \frac{\vec{m} \times \vec{r}}{r^3} \tag{7.21}$$

where we have defined the magnetic dipole moment $\vec{m} \equiv (1/2) \sum e_a \vec{R}_a \times \vec{v}_a / c$. Substituting this in Eq. 7.7 we find the magnetic field for a magnetic dipole, valid at large distance of the charge currents

$$\vec{H} = \frac{3\vec{n}(\vec{m} \cdot \vec{n}) - \vec{m}}{r^3} \tag{7.22}$$

With Eq. 7.22 we conclude that a sphere has a magnetic field if its interior contains and electric current $\vec{J}$. This is as true for a copper sphere as for a neutron star, an ordinary star, or the Earth. We can write the magnetic dipole moment in terms of the magnetic field B_o at the pole, where $\vec{n} \parallel \vec{m}$ so that

$$B_o = \frac{2m}{R^3} \qquad \Rightarrow \qquad m = \frac{B_o R^3}{2} \tag{7.23}$$

In this equation R is the radius of the sphere.

7.3 The pulsar magnetosphere

In this section we derive the charge distribution inside a rotating neutron star caused by the magnetic field. This charge distribution in turn causes an electric field which draws charged particles from the neutron star into the magnetosphere.

The magnetic field given by Eq. 7.22 is attached to the crust of the neutron star, and rotates with it. We'll consider the simple case where the magnetic axis is parallel or anti-parallel to the rotation axis. The velocity is then given by $\vec{v} = \vec{\Omega} \times \vec{r}$. In the corotating coordinate system the electric field is zero. Application of a Lorentz transformation thus gives the electric field in a non-rotating, resting coordinate system as

$$\vec{E} = -\frac{1}{c}\vec{v} \times \vec{H} \tag{7.24}$$

This implies that the electric field is perpendicular to the magnetic field: $\vec{E} \cdot \vec{H} = 0$. According to Eq. 7.1 the electric field leads to a charge redistribution inside the conducting neutron star, so that the difference between the number densities n_+ and n_- of positive and negative charges is given by

$$4\pi(n_+ - n_-)e = -\frac{1}{c}\nabla \cdot (\vec{v} \times \vec{H}) = -\frac{1}{c}\left[\vec{H} \cdot (\nabla \times \vec{v}) - \vec{v} \cdot (\nabla \times \vec{H})\right] \tag{7.25}$$

The last term includes a rotation of $\vec{H}$, and is negligible as long as $v \ll c$. Ignoring this term and using $\nabla \times \vec{v} = \nabla \times (\vec{\Omega} \times \vec{r}) = 2\vec{\Omega}$ we obtain

$$n_- - n_+ = \frac{\vec{H} \cdot \vec{\Omega}}{2\pi ec} = \pm\frac{m\Omega}{2\pi ec}\frac{3\cos^2\theta - 1}{2} \tag{7.26}$$

where we used Eq. 7.22 for $\vec{H}$ and where θ is the angle between $\vec{n}$ and $\vec{m}$. The sign of the right hand side is + when the magnetic field is parallel to the rotation axis, and − when the magnetic field is anti-parallel. Eq. 7.26 shows that the rotating dipole magnetic field causes a quadrupole charge distribution. At the poles of a parallel field the positive charges dominate, and around the equator (for $\cos\theta < \sqrt{1/3}$ i.e. $55° \lesssim \theta \lesssim 125°$) the negative charges.

This charge distribution inside the neutron star causes an electric field outside the neutron star, which we derive by writing Eq. 7.11 in spherical coordinates:

$$\frac{1}{r}\frac{\partial^2}{\partial r^2}r\Phi + \frac{1}{r^2\sin\theta}\frac{\partial}{\partial\theta}\left(\sin\theta\frac{\partial\Phi}{\partial\theta}\right) + \frac{1}{r^2\sin^2\theta}\frac{\partial^2\Phi}{\partial\phi^2} = 0 \tag{7.27}$$

When the rotation and magnetic axes coincide, Φ does not depend on ϕ, and the third term in Eq. 7.27 is zero. We write Φ as the product of a function $U(r)/r$ of r and a function $P(\cos\theta)$ of θ, i.e. $\Phi = U(r)P(\cos\theta)/r$ and rewrite Eq. 7.27 as

$$\frac{r^2}{U}\frac{\partial^2 U}{\partial r^2} = -\frac{1}{P\sin\theta}\frac{\partial}{\partial\theta}\left(\sin\theta\frac{\partial P}{\partial\theta}\right) = l(l+1) \tag{7.28}$$

The last equality we find by noting that the first term in Eq. 7.28 depends only on r and the second term only on θ, so that both must be equal to a constant; we write this constant as $l(l+1)$. Solving U from Eq. 7.28 gives

$$U(r) = Ar^{l+1} + Br^{-l} \tag{7.29}$$

with A and B arbitrary constants. The solution of P from Eq. 7.28 is given by the Legendre polynomials, which are finite at the interval $-1 < \cos\theta < 1$ only for integer l. The first three Legendre polynomials are $P_0(\cos\theta) = 1$, $P_1(\cos\theta) = \cos\theta$ and $P_2(\cos\theta) = (3\cos^2\theta - 1)/2$. The normalization of the Legendre polynomials is chosen such that $P_l(0) = 1$ and the polynomials are orthogonal in the sense that

$$\int_{-1}^{+1} P_l(\cos\theta) P_{l'}(\cos\theta) d\cos\theta = \frac{2}{2l+1}\delta_{ll'} \tag{7.30}$$

For the potential Φ we thus have found

$$\Phi = \sum_{l=0}^{\infty} (A_l r^l + B_l r^{-(l+1)}) P_l(\cos\theta) \tag{7.31}$$

If we can determine the constants A_l and B_l along the symmetry axis $\theta = 0$, we can find the potential at arbitrary angle with Eq. 7.31.

As an example consider the potential at position $\vec{r}$ of a single charge at location R_a: $\phi = e_a/|\vec{r} - \vec{R}_a|$. Choosing $\vec{r}$ along the direction $\vec{R}_a$ we may expand $1/|\vec{r} - \vec{R}_a|$ for $|\vec{r}| > |\vec{R}_a|$ as $(1/r)\sum_0^\infty (R_a/r)^l$. For an arbitrary angle γ between $\vec{r}$ and $\vec{R}_a$ we obtain

$$\phi(\vec{r}, \gamma) = \frac{e}{|\vec{r} - \vec{R}_a|} = \frac{1}{r}\sum_0^\infty \left(\frac{R_a}{r}\right)^l P_l(\cos\theta) \tag{7.32}$$

Now enter the charge distribution of Eq. 7.26 into Eq. 7.11, using the expansion Eq. 7.32. Along the magnetic axis $\gamma = \theta$, and the solution is given by

$$\Phi(\vec{r}) = \int \frac{\rho(\vec{R}_a)}{|\vec{R}_a - \vec{r}|} d\vec{R}_a = \sum_{l=0}^{\infty} \frac{m\Omega}{\pi c r^{l+1}} \int_{-1}^{+1} P_2(\cos\theta) P_l(\cos\theta) d\cos\theta \int_o^R 2\pi R^{l-3+2} dR \tag{7.33}$$

The orthogonality of the Legendre polynomials ensures that only the term with $l = 2$ contributes to the summation. Computing this term we get

$$\Phi(\vec{r}, \theta) = -\frac{2m\Omega R^2}{5cr^3} \frac{3\cos^2\theta - 1}{2} \tag{7.34}$$

This is an enormous field! Entering $R = 10\,\mathrm{km}$ and m from $B = 10^{12}\,\mathrm{G}$ we obtain a voltage $\Phi \simeq 10^{15}\,\mathrm{Volt/cm}$. The electric force exerted on a proton is thus 10^9 times stronger than the gravitational force, and on an electron 10^{12} times. The consequence of the strong electric field is that charges are pulled from the neutron star, which enter the magnetosphere. This process continues until the charge density in the magnetosphere becomes high enough to make $\vec{E} \cdot \vec{H}$ equal to zero. Eq. 7.26 tells us that the charge density required to do this is of the order 10^{12} charges per cubic centimeter.

7.4 The radiation loss of a rotating neutron star

We write the current $\vec{J}$ at location $\vec{x}$ as due to the sum of the individual moving charges e_a at locations $\vec{r}_a$:

$$\vec{J}(\vec{x}, t) = \sum_a e_a c\vec{\beta}\delta\left[\vec{x} - \vec{r}_a(t)\right] \tag{7.35}$$

where $\vec{\beta} \equiv \vec{v}/c$. For this current, eqs. 7.11, 7.12 can be solved, via the use of Green's function. We omit the mathematics involved in this, and give the solutions for $\vec{E}$ and $\vec{H}$ directly, for one point charge:

$$\vec{E}(\vec{x},t) = e\left[\frac{(\vec{n}-\vec{\beta})(1-\beta^2)}{\kappa^3 R^2}\right]_{ret} + \frac{e}{c}\left[\frac{\vec{n}}{\kappa^3 R} \times \{(\vec{n}-\vec{\beta}) \times \dot{\vec{\beta}}\}\right]_{ret} \tag{7.36}$$

and

$$\vec{H} = \vec{n} \times \vec{E} \tag{7.37}$$

In these equations we use the definitions $\vec{R}(t) \equiv \vec{x} - \vec{r}(t)$, $R \equiv |\vec{R}|$, $\vec{n} \equiv \vec{R}/R$ and $\kappa \equiv 1 - \vec{n} \cdot \vec{\beta}$. The subscript ret indicates that the term between brackets must be evaluated at the retarded time $t' = t - R(t')/c$.

An important result follows from Eq. 7.37: the magnetic field is perpendicular to the electric field, and has the same magnitude. This enables us to write the Poynting flux as

$$\vec{S} \equiv \frac{c}{4\pi}\vec{E} \times \vec{H} = \frac{c}{4\pi}|\vec{E}^2| = \frac{c}{4\pi}|\vec{H}^2| = \frac{c}{8\pi}(|\vec{E}^2| + |\vec{H}^2|) \tag{7.38}$$

This equation explains our interpretation of the third term in Eq. 7.3 as the flow of energy through the volume surface. We consider the Poynting flux of a sum of accelerated particles in some more detail. At large distances, the second term in Eq. 7.36 dominates. Expanding this term to orders of $\beta \equiv v/c$, we write

$$\vec{E} = \sum \frac{e_a}{cR}\left[\vec{n} \times (\vec{n} \times \dot{\vec{\beta}}) - \vec{n} \times (\vec{\beta} \times \dot{\vec{\beta}}) + 3(\vec{n} \cdot \vec{\beta})\vec{n} \times (\vec{n} \times \dot{\vec{\beta}})\right] \tag{7.39}$$

We rewrite this in terms of the electric and magnetic dipoles defined above, and of the quadrupole moment defined as $D_{ij} \equiv \sum e_a(3r_i r_j - \delta_{ij} r^2)$. We find

$$\vec{E} = \frac{1}{c^2 R}\left[\vec{n} \times (\vec{n} \times \ddot{\vec{d}}) - \vec{n} \times \ddot{\vec{m}} + \frac{1}{6c}\vec{n} \times (\vec{n} \times \dddot{\vec{D}})\right] \tag{7.40}$$

With Eq. 7.38 we see that the radiation of a system of accelerated charges is dominated by the electric dipole radiation. We obtain the radiated power by integrating the Poynting flux over a sphere with radius R. For an angle θ between $\vec{n}$ and $\ddot{\vec{d}}$ we have

$$P_d = \int_0^{\pi}\int_0^{2\pi} |\ddot{\vec{d}}|^2 \sin^2\theta R^2 \sin\theta d\theta d\phi = \frac{2}{3c^3}|\ddot{\vec{d}}|^2 \tag{7.41}$$

When the (second derivative of the) electric dipole moment is zero, the most important radiation term is given by the second derivative of the magnetic dipole:

$$P_m = \int_0^{\pi}\int_0^{2\pi} |\ddot{\vec{m}}|^2 \sin^2\theta R^2 \sin\theta d\theta d\phi = \frac{2}{3c^3}|\ddot{\vec{m}}|^2 \tag{7.42}$$

The next important term is that of the quadrupole radiation, and keeping more terms in the expansion of R gives rise to even higher order terms.

Denoting the angle between the rotation and magnetic axes with α we can write the magnetic moment of a rotating neutron star in the nonrotating coordinate frame as

$$\vec{m} = BR^3\left(\vec{e}_{\parallel}\cos\alpha + \vec{e}_{\perp}\sin\alpha\cos\Omega t + \vec{e}_{\perp}\sin\alpha\sin\Omega t\right) \tag{7.43}$$

where R now is the radius of the neutron star, and $\vec{e}_{\parallel}$ and $\vec{e}_{\perp}$ are unit vectors in the nonrotating coordinate frame along the dipole momnet and perpendicular to it. The energy loss of a rotating neutron star with a dipole magnetic field is obtained by entering Eq. 7.43 into Eq. 7.42 and we then obtain:

$$P_m = -\frac{2B^2R^6\Omega^4 \sin^2\alpha}{3c^3} \tag{7.44}$$

Chapter 8

Accretion

The energy emitted by many sources that emit high-energy radiation directly or indirectly derives from accretion of matter onto a compact object. In this chapter we derive some basic properties of accretion. Before doing so we recapitulate some physics that we need in describing accretion processes.

8.1 Recapitulation of some thermodynamics

N.B. Thermodynamci quantities can be (and are!) defined in various ways: per unit of mass, per unit of volume, per particle, etc.... When reading the literature or using equations from others, take care to know which definitions are used. In these lecture notes we use quantities per unit mass.

For the pressure of an ideal gas we have $PV = NkT$, with V the specific volume (= the volume of 1 kg) and N the number of particles per kg. The average weight of 1 particle is usually written μm_p, with m_p the proton mass; for brevity we will write $m \equiv \mu m_p$. Hence

$$PV = \frac{k}{m}T \tag{8.1}$$

and thus

$$PdV + VdP = \frac{k}{m}dT \tag{8.2}$$

Each particle has an energy $0.5fkT$, with f the number of degrees of freedom. For an ideal, one-atomic gas $f = 3$. The internal energy of 1 kg follows

$$\epsilon = \frac{fk}{2m}T \tag{8.3}$$

and since ϵ is a function temperature only, we may write

$$d\epsilon = \frac{d\epsilon}{dT}dT \tag{8.4}$$

When energy $đq$ is added, it may be used to add to the internal energy of the kg or to expand its volume:

$$Tds \equiv đq = d\epsilon + PdV \tag{8.5}$$

where the first equality defines the entropy s.

The last equation allows us to compute the specific heat at constant volume:

$$c_V \equiv \left(\frac{đ\,q}{dT}\right)_V = \frac{d\epsilon}{dT} = \frac{fk}{2m} \tag{8.6}$$

By entering Eqs. 8.2,8.4 into Eq. 8.5 we may write

$$đ\,q = \left(\frac{d\epsilon}{dT} + \frac{k}{m}\right) dT - V dP \tag{8.7}$$

and from this obtain the specific heat at constant pressure

$$C_p \equiv \left(\frac{đ\,q}{dT}\right)_P = \frac{d\epsilon}{dT} + \frac{k}{m} = C_V + \frac{k}{m} \tag{8.8}$$

The ratio fo the two specific heats follows

$$\gamma \equiv \frac{C_P}{C_V} = 1 + \frac{2}{f} \tag{8.9}$$

A change is called adiabatic when no energy is removed or added, i.e. when $đ\,q = 0$. For an adiabatic change, the change in temperature is related to the change in specific volume as

$$\begin{aligned} 0 = d\epsilon + PdV = \frac{d\epsilon}{dT} + \frac{k}{m}\frac{T}{V}dV = C_V dT + (C_P - C_V)\frac{T}{V}dV \\ \Rightarrow \frac{dT}{T} = \left((1 - \frac{C_P}{C_C}\right)\frac{dV}{V} \Rightarrow T = \text{const}C^{1-\gamma} \end{aligned} \tag{8.10}$$

Once more using the equation of state Eq. 8.1 we find

$$P = \text{const}V^{-\gamma} = \text{const}\rho^{\gamma} \qquad \text{and} \qquad T = \text{const}\rho^{\gamma-1} \tag{8.11}$$

Finally defining enthalpy $w \equiv \epsilon + P/\rho$ we may write

$$w = \left(\frac{f}{2} + 1\right)\frac{P}{\rho} = \frac{\gamma}{\gamma - 1}\frac{P}{\rho} \tag{8.12}$$

8.2 Recapitulation of some fluid mechanics

Consider a fluid element which at time t is at location (x, y, z) and has velocity (v_x, v_y, v_z). Some time later, at $t + dt$, the element is at position $(x + v_x dt, y + v_y dt, z + v_z dt)$. To compute the change of a physical quantity of the element, we must take its movement into account:

$$\begin{aligned} \frac{df}{dt} &= \frac{f(x + v_x dt, y + v_y dt, z + v_z dt, t + dt) - f(x, y, z, t)}{dt} \\ &= \frac{\frac{\partial f}{\partial x}v_x dt + \frac{\partial f}{\partial y}v_y dt + \frac{\partial f}{\partial z}v_z dt + \frac{\partial f}{\partial t}dt}{dt} = (\vec{v}\cdot\nabla)\,f + \frac{\partial f}{\partial t} \end{aligned} \tag{8.13}$$

Now consider a **fixed** volume in a flow. Conservation of mass implies that any change in the mass of the volume corresponds to a net in- or outflow of mass through its surface S:

$$\frac{d}{dt}\int_V \rho dV + \int_{dS}(\rho\vec{v})\cdot d\vec{S} = 0 \rightarrow \int_V \left[\frac{\partial\rho}{\partial t} + \nabla\cdot(\rho\vec{v})\right] dV = 0$$

Because this applies to *any* volume, we conclude

$$\frac{\partial \rho}{\partial t} + \nabla \cdot (\rho \vec{v}) = 0 \tag{8.14}$$

A change in velocity of the fluid element, i.e. its acceleration, arises when forces operate, as expressed in the Navier-Stokes equation

$$\frac{d\vec{v}}{dt} = \frac{\partial \vec{v}}{\partial t} + (\vec{v} \cdot \nabla)\vec{v} = -\frac{\nabla P}{\rho} - \nabla \Phi - \frac{\nabla \cdot \vec{\vec{W}}}{\rho} \tag{8.15}$$

Here Φ is the gravitational potential, and W a tensor describing the viscous forces.

Finally, the conservation of energy is described with

$$\rho \left(\frac{\partial \epsilon}{\partial t} + (\vec{v} \cdot \nabla)\epsilon \right) = -P \nabla \cdot \vec{v} - (\vec{\vec{w}} \cdot \nabla) \cdot \vec{v} - \nabla \cdot \vec{q} \tag{8.16}$$

The left hand side gives the change in internal energy ϵ, due to the terms on the right hand side: work by pressure, energy release due to friction, and the net result of energy flow into and out of the unit volume. Examples of energy flows are radiation or conduction, and it is the divergence of such flow that enters the energy equation..

When gravity and viscosity are unimportant, Eq. 8.15 simplifies into the Equation of Euler

$$\frac{\partial \vec{v}}{\partial t} + (\vec{v} \cdot \nabla)\vec{v} = -\frac{\nabla P}{\rho} \tag{8.17}$$

For an adiabatic gas we now derive the Equation of Bernoulli. From Eq. 8.11 we write

$$\frac{\nabla P}{\rho} = \frac{1}{\rho} \nabla (K \rho^\gamma) = \gamma \rho^{\gamma - 2} K \nabla \rho = \gamma \nabla \frac{K}{\gamma - 1} \rho^{\gamma - 1} = \nabla \frac{\gamma}{\gamma - 1} \frac{P}{\rho} \tag{8.18}$$

Substitute this in the equation of Navier-Stokes for the stationary case ($\partial / \partial t = 0$) and without friction, and find

$$(\vec{v} \cdot \nabla)\vec{v} + \nabla \frac{\gamma}{\gamma - 1} \frac{P}{\rho} + \nabla \Phi = 0$$

The derivative along the line of flow is found by taking the inner product of the velocity with the derivative. Thus

$$\vec{v} \cdot \nabla \left(\frac{v^2}{2} + w + \Phi \right) = 0 \quad \Rightarrow \quad \frac{v^2}{2} + w + \Phi = \text{constant along the line of flow} \tag{8.19}$$

A different form of this equation uses the velocity of sound, given by

$$a^2 = \frac{dP}{d\rho} = \gamma \frac{P}{\rho} \tag{8.20}$$

and with this we write the law of Bernoulli as

$$\frac{v^2}{2} + \frac{a^2}{\gamma - 1} + \Phi = \text{constant along the line of flow} \tag{8.21}$$

8.3 Diffusion by particles

In a gas in which a quantity G carried by the particles varies with location, the differences are gradually removed by the random motion of the particles. We derive a general diffusion equation and then give some applications. We choose the z-axis along the gradient in G. Consider a particle that first moves along the free path length l in a direction with angle θ to the z-axis, and then collides with another particle. At the point of collision the difference in G with respect to its surrroundings is $dG = l\cos\theta(\partial G/\partial z)$. The number of particles moving with velocity v_{th} in direction θ that passes per unit of time through a unit area perpendicular to the z-axis is $(n/4\pi)v_{th}\cos\theta\sin\theta d\theta d\pi$. To find the flux Q of G through the surface we integrate over angles θ and ϕ to obtain

$$Q = \int_0^{\pi}\int_0^{2\pi} l\cos\theta\frac{\partial G}{\partial z}\frac{n}{4\pi}v_{th}\cos\theta\sin\theta d\theta d\phi = \frac{lnv_{th}}{3}\frac{\partial G}{\partial z} \tag{8.22}$$

We have made the simplifying assumption in the last step that the free path length does not depend on velocity.

Some examples:

Heat conduction. Each particle carries an energy $G = \frac{3}{2}kT$ and the general diffusion equation becomes the Equation of Fourier:

$$Q = \frac{lnv_{th}k}{2}\nabla T \tag{8.23}$$

Transfer of momentum: atomic viscosity. Each particle carries momentum mv, hence the diffusion flow of momentum is

$$Q \equiv w = \frac{nlv_{th}m}{3}\nabla v \equiv \nu\nabla v \Rightarrow \nu = \frac{\rho l v_{th}}{3} \tag{8.24}$$

where we use $\rho = nm$ and discriminate between the thermal (random) velocity v_{th} and the large-scale systemic velocity v, and where we have defined the viscosity coefficient ν. If the free path length is determined by collisions between the particles, it may be written $l = 1/(n\sigma)$ with σ the collision cross section. Further entering the thermal velocity $\frac{1}{2}m{v_{th}}^2 = \frac{3}{2}kT$ we obtain for atomic viscosity

$$\nu = \frac{\sqrt{3kmT}}{3\sigma} \simeq 0.03\frac{\mathrm{kg}}{\mathrm{m\,s}}\left(\frac{m}{m_p}\right)^{0.5}\left(\frac{T}{10^7\,\mathrm{K}}\right)^{0.5}\frac{10^{-20}\,\mathrm{m}^2}{\sigma} \tag{8.25}$$

where we scale temperature on a typical temperature for an X-ray emitting gas, and the cross section on the rough cross section of a hydrogen atom.

Transfer of momentum: radiative viscosity. If the free path length of the particles is dominated by interacting with radiation, and the photons exchange momentum with the particles, we may approximate $v_{th} = c$ and use the equation defining opacity $l \equiv 1/(\rho\kappa)$. For a sufficiently hot gas the opacity is given by the Thomson cross section σ_T. Hence the viscosity is given by

$$\nu \simeq \frac{c}{3\sigma_T} \tag{8.26}$$

Note that the above equations describe the flow of heat and momentum, and that a net change in heat content (temperature) or momentum arises only via a derivative of the flow, i.e. from a difference between the flow into and the flow out of a volume.

8.4 Scaling equations for accretion

Before we go into detailed descriptions, it is useful to make some rough estimates of what we may expect.

If a mass M with radius R accretes at a rate $\dot{M}$ we expect a bolometric luminosity of about

$$L = \frac{GM\dot{M}}{R} \tag{8.27}$$

This luminosity may be emitted as radiation, and we consider two extreme cases. If the radiation is fully thermalized, and emitted from an area comparable to $4\pi R^2$, we may write

$$L = 4\pi R^2 \sigma {T_{eff}}^4 \tag{8.28}$$

hence with Eq. 8.27

$$\sigma {T_{eff}}^4 = \frac{GM\dot{M}}{4\pi R^3} \tag{8.29}$$

In the other extreme, all the energy gained by one particle goes into a single photon. This gives the maximum energy of that photon:

$$h\nu_{\max} \equiv kT_{\max} = \frac{GMm_p}{R} \tag{8.30}$$

The shortest time scales on which we may expect to see variation are on the order of the rotation period near the surface of the accreting object:

$$\tau = \left(\frac{R^3}{GM}\right)^{0.5} \tag{8.31}$$

Finally we discuss an upper bound to the accretion rate, which arises because the force of the emitted radiation stops more mass from accreting. For simplicity we consider the spherically symmetric case. A photon with energy $\epsilon = h\nu$ has a momentum ϵ/c. Thus, if the photons moving away radially from the accreting source are scattered in an arbitrary direction, the net transfer of momentum per photon is ϵ/c, and thus for a unit surface at radius r together $L/(4\pi r^2 c)$. The cross section for scattering for a sufficiently hot gas is the Thomson cross section $\kappa_T = n_e\sigma_T/\rho$. Thus the maximum accretion luminosity $L_{\rm Edd}$ arises when the momentum transfer from the emitted radiation balances the gravitational force:

$$\frac{L_{\rm Edd}}{4\pi r^2}\frac{\kappa_T}{c} = \frac{GM}{r^2} \Rightarrow L_{\rm Edd} = \frac{4\pi cGM}{\kappa_T} \tag{8.32}$$

and this occurs at an accretion rate $\dot{M}_{\rm Edd}$ given by

$$\dot{M}_{\rm Edd} = \frac{4\pi cR}{\kappa_T} \tag{8.33}$$

The opacity κ is defined per kg; the cross section $\sigma_T = 6.652 \times 10^{-29}\,{\rm m}^2$ is for one electron. Define $\rho \equiv \mu_e n_e m_H$, where m_H is the mass of a hydrogen atom. For pure hydrogen $\mu_e = 1$, for pure helium $\mu_e \simeq 2$, and for a mixture $\mu_e \simeq 2/(1+X)$. Thus

$$\kappa_T = \frac{\sigma_T}{m_H}\frac{1}{\mu_e} = 0.04\frac{1+X}{2}\,{\rm m^2 kg^{-1}}$$

These rough scaling equations may be used to compare systems with accreting black holes, neutron stars, and white dwarfs.

Table 8.1: *Estimated values of properties for accreting compact objects; for κ_T we assume $X = 0.7$.*

		black hole	neutron star	white dwarf
mass	M	$10\,M_\odot$	$1.4\,M_\odot$	$0.6\,M_\odot$
radius	R	30 km	10 km	8600 km
Eq. 8.33	$\dot{M}_{\rm Edd}$(kg/s)	3.3×10^{15}	1.1×10^{15}	9.6×10^{17}
	$(M_\odot\,{\rm yr}^{-1})$	5.3×10^{-8}	1.8×10^{-8}	1.5×10^{-5}
Eq. 8.32	$L_{\rm Edd}$ (W)	1.5×10^{32}	2.1×10^{31}	8.9×10^{30}
Eq. 8.28	$T_{\rm eff}$ (K)	2.2×10^{7}	2.3×10^{7}	6.4×10^{5}
	$kT_{\rm eff}$ (eV)	1900	2000	55
Eq. 8.30	$kT_{\rm max}$ (MeV)	460	190	0.10

8.5 Spherically symmetric accretion

We start with the description of spherically symmetric flows. We assume that gas from the interstellar medium is flowing radially towards a compact object; and we furthermore assume that to first order this flow is adiabatic, i.e. the gas does not radiate energy. For an adiabatic gas we have

$$P \propto \rho^\gamma \quad \Rightarrow \quad \frac{P}{P_\infty} = \left(\frac{\rho}{\rho_\infty}\right)^\gamma; \quad \frac{T}{T_\infty} = \left(\frac{\rho}{\rho_\infty}\right)^{\gamma-1} \tag{8.34}$$

For the speed of sound we get

$$a^2 = \frac{dP}{d\rho} \quad \Rightarrow \quad \frac{a}{a_\infty} = \left(\frac{\rho}{\rho_\infty}\right)^{(\gamma-1)/2} \tag{8.35}$$

The form that Eq. 8.15 takes for a stationary, radially symmetric, friction-less fluid is

$$v_r \frac{dv_r}{dr} = -\frac{1}{\rho}\frac{dP}{dr} - \frac{d\Phi}{dr} \tag{8.36}$$

Using the relation between pressure and density for an adiabatic fluid we integrate this equation and find

$$\frac{1}{2}{v_r}^2 + \frac{a^2}{\gamma-1} - \frac{GM}{r} = \frac{{a_\infty}^2}{\gamma-1} \tag{8.37}$$

We recognize here he Equation of Bernoulli, Eq. 8.21.

Conservation of mass, Eq. 8.14, can be written

$$\dot{M} = 4\pi r^2 \rho v_r = \text{constant} \tag{8.38}$$

We change to dimensionless variables by scaling the gas velocity on the velocity of sound, and the radius on a fiducial radius where the escape velocity would equal the escape velocity:

$$\mu \equiv \frac{v_r}{a}; \qquad x \equiv \frac{r}{r_B} \qquad \text{with } r_B \equiv \frac{GM}{{a_\infty}^2} \tag{8.39}$$

and thus rewrite the equation of motion and the equation of mass conservation

$$\frac{1}{2}\mu^2 + \frac{1}{\gamma-1} = \left(\frac{a_\infty}{a}\right)^2 \left(\frac{1}{2x} + \frac{1}{\gamma-1}\right) \tag{8.40}$$

$$\dot{M} = 4\pi {a_\infty}^2 \rho_\infty {r_B}^2 \left(\frac{a_\infty}{a}\right)^{(\gamma+1)/(\gamma-1)} x^2 \mu \tag{8.41}$$

To analyze these equations we eliminate a/a_∞, and separate the variables μ^2 and x to obtain:

$$f(\mu^2) = Ag(x) \tag{8.42}$$

with

$$f(\mu^2) \equiv \left(\frac{\mu^2}{2} + \frac{1}{\gamma-1}\right)\left(\mu^2\right)^{-(\gamma-1)/(\gamma+1)} \tag{8.43}$$

$$g(x) \equiv \left(\frac{1}{2x} + \frac{1}{\gamma-1}\right) x^{4(\gamma-1)/(\gamma+1)} \tag{8.44}$$

and

$$A \equiv \left(\frac{4\pi\rho_\infty a_\infty {r_B}^2}{\dot{M}}\right)^{2(\gamma-1)/(\gamma+1)} \tag{8.45}$$

The function $f(\mu^2)$ has a minimum at $\mu^2 = 1$ and the function $g(x)$ a maximum at $x = (5-3\gamma)/8$. Solutions for all x ($0 \le x < \infty$)exist only when $A > \min(f)/\max(g)$. Because $\gamma > 1$, the maximum value for $\dot{M}$ corresponds to the smallest value for A, and we find it from $\min(f)$ and $\max(g)$ as

$$\dot{M}_o = \frac{\pi}{4}\rho_\infty a_\infty {r_B}^2 \beta(\gamma) \quad \text{with} \quad \begin{array}{l} \beta = e^{3/2} \text{ for } \gamma = 1 \\ \beta = 2^{3/2} \text{ for } \gamma = 4/3 \\ \beta = 1 \text{ for } \gamma = 5/3 \end{array} \tag{8.46}$$

This value for the accretion rate $\dot{M}_o$ exceeds the value $\dot{M}_f$ for freely falling particles by a factor

$$\frac{\dot{M}_o}{\dot{M}_f} = \left(\frac{v_f}{a_\infty}\right)^3 \frac{\beta(\gamma)}{4} \tag{8.47}$$

Because f is a function of μ^2, the solution is the same for μ and $-\mu$, i.e. for inflow (accretion) and for outflow (e.g. stellar wind)! In Fig. 8.1 we show the solutions of Eq. 8.42 for $1 < \gamma < 5/3$. We may discriminate five classes of solutions:

1. these are solutions with $\dot{M} < \dot{M}_o$ and $\mu < 1$ for all x. It describes subsonic accretion with a low accretion rate. With decreasing radius the Mach number first increases and then decreases. The limiting case $\dot{M} \to 0$ describes an adiabatic atmosphere around the accreting object.

2. the most interesting solution has a monotonically increasing Mach number for decreasing r. The flow becomes supersonic at the critical point $x = x_{\rm cr}$ where $f(\mu)$ has its minimum value and $g(x)$ it maximum value:

$$x = x_{\rm cr} = \frac{5-3\gamma}{8} \tag{8.48}$$

   This is the flow with the maximum accretion rate, given by Eq. 8.47, which is determined by the sound velocity of the interstellar medium.

3. This is the solution where the Mach number is increasing monotonically with increasing radius: it is the Parker solution for the supersonic stellar wind.

Figure 8.1: *Solutions of radially symmetric flows (Eq. 8.42) for $\gamma < 5/3$ (left) and for $\gamma = 5/3$ (right)*

4. For these solutions the Mach number is larger than 1 everywhere: this doesn't match the boundary condition for accretion from a gas at rest in infinity. (It also doesn't match a stellar wind starting at the star surface with velocity zero.)

5. These solutions are valid only in limited ranges of x and therefore not physical.

We focus now on the second class of solutions. Far from the sonic point, at $x \ll x_{\rm cr}$, the inflow velocity approaches free-fall velocity

$$v_r = -\sqrt{\frac{2GM}{r}} \tag{8.49}$$

and with the equation of mass conservation this gives the density as

$$\rho = \frac{\dot{M}}{4\pi r^2 v_r} = \frac{\beta(\gamma)}{4}\rho_\infty x^{-3/2} \tag{8.50}$$

The sound velocity and temperature then are

$$\frac{a}{a_\infty} = \left(\frac{\beta(\gamma)}{16}\right)^{(\gamma-1)/2} x^{-3(\gamma-1)/4}; \qquad \frac{T}{T_\infty} = \left(\frac{\beta(\gamma)}{16}\right)^{\gamma-1} x^{-3(\gamma-1)/2} \tag{8.51}$$

As the gas is flowing in, it is compressed and its internal energy changes accordingly:

$$\epsilon_{\rm ad} = -P\frac{dV}{dt} = \frac{P}{\rho^2}\frac{d\rho}{dt} = \frac{P}{\rho}\frac{d\ln\rho}{dr}\frac{dr}{dt} = \frac{k}{0.5m_p} \times (-\frac{3}{2r}) \times \left(-\sqrt{\frac{2GM}{r}}\right) \tag{8.52}$$

8.6 Accretion disks

Gas with angular momentum cannot flow radially towards a central source: in general one may expect it to form a disk perpendicular to the angular-momentum vector. We will use a cylindrical coordinate system r, ϕ, z, with $z = 0$ the central plane of the disk.

8.6.1 The hydrodynamic equations

The disk is symmetric with respect tot this plane. A simple model for a disk through which mass flows towards the center is based on a number of simplifying assumptions:

1. the disk is axisymmetric: $\frac{\partial}{\partial \phi} = 0$
2. the disk is thin: $h/r \ll 1$. This implies that the pressure forces in the disk are much smaller than the gravitational forces: pressure thickens the disk (see Eq. 8.60 below): $P \ll \rho v^2$. It also implies that the vertical velocity, which changes the thickness of a fluid element as it moves inwards (hence $v_z \simeq (h/r)v_r$) is much smaller than the radial velocity: $v_z \ll v_r$.
3. the elements of the viscous force tensor are smaller than the pressure: $w_{ij} \leq P$, hence, from the previous assumption: $w_{ij} \ll \rho v^2$. This implies that the viscous force gives rise to a small radial velocity only (see Eq. 8.56 below): $v_r \ll v_\phi$
4. the disk is stationary

With these assumptions we can write down the lowest order approximations of the hydrodynamical equations. We integrate over the vertical direction, and from here on P, ρ, and T refer to the pressure, density and temperature in the central plane (z=0) of the disk, whereas the half-thickness is defined by

$$\rho \equiv \int_o^\infty \rho(z) dz \tag{8.53}$$

Thus, Eq. 8.14 for conservation of mass becomes

$$\frac{\partial}{\partial r}(r\rho h v_r) = 0 \Rightarrow r\rho h v_r = -\frac{\dot{M}}{4\pi} \tag{8.54}$$

where the constant of integration is chosen such that $\dot{M}$ is the accretion rate. This equation expresses the fact that in a stationary disk all the mass entering it at the outside is transported all the way through to the center.

Eq. 8.15 can be written for the three components separately. The *radial component* becomes

$$v_\phi{}^2 = \frac{GM}{r} \tag{8.55}$$

expressing the fact that for small friction (assumption 3 above) the circular velocity of the gas is (almost) Keplerian.

The *tangential component* becomes

$$r\rho h v_r \frac{\partial}{\partial r}(r v_\phi) = -\frac{\partial}{\partial r}(r^2 W_{r\phi}) \quad \text{with} \quad W_{r\phi} \equiv \int_0^\infty w_{r\phi} dz \tag{8.56}$$

In cylindrical coordinates the tensor vector can be written

$$w_{r\phi} \simeq -\nu \left(\frac{\partial v_\phi}{\partial r} - \frac{v_\phi}{r} \right) \simeq \frac{3}{2} \nu \frac{v_\phi}{r} \tag{8.57}$$

where ν is the dynamic viscosity coefficient, and where the last equality follows with Eq. 8.55. We can integrate this equation using Eq. 8.54 and obtain

$$\frac{\dot{M}}{4\pi} r v_\phi = r^2 W_{r\phi} - \frac{\dot{J}}{4\pi} \tag{8.58}$$

The integration constant $\dot{J}$ represents the angular momentum lost from the disk by the mass flow through the inner radius. It is usually assumed that the torque $W_{r\phi}$ disappears at the inner edge of the accretion disk. Hence, using Eq. 8.55 again,

$$\dot{M} r v_\phi \left(1 - \sqrt{\frac{r_i}{r}}\right) = 4\pi r^2 W_{r\phi} \tag{8.59}$$

For large radii $r \gg r_i$, where the specific angular momentum is large with respect to that at the inner radius of the disk, the correction fact $\sqrt{r_i/r}$ can be ignored.

The *vertical component* becomes

$$P = \frac{1}{2}\rho h^2 \frac{GM}{r^3} \tag{8.60}$$

Finally, conservation of energy may be written

$$Q^- \equiv \int_0^\infty \frac{dq}{dz} dz = Q^+ \equiv -W_{r\phi} r \frac{\partial}{\partial r}\left(\frac{v_\phi}{r}\right) \tag{8.61}$$

where Q^- is the flux emitted at the disk surface, and Q^+ the vertically integrated production of energy due to viscosity. Writing $Q^- = \sigma {T_{\rm eff}}^4$ and using Eq. 8.58 this can be written:

$$\sigma {T_{\rm eff}}^4 = \frac{3GM\dot{M}}{r^3}\left(1 - \sqrt{\frac{r_i}{r}}\right) \tag{8.62}$$

Again, for large radii the correction factor can be omitted.

We have a closer look at the last equation, to stress two important points. *First*, we find that the effective temperature of the accretion disk, as given by Eq. 8.62, does not depend on the viscosity! This seemingly rather strange fact is a consequence of our assumption that the disk is stationary: when a certain amount of $\dot{M}$ is delivered to the outside of the disk, this amount must be transported through the disk. If the viscosity is too small, mass will build up in the disk, and with it presumably the viscosity, until the viscosity is adjusted to produce the required mass flow. If the viscosity is too high, the disk will empty itself onto the central object, and with the drop in density the viscosity drops, again until equilibrium is reached.

Second the effective energy loss from the disk at radius r differs from the loss than one may calculate from the change in total mechanical (kinetic plus potential) energy alone by a factor $3(1 - \sqrt{r_i/r})$. The difference results from the transport of energy in the disk by visous stresses. At radii $r > \frac{9}{4} r_i$, the energy loss $\sigma {T_{\rm eff}}^4$ is larger, at radii $r < \frac{9}{4} r_i$, lower, such that the total energy emitted from the disk is still equal to the total mechanical energy lost by the accreting matter on its way from infinity to the inner radius:

$$2Q^-_{\rm disk} \equiv 2\int_0^\infty 2\pi r Q^+ dr = \frac{GM\dot{M}}{2r_i} \tag{8.63}$$

In order to solve the disk structure these five hydrodynamic equations must be supplemented by three auxilliary equations: the equation of state, an equation for the energy flow Q, and an equation defining the dynamical viscosity coefficient ν, or equivalently the viscous stress tensor.

Most authors use the hydrodynamic equations in their vertically integrated form as given in the table above. The reason for this is that it allows separation of the

radial and vertical structure, and thus the reduction of a two-dimensional problem to two one-dimensional problems. This is paind for, however, by an intrinsic unceertainty in the vertical structure. Once we have chosen the auxilliary equations we can first solve the disk variables as a function of radius, and then go back to the non-integrated equations of vertical hydrostatic equilibrium and cooling to solve the vertical structure.

8.6.2 Auxilliary equations: the Shakura-Sunyaev disk

For the equation of state we may use the version alo used in stellar structure

$$P = \frac{1}{3}aT^4 + \frac{k}{\mu m_p}\rho T \tag{8.64}$$

expressing the total pressure as the sum of radiation pressure P_r and gas pressure P_g.

For the radiative transport equation we start with

$$4\pi\frac{\partial^2 K}{\partial\tau^2} = \frac{1}{\kappa\rho}\frac{\partial q}{\partial z} \tag{8.65}$$

with K the second moment of the intensity and $\tau = \kappa\rho z$ the optical depth. This differs from the usual form of this equation in stellar atmospheres in having a non-zero right-hand side, denoting radiation production per unit optical depth. Approximating $4\pi K = cP_r$ and integrating twice, we find for large optical depth $\tau \gg 1$ and for surface temperature much smaller than central temperature:

$$Q^- = \frac{2}{3}\frac{caT^4}{\kappa\rho h} \tag{8.66}$$

The main contributions to the opacity are expected to come from Thomson scattering (for hot gas) and free-free opacity (for less hot gas):

$$\kappa = 0.40 + 0.66 \times 10^{22}\rho T^{-7/2}\mathrm{m^2 kg^{-1}} \tag{8.67}$$

Different authors use soemwhat different numerical factors in Eq. 8.66, dependent on the assumptions they make on the vertical distribution of density and energy production. These differences do not have much effect on the solution of he radial structure.

The problem arises with the viscosity. From Eqs. 8.56, 8.57 and 8.59 we may write

$$\dot{M}\left(1 - \sqrt{\frac{r_i}{r}}\right) = 6\pi h\nu \tag{8.68}$$

In a typical X-ray binary, the accretion flow may be $\dot{M} = 10^{14}\,\mathrm{kg\,s^{-1}}$ and the height of the disk $h < 10^8\,\mathrm{m}$, leading to $\nu > 10^6\,\mathrm{kg\,s^{-1}\,m^{-1}}$, and this is many, many orders of magnitude larger than ordinary particle viscosity as given by Eq. 8.25.

The clever trick that Shakura and Sunyave (1973) made is to note that the dimension of the viscosity tensor is that of pressure, and to write

$$w_{r\phi} = \alpha P \tag{8.69}$$

where α is a dimensionless constant, whose magnitude depends on the details of the viscous process. One usually takes $\alpha \simeq 0.1 - 1$.

8.6.3 Solving the Shakura-Sunyaev disk equations

To solve the Shakura-Sunyaev disk equations it is useful to simplify their appearance by entering some notations

$$\eta \equiv \left(1 - \sqrt{\frac{r_i}{r}}\right) \qquad \omega^2 = \frac{GM}{r^3}; \qquad \dot{H} \equiv \frac{\dot{M}\eta}{4\pi}$$

The tangential and vertical components Eqs. 8.59, 8.60 may be combined with Eq. 8.69 into

$$\dot{H}\omega = h\alpha P \tag{8.70}$$

$$P = \frac{1}{2}\rho h^2 \omega^2 \tag{8.71}$$

and the equations Eqs. 8.62,8.66 for energy production and energy loss are combined into

$$\frac{3}{2}\dot{H}\omega^2 = \frac{2cP}{\kappa\rho h} \tag{8.72}$$

These three equations are valid for all three regions of the disk.

In the *inner region* the pressure is dominated by the radiation pressure, $P = \frac{1}{3}aT^4$, and the opacity by the Thomson cross section: $\kappa = \sigma_T$. Substituting the pressure Eq. 8.71 into Eq. 8.72 immediately gives the half-height of the disk:

$$h = \frac{3}{2}\frac{\sigma_T}{c}\dot{H} = \frac{3\sigma_T}{8\pi c}\dot{M}\eta \tag{8.73}$$

Two things may be noted here. First: the disk thickness in the inner region does not depend on the viscosity parameter α. Second, comparing Eq. 8.73 with Eq. 8.68 we see that indeed $\nu \propto \sigma_T/c$, as expected. The surface density $\Sigma \equiv 2\rho h$ may be derived by substituting the pressure Eq. 8.71 into Eq. 8.70 and using Eq. 8.73:

$$\Sigma = \frac{2}{\alpha\omega}\left(\frac{2c}{3\sigma_T}\right)^2 \frac{1}{\dot{H}} = \frac{32\pi c^2}{9{\sigma_T}^2}\frac{1}{\alpha\omega\dot{M}\eta} \tag{8.74}$$

The pressure in the $z = 0$ plane may be derived by entering Eqs. 8.74 and 8.73 into Eq. 8.71, and the temperature by subsequently using $P = \frac{1}{3}aT^4$

In the *middle region* of the disk the opacity is still dominated by the Thomson cross section, but the gas pressure dominates over the radiation pressure $P = \frac{k}{m}\rho T$, where we write $\mu m_p \equiv m$. One may now derive:

$$h = \left(\frac{9\sigma_T}{2ca}\right)^{1/10}\left(\frac{2k}{m}\right)^{\frac{2}{5}}\frac{\dot{H}^{1/5}}{\alpha^{1/10}\omega^{7/10}} \tag{8.75}$$

The boundary between the inner and outer regions may be found by equating the disk thicknesses according to Eqs. 8.73,8.75.

8.7 Observations of accretion disks

Accretion diks are observed directly in several classes of binaries: cataclysmic variables, in which a white dware accretes matter from a main-sequence binary companion; and in X-ray binaries, in which a neutron star or black hole accretes matter

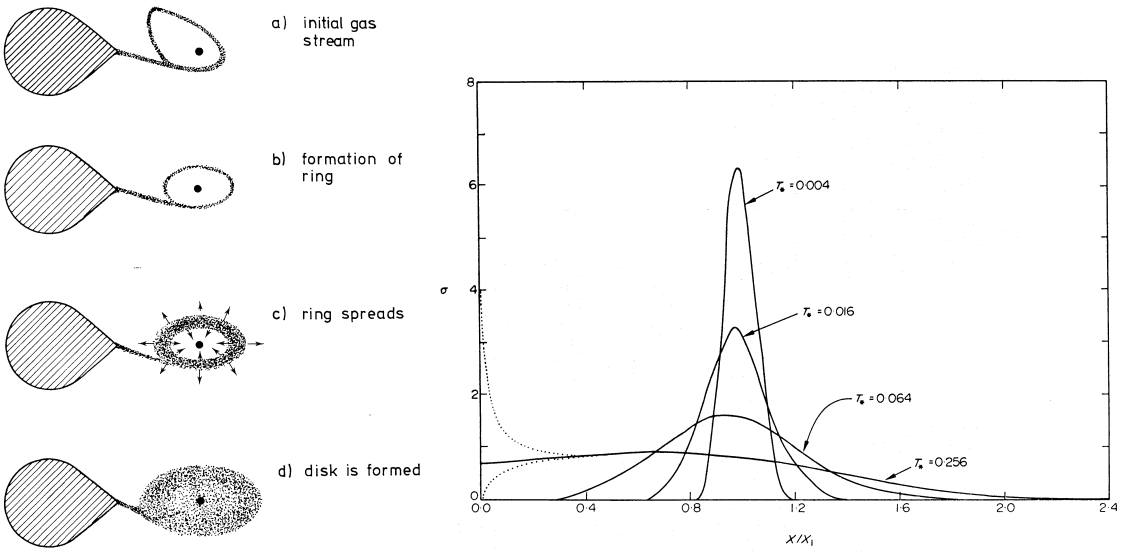

Figure 8.2: *Formation of an accretion disk in a binary according to theory. Left: schematic drawing; right: density vs. radius as a function of time from computer simulation: the rings spreads (from Verbunt 1982 SSR 32, 379;Lynden Bell & Pringle 1974 MNRAS 168, 603).*

from a binary companion. Algol systems, in which a main-sequence star accretes mass from a (sub)giant binary companion sometimes have disks. Because of their larger surface, main-sequence stars are more luminous than white dwarfs, and these more luminous than neutron stars. On the other hand, according to Eq. 8.27 the disk luminosity is higher when the accreting star is smaller. This means that accretion disks dominate the light in cataclysmic variables, but are not very conspicuous in Algol binaries with a disk. In X-ray binaries, the surface of the disk is heated by the high X-ray flux from near the neutron star, and as a result the accretion disk may contribute significantly to the total flux in the optical.

To some extent, a proto-planetary disk can also be described as an accretion disk. The main difference is that such disks are not in equilibrium, mainly becaue – initially at least – the mass in the disk is relatively high (i.e. a much higher fraction of the mass in the central star than in the above-mentioned cases).

Accretion disks are thought to exist in active galactic nuclei, but the evidence for them is indirect. The most convincing evidence is the presence of jets in these systems, which are assumed to flow perpendicularly to the plane of the accretion disk.

8.7.1 Accretion disks in cataclysmic variables

Gas at the surface of one star in a binary also feels the gravitation of the other star. When the surface of one star gets too close to the (center of gravity of the) other star, gas from the surface will start flowing towards that other star. The maximum size that a star can reach before this happens is called the Roche lobe: it scales linearly with the distance between the two stars and it is a function of the mass ratio of the two stars and of the rotation velocity of the stars with respect to the binary revolution. The point from where the mass flows is called the inner Lagrangian point.

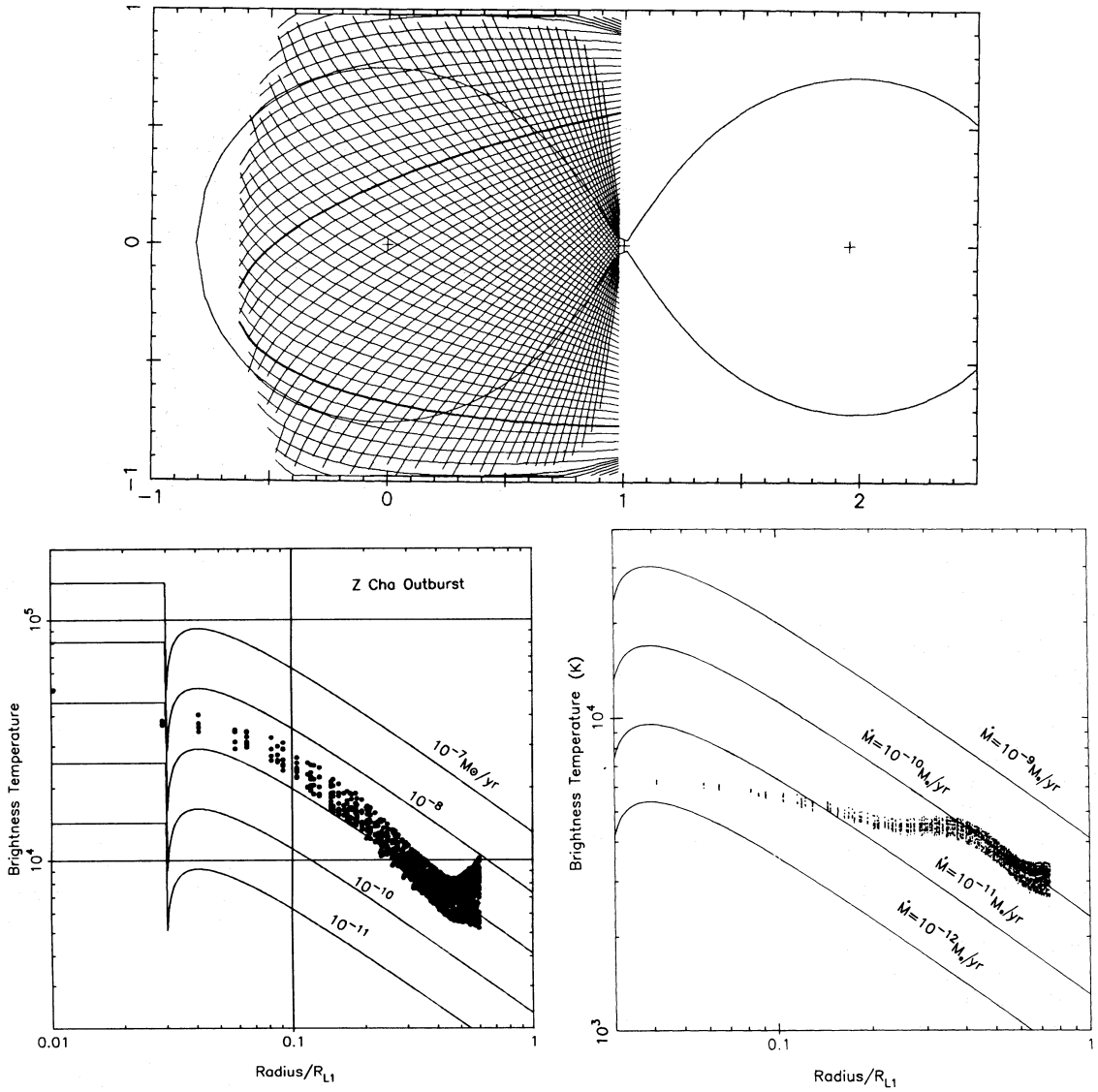

Figure 8.3: *Top: geometry of the disk eclipse: the curved lines on the disk are loci of simultaneous ingress or egress (for given mass ratio and inclination). Below: radial temperature distribution derived from eclipse mapping of the cataclysmic variable Z Cha at maximum (left) and at minimum (right), together with theoretical curves according to Eq. 8.62. From Horne 1985 MNRAS 213, 129; Horne & Cook 1985 MNRAS 214, 307; Wood et al. 1986 MNRAS 219, 629.*

The orbit of the gas initially is close to that of free particles: in the Bernoulli equation (Eq. 8.21) the gas pressure term is negligible with respect to the gravitational potential. The orbital motion gives the gas stream an angular momentum with respect to the mass receiving star, and thus the gas stream reaches a minimum distance to (the center of gravity) of the other star in its flow. If the mass-receiving star is bigger than this minimum distance, the gas hits it directly and probably no disk is formed. If the star is small enough, the gas stream flows around it and hits itself, after which it settles in the radius with the appropriate angular momentum. Viscous forces then may lead to transport of most of the mass inwards, and angular momentum (with a little mass) outwards. This is illustrated in Figure 8.2.

Cataclysmic variables are common, and the nearest systems can be found within

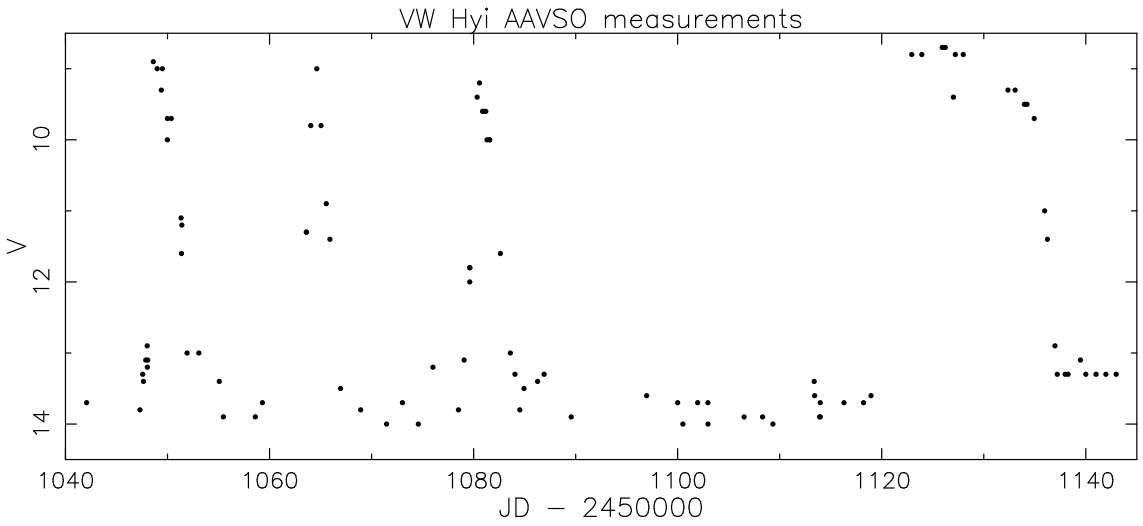

Figure 8.4: *Light curve of the dwarf nova VW Hyi from 1998 Aug 14 to Nov 18, as observed by the* American Association of Variable Star Observers. *Three ordinary outbursts are followed by a super-outburst.*

100 pc. In systems with a sufficiently high inclination the mass donor eclipses the accretion disk every orbit, and thus provides a one-dimensional scan of its surface brightness. By making suitable assumptions, in particular by demanding that the flux distribution of the disk surface is as rotationally symmetric as the data allow, one can construct a map of the surface flux. By doing this at different wavelengths, a temperature map of the disk surface can be made and compared to Eq. 8.62. The method has been developed by Keith Horne and applied by him to a number of cataclysmic variables, one of which is illustrated in Fig. 8.3. The system in question is a dwarf nova, i.e. a cataclysmic variable which occasionally shows outbursts to a higher flux. At outburst maximum, the radial temperature dependence is as expected for a stationary disk, but in quiescence, i.e. at the low flux between outbursts, the temperatures in the inner disk are below the values expected for a stationary disk. The interpretation may be that in quiescence mass stays at the outer region of the disk – until enough mass has built up to set the flow through the disk going.

Important information about the viscosity can be derived from the light curves of dwarf novae: the time scale on which the mass flow through the disk changes is less than a week (Fig. 8.4). We may compare this with the viscous time scale of the radial flow Eq. **??**, where we use the disk solution for the outer region. By entering the size of the accretion disk in dwarf novae, typically of the order of the solar radius, the mass flow rate $\dot{M} \simeq 10^{14}$ kg/s, and mass of the white dwarf $M \simeq 0.5 M_\odot$, we find that $\alpha \sim 1$.

The explanation for the variability of the accretion in cataclysmic variables is thought to be an instability in the accretion disk; or an instability in the transfer of matter from the donor; or a combination of both. The disk instability is related to the details of the solution of the vertical structure, which is thermally unstable in a range of surface densities $\Sigma \equiv \rho h$. If a ring in a disk has such a Σ it will either cool to a lower stable temperature or heat up to a higher stable temperature. For $\alpha = 1$ numerical calculations show that the disk would be split in many rings which are alternately hot and cold. This means that the total flux fluctuates only little. To obtain outbursts as large as observed, one postulates that α in quiescence is an order

of magnitude lower than in outburst: then the whole disk will change from cool to hot and back again, giving rise to large flux variations. This *ad hoc* assumption is a major problem for the disk-instability theory (although the supporters of this model don't seem to mind).

An argument in favour of variable mass transfer from the donor is the observation that cataclysmic variables without a disk – in which the white dwarf has a very strong magnetic field which forces the gas to flow along the field lines and thereby prevents the formation of a disk – also show large variations in luminosity. Also, even the disk-instability supporters admit that superoutbursts are caused by variable mass transfer to the disk. However, there is currently no theory which may explain the variation in the mass flow from the inner lagrangian point.

8.8 Exercises

Exercise 26. Derive the equation for the radius where the effective temperature in an accretion disk reaches its maximum and derive this temperature.

Exercise 27. Derive the equation of the radius where the transition occurs of the inner region to the middle region of the Shakura-Sunyaev disk.

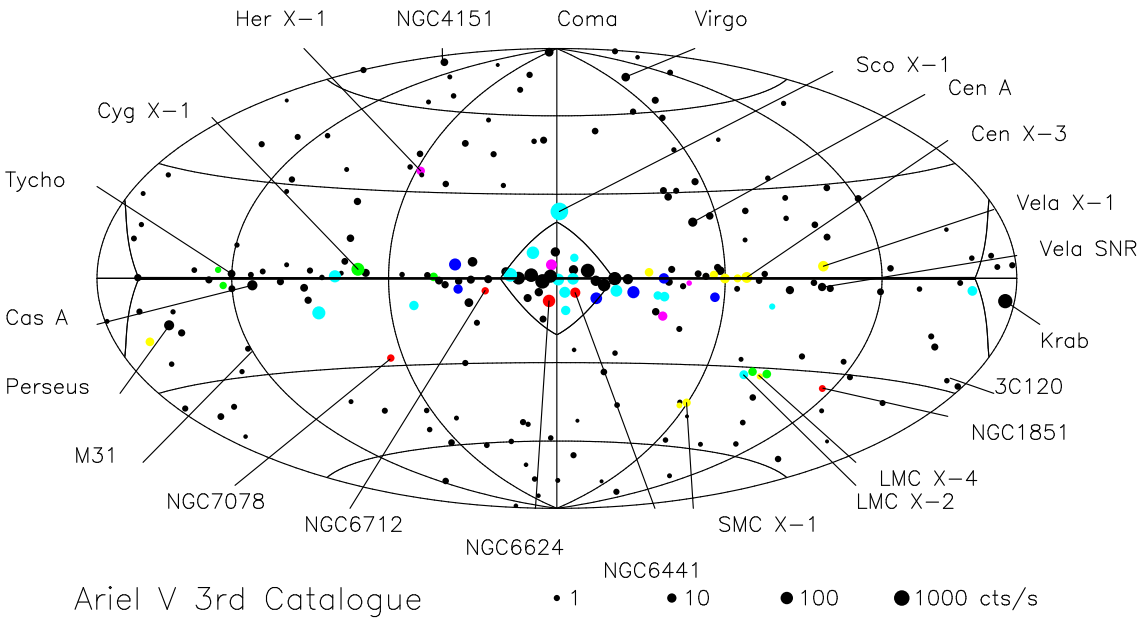

Figure 8.5: *Top: map of the X-ray sky made with the British Ariel V satellite in the 1970s. The central horizontal line is the galactic plane, with the gaalctic center in the middle. Systems with a low-mass donor to a neutron-star accretor are indicated dark blue (bursters), light blue (non-bursting), red (in globular cluster) and purple (pulsars). High-mass systems are indicated yellow (pulsars) and green (black holes). Below: map of the X-ray sky made with the German ROSAT satellite in the 1990s.*

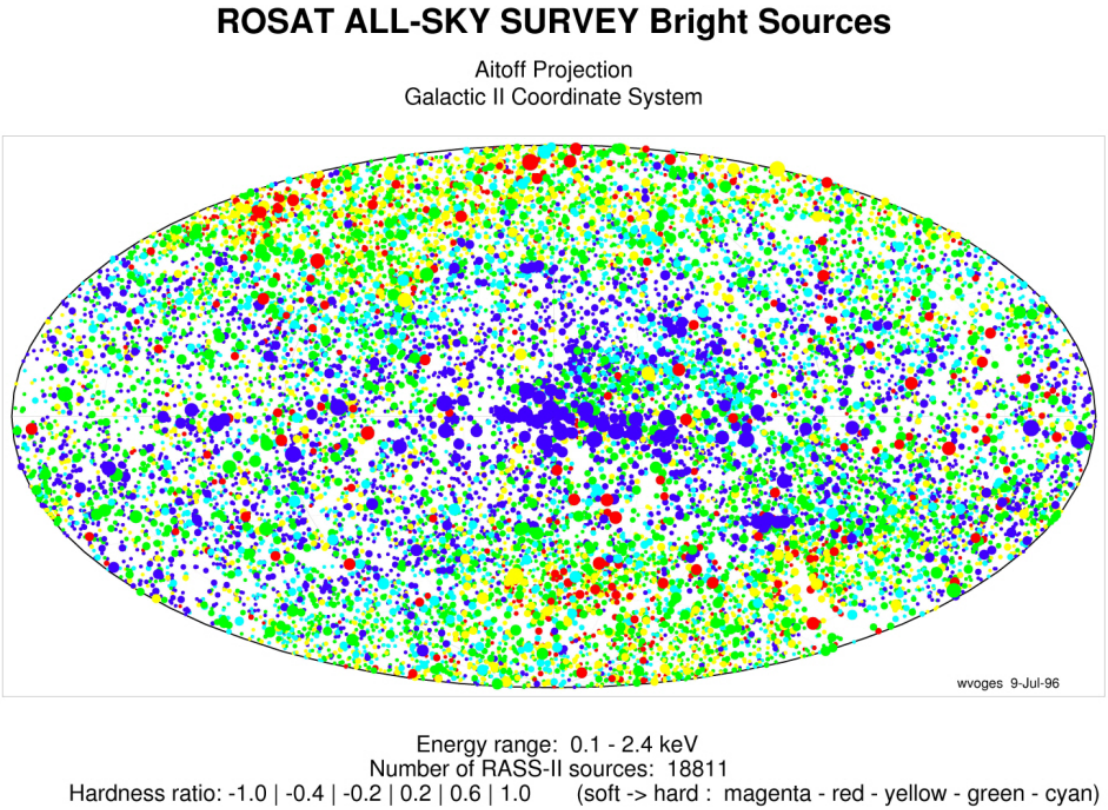

Chapter 9

X-ray binaries

The number of X-ray sources detected in the ROSAT All Sky Survey is 77,549, rather higher than the number of stars one can see with the naked eye. Most of these sources are nearby chromospherically active stars, or black holes in the centers of galaxies far away. If one limits oneself to the brightest sources only, as perforce was the case with the earliest X-ray satellites in the 1970s, one finds that these are concentrated towards the Galactic Plane, and in this towards the Galactic Center (Figure 8.5). Many of these bright sources turn out to be neutron stars or black holes that accrete from an accompanying star. The origin and evolution of these X-ray binaries, and their relation to recycled radio pulsars in binaries, are the subject of this chapter.

9.1 Observations

Investigation of the properties of the brightest X-ray sources soon showed that they can be divided in two clearly separate types (Figure 8.5). Some sources emit their X-rays partially pulsed, others only show irregular variations. Many systems in the latter category occasionally show sudden surges in the X-ray flux: the X-ray bursts.

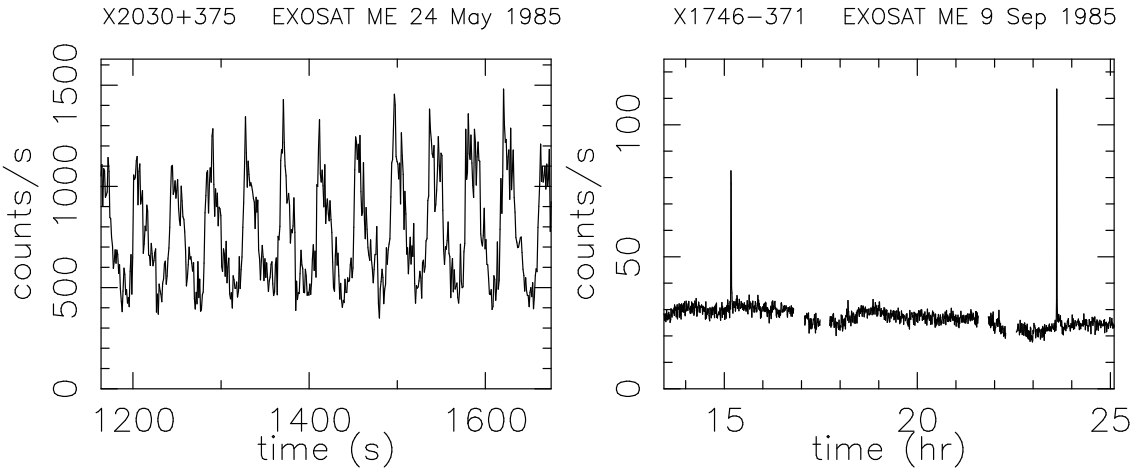

Figure 9.1: *X-ray lightcurves, obtained with EXOSAT, of an X-ray pulsar, EXO 2030+375 (left), and of a burster, X1746-371, with two bursts visible (right).*

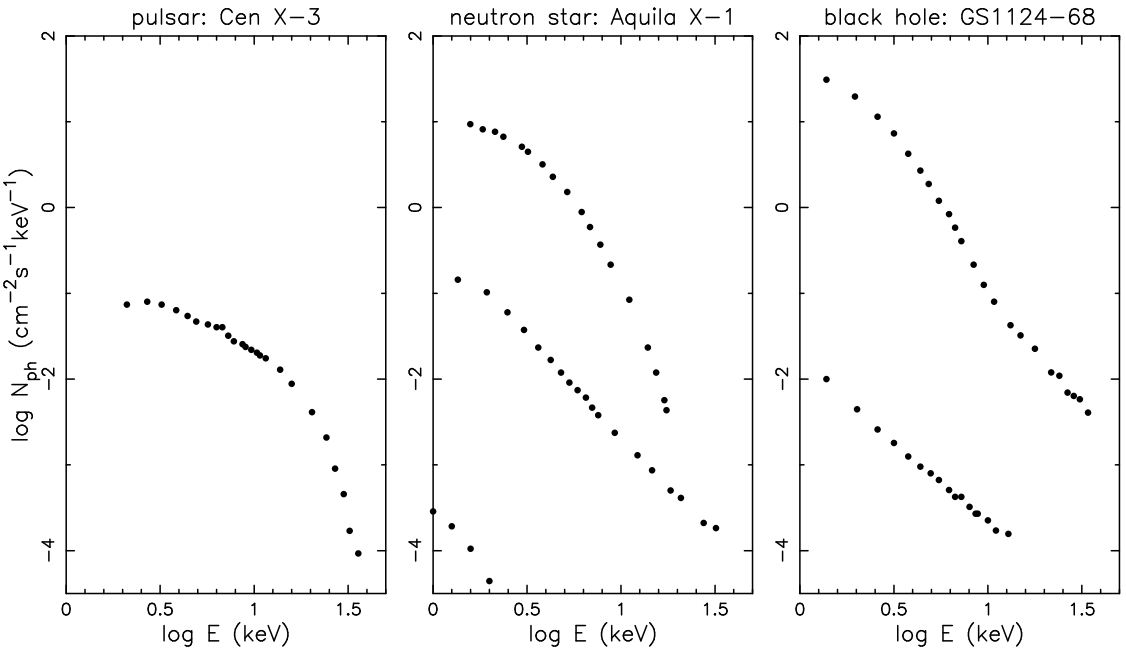

Figure 9.2: *X-ray spectra of an X-ray pulsar (left), an X-ray burster transient (at three different flux levels; middle), and a black hole transient (at two flux levels; right). Shown are the photons number fluxes that would arrive at Earth if there were no interstellar absorption.*

9.1.1 X-ray pulsars: high-mass X-ray binaries

The model for X-ray pulsars is that they are neutron stars with a strong dipolar magnetic field, which focusses the accreting matter to the magnetic poles, where it is stopped and emits X-rays. As the poles rotate in and out of view, we observe pulses of X-rays. The spectra of X-ray pulsars are hard, and photons are detected to energies above 50 keV (Figure 9.2). Signs of the magnetic fields are thought to have been detected in the form of cyclotron absorption lines in the X-ray spectra.

Optical identification was not easy in the early days, as the X-ray pulsars are located in the Galactic Plane, which means that the relatively large positional error boxes are crowded with stars. Nonetheless, many X-ray pulsars were succesfully identified, and their optical counterparts almost invariably are massive O or B stars. The X-ray pulse period varies due to the orbital motion of the neutron star around its companion; when the radial velocity curve of the O or B star can be measured as well, we have a double-lined spectroscopic binary. If in addition the neutron star is eclipsed by its companion, classical binary techniques can be employed to determine the masses of both stars. The neutron star masses cluster around 1.4 $M_\odot$, as expected from theory.

Some X-ray sources with an O or B companion star do not show pulses. The X-ray source in these may still be a neutron star. In some cases, however, which include Cyg X-1 and LMC X-3, the orbital velocity of the O or B supergiant indicates a mass for the compact star in excess of the maximum mass that is possible for a neutron star, and it is concluded that the compact star must be a black hole. The X-ray spectra of these black hole candidates contain more photons both at low energies ($< 1\,\mathrm{keV}$) and at high energies (up to $> 100\,\mathrm{keV}$) than the pulsar spectra.

The mass determinations are feasible in the systems with relatively short orbital

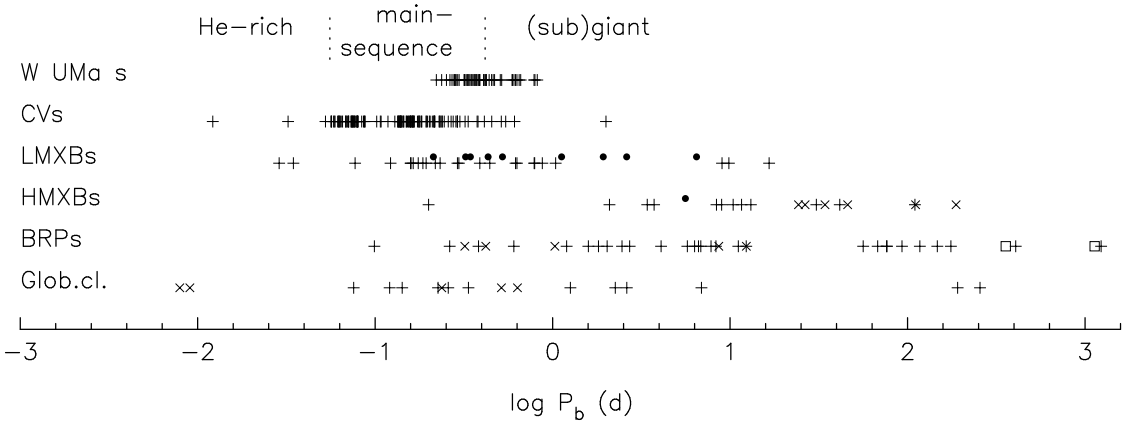

Figure 9.3: *Orbital periods of X-ray binaries and binary radio pulsars in our Galaxy, and, for comparison, cataclysmic variables and contact binaries (also called W UMa binaries). Each symbol indicates one system. For the X-ray binaries • indicates a system with a black hole, and × a Be donor star. For the binary radio pulsars + indicates a system with a low-mass white dwarf companion, × a system with a high-mass white dwarf or neutron star companion, and □ a main-sequence companion. For globular clusters a × indicates an X-ray binary, a + a radio pulsar binary.*

periods, $P_b \lesssim 10\,\mathrm{d}$, in which the companion of the neutron star is an O or B supergiant. Many systems have rather longer orbital periods, up to more than a year. In these, the companion is usually a Be star, i.e. a rapidly rotating B star, and the X-ray emission is only detected occasionally. Taking selection effects against detection of such transient hard X-ray sources into account, we conclude that the Be-star + X-ray-pulsar binaries are in fact much more common (a few thousand in the Galaxy) than the supergiant + X-ray-pulsar systems (a dozen in the Galaxy). For both types of systems we find that the X-ray luminosity emitted near the neutron star is of the order of the optical luminosity of the O or B star.

The pulse periods of all X-ray pulsars vary, on time scales ranging from $P/\dot{P} \simeq 100\,\mathrm{yr}$ to $10^6\mathrm{yr}$. These short time scales indicate that the moment of inertia, and hence the radius, of these objects are very small, in agreement with the theoretical estimates for neutron-star radii of $\sim 10\,\mathrm{km}$.

Finally, it is somewhat of a surprise that many of the first detected X-ray pulsars are located in one spiral arm, Carina, close to the Sun, even though their brightness ought to make them detectable, even with early X-ray satellites, throughout our Galaxy. With the GINGA satellite Be X-ray transients have been detected also in spiral arms closer to the Galactic Center.

9.1.2 X-ray bursters: low-mass X-ray binaries

Soon after the discovery of the X-ray bursts, it was realized that these are caused by the sudden fusion into carbon of a helium layer on a neutron star, deposited there by the accretion of hydrogen which fuses immediately into helium. Thus, a burst is the neutron-star analogue of a nova outburst for a white dwarf. The X-ray spectra of the X-ray bursts have characteristic temperatures of $kT \lesssim 5\,\mathrm{keV}$.

The steady X-ray spectrum of the luminous burst sources is soft; less luminous sources have power-law spectra. The spectra of sources of variable luminosity change

Table 9.1: *Name, position, pulse period, X-ray luminosity, orbital period and eccentricity, and (for high-mass systems) the spectral type of the donor, for representative X-ray binaries. Binaries containing a black hole, and transients are indicated with B and T, respectively. For transients, the luminosity is the luminosity at outburst maximum. It should be noted that luminosities are uncertain due to uncertain distances for many sources.*

Selected X-ray binaries

name	position	P (s)	logL_x (erg/s)	P_b (d)	e	sp.type
high-mass X-ray binaries						
LMC X-4	$0532-66$	13.5	38.6	1.4	0.011	O7III
LMC X-3	$0538-64$	-	B38.5	1.7	$\sim$0	BIII-IV
Cen X-3	$1119-60$	4.8	37.9	2.1	0.0007	O6.5II
SMC X-1	$0115-74$	0.7	38.8	3.9	$<$0.0008	B0I
Cyg X-1	$1956+35$	-	B37.3	5.6	$\sim$0	O9.7I
Vela X-1	$0900-40$	283	36.8	9.0	0.092	B0.5I
LMC tran	$0535-67$	.069	T39.0	16.7	$\sim$0.7	B2IV
V635 Cas	$0115+63$	3.6	T36.9	24.3	0.34	Be
BQ Cam	$0331+53$	4.4	T35.8	34.3	0.31	Be
GX301-2	$1223-62$	696	37.0	41.5	0.47	B1-1.5
V725 Tau	$0535+26$	104	T37.3	111.0	0.3-0.4	Be
low-mass X-ray binaries						
KZ TrA	$1627-67$	7.7	36.8	0.029		
V1405 Aql	$1916-05$		36.9	0.035		
UY Vol	$0748-68$		T37.0	0.159		
V4134 Sgr	$1755-34$		36.8	0.186		
V616 Mon	$0620-00$		BT38.3	0.323		
N Mus 1991	$1124-68$		BT37.6	0.427		
Cen X-4	$1455-31$		T38.0	0.629		
Sco X-1	$1617-16$		37.5	0.787		
V404 Cyg	$2023+33$		BT38.4	6.500		
Cyg X-2	$2142+38$		38.0	9.843		
peculiar systems						
Her X-1	$1656+35$	1.2	36.8	1.7	<0.0003	A9-B
Cyg X-3	$2030+41$		38.0	0.2		WN
Cir X-1	$1516-57$		T38.9	16.6		
SS433	$1909+05$		35.8	13.2		
bursting pulsar	$1744-28$	0.467	T38.9	11.8		accretion bursts
bursting pulsar	$1808-36$	0.0025	T36.8	0.084		thermonuclear bursts

accordingly (Figure 9.2).

Orbital periods for X-ray sources without pulses could be determined in larger numbers only after the launch of EXOSAT, whose wide orbit allowed four days of uninterrupted observing, and after the introduction of CCD photometry, which is capable of detecting small flux variations accurately. The orbital periods span the same range as those of the cataclysmic variables, which by analogy is taken to suggest that the companion to the neutron star is a low-mass star, close to the main sequence. These X-ray sources are therefore called low-mass X-ray binaries. Direct measurements of the properties of the donor star are hard to obtain, because

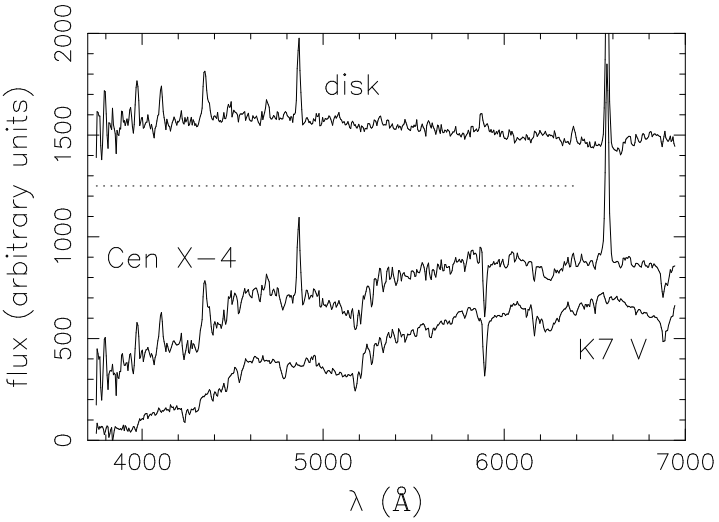

Figure 9.4: *The quiescent optical spectrum of Cen X-4 and the spectrum of a K7 V star. The Cen X-4 spectrum shows features of the K7 V spectrum. Subtraction of the K7 V stellar spectrum from that of Cen X-4 leaves a spectrum which is featureless apart from Balmer emission lines. This spectrum is shown also (shifted for clarity, its zero level indicated with the dotted line).*

the optical luminosity is dominated by reprocessing into the optical of X-rays that impinge on the accretion disk around the neutron star. The optical luminosity of these systems is much less than the X-ray luminosity, $L_{\rm opt} \lesssim 0.01 L_{\rm x}$, say. Even though the low-mass X-ray binaries often are well away from the Galactic Plane, with $|z| \simeq 1\,$kpc, their low visual brightness impedes easy optical identification.

The thick accretion disk also is responsible for the paucity of eclipsing low-mass X-ray binaries: when the inclination is high enough for the neutron star to be eclipsed by its companion, the probability is high that it is hidden altogether by the accretion disk.

Some low-mass X-ray binaries are transient sources. In these, the optical flux from the disk disappears with the X-ray flux, and the companion becomes optically detectable. The radial velocity curve of the companion can then be measured. The companions in transients indeed appear to be low-mass stars (Figure 9.4). In an increasing number of such transients the mass function indicates that the compact accreting star is a black hole. The X-ray spectra of transients with a black hole are remarkably similar to those of transients with a neutron star; the difference being that at the brightest levels they have (relatively) more soft as well as more hard photons (Figure 9.2). The case of Cyg X-3 (see chapter 9.1.4) illustrates that the assumption of a low-mass donor remains insecure for most of the low-mass X-ray binaries.

9.1.3 Relation with recycled radio pulsars

In the last decade, an increasing number of radio pulsars have been discovered in binaries. Two of these pulsars have a companion which is a massive O or B star. Most of the others have a companion believed to be a neutron star or a white dwarf. The pulsars in these other binaries are called recycled radio pulsars, and are generally characterized by short pulse periods, $P \gtrsim 1.5\,$ms, and very low period derivatives, $P/\dot{P} \gtrsim 10^8$yr, as compared to the pulse periods and period derivatives of ordinary radio pulsars, which have $P \sim 1\,$s and $P/\dot{P} \lesssim 10^7$yr.

The pulse periods of binary radio pulsars vary with the orbital motion, which provides an indication of the mass of its companion. In three close binaries with two neutron stars, and one binary with a white dwarf and a neutron star, general relativistic effects allow accurate mass determinations. In some binaries, the com-

Table 9.2: *Position, pulse period, characteristic age ($\tau_c \equiv P/(2\dot{P})$, magnetic field strength, orbital period and eccentricity, and companion mass, for representative radio pulsar binaries. The companion masses marked $*$ were calculated for an assumed inclination of* $60°$.

Selected binary radio pulsars

position	P (ms)	$\log\tau_c$ (yr)	$\log B$ (G)	P_b (d)	e	M_c ($M_\odot$)
high-mass binary radio pulsars						
$1534+12$	37.9	8.4	10.0	0.42	0.2737	1.36
$1913+16$	59.0	8.0	10.4	0.32	0.6171	1.39
$0655+64$	195.6	9.7	10.1	1.03	<0.00005	>0.7
$2303+46$	1066.4	7.5	11.9	12.34	0.6584	1.5
low-mass binary radio pulsars						
$1957+20$	1.6	9.2	8.2	0.38	<0.001	0.02
$1831-00$	521.0	8.8	10.9	1.81	<0.005	0.07^*
$J0437-47$	5.8	8.9	8.9	5.74	0.000018	0.17^*
$1855+09$	5.4	9.7	8.5	12.33	0.000021	0.23
$1953+29$	6.1	9.5	8.6	117.35	0.00033	0.22^*
$0820+02$	864.9	8.1	11.5	1232.40	0.0119	0.23^*
antediluvian[a] radio pulsars						
$1259-63$	47.8			1236.8	0.870	Be
$1820-11$[b]	279.8	6.5	11.8	357.8	0.795	0.8^*
single recycled radio pulsars						
$1937+21$	1.6	8.4	8.6			
$1257+12$[c]	6.2					

[a] *i.e. in an evolutionary stage preceding mass transfer*

[b] *this pulsar is tentatively listed as antediluvian; alternatively, this system may be a high-mass binary radio pulsar*

[c] *this pulsar has three, possibly four planets; see Table* **??**

panion to the recycled pulsar has a mass $M_c \gtrsim 1\ M_\odot$, and – with one exception – these orbits are eccentric. In the other binaries the mass of the companion is lower, $M_c \sim 0.2\ M_\odot$, and the orbits are (almost perfectly) circular (Fig. 9.5). As we will see, the first are thought to have evolved from high-mass X-ray binaries, the latter from low-mass X-ray binaries.

9.1.4 Peculiar systems

Pulsars with low-mass donors. Whereas most X-ray pulsars have O or B star companions, some have low- or intermediate-mass companions. The best known of these is Her X-1, which has a $\simeq 2\ M_\odot$ companion, which is slightly evolved. Its age is therefore in excess of $\simeq 5 \times 10^8$yr, and Her X-1 is an excellent example of an old neutron star with a strong magnetic field. The binary is also striking in being removed from the Galactic Plane, at $|z| \simeq 3\,$kpc. The X-ray pulsar 4U1626-67 has a companion in a $\simeq 40\,$min orbit, whose mass must be less than $0.1\ M_\odot$. For some other pulsars, including 1E2259+59, there is no sign of any companion. It has been suggested that these are single, accreting from a disk; or that they do not accrete, but have very high magnetic fields. This will be discussed in the next chapter.

Radio sources. The X-ray source 3A1909+05, with optical counterpart SS 433,

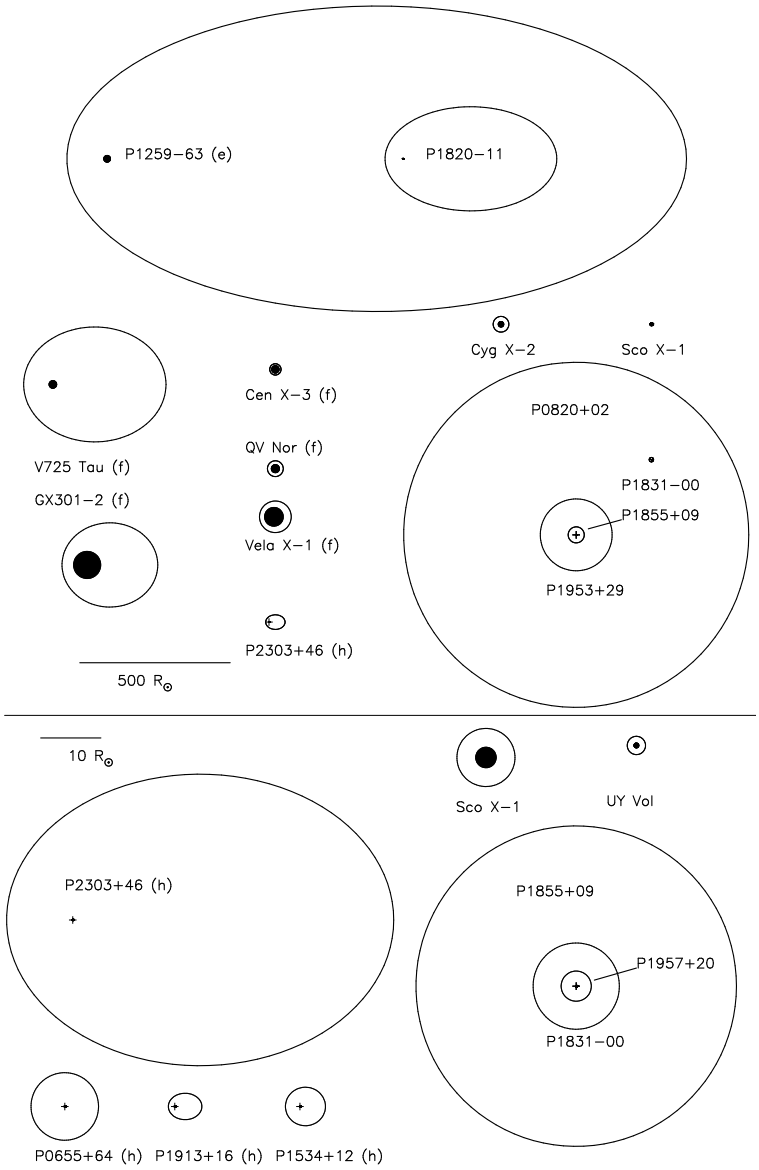

Figure 9.5: *Drawing – to scale – of orbits of binaries with compact stars. An example of a massive binary in which one star has already exploded is PSR1259-63. Once the neutron star captures mass from its companion, it becomes an X-ray source like V725 Tau or GX301−2, which after spiral-in may form a binary with a recycled radio pulsar accompanied by a massive white dwarf (PSR0655+64) or after a second supernova by a second neutron star (PSR1913+16). PSR1820−11 may have a low-mass main-sequence companion, and evolve into a low-mass X-ray binary like Cyg X-2, which in turn may form a binary in which a recycled radio pulsar is accompanied by an undermassive white dwarf (PSR1855+09). (e,f,h): see Figure 9.8.*

is located in a shell of radio emission. The optical and X-ray spectra of this source show emission lines from a jet with velocity $v \simeq 0.26c$, which precesses in about 165 days. The jet is detected directly in Very Long Baseline Interferometry radio observations. It is not clear whether the X-ray source is a neutron star or a black hole. Cyg X-3 has a 4.8 hr orbital period and was classified as a low-mass X-ray binary, until an infrared spectrum was obtained which shows the strong and broad Balmer emission lines characteristic of a Wolf Rayet star. Cyg X-3 has a double

radio jet. Cir X-1 is another X-ray source with a radio jet, and is remarkable for the sudden, extreme surges of the X-ray flux, possibly related to the periastron passage of the donor star.

Very soft X-ray sources. The sensitivity of ROSAT to photons with energies $\lesssim 500\,\mathrm{eV}$ has led to the discovery of a new class of sources that emits only at these low energies. The sources are called supersoft sources. Various types of objects could give rise to such very soft X-ray emission, including white dwarfs that immediately process accreting hydrogen into helium, hot sdO stars in the centers of planetary nebulae, and white dwarfs still hot following a recent nova outburst. Correct luminosity estimates of these sources require the use of stellar atmosphere model spectra.

The first *bursting pulsar* is a very bright transient which shows both pulses and bursts. The bursts are not thermonuclear, but probably due to variation in the accretion onto the neutron star. The second bursting pulsar is also a transient. Its bursts are genuine thermonuclear bursts. Its pulse period is very short, so that we may observe in this system a progenitor of a binary radio pulsar.

9.1.5 Ingredients of binary evolution

To facilitate the discussion of the scenarios for the evolution of X-ray binaries, we first describe some of the important ingredients of these scenarios.

9.1.6 Stellar time scales

Three time scales associated with single stars are important for the study of binary evolution. In order of increasing length these are:

- the pulsational time scale. This is the time scale on which a star counteracts a perturbation of its hydrostatic equilibrium. It is given by the ratio of the radius of the star R and the average sound velocity of the stellar matter c_s:

$$\tau_p = \frac{R}{c_s} \simeq 0.04 \left(\frac{M_\odot}{M}\right)^{1/2} \left(\frac{R}{R_\odot}\right)^{3/2} \mathrm{day} \tag{9.1}$$

- the thermal time scale. This is the time scale on which a star reacts when energy loss and energy production are no longer in equilibrium. It is given by the ratio of the thermal energy content of the star E_{th} and the luminosity L:

$$\tau_{th} = \frac{E_{th}}{L} \simeq 3.1 \times 10^7 \left(\frac{M}{M_\odot}\right)^2 \frac{R_\odot}{R} \frac{L_\odot}{L} \mathrm{yr} \tag{9.2}$$

- the nuclear time scale. This is the time scale on which a star uses its nuclear fuel. It is given by the product of the available fusable matter M_{core} and the fusion energy ϵ_N, divided by the stellar luminosity. For hydrogen fusion, this is:

$$\tau_N = \frac{M_{core}\epsilon_N}{L} \simeq 10^{10} \frac{M}{M_\odot} \frac{L_\odot}{L} \mathrm{yr} \tag{9.3}$$

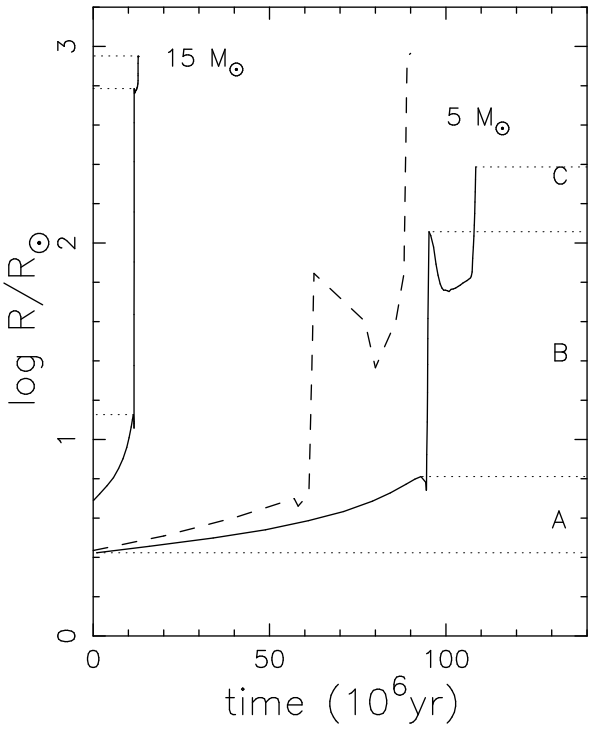

Figure 9.6: *Evolution of the radius of stars of $5\,M_\odot$ and $15\,M_\odot$ until the onset of carbon burning. The solid lines give the results of calculations by Schaller et al. (1992) which include overshooting. For comparison, the dashed line gives radii from calculations by Paczyński (1970) for a 5 $M_\odot$ star that do not include effects of overshooting. The horizontal thin-dashed lines delineate the radius ranges on the main-sequence and on first and second ascent of the giant branch. Mass transfer while a stellar radius is in these ranges are referred to as case A, case B and case C, respectively, as indicated for the $5\,M_\odot$ track.*

In the course of its evolution, a star fuses hydrogen in its core on the nuclear time scale. During this time, on the main sequence, the star does not change its radius very much. On the main-sequence we can use the following mass-radius and mass-luminosity relations in Eqs. 9.1-9.3:

$$\frac{R}{R_\odot} \simeq \left(\frac{M}{M_\odot}\right)^{0.75} \tag{9.4}$$

$$\frac{L}{L_\odot} \simeq \left(\frac{M}{M_\odot}\right)^{3.8} \tag{9.5}$$

After exhaustion of the hydrogen in the core, the star starts expanding, on a thermal time scale.

9.1.7 Roche lobe overlow

A particle within the Roche lobe is attached to one star; a particle on the Roche lobe can move to the other star. Thus, if a star reaches the size of the Roche lobe, mass transfer may ensue. This can occur because the star expands in the course of its evolution, or because the binary shrinks. An evolving star in a binary can fill its Roche lobe for the first time as it expands on the main sequence (Case A), as it expands after hydrogen exhaustion (Case B), or as it expands after helium exhaustion (Case C), see Figure 9.6. Which of the three cases applies, depends on the size of the Roche lobe, which in turn depends on the distance between the two stars and (to a lesser extent) on the mass ratio (see Eqs. 3.33-3.35).

9.1.8 Conservative mass transfer

We illustrate the effects of mass transfer for the *conservative case*, in which both the total mass and the angular momentum of the binary are conserved. In this case, all

mass lost by one binary is gained by the other:

$$M_1 + M_2 = \text{constant} \quad \Rightarrow \quad \dot{M}_1 = -\dot{M}_2 \tag{9.6}$$

The angular momentum of the binary may be written:

$$J_b = M_1 M_2 \sqrt{\frac{Ga}{M_1 + M_2}} \tag{9.7}$$

In Eq. 9.7 it is assumed that the angular momentum residing in the rotation of the two stars, or in the rotation of the accretion disk, is negligible with respect to the angular momentum of the orbital revolution. This assumption is almost always justified. The time derivative of Eq. 9.7 can be written

$$\frac{\dot{a}}{a} = 2\frac{\dot{J}_b}{J_b} - 2\left(1 - \frac{M_2}{M_1}\right)\frac{\dot{M}_2}{M_2} \tag{9.8}$$

Consider first a binary whose angular momentum is conserved: $\dot{J}_b = 0$. Use subscript 2 to label the mass donor, i.e. $\dot{M}_2 < 0$. According to Eq. 9.8, transfer from the more massive star to the less massive star causes a decrease of the distance between the stars: if $M_2 > M_1$, $\dot{a} < 0$. Conversely, transfer from the less massive star causes a to increase.

To see whether the mass exchange is stable one must study the effect of the mass transfer on the stellar radius of the mass-losing star and on the Roche lobe. After the loss of a certain amount of mass, a star adjusts its radius. The star first restores hydrodynamical equilibrium, on a dynamical time scale given by Equation 9.1. This adjustment happens so rapidly, that the change is adiabatic. Next the star tries to adjust its thermal equilibrium, on the thermal time scale given by Equation 9.2. If after exchange of an infinitesimal amount of mass, the donor star becomes larger than its Roche lobe, more mass transfer ensues, causing the donor to become still larger with respect to its Roche radius, etc. The mass transfer is unstable, and runs away. The time scale of the instability is the dynamical time scale if the star exceeds its Roche lobe after restoring hydrodynamical equilibrium. If it only exceeds its Roche lobe after adjusting its thermal structure, the time scale of the instability is given by the thermal time scale.

If mass transfer is stable, it proceeds on the time scale at which the donor star expands, or on which the Roche lobe shrinks. For conservative evolution, the distance between the stars and the orbital period depends on the initial values and on the masses of the two stars only! Denoting the initial values with index i and the values after mass transfer with index f, one finds from combining Eqs. 9.6 and 9.7 (where J_b =constant for the conservative case)

$$\frac{a_f}{a_i} = \left(\frac{M_{1i} M_{2i}}{M_{1f} M_{2f}}\right)^2 \tag{9.9}$$

and with Kepler's law Eq. 3.32

$$\frac{P_{bf}}{P_{bi}} = \left(\frac{M_{1i} M_{2i}}{M_{1f} M_{2f}}\right)^3 \tag{9.10}$$

9.1.9 Nonconservative mass transfer, mass loss in wind

If mass is lost from the binary, the equations become more complicated. Equation 9.6 becomes

$$\dot{M}_1 = -\beta \dot{M}_2 \qquad \text{or} \qquad \dot{M}_1 + \dot{M}_2 = (1-\beta)\dot{M}_2 \tag{9.11}$$

i.e. a fraction β of the mass lost by the donor star is accreted onto its companion, the rest leaves the system. The mass lost from the system will carry angular momentum. If we write the specific angular momentum of the mass that is lost as α times the specific angular momentum of the mass-losing star, we may replace Equation 9.7 with

$$\frac{\dot{J}_{\dot{M}}}{J} = \alpha(1-\beta)\frac{M_1}{M_1+M_2}\frac{\dot{M}_2}{M_2} \tag{9.12}$$

where $\dot{J}_{\dot{M}}$ indicates the loss of angular momentum due to loss of matter. If other loss of angular momentum, e.g. the loss associated with the emission of gravitational radiation, is written as $\dot{J}$, Equation 9.8 may be replaced with

$$\frac{\dot{a}}{a} = 2\frac{\dot{J}}{J} - 2\frac{\dot{M}_2}{M_2}\left(1 - \frac{\beta M_2}{M_1} - \frac{(1-\beta)M_2}{2(M_1+M_2)} - \alpha(1-\beta)\frac{M_1}{M_1+M_2}\right) \tag{9.13}$$

To see the effect of mass loss on the orbit, consider the case where almost all the mass lost by the donor is also lost from the system, $\beta \simeq 0$), and where no loss of angular momentum occurs other than that concomitant with the mass loss. In that case, the orbit will widen provided that $\alpha < 1 + M_2/(2M_1)$. This is the case if the mass lost leaves with specific angular momentum equal to that of the mass-losing star, i.e. if $\alpha = 1$. Equation 9.13 then simplifies into

$$a(M_1 + M_2) = \text{constant} \tag{9.14}$$

9.1.10 Mass loss in a supernova explosion

A neutron star or black hole can be formed from a massive star via a supernova explosion. The envelope of the exploding star is expelled. In a binary the loss of the envelope mass changes the binary parameters. To estimate this effect in a simple way, it is often assumed that the explosion occurs in a circular orbit, is instantaneous, and that the position and velocities of the stars are the same after the explosion as before the explosion. This implies that the distance a_i between the two stars before the explosion is the periastron distance after the explosion

$$a_i = (1-e)a_f \tag{9.15}$$

and that the periastron velocity of the new orbit is the same as the orbital velocity in the pre-supernova orbit:

$$\frac{G(M_1+M_2)}{a_i} = \frac{G(M_1+M_2-\Delta M)}{a_f}\frac{1+e}{1-e} \tag{9.16}$$

Substituting Eq. 9.15 in Eq. 9.16 gives the eccentricity of the post-supernova orbit:

$$e = \frac{\Delta M}{M_1 + M_2 - \Delta M} \tag{9.17}$$

We see that the binary is disrupted ($e > 1$) when more than half of the total mass is lost in the explosion, i.e. when $\Delta M > (M_1 + M_2)/2$.

Because of the mass loss, the velocity of the center of mass of the binary changes by v_s, given by

$$v_s = \frac{M_2 v_2 - (M_1 - \Delta M) v_1}{M_1 + M_2 - \Delta M} = e v_1 \tag{9.18}$$

where v_i is the orbital velocity of the star with mass M_i before the explosion. Massive binaries have small velocities; thus v_s is a good estimate for the system velocity of the binary after the supernova explosion.

If the orbit after the explosion is sufficiently small, it may be circularized by tidal interaction. From conservation of angular momentum, the radius a_c of the circular orbit can be written in terms of the semi-major axis of the eccentric orbit, or of the radius of the pre-supernova orbit

$$a_c = (1 - e^2) a_f = (1 + e) a_i \tag{9.19}$$

In reality, the correctness of the assumptions made to derive Equations (9.15-9.19) is rather doubtful. Wide binaries are expected to have initially eccentric orbits. And from measurements of velocities of single radio pulsars, it appears that a single neutron star may receive an appreciable kick velocity at its birth, of several hundred km/s. It may be expected that a neutron star formed in a binary will also obtain a kick velocity at birth. This velocity can have an arbitrary direction and its effect on the orbit is therefore unpredictable. The presence of kick velocities introduces a major uncertainty in the evolution of a binary in which one star undergoes a supernova explosion.

9.1.11 Supernova explosion in an eccentric orbit

In an eccentric orbit, the relative velocity of the two stars when their distance to one another is r is given by

$$v^2 = G(M_1 + M_2) \left(\frac{2}{r} - \frac{1}{a} \right) \tag{9.20}$$

Denote the supernova progenitor mass with M_1, and the pre-explosion semi-major axis with a, and combine Eq. 9.20 with a similar equation for the post-explosion orbit, with a compact star of mass $M_{1\mathrm{n}}$ and semi-major axis a_n. Assuming that the instantaneous position r is not changed by the explosion, we then may write the ratio a/a_n as

$$\frac{a}{a_\mathrm{n}} = \frac{2a}{r} - \left(\frac{v_\mathrm{n}}{v} \right)^2 \frac{M_1 + M_2}{M_{1\mathrm{n}} + M_2} \left(\frac{2a}{r} - 1 \right) \tag{9.21}$$

where v_n is the relative velocity between the two stars immediately after explosion.

The binary will be disrupted if the right hand side of Eq. 9.21 is zero, which is the case for

$$\frac{r_\mathrm{d}}{2a} = 1 - \left(\frac{v}{v_\mathrm{n}} \right)^2 \frac{M_{1\mathrm{n}} + M_2}{M_1 + M_2} \tag{9.22}$$

r_d must be on the pre-explosion orbit, i.e. $1 - e < r_\mathrm{d}/a < 1 + e$, with e the eccentricity of the pre-explosion orbit. If the value for r_d/a found with Eq. 9.22 is less than $1 - e$, e.g. when virtually no mass is lost, then the binary remains bound

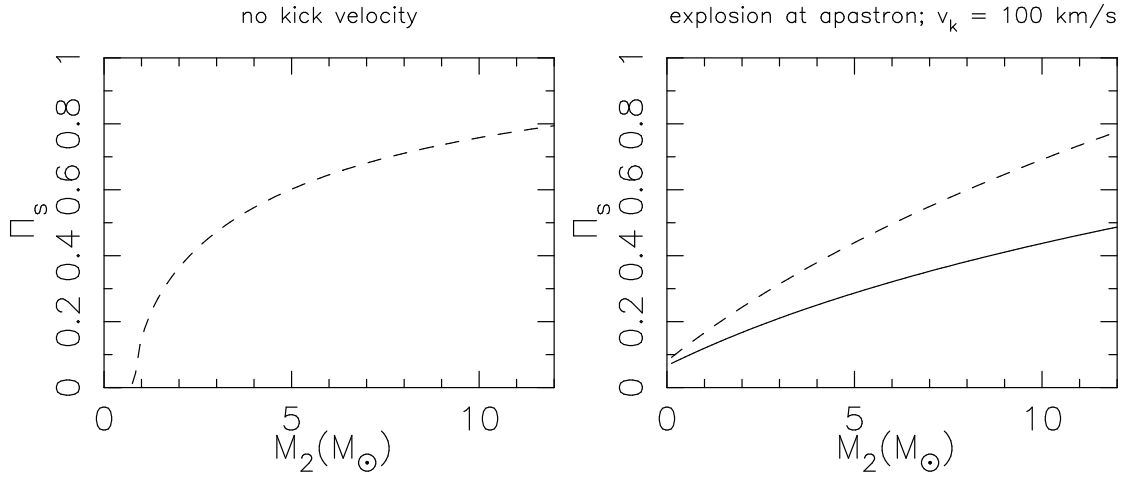

Figure 9.7: *The probability* Π_s*, as a function of the mass* M_2 *of the non-exploding star, that the binary remains bound after a supernova explosion in which a 10* $M_\odot$ *star leaves a 1.34* $M_\odot$ *neutron star. (Left) without kick velocity in an eccentric orbit with* $e = 0.6$*. (Right) for the case in which the neutron star receives a kick velocity of* $v_k = 100$ *km/s in a cicular orbit (solid line) and in an orbit with* $e = 0.6$ *in which the explosion occurs at apastron (dashed line).*

at all pre-explosion radii. If it is larger than $1 + e$, e.g. when virtually all mass is lost, then the binary is disrupted at all radii.

For intermediate values of r_d/a, the binary will be disrupted at all $r < r_d$, and thus the probability that this will happen is given by the fraction of the time that $r < r_d$ in the binary orbit. We calculate this fraction by writing r in terms of the eccentric anomaly $\mathcal{E}$ (see, e.g. R.M. Green, 1985, Spherical Astronomy, p.137 sqq.)

$$r = a(1 - e\cos\mathcal{E}) \tag{9.23}$$

The eccentric anomaly may be related to the mean anomaly $\mathcal{M}$, which progresses linearly with time, via the equation of Kepler

$$\mathcal{M} = \mathcal{E} - e\cos\mathcal{E} \tag{9.24}$$

To calculate the probability that the supernova will dissolve the binary, we start by calculating r_d/a with Eq. 9.22, and check whether $1 - e < r_d/a < 1 + e$. If so, we continue by calculating the eccentric anomaly $\mathcal{E}_d$ corresponding to r_d with Eq. 9.23, and find the probability that the binary will be disrupted as the probability that the two stars are found at an r between periastron and r_d from Eq. 9.24 as

$$\Pi_d = \frac{\mathcal{E}_d - e\cos\mathcal{E}_d}{\pi} \tag{9.25}$$

In Fig. 9.7 the probability of survival, $\Pi_s \equiv 1 - \Pi_d$ is illustrated for a binary with initial semi-major axis of 100 $R_\odot$, in which a 10 $M_\odot$ star explodes to leave a 1.34 $M_\odot$ neutron star, and where the velocity is unchanged: $v_n = v$, as a function of the companion mass M_2. For an initial circular orbit, Eq. 9.23 shows that the binary is always disrupted for $M_2 < M_{2\mathrm{crit}} = 7.32\ M_\odot$, and always remains bound for $M_2 > M_{2\mathrm{crit}}$. For an initial orbit with eccentricity $e = 0.6$, we find that there is a finite probability that the binary survives down to very low companion masses,

or that it is disrupted up to relatively high companion masses. The lowest possible companion mass for which the binary can remain bound is found by equating the pre-explosion velocity at apastron to the escape velocity after the explosion, at the same position:

$$v^2 = \frac{G(M_1 + M_2)(1-e)}{a(1+e)} = \frac{2G(M_{1\rm n} + M_2)}{a(1+e)} \Rightarrow M_2 = \frac{(1-e)M_1 - 2M_{1\rm n}}{1+e} \quad (9.26)$$

For the example shown in Fig. 9.7 this minimum mass is $M_2 = 0.825\ M_\odot$. Thus, in the absence of velocity kicks, even very low-mass stars have a finite probability of surviving the supernova explosion of their companion – after all, in an eccentric orbit more time is spent near apastron than near periastron.

9.1.12 Supernova with velocity kick

The calculations that we just discussed would lead to the conclusion that there could be many wide binaries in which a neutron star is accompanied by a low-mass companion, i.e. many radio pulsars would have an optical counterpart. As this appears not to be the case, we must conclude that most neutron stars acquire a kick velocity $v_{\rm k}$ at birth, which is added to the pre-explosion orbital velocity:

$$v_{\rm n}^2 = v^2 + v_{\rm k}^2 + 2vv_{\rm k}\cos\theta \equiv (1 + f^2 + 2f\cos\theta)v^2 \quad (9.27)$$

where θ is the angle between the kick velocity and the orbital velocity before explosion, and where we have written the kick velocity in units of the pre-explosion velocity, $v_{\rm kick} \equiv fv$. This equation may be entered into Eq. 9.22 to check whether the supernova explosion dissolves the binary in the presence of a kick.

To illustrate the effect of a kick we consider an explosion at apastron. The binary remains bound if the post-explosion velocity is less than the escape velocity:

$$(1 + f^2 + 2f\cos\theta)\frac{G(M_1 + M_2)(1-e)}{a(1+e)} \leq \frac{2G(M_{1\rm n} + M_2)}{a(1+e)} \Rightarrow$$

$$\cos\theta \leq \cos\theta_{\rm crit} \equiv \frac{1}{2f}\left(\frac{2(M_{1\rm n} + M_2)}{(M_1 + M_2)(1-e)} - 1 - f^2\right) \quad (9.28)$$

The probability for this to happen is given by the probability that $\theta \geq \theta_{\rm crit}$, which for arbitrary direction of the kick is given by

$$\Pi_{\rm s} = \left(\int_{\theta_{\rm crit}}^{\pi} \sin\theta d\theta\right) / \left(\int_0^{\pi} \sin\theta d\theta\right) = \frac{1 + \cos\theta_{\rm crit}}{2} \quad (9.29)$$

and may be found directly from Eq. 9.28, as illustrated in Fig. 9.7.

9.1.13 Spiral-in

If a mass donor expands very rapidly, or if the distance between two binary stars decreases very rapidly due to mass transfer (see Eq. 9.8), the companion of the mass-losing star may find itself engulfed by the envelope of the donor. This is thought to happen in particular when the mass transfer is dynamically unstable. The friction between the motion of the companion and the envelope removes angular momentum from the orbital motion, and releases energy. Thus, the orbit shrinks,

and the envelope is brought into rotation and heated. This process continues until enough energy is added to the envelope to expel it. Alternatively, the companion star may spiral-in until it merges with the core of the mass donor.

Consider a star with mass M_1, composed of a core with mass M_c and an envelope of mass M_e, that comes into contact with its Roche lobe at radius R_1, causing its companion with mass M_2 to spiral in. We may compare the binding energy of the envelope with the difference in total energy of the binary before and after the spiral in:

$$\frac{GM_1M_e}{\lambda R_1} = \alpha \left(\frac{GM_cM_2}{2a_f} - \frac{GM_1M_2}{2a_i} \right) \tag{9.30}$$

where λ is a weighting factor for the gravitational binding of the envelope to the core, and a_i and a_f are the distances between the binary stars before and after the spiral-in, respectively.

When $a_f \ll a_i$, as is usually the case when spiral-in occurs, we may ignore the second term on the right hand side of Eq. 9.30, and rewrite the equation as

$$\frac{a_f}{a_i} \simeq \frac{\lambda\alpha}{2} \frac{M_cM_2}{M_eM_1} \frac{R_1}{a_i} \tag{9.31}$$

Because spiral-in start when the star with radius R_1 fills its Roche-lobe, the ratio R_1/a_i is a function of the mass ratio M_1/M_2 only (see Eqs. 3.33-3.35).

The parameter λ can be calculated from a the stellar structure model of the star that fills its Roche lobe, and this can be done with reasonable accuracy. The efficiency parameter α must be calculated from a three-dimensional hydrodynamic calculation of the spiral-in process, and this is not yet possible.

Another approach is to determine α observationally. Central binaries of planetary nebulae are very good objects for such a study, because the 'smoking gun' of the nebula shows that such binaries have only just emerged from a common envelope, i.e. they represent the conditions immediately following the spiral-in. The determination goes as follows. The progenitor of the white dwarf must have had a mass in excess of $0.8\,M_\odot$, in order to have evolved from the main sequence within a Hubble time. The stellar mass is divided between the core and the envelope: if a relatively low-mass core remains as a white dwarf, this means that a relatively massive envelope has been expelled. Applying Eq. 9.30 to systems with a low-mass white dwarf and a main-sequence or other white-dwarf companion shows that $\alpha \simeq 1$. However, if one applies Eq. 9.30 to the binary 14 Aur, which consists of a white dwarf and a δ Scuti star[1], one gets $\alpha = -7$! What this probably means is that the progenitor of the white dwarf had already lost a fair amount of mass – and thereby widened the orbit (see Eq. 9.14) before it filled its Roche lobe.

We really do not understand the details of the spiral-in process, and any calculation involving spiral-in is highly uncertain.

9.1.14 Accretion, magnetosphere and spin-up

Accretion of matter onto a neutron star leads to energy release mainly at X-ray wavelengths. Therefore the X-ray luminosity L_x is related to the accretion rate $\dot{M}$ via Eq. 8.27, with $L \simeq L_x$, and where we take the neutron star mass and radius,

[1] δ Scuti stars are pulsating A or F main-sequence stars; the pulsation mechanism is the κ mechanism in the He II and hydrogen ionization zones

respectively, for M and R. The accretion rate has an upper bound, given by the Eddington limit: if the outward radiation pressure caused by L_x is larger than the gravitational attraction, matter will be blown away rather than accreted. The limiting luminosity is thus given by the condition:

$$\frac{L_{Edd}}{4\pi r^2}\frac{\sigma}{c} = \frac{GM}{r^2} \Rightarrow L_{Edd} = \frac{4\pi cGM}{\sigma} \simeq 1.8 \times 10^{38} \frac{M}{1.4\,M_\odot} \text{erg s}^{-1} \tag{9.32}$$

where σ is the radiation absorption coefficient, for which in the X-ray regime we can use the Thomson cross section. With Eq. 8.27 the luminosity limit can be translated into a limit to the accretion rate:

$$\dot{M}_{Edd} = \frac{4\pi cR}{\sigma} \simeq 1.5 \times 10^{-8} \frac{R}{10^6 \text{cm}}\, M_\odot \text{yr}^{-1} \tag{9.33}$$

An accreting neutron star with a finite magnetic field is surrounded by a volume in which the motion of the accreting matter is dominated by the magnetic forces. Heuristically, a radius r_m of this magnetosphere is estimated by equating the magnetic pressure $B(r_m)^2/8\pi$ of a dipole to a ram pressure ρv^2. For spherical accretion $\rho = \dot{M}/(4\pi r^2 v)$, and with v equal to the free fall velocity this leads to

$$\frac{B^2R^6}{8\pi r_m^6} = \frac{\dot{M}}{4\pi r_m^2}\sqrt{\frac{2GM}{r_m}} \Rightarrow \frac{r_m}{R} = \left(\frac{B^2R^{5/2}}{2\dot{M}\sqrt{2GM}}\right)^{2/7} \tag{9.34}$$

For accretion via an accretion disk, this formula is thought to be a reasonable approximation as well. The interaction between the accretion disk and the neutron star drives the neutron star rotation towards an equilibrium period approximately given by the Keplerian rotation period at the magnetospheric radius. With Eq. 9.34 this gives:

$$P_{eq} = 2\pi \left(\frac{B^2R^6}{2\sqrt{2}\dot{M}}\right)^{3/7} \left(\frac{1}{GM}\right)^{5/7}$$

$$\simeq 6 \times 10^{-3} \text{sec} \left(\frac{B}{10^9 \text{G}}\right)^{6/7} \left(\frac{R}{10^6 \text{cm}}\right)^{18/7} \left(\frac{1.4\,M_\odot}{M_{ns}}\right)^{5/7} \left(\frac{10^{-9}\,M_\odot \text{yr}^{-1}}{\dot{M}}\right)^{3/7} \tag{9.35}$$

It is necessary to remember that Eqs. 9.33-9.35 are heuristic in nature. Our very limited understanding of the accretion process does not enable us to derive rigorous formulae.

9.1.15 Origin and evolution of high-mass X-ray binaries

The observed presence of a neutron star in a binary poses the following problem. According to the theory of stellar evolution, it is always the more massive star in a binary that explodes first as a supernova. According to Eq. 9.17 this means that the binary is disrupted ($e > 1$) by the supernova explosion, unless the masses of the two stars are very close to one another (more specifically: $M > m > M - 2M_{\text{ns}}$, where M_{ns} is the mass of the compact remnant, i.e. the neutron star), One does not expect to find (many) binaries with a neutron star. Two possible solutions have already been discussed above: the supernova can occur at apastron of an eccentric orbit (Eq. 9.26) and the new neutron star may be born with a kick velocity (Eq. 9.28).

More important, however, is yet another solution: that the more massive star becomes the less massive star before it explodes. We discuss three scenarios for this.

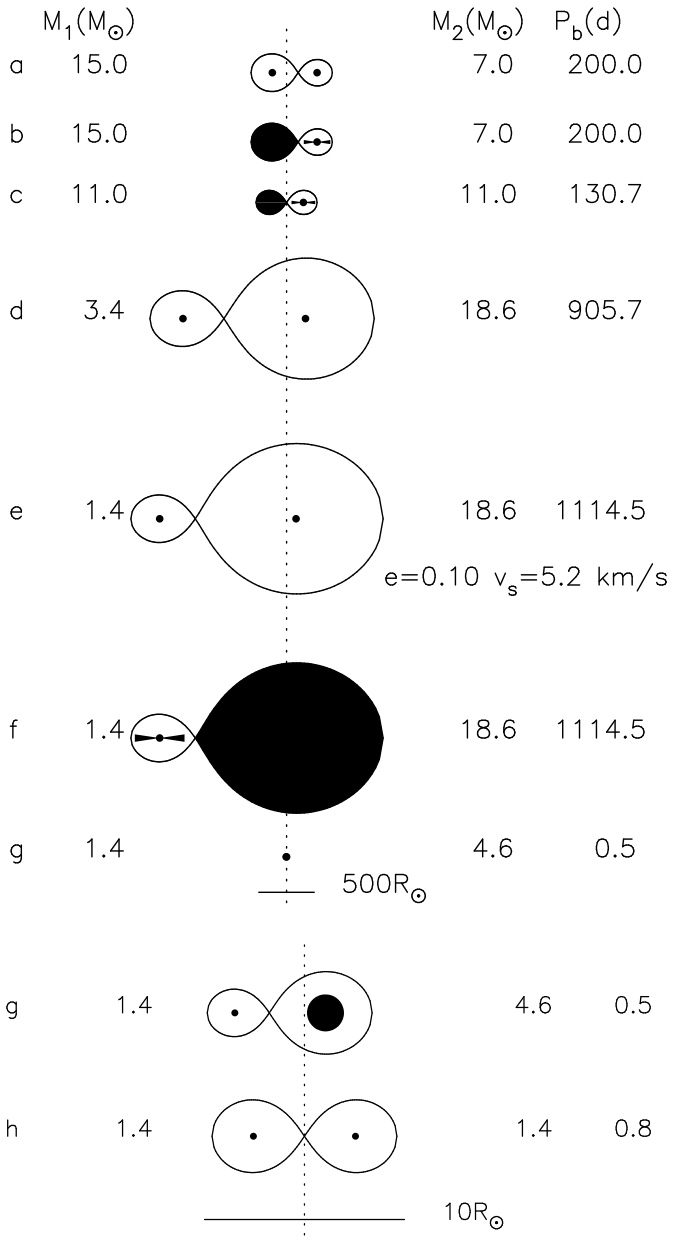

Figure 9.8: *Conservative evolution of high-mass binary into a Be X-ray binary, and then into a binary radio pulsar. For explanation see text. Note the change of scale at phase g.*

9.1.16 Pre-supernova mass transfer and the Be X-ray binaries

Consider a binary of stars of 15 and 7 $M_\odot$, with an orbital period $P_b = 200\,$days. Its evolution is illustrated in Figure 9.8. The 15 $M_\odot$ star evolves first, and exhausts its hydrogen after $3.6 \times 10^6\,$yr, according to Eqs. 9.3-9.5. It then expands into a giant, and while doing so reaches its Roche lobe (Fig 9.8b). In a circular orbit of 200 d, this happens at $R_1 \simeq 180\,R_\odot$, and thus the mass transfer is case B (see Figure 9.6). The expanding star loses mass to its companion through the inner Lagrangian point. A mainly radiative star shrinks dynamically due to mass loss, but expands on the thermal time scale. When the mass donor is the more massive star in the binary, its Roche lobe shrinks (Eqs. 3.35,9.8). Thus mass transfer from a massive, mainly radiative star to a less massive star is unstable on the thermal time scale. The mass transfer therefore occurs on the thermal time scale, $\sim 3 \times 10^4\,$yr for a 15 $M_\odot$ star, according to Eq. 9.2. Mass continues to be transferred until the mass

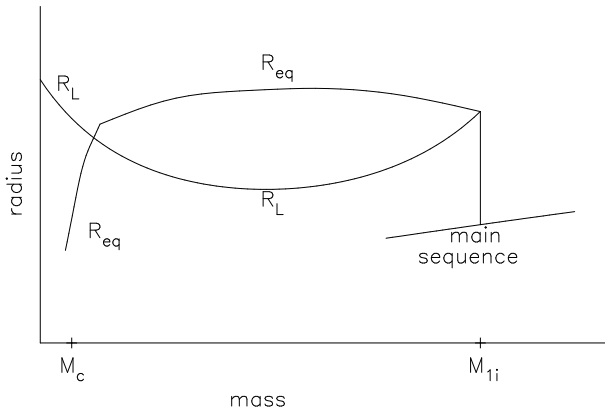

Figure 9.9: *Schematic representation of the change of the radius of the Roche lobe R_L and of the equilibrium radius of a massive mass losing star R_{eq}. Mass transfer begins after the star has expanded from the main sequence to its Roche lobe. Mass transfer is unstable because the Roche lobe shrinks, whereas the equilibrium radius becomes larger. It stays unstable until R_{eq} becomes equal to R_L. This occurs after reversal of the mass ratio, for donor mass close to the core mass M_c.*

receiving star has become more massive than the mass losing star: then the Roche lobe of the donor increases with further mass transfer (Fig 9.8c). Once it increases faster than the donor radius, mass transfer can stabilize again. In practice, mass transfer stabilizes only after the mass donor has lost most of its envelope, and has reached a total mass close to its core mass (Fig 9.8d). The evolution of the stellar and Roche-lobe radii during transfer from a massive star is shown schematically in Figure 9.9. The 7 $M_\odot$ star has gained appreciably in mass, and rotates rapidly, due to the accretion of angular momentum with the mass. The result of the first phase of mass transfer is a binary in which the almost naked core of the initially more massive star is in a wide orbit around an Oe or Be star companion.

The mass M_c of the helium core of a star with initial mass M_1 is found from full stellar evolution calculations, and may be estimated from

$$M_c \simeq 0.073 {M_1}^{1.42} \tag{9.36}$$

The core continues its evolution, and after a short time explodes as a supernova, leaving a neutron star of 1.4 $M_\odot$ (Fig. 9.8e). The sudden mass loss leads to an eccentricity of $e = 0.10$ and a velocity of the center of mass of the new binary of $v_s = 5.2\,\mathrm{km/s}$, according to Eqs. 9.17–9.18. The neutron star may catch matter from the wind of the Be star. Because of the rapid rotation of the Be star, this wind is concentrated in the equatorial plane. The wind of Be star, too, often is transient; thus the binary is often a transient source of hard X-rays.

Overflow via the inner Lagrangian point starts when the companion reaches its Roche lobe (Fig 9.8f). The extreme mass ratio almost certainly causes the mass transfer to be unstable dynamically as the orbit shrinks rapidly (see Eq. 9.8), and the neutron star eventually will plunge into the envelope of its companion. In the case shown in Figure 9.8, the spiral-in leads to a very close binary consisting of the neutron star and the core of the Be star (Fig. 9.8g). If the helium core has too low a mass to evolve into a supernova, it will cool into a white dwarf, and the resulting binary looks like the one in which PSR 0655 + 64 is accompanied by a relatively massive white dwarf. In that case, the orbit retains the circular shape it obtained during spiral-in. Alternatively, continued evolution of the core leads to a second supernova explosion, which may lead to the formation of a high-mass radio pulsar binary like PSR 1913+16, consisting of two neutron stars in an eccentric orbit (Fig. 9.8h); or which may disrupt the binary, especially when the second neutron star is born with a kick velocity.

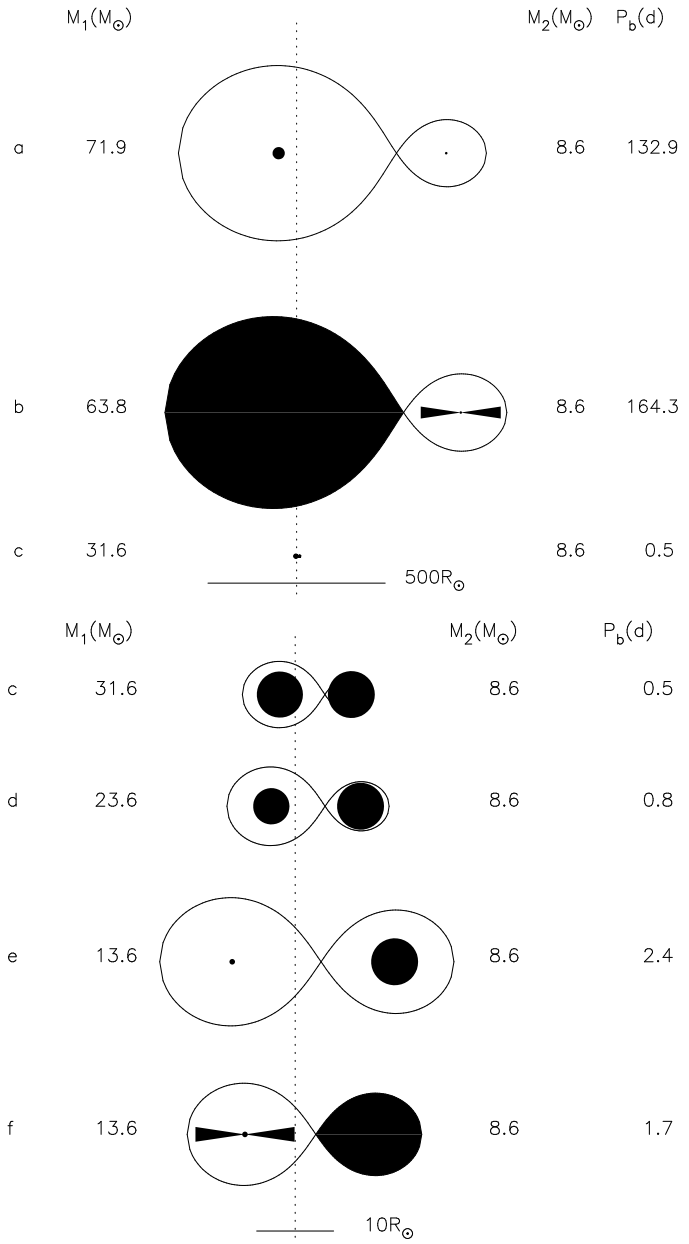

Figure 9.10: *Drawing – to scale – of the evolution of a high-mass binary with a close initial orbit. For explanation see text; note the change in scale at phase c. The 8.6 $M_\odot$ star in phase c only barely fits in its Roche lobe. The final binary is modelled on LMC X-3.*

9.1.17 Pre-supernova spiral-in and the supergiant X-ray binaries

When the initial orbital period is small, the combination of the expansion of the donor and the reduction of the orbital separation may bring the mass receiving star inside the envelope of the donor star. Friction then transfers angular momentum and energy from the orbital motion to the envelope of the mass donor. As a result, the orbit shrinks dramatically, until the envelope is heated so much that it escapes, leaving the core of the donor in orbit around the mass-receiver, or until both stars merge completely. This spiral-in process happens so rapidly, that the mass receiving star accretes only a tiny fraction of the envelope of the donor.

In Figure 9.10 the formation of a high-mass X-ray binary via a spiral-in process is illustrated with a scenario for the formation of the black-hole high-mass X-ray binary LMC X-3. The more massive star of the binary loses some mass in a stellar wind before it fills its Roche lobe. The mass transfer is unstable, and a spiral-in

ensues, bringing the core of the donor in close orbit around the virtually unchanged receiver (see Eq. 9.31; phases b-c in Fig. 9.10). The donor only fits inside its Roche lobe because stars in the LMC, due to their lower metallicity, are smaller at the same mass than stars in our Galaxy. The core loses some more mass in stellar wind as it evolves to supernova, and forms a black hole(Fig. 9.10c-e). It is now thought that all high-mass X-ray binaries with short orbital periods, in which a supergiant is the donor, are formed via a spiral-in or via Case A mass transfer.

9.1.18 Recent developments

Two interesting developments have occurred in our thinking about the formation of high-mass X-ray binaries in recent years. The first of these concerns the evolution of the helium core of a star which has lost its envelope. In early computations of binary evolution it has mostly been assumed that such an unwrapped core evolves pretty much in the same way as it would have done inside the whole star. By computing the evolution of unwrapped cores explicitly several authors have shown that this assumption is not correct. In particular, even the cores of very massive stars, which would have evolved into a black hole inside the full star, evolve into a neutron star instead when the star loses its envelope at an early evolutionary stage. This explains why no Be X-ray binary (formed via case B mass transfer) contains a black hole. An important consequence is that one can no longer transfer conclusions about the progenitor mass of a black hole from single-star evolution to binary evolution or vice versa. The presence of black holes in close binaries can only come about via a spiral-in initiated by case C mass transfer, when the core of the mass-losing star has evolved far enough before it loses its envelope.

The second development is the realization that case A mass transfer may lead to supergiant binaries, which explains that a neutron star can be accompanied by a very massive donor. As a result, one can no longer conclude from the binary Wray 977, in which a $48\,M_\odot$ star transfers mass to a neutron star, that the progenitor of the neutron star had an initial mass higher than $48\,M_\odot$; it may be as low as $25\,M_\odot$. An interesting question regarding the systems arising from case A mass transfer is whether the mass donor to the compact star rotates rapidly or not: the donor in Wray 977 does not rotate rapidly, even though almost half of its mass may have been accreted from its companion. If this slow rotation is generally the case, it may be used to discriminate between systems evolved via case A and case B evolution; more research is needed into this question, however.

9.1.19 Low-mass X-ray binaries

The problem in producing a high-mass X-ray binary, i.e. avoiding a disruption of the binary during the supernova event, holds even more for the low-mass X-ray binaries. Mass loss via a wind of a massive star will not bring its mass below the $1\,M_\odot$ of a low-mass companion. In order to keep the binary intact, one may have to invoke both a spiral-in phase and a rightly aimed kick velocity of the newly born compact star. An alternative that has been in vogue during the past few years is a quiet supernova explosion, when a white dwarf is pushed over the Chandrasekhar limit and implodes. Yet another alternative is evolution of a multiple system of three or more stars.

9.1.20 Origin of low-mass X-ray binaries via spiral-in

The spiral-in scenario was suggested first by van den Heuvel in 1983. Eqs. 9.30,9.31 show that the initial binary must have been rather wide if a merger is to be avoided. To avoid a merger, case C mass transfer is preferred above case B, as the core mass will be higher and the envelope mass smaller. Consider for example a star just massive enough to evolve into a neutron star, with an initial mass of $5\,M_\odot$. Suppose it evolves a carbon core of $2\,M_\odot$. A $1\,M_\odot$ companion to this core fits within its Roche lobe provided the semimajor axis is larger than $3.1\,R_\odot$. With Equation 9.31 we find that this requires a semimajor axis before spiral-in that is $190\,R_\odot$. A $5\,M_\odot$ star expands to the $100\,R_\odot$ required to fill its Roche lobe in this binary during the second giant ascent, i.e. mass transfer is case C (see Figure 9.6). The supernova explosion causes an eccentricity $e = 0.25$, if a $1.4\,M_\odot$ neutron star is formed without a kick velocity.

The main-sequence star is hardly affected by the spiral-in process, and emerges pretty much as it entered. Angular momentum losses may bring the $1\,M_\odot$ star in contact with its Roche lobe, provided the post-supernova orbit is not too wide. In a system with a longer orbital period, mass transfer can start only after the $1\,M_\odot$ star evolves away from the main sequence, and expands into a (sub)giant. The boundary between these two cases depends on the mechanism for loss of angular momentum. Thus, the spiral-in scenario does allow the formation of low-mass X-ray binaries. The crucial moment in the evolution is the moment of the supernova explosion. If the binary is to remain bound, not too much mass must be lost from the system with the explosion (see Equation 9.17). This may be the case if the core of the neutron star progenitor is not too massive, i.e. if the progenitor itself is not too massive, as in the example just described. Alternatively, a well-directed kick may help to keep the binary bound. Interestingly, collapse of a massive evolved core into a black hole may also make it easier for the binary to remain bound, as a smaller fraction of the mass is expelled in that case.

PSR1820 − 11 has already been mentioned as a possible high-mass radio pulsar binary. The available observations also allow the companion to the pulsar to be a low-mass main-sequence star; if so, the binary would be a progenitor of a low-mass X-ray binary, along the scenario just sketched.

9.1.21 Origin via accretion-induced collapse

Accretion-induced collapse of a massive white dwarf as a mechanism for the formation of a neutron star was first suggested by Whelan & Iben in 1973. The progenitor of a massive white dwarf must have a mass close to those of direct progenitors of neutron stars. The close binary is therefore formed through a spiral-in, very similar to the spiral-in just described: however, the core that emerges from the spiral in now evolves into a massive white dwarf, and avoids the supernova explosion. When mass transfer is initiated, either by loss of angular momentum or by expansion of the secondary into a (sub)giant, the white dwarf accretes mass until it transgresses the Chandrasekhar limit, at which point it implodes. Little mass is lost in the implosion; most of the loss in fact may come from the change in binding energy, which is roughly:

$$\Delta M \simeq \frac{3G{M_{wd}}^2}{5R_{ns}c^2} \simeq 0.2\,M_\odot \tag{9.37}$$

Table 9.3: Mass-radius relations and derived mass-orbital-period relations for low-mass X-ray binaries. Valid for donors in thermal equilibrium.

main sequence	$R_2/\,R_\odot \simeq M_2/\,M_\odot$	$P_b \simeq 8.9\,\mathrm{hr}\,M_2/\,M_\odot$
He main sequence	$R_2/\,R_\odot \simeq 0.2\,M_2/\,M_\odot$	$P_b \simeq 0.89\mathrm{hr}\,M_2/\,M_\odot$
white dwarf	$R_2/\,R_\odot \simeq 0.0115\,(M_2/\,M_\odot)^{-1/3}$	$P_b \simeq 40\,\mathrm{secs}\,M_\odot/M_2$

where M_{wd} is the mass of the white dwarf and R_{ns} the radius of the neutron star. The smaller mass loss makes it easier for the binary to survive the supernova explosion. It is often implicitly assumed that the kick velocity is also less for a neutron star formed by white dwarf collapse. As long as the mechanism causing the kick velocity is not known, however, there is no good reason for such an assumption.

Accretion-induced collapse as a mechanism to form a neutron star gained widespread recognition once it was realized that the magnetic field of the radio pulsar in old binaries was still in excess of 10^8G. Combined with the view that the magnetic field of a neutron star decays on a time scale of a few million years, this meant that there must be young neutron stars in old binaries: accretion-induced collapse can achieve this. It has recently become less clear, however, that the magnetic field of neutron stars does indeed decay so rapidly. In the absence of rapid decay of the magnetic field of neutron stars, there is no reason anymore to invoke accretion-induced collapse for the formation of low-mass X-ray binaries.

9.1.22 Relation between orbital period and donor mass

By combining Kepler's law Eq. 3.32 with Eq. 3.34, we get an approximate relation between orbital period and the mass and radius of the Roche-lobe-filling star:

$$P_{orb} \simeq 8.9\,\mathrm{hr}\left(\frac{R_2}{R_\odot}\right)^{3/2}\left(\frac{M_\odot}{M_2}\right)^{1/2} \tag{9.38}$$

Thus, by assuming a mass-radius relation for the donor star, we may determine its mass from the observed orbital period, as summarized in Table 9.3. In Fig 9.3 the known orbital periods for low-mass X-ray binaries are shown.

The equation giving the size of the Roche lobe Eq. 3.34, may also be combined with the equation for mass exchange in a binary Eq. 9.8, to give the change in the size of the lobe as mass is transferred. In stable mass transfer, the radius of the donor equals the radius of the Roche lobe, at all times in this process: $R_L = R_2$ and $\dot{R}_L = \dot{R}_2$ where the index 2 identifies the donor star. The change in radius of the donor star may be due to internal evolution of the star, or to the mass-transfer process. We may thus write

$$\frac{\dot{R}_L}{R_L} = \left(\frac{\dot{R}_2}{R_2}\right)_{ev} + \frac{d\ln R_2}{d\ln M_2}\frac{\dot{M}_2}{M_2} = 2\frac{\dot{J}}{J} - 2\frac{\dot{M}_2}{M_2}\left(\frac{5}{6} - \frac{M_2}{M_1}\right) \tag{9.39}$$

This equation shows that mass transfer may be driven by loss of angular momentum from the binary ($\dot{J} < 0$), or by expansion of the donor star ($\dot{R}_2 > 0$) due to, for example, the ascent of the donor on the (sub)giant branch, or due to irradiation of the donor. We discuss these possibilities in turn.

9.1.23 Evolution via loss of angular momentum

The low-mass X-ray binaries with orbital periods between 80 min and 9.0 h may have main-sequence donors with masses between $0.1\,M_\odot$ and $1.0\,M_\odot$, according to Table 9.3. These masses are less than the $1.4\,M_\odot$ characteristic for a neutron star. The evolutionary time scale of such low-mass stars are very long (see Eq. 9.3). As shown by Equation 9.8, the orbit of such a low-mass X-ray binary expands when mass is transferred conservatively from the donor. Unless the donor star expands more than its Roche lobe, this expansion will put an end to the mass transfer. It appears then that angular momentum must be lost from the binary to keep mass transfer going.

It was realized by Kraft et al. in 1962 that gravitational radiation provides a sufficiently high loss of angular momentum to drive observable mass transfer in a close binary. The loss of angular momentum via gravitational radiation may be written:

$$-\left(\frac{\dot{J}}{J}\right)_{GR} = \frac{32G^3}{5c^5}\frac{M_1 M_2 (M_1+M_2)}{a^4} \tag{9.40}$$

If we write the mass-radius relation of the donor star as $R_2 \propto {M_2}^n$, Equation 9.39 can be re-written as

$$-\frac{\dot{J}}{J} = -\frac{\dot{M}_2}{M_2}\left(\frac{5}{6}+\frac{n}{2}-\frac{M_2}{M_2}\right) \tag{9.41}$$

This equation assumes that no mass is lost from the binary; extension to the more general case is straightforward (see Equation 9.13).

By equating the loss of angular momentum with the loss due to the emission of gravitational radiation, we may combine Equations 9.40 and 9.41 to calculate the evolution of a low-mass X-ray binary. Mass-transfer rates can be calculated this way for main-sequence stars, with $n = 1$, and for white-dwarf donor stars, with $n = -1/3$. The results are shown in Figure 9.11, for the three types of donors given in Table 9.3, i.e. stars on the main sequence, stars on the helium main sequence, and white dwarfs.

For stars on the main sequence, the mass-transfer rate is about $\dot{M} \simeq 10^{-10} M_\odot\,\mathrm{yr}^{-1}$, for donor masses between 0.2 and 1 $M_\odot$. Stars on the helium main sequence are smaller, and fill their Roche lobes in more compact binaries, leading to higher mass-transfer rates. Consider a main-sequence donor star. The mass transfer causes this star to become less massive, and the binary thus evolves towards shorter periods. At some point, the mass of the donor becomes too small to sustain significant hydrogen burning, and the core becomes degenerate. At this point, which is reached for a donor mass of about $0.08\,M_\odot$, further mass loss of the donor causes it to expand. The orbit expands with it, according to Equation 9.38. Thus, the evolution of the orbital period passes through a minimum. Detailed calculations show that this minimum may be identified with the cutoff at around 80 min observed in the period distribution of cataclysmic variables.

A similar line of reasoning shows that binaries with donors that initially burn helium must also show a minimum period, which detailed calculations put at around 10 min.

The minimum period for a binary whose donor is a main-sequence star depends on the chemical composition of the core of this star. If its helium abundance is higher, the star is relatively more compact, and becomes degenerate at a smaller

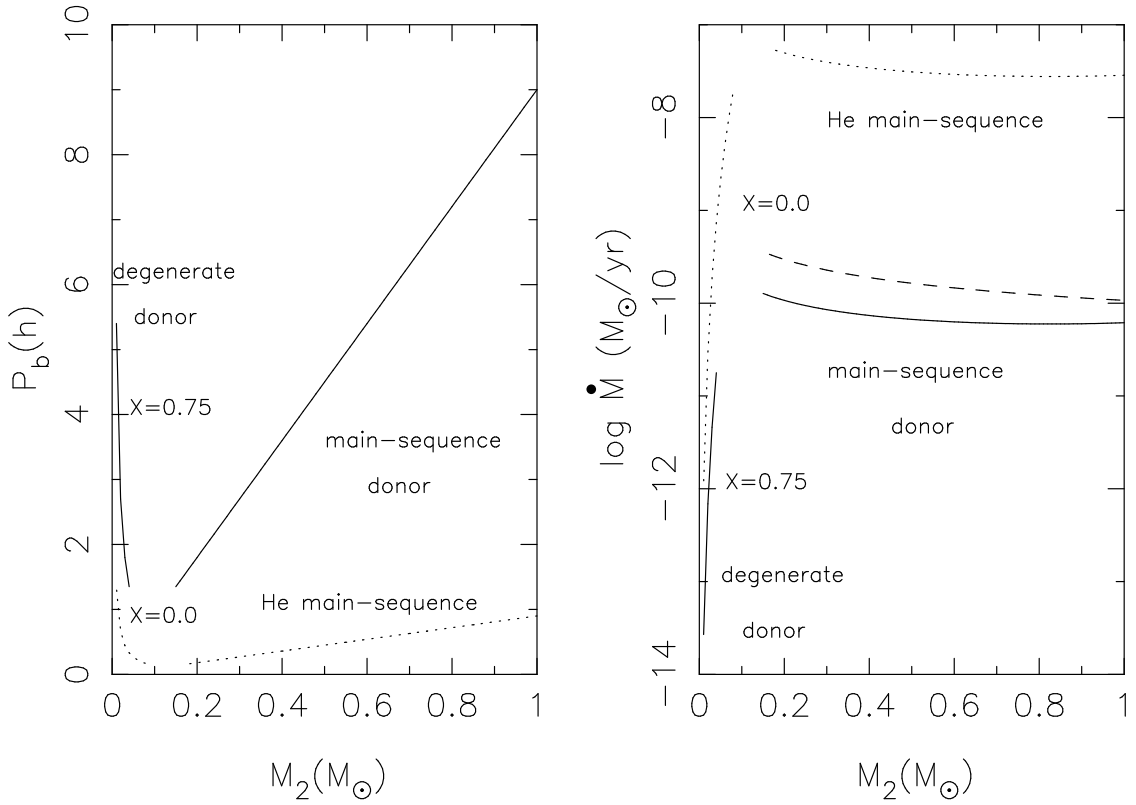

Figure 9.11: *Orbital period and mass-transfer rate as a function of donor mass M_2, for binary evolution driven by loss of angular momentum via gravitational radiation. For degenerate donors (shown for $M_2 < 0.15\,M_\odot$; solid and dashed lines for the indicated values of the hydrogen abundance) the orbital period increases and the mass-transfer rate drops precipitously, as the donor mass decreases. For main-sequence donors (shown for $M_2 > 0.15\,M_\odot$; solid and dashed line for stars on the hydrogen and helium main sequence, respectively) the orbital period decreases and the mass-transfer rate hardly changes, as the donor mass decreases. The mass-transfer rates shown all assume $M_1 = 1.4\,M_\odot$, except for the dashed line, which assumes that the mass receiver is a 7 $M_\odot$ black hole.*

radius. Thus, such binaries may evolve to periods shorter than 80 min. A main-sequence star with a helium-enriched core may be formed when the donor starts transferring mass to its companion very soon after expanding away from the main sequence. The mass loss stops further evolution of this donor star, which reverts to the main sequence, but with an enhanced He abundance in the core.

A number of low-mass X-ray binaries have X-ray luminosities well in excess of $10^{36}\,\mathrm{erg\,s^{-1}}$, and hence mass accretion rates well in excess of $10^{-10} M_\odot\,\mathrm{yr}^{-1}$, according to Equation 8.27. The orbital periods of several of these systems are too long for helium-burning donor stars, and more indicative of main-sequence donors. If one assumes that the currently observed $\dot{M}$ is also indicative of the $\dot{M}$ averaged over the time scale on which the binary evolves, such high mass-transfer rates require explanation. It is worthwhile to remark that many X-ray binaries have shown appreciable variability already during the few decades that X-ray observations have been possible, and to stress that therefore it is not possible to determine the long-term averaged values of $\dot{M}$. Nonetheless, the high observed values for mass-transfer

Table 9.4: Constants for the fits to the core-mass - radius and core-mass - luminosity relations for low-mass giants, according to Webbink, Rappaport and Savonije (1983).

	a_0	a_1	a_2	a_3	b_0	b_1	b_2	b_3	mass range
$Z = 0.02$	2.53	5.10	-0.05	-1.71	3.50	8.11	-0.61	-2.13	$0.16 < M_c/\,M_\odot < 0.45$
$Z = 0.0001$	2.02	2.94	2.39	-3.89	3.27	5.15	4.03	-7.06	$0.20 < M_c/\,M_\odot < 0.37$

rates in low-mass X-ray binaries and, less accurately, in cataclysmic variables have led to investigations of mechanisms that may enhance the mass-transfer rate with respect to the values given by gravitational radiation alone.

As suggested by Equation 9.41, any additional mechanism of loss of angular momentum increases the mass-transfer rate. A mechanism that has received appreciable interest is that of magnetic braking. Observations of single G stars show that the rotation of these stars slows down with age. It has been suggested that this is due to loss of angular momentum via the stellar wind of the stars. Even though the amount of mass lost with the wind is small, the concurrent loss of angular momentum may be appreciable, because the magnetic field of the star forces the wind matter to corotate to a large distance from the stellar surface. If the donor star in a binary loses angular momentum in this way, it will not be able to rotate slower, as it is kept in corotation with the orbit by tidal forces. Thus loss of angular momentum is transferred from the donor rotation to the orbital revolution, i.e. the binary loses angular momentum.

Whereas magnetic braking remains an attractive possibility to explain mass-transfer rates $\dot{M} \gtrsim 10^{-9} M_\odot\,\mathrm{yr}^{-1}$ in low-mass X-ray binaries with main-sequence-like donor stars, the details and actual efficiency of this process are not well understood. In view of our ignorance of long-term averages of $\dot{M}$, the necessity of a mechanism in addition to gravitational radiation in these low-mass systems should not be considered as established.

9.1.24 Evolution via donor expansion

A number of low-mass X-ray binaries, including the well-known systems Sco X-1 and Cyg X-2, have orbital periods in excess of 0.5 days, indicating that their donor stars are (sub)giants (see Fig. 9.3). In these systems, mass transfer is driven by the evolutionary expansion of the donor star. The radius and luminosity of a low-mass giant are determined mainly by its core mass. Results of detailed calculations can be represented with simple polynomial relations in $y \equiv \ln M_c/0.25\,M_\odot$:

$$\ln(R_2/\,R_\odot) = a_0 + a_1 y + a_2 y^2 + a_3 y^3 \tag{9.42}$$

$$\ln(L_2/\,L_\odot) = b_0 + b_1 y + b_2 y^2 + b_3 y^3 \tag{9.43}$$

The values of the fitting constants a_i, b_i depend on the metallicity of the star, and are given for two metallicities, for stars in the Galactic disk, and for stars in low-metallicity globular clusters, in Table 9.4.

The luminosity on the giant branch is almost completely due to hydrogen shell

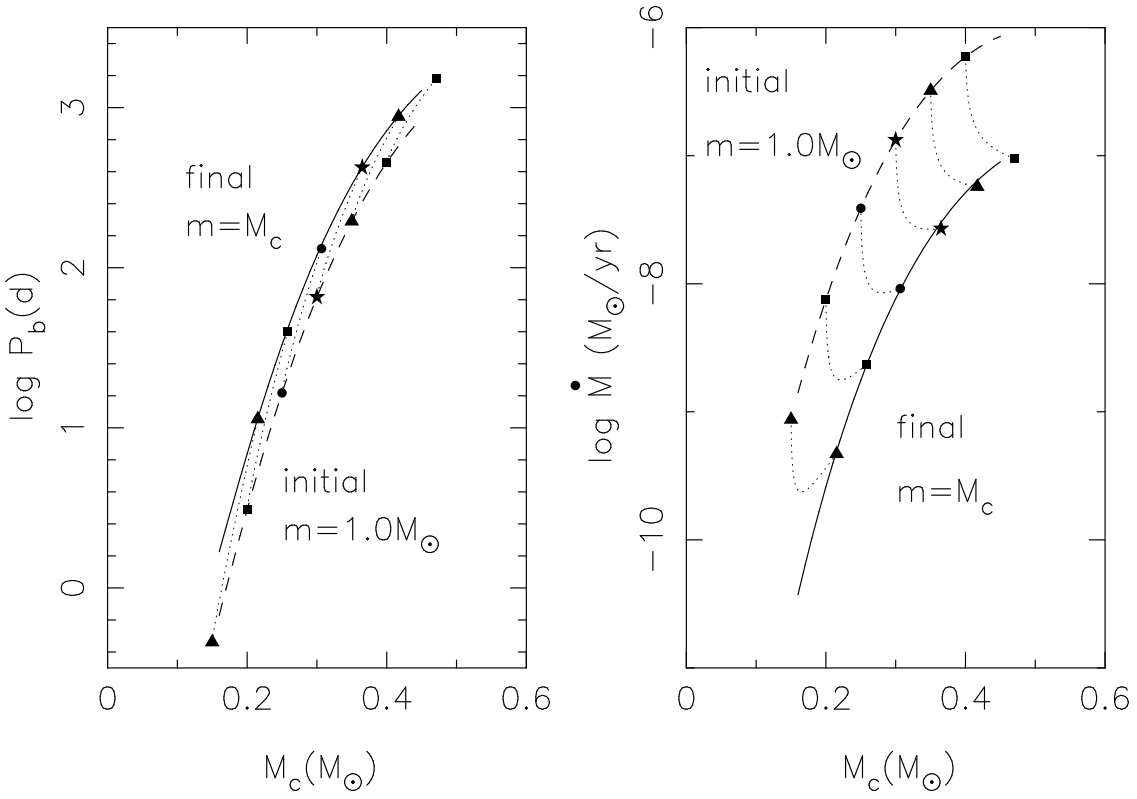

Figure 9.12: *Orbital period and mass-transfer rate as a function of the mass of the donor core M_c, for binary evolution driven by expansion of a giant donor star. The mass-transfer rates shown all assume $M_1 = 1.4\,M_\odot$ and $\dot{M}_1 = -\dot{M}_2$.*

burning, and is related to the core mass M_c by

$$\dot{M}_c \simeq 1.37 \times 10^{-11} \left(\frac{L}{L_\odot}\right) M_\odot\,\mathrm{yr}^{-1} \tag{9.44}$$

Combining Equations 9.42 and 9.44 gives the relation between the change in radius and the change in core mass:

$$\frac{\dot{R}_2}{R_2} = [a_1 + 2a_2 y + 3a_3 y^2]\frac{\dot{M}_c}{M_c} \tag{9.45}$$

In the absence of loss of angular momentum, Equation 9.39 may be rewritten

$$\frac{\dot{R}_2}{R_2} = -2\frac{\dot{M}_2}{M_2}\left(\frac{5}{6} - \frac{M_2}{M_1}\right) \tag{9.46}$$

which completes the set of equations required to calculate the binary evolution. The orbital period and the two masses determine the radius of the giant via Eq. 9.38 and hence its core mass via Eq. 9.42; the core mass determines the rate of radius expansion via Eq. 9.45, and with this the mass-transfer rate via Eq. 9.46. Thus the evolution can be calculated without resort to complete stellar evolution codes.

The results are shown in Figure 9.12 for $Z = 0.02$, the metallicity of ordinary disk stars. It is seen that there is a strong correlation between orbital period and mass-transfer rate: in a binary with a long orbital period, only a large giant fills its Roche lobe, and a large giant evolves more rapidly.

The simple calculations hold for stars beyond the subgiant branch; for subgiants, Eq. 9.44 doesn't apply. Equations 9.42 and 9.43 are valid for giants at thermal equilibrium. Detailed calculations show that this is a good approximation until the donor envelope has been almost fully exhausted.

9.1.25 Origin of low-mass binary radio pulsars

The evolutionary scenario for low-mass X-ray binaries with (sub)giant donors received strong confirmation with the discovery of radio pulsars in circular orbits with a very low mass-function, and hence a probable companion mass of $0.2 - 0.4\,M_\odot$ listed as low-mass binary radio pulsars in Table 9.2. The scenario discussed in the previous subsection automatically leads to such a binary: once the envelope of the giant donor is exhausted, the giant's core remains and cools into a white dwarf. The orbital period of the current binary sets the radius of the giant immediately prior to the end of mass transfer, and thus its core mass. Thus, the orbital period P_b of the radio pulsar should be correlated to the mass M_{wd} of its white-dwarf companion. Approximately:

$$P_b \simeq 8.4 \times 10^4 \,\mathrm{days} \left(\frac{M_{wd}}{M_\odot}\right)^{11/2} \tag{9.47}$$

valid for for circular orbits with $P_b \gtrsim 20\,\mathrm{days}$.

The low eccentricity of the orbits of low-mass binary radio pulsars indicates that orbital circularization must have occurred following the formation of the neutron star. The low mass-functions indicate white dwarf companions to the radio pulsars with masses lower than the $\simeq 0.6\,M_\odot$ expected for a white dwarf evolved from a single star. Both these observations are explained by the scenario in which a giant fills its Roche-lobe — causing strong tidal forces and hence rapid circularization, and transfers its envelope to the neutron star — thereby cutting off the growth of its core. The mass transfer also explains the short pulse period of the radio pulsars in these binaries as a consequence of the spin-up of the neutron star as it accretes mass from an accretion disk.

Interestingly, the realization that rapidly rotating radio pulsars may emerge from low-mass X-ray binaries came with the discovery of a single radio pulsar, PSR1937+21. Its extremely rapid rotation can be understood as the consequence of accretion of a substantial amount of mass $\gtrsim 0.1\,M_\odot$ from an accretion disk, by a neutron star with a low magnetic field. The magnetic field of PSR1937 + 21 is indeed low (see Table 9.2). In order to explain the absence of any companion, several destruction mechanisms were suggested. Detailed scrutiny of these mechanisms showed that none of them are convincing. The discovery of another millisecond pulsar brought a more likely solution: PSR1957 + 20 is heating its companion enough to evaporate it.

9.1.26 Recent developments

Three recent developments are changing our picture of the low-mass X-ray binaries. First, it has been found that several low-mass X-ray binaries have donors with masses that aren't as low (viz. $\leq 1M_\odot$) as hitherto assumed for low-mass X-ray binaries. For example, the black-hole binary GRO J1655 − 40 has donor with a mass of about $2.3\,M_\odot$. It would appear that the donor must be a subgiant to fill

its Roche lobe in the 2.6 d orbit. However, accurate radius determinations of main-sequence stars in double-lined eclipsing binaries show that stars with masses in the range 2-4 $M_\odot$ expand sufficiently on the main-sequence to explain mass transfer from a main-sequence star in GRO J 1655 − 40.

Secondly, the observation of black-hole binaries in low-mass systems with evolved donors implies that there are many times more – in the ratio of the main-sequence life time to the giant life time, i.e. a factor ~ 100 – black hole binaries with an unevolved companion which doesn't fill its Roche lobe. This has obvious consequences for the estimated birth rate of black-hole binaries.

And finally, the Wide Field Camera on board of the BeppoSAX X-ray satellite has discovered relatively dim X-ray transients, with peak luminosities $\leq 10^{37}$ erg/s, thanks to its unique combination of a large field of view and small angular separation. Most of these dim transients are bursters, i.e. neutron stars, which confounds the recent speculations that the vast majority of X-ray transients with low-mass donors are black hole systems.

9.1.27 X-ray sources in globular clusters

While one can assume in the galactic disk that the two stars in a binary evolved from their progenitors in the same binary, this need not be true in the dense core of a globular cluster. In the core, the stars may be so closely packed that encounters between the binary and other cluster stars become an important factor in its development. Routes of binary evolution are thus opened that are not available to binaries in the galactic disk.

That something special is happening in globular clusters is obvious from the census of X-ray sources in our Galaxy. Some ten percent of the X-ray binaries that we know are located in globular clusters, even though the clusters only contain about 10^{-4} of the number of stars of our Galaxy. A similar situation holds for the nearby galaxy M31, in which about 20 out of several hundred X-ray sources are located in globular clusters. Recycled radio pulsars are also present in globular clusters in larger numbers than expected from simply scaling with total numbers of stars. In the cluster 47 Tuc alone, 10 such pulsars have been discovered.

The observation that the X-ray sources are located especially in the clusters with the densest cores points to close encounters between stars as the physical mechanism for the formation of binaries with neutron stars. Two mechanisms have been proposed: tidal capture of neutron stars by ordinary stars in a two-body interaction, and the exchange of an ordinary star in a binary by a neutron star in a three-body interaction.

9.1.28 Tidal capture

The basic principle of tidal capture can be understood with a simple calculation: consider a neutron star with mass m and velocity v at large distance ('infinity') relative to a target star with mass M and radius R. The relative kinetic energy E_k of the two stars is given by

$$E_k = \frac{1}{2}\frac{mM}{m+M}v^2 \tag{9.48}$$

As the neutron star closes in on the target star, it causes this star to deform. The height h of the bulge, and its mass m_t can be estimated for distance d with

$$h \simeq \frac{m}{M}\frac{R^4}{d^3}; \qquad m_t \simeq k\frac{h}{R}M \simeq k(\frac{R}{d})^3 m \tag{9.49}$$

where k is the apsidal motion constant, which depends on the central condensation of the star, and indicates how easy it is to deform the star (see, e.g., Schwarzschild, *Structure and evolution of the stars*, 1958). For a star with a deep convective envelope $k \simeq 0.14$. Thus the energy E_t in the tidal deformation is of order

$$E_t \simeq m_t \frac{GM}{R^2} h \simeq k\frac{Gm^2}{R}\left(\frac{R}{d}\right)^6 \tag{9.50}$$

If $E_t > E_k$, the two stars cannot escape from one another anymore, and a binary is formed. This condition can be written:

$$d \lesssim 3R\left(\frac{k}{0.14}\frac{m}{M}\frac{m+M}{2M_\odot}\frac{R_\odot}{R}\right)^{1/6}\left(\frac{10km\ s^{-1}}{v}\right)^{1/3} \tag{9.51}$$

Because of the strong dependence of E_t on d, this rough estimate is in fact pretty accurate, as more detailed calculations confirm.

The initial binary orbit is highly eccentric, with $e \lesssim 1$, and with a velocity at periastron close to the escape velocity. Tidal forces are expected to circularize the orbit, during which process angular momentum is conserved. For an initial periastron velocity less than the escape velocity, the semi-major axis of the circularized orbit is given by

$$a_c \leq 2d \tag{9.52}$$

Thus the final orbital after circularization can have a semimajor axis of up to two times the capture distance.

The cross section σ for closest passage within distance d follows from conservation of energy and angular momentum in a Keplerian orbit:

$$\sigma = \pi d^2\left(1 + \frac{2G(m+M)}{v^2 d}\right) \simeq \pi d\ \frac{2G(m+M)}{v^2} \tag{9.53}$$

The second term within brackets gives the effects of gravitational focussing. This term dominates for the small relative velocities between stars in globular clusters, which justifies the subsequent approximation.

With number densities n_c and n for the neutron and target stars, respectively, the capture rate of neutron stars per unit volume can be written:

$$\Gamma = n_c n v\sigma \simeq 6\times 10^{-11}\frac{n_c}{10^2 pc^{-3}}\frac{n}{10^4 pc^{-3}}\frac{m+M}{M_\odot}\frac{3R}{R_\odot}\frac{10km\ s^{-1}}{v}\ yr^{-1}pc^{-3} \tag{9.54}$$

To obtain the formation rate in a cluster, one must integrate Eq. 9.54 over the cluster volume. To give an idea of the characteristic numbers, a simple example may do. In a relatively dense core of a globular cluster, $n_c \sim 100\mathrm{pc}^{-3}$ and $n \sim 10^5\mathrm{pc}^{-3}$. With a characteristic core volume of $\sim 1\mathrm{pc}^3$ it follows that a close binary with a neutron star is formed every 10^9yr. For an average life time of a bright source of 10^9yr, we then expect to see of order 1 X-ray source in such a cluster, in accordance with observations.

The capture cross section for a main-sequence star or for a white dwarf is similar to that for a neutron star. The relative numbers of main-sequence stars, white dwarfs, and neutron stars captured in a cluster core are therefore roughly proportional to their respective number densities. In the galactic disk, on the other hand, binaries with white dwarfs and neutron stars rarely arise from binary evolution, as compared to the formation of single white dwarfs or neutron stars. Therefore, the fraction of main-sequence stars captured into a binary in globular clusters is small compared to the fraction of main-sequence stars in binaries in the galactic disk, but the fraction of white dwarfs and especially of neutron stars captured into binaries in globular clusters is very high compared to the fraction in binaries in the galactic disk.

9.1.29 Exchange collisions

For many years no binaries, other than the X-ray sources, were known in globular clusters. With the improved spatial resolution of recent telescopes and software techniques, and with the improved accuracy of photometry with CCDs, a growing number of ordinary binaries is now being discovered. This leads to another way of getting a neutron star in a binary: when a neutron star approaches a binary to a distance comparable with the semi-major axis of the binary, the three stars may temporarily move in complicated orbits around one another. Such a three-body system is not stable, and one star is ejected at the end, usually the lightest star. In this way, a neutron star may take the place of an ordinary star in a binary. If mass is transferred in the binary newly containing a neutron star, an X-ray source becomes visible. Once the mass transfer stops the neutron star may switch on as a pulsar. It is also possible that both original members of a binary are exchanged for a neutron star, and form a binary of neutron stars. The recoil velocity of the three-body interaction may be large enough to explain that the neutron-star binary in M15 is some distance away from the cluster core.

The frequency of such encounters is proportional to the number density of binaries in the cluster core, and to the sizes of these binaries. Roughly:

$$\Gamma \simeq 5 \times 10^{-10} \frac{n_c}{10^2 pc^{-3}} \frac{n_{bin}}{10^2 pc^{-3}} \frac{m}{M_\odot} \frac{a}{1\,AU} \frac{10km\ s^{-1}}{v}\ yr^{-1} pc^{-3} \tag{9.55}$$

when all three masses are equal to m. The smaller numbers of binaries can be offset by their larger size, as compared to single stars.

9.1.30 Destruction of stars

In the last years it has been suggested that tidal capture may be less efficient in forming binaries than previously thought. One reason for this is that the energy dissipated as the orbit of the neutron star is circularized is comparable to the total binding energy of the main-sequence star, or of the giant's envelope. A simple estimate may serve to illustrate this. Consider a star of mass M and radius R that captures a compact star of mass m. Immediately after capture, the orbit has a large semi-major axis a_e, as its eccentricity is close to unity. As tidal interaction circularizes the orbit, angular momentum is conserved, and this allows us to derive that the radius a_c of the circularized orbit is twice the distance of the initial close

passage, i.e. $a_c << a_e$. Thus the energy difference ΔE between the initial, highly eccentric, and the final circularized orbit is comparable to the binding energy E_* of the main-sequence star.

$$\frac{\Delta E}{E_*} = \left(\frac{-GMm}{2a_e} - \frac{-GMm}{2a_c} \right) / \left(\frac{3GM^2}{5R} \right) \simeq \frac{5}{6} \frac{m}{M} \frac{R}{a_c} \tag{9.56}$$

The circularization process provides enough energy to destroy the main-sequence star.

Whether this really happens is currently the subject of debate. If the energy has to be dissipated very rapidly, it is hard to avoid destruction of the donor. It has been suggested recently, however, that the energy present in the tidally induced oscillations of the star can be fed back into the orbit; in the very eccentric orbit, the energy exchange between (oscillations in) the star and the orbit is chaotic. This would mean that the star has much more time to dissipate, and thus has a much better chance to survive.

If the number of encounters between stars is directly proportional to the closest distance (Eq. 9.53), and if capture occurs out to three times the stellar radius (Eq. 9.51), then one in three captures correspond to a direct collision between the stars. If a neutron star thus hits a main-sequence star, it will completely destroy it. Perhaps a disk forms around the neutron star, and if enough matter from this disk can be accreted, the end result will be a single recycled radio pulsar. About half of the recycled radio pulsars in globular clusters indeed is single, and this is a possible way to make them.

If a neutron star directly hits a giant, then the core of the giant and the neutron star may spiral-in towards one another, leaving a close binary of an undermassive white dwarf and a neutron star. Two orbital periods of X-ray binaries in globular clusters have been determined to be very short: one at 11 minutes in NGC 6624 and 20 or 13 minutes in NGC 6712. These are neutron stars accreting from very low-mass white dwarfs (see Table 9.3).

Collisions can also occur in the temporary triple system formed when a single star encounters a binary, or in the quadruple system formed in the encounter between two binaries....

The relative importance of various possible processes to form X-ray binaries and to recycle pulsars in globular clusters is a subject of active investigation.

9.1.31 Literature

The book *Compact stellar X-ray sources*, eds. W.H.G. Lewin and M. van der Klis, gives a good overview of our observational and theoretical knowledge of X-ray binaries. Further useful articles are those by F. Verbunt 1993 Ann.Rev.A.A. 31, 93 on the formation and evolution of X-ray and radio pulsar binaries; and by E.S. Phiney and S.R. Kulkarni 1994 Ann.Rev.A.A. 32, 591 on recycled radio pulsars. P. Hut et al. 1992 PASP 104, 981 give an extensive review on binaries in globular clusters. Long-term studies of bright X-ray sources are made with the BATSE instrument on GRO; a beautiful study of pulse periods is given by Bildsten et al. 1997, ApJ Suppl. 113, 367.